

SWITCHED RELUCTANCE MACHINE

AS A VARIABLE-SPEED DRIVE

Jasmin Čorda
2

Submitted in fulfilment of the requirements for
the Degree of Doctor of Philosophy

The University of Leeds
Department of Electrical and Electronic Engineering

May 1979

ABSTRACT

This thesis is concerned with the theoretical and experimental investigation and development of a new variable-speed switched reluctance motor drive for industrial and traction applications intended to provide a more attractive alternative than is available using existing systems.

The new drive is 'brushless' and is distinguished by the simplicity of both the motor and the power electronics. It is capable of both motoring and regenerative operation with high performance over a wide speed range.

THE RESEARCH REPORTED HEREIN WAS
PERFORMED IN THE DEPARTMENT OF ELECTRICAL
AND ELECTRONIC ENGINEERING OF THE
UNIVERSITY OF LEEDS IN THE PERIOD
BETWEEN OCTOBER 1976 AND MAY 1979

ACKNOWLEDGEMENTS

The author is indebted to Professor P J Lawrenson, Head of the Department of Electrical and Electronic Engineering of the University of Leeds, for arranging a University scholarship and the Departmental facilities to carry out the research.

The University of Leeds provided funds to make the research possible.

The author expresses his deep gratitude to Dr J M Stephenson, a man of wide scientific and academic experience, whose supervision and suggestions have been of enormous value and to Dr N N Fulton for valuable advice, information and comment. They have been helpful throughout all research and preparation of the thesis.

The author also appreciates the encouragement of members of the Universities of Sarajevo and Zagreb, of colleagues of the University of Leeds and of his family.

LIST OF PRINCIPLE SYMBOLS

B	flux density
c	back iron width
d	rotor diameter
d_o	stator outside diameter
g	air-gap length
g_i	rotor interpolar air-gap length
I, i	current
J	moment of inertia
k_c	'early switch-on' coefficient
k_d	'dead zone' coefficient
k_e	'early switch-off' coefficient
L	inductance
L_i	maximum inductance
L_o	minimum inductance
ℓ	core length
N	number of turns
N_r, N_s	numbers of rotor and stator poles
n	speed $\left[\frac{\text{rev}}{\text{min}} \right]$
P_i, P_o	permeances corresponding to L_i and L_o
P_{in}, P_{out}	input and output powers
q	number of phases
r	rotor pole arc
s	stator pole arc
T	torque
t	time
V, v	voltage
Ψ'	magnetic co-energy
α	the ratio of L_i/L_o ($= P_i/P_o$)
δ	stator pole pitch
ϵ	angular displacement between two consecutive phases
Ψ	flux-linkage
ω	angular velocity
θ	rotor angle
θ_c	'switch-on' angle
θ_{con}	conduction angle
ϕ	rotor pole pitch (angle of complete cycle)

SI units are used throughout

CONTENTS

	<u>Page</u>
1. INTRODUCTION	1
2. DESCRIPTION OF MACHINE PRINCIPLES OF OPERATION STUDY OF BASIC DESIGN PARAMETERS	6
2.1 Introduction	6
2.2 Basic elements of construction	6
2.3 Idealised inductance variation	7
2.4 Basic principles of operation	8
2.5 Switching circuits	11
2.6 Derivation of necessary conditions for self- starting, symmetrical reversible performance	14
2.6.1 Deductions from rotor and stator pole geometry	14
2.6.2 Practical implications of the conditions	16
2.7 Derivation for preferable conditions for design parameters	18
2.7.1 Rotor and stator pole arcs	18
2.7.2 Number of rotor poles	18
2.8 Examples to illustrate the conclusions of 2.6 and 2.7	19
2.9 Flux waveforms	22

2.10	Number of phases	24
2.11	Effect of grading the rotor pole profile	25
2.12	Conclusions	27
3.	ANALYTICAL ESTIMATION OF THE MINIMUM AND MAXIMUM INDUCTANCES OF DOUBLY-SALIENT MACHINE	29
3.1	Introduction	29
3.2	General approach	29
3.3	Estimation of the minimum inductances	31
3.3.1	Parameters of the magnetic configuration	34
3.3.2	Calculation of the minimum inductance components	38
3.3.3	Fringe flux at the ends of core Effective core length	43
3.3.4	Comparison of estimated and measured results	44
3.4	Recommendation for the rotor profile	45
3.5	Estimation of the maximum inductance using B-H curve	47
3.6	Conclusions	49
4.	LINEAR ANALYSIS OF SWITCHED RELUCTANCE MOTOR	50
4.1	Introduction	50
4.2	Assumptions and approach to the analysis	50

4.3	Derivation of the expressions for torque and mean and rms primary and secondary currents	53
4.4	Linear optimisation of a switched reluctance motor	62
4.4.1	Basic equations and constraints imposed upon parameters	62
4.4.2	Optimisation of torque with respect to peak flux density at selected values of rotor diameter and core length	65
4.4.3	Optimisation of torque with respect to primary rms current at a given voltage	70
4.5	Speed control of a switched reluctance motor	72
4.5.1	Speed control by voltage	73
4.5.2	Speed control by switching angles	73
4.6	Regenerative mode of operation of switched reluctance machine	77
4.7	Conclusions	78
5.	DESIGN AND PERFORMANCE OF EXPERIMENTAL MOTORS	79
5.1	Introduction	79
5.2	Design philosophy of an experimental motor	79
5.2.1	Stator pole arc and pole profile	80
5.2.2	Rotor pole arc and pole profile	80
5.2.3	Back iron width	81

5.2.4	Air-gap length	81
5.2.5	Stator outside diameter, rotor diameter and core length	81
5.2.6	Primary to secondary turns ratio	82
5.2.7	Primary to secondary copper cross-sectional area	82
5.2.8	Number of turns per phase	83
5.2.9	Wire diameter	85
5.2.10	Primary and secondary coil resistances	86
5.3	Motor assembly	86
5.3.1	Stator assembly	86
5.3.2	Rotor assembly	87
5.3.3	Rotor-position sensor	87
5.3.4	Complete assembly	87
5.4	Inductances	89
5.4.1	Method of measurement	89
5.4.2	Results of measurement	90
5.4.3	Observations on the shape of the $L(\theta, i) \Big _{i=\text{const}}$ curves	90
5.4.4	Observations on the shape of the $\Psi(\theta, i) \Big _{\theta=\text{const}}$ curves	92

5.4.5	Comparison of motors	93
5.4.6	Mutual inductances	94
5.5	Static torque	94
5.5.1	Method of measurement and test results	95
5.5.2	Observations from the static torque curves	95
5.5.3	Comparison of motors	96
5.6	Running performance: base speed to top speed	96
5.6.1	Equipment and methods	96
5.6.2	Test results	98
5.6.3	Comparison of motors	100
5.7	Graphical prediction of current waveform	102
5.8	Conclusions	103
	Appendix 5A	105
6.	NON-LINEAR MODEL OF DOUBLY-SALIENT RELUCTANCE MOTOR	107
6.1	Introduction	107
6.2	Model equations	108
6.3	Review of known methods	109
6.4	New improved method	113
6.4.1	Voltage equations	113

6.4.2	Method of solution	114
6.4.3	Production of table $i(\theta, \psi)$ Quadratic interpolation	115
6.4.4	Numerical solution of the model equations	117
6.4.5	Computation of instantaneous torque	120
6.4.6	The program arrangement	122
6.4.7	Choice of number of elements in input table $\psi(\theta, i)$	122
6.4.8	Choice of number of integration steps	124
6.4.9	Comparison between computed and measured results	125
6.5	Conclusions	127
	Appendix 6A	129
	Appendix 6B	131
	Appendix 6C	132
7.	APPLICATION OF THE NON-LINEAR MATHEMATICAL MODEL	134
7.1	Introduction	134
7.2	Searching for the optimum switching angles using computed results	134
7.3	Finding the current needed for producing base torque at standstill	136

7.4	Effects of changing the number of turns on the performance of the machine	136
7.5	Computational design procedure	140
7.5.1	Design method	140
7.5.2	Production of the $\psi(\theta, i)$ table	141
7.5.3	Basic design procedure	143
7.6	Conclusions	146
8.	PROTOTYPE OF VOLTAGE CONTROLLED DRIVE	148
8.1	Introduction	148
8.2	Rotor-position sensor	148
8.3	Converter	151
8.3.1	Switching unit and overcurrent detector	152
8.3.2	Frequency-voltage converter	152
8.3.4	Mode selector	153
8.3.5	DC chopper	153
8.4	Drive assembly	154
8.5	Performance of the motor	154
8.6	Conclusions	156
9.	CONCLUSION	157
	REFERENCES	159

CHAPTER 1

INTRODUCTION

There is a very great demand in industry and traction applications for a motor which can provide controlled power over a very wide range of speeds. This thesis is concerned with the development of a new drive intended to provide a more attractive alternative than is available using existing systems.

The dc commutator motor predominates among variable-speed drives for industrial and traction applications, because of its flexible high performance over a wide speed range and relative simplicity of the associated power electronic. However, the complexity of the motor and in particular the mechanical commutator, result in an expensive machine with the added disadvantage of the need for routine servicing.

With the development of high-voltage, high-current semi-conductor switching devices many attempts have been made to find a 'brushless' alternative for the dc commutator motor. Particular advantages of such a motor are its greater reliability, reduced maintenance and the ability to operate submerged and in hazardous environments. However, the basic design objective of alternative variable-speed systems is that the saving on the cheaper ac motor should compensate for the additional cost of the more complex power electronic circuitry needed and so yield a commercially attractive alternative to dc systems in general, variable-speed, industrial applications.

The combination of a thyristor or transistor inverter with a simple induction motor with a cage rotor has been developed to fulfill the above requirements. The complexity and cost of the variable-frequency inverter are the main reasons for them still being generally uncompetitive with dc drives.

Another example of a brushless drive is the combination of a thyristor or transistor inverter with a simple reluctance motor with a conventional 3-phase winding. When the winding of this machine is supplied with bidirectional currents from a variable-frequency inverter it

produces a travelling field which 'pulls' the rotor synchronously with the supply frequency. The inverter for this drive is equally complex and costly as that for induction motor drives.

There is clearly a need for a brushless drive which uses simpler and cheaper power electronics than is involved in the conventional 3-phase inverter with its 6 main switching devices.

If the motor can be derived which requires only unidirectional currents in its windings then only one switching device per phase may be required. When the conventional polyphase reluctance motor is supplied with unidirectional currents a simple travelling field is not established and flux reversals take place in the rotor. The losses in the rotor cage winding would be intolerable at higher speeds. However, with rotor position switching, which gives a 'series' characteristic to the drive, it would be possible to dispense with the rotor winding.

There is however a basic difficulty in the operation of this type of motor with unidirectional excitation. This arises from the use of the distributed stator winding which inevitably has large mutual inductances between the phase windings. Whereas with bidirectional excitation the mutual inductances contribute to the development of positive torque, the opposite applies with unidirectional excitation⁽⁹⁾.

Small motors which are designed to be operated on electronically switched supplies with unidirectional excitation and which are based on the changing inductance of stator coils wound on salient poles as salient rotor poles move past, are a well known form of stepping motor. If the switches are operated according to the position of the rotor poles relative to those of the stator and the motor is designed for continuous variable-speed running rather than stepping, then the machine is called a switched reluctance motor. The reasons why the stator coils are switched according to the position of the rotor poles are that in this way the appropriate torque is always produced (even at zero speed) and that resonance and instability problems are avoided.

In 1974 Unnewehr and Koch⁽⁵⁾ described a disc type of switched reluctance motor developed for vehicle traction applications. Separate

stacks of laminations for each phase were used to avoid mutual inductance between phases. The principle drawback of this form of motor is the complexity of the construction compared with the conventional radial air-gap machines. It does not meet the requirements of cheapness and ruggedness.

Consideration of the simple single-stack switched reluctance motor with an equal number of north and south poles (diametrically opposite) for each phase, assuming infinitely permeable iron shows that there is no tendency for flux excited by one phase to link with any other phase, since the rotor magnetic potential is zero. It is therefore possible to obtain efficient operation of this form of machine with unidirectional excitation. Such a machine has extremely simple construction: salient poles on both the stator and rotor; no coils slots or moving coils; spool wound excitation coils on the stator poles.

An analysis of the 2-phase single-stack switched reluctance motor for fractional horsepower applications has been presented by P T Blenkinsop⁽¹⁾ in his doctoral thesis. Initial investigation of an experimental motor revealed the concept to be feasible and showed that this type of motor is capable of producing specific outputs comparable with a wide range of small motors. The analysis brought basic understanding of the motor operation but was related to the 2-phase motor in which the magnetic circuit was not highly saturated. This analysis revealed that the simplicity of the motor's construction concealed a number of complex interactions between electrical and dimensional parameters, several of which could be adjusted to improve performance. A comprehensive consideration of the effect of these parameters on motor performance in variable-speed operation was not made. The most significant result of Blenkinsop's work is that the switched reluctance motor is capable of matching the performance of a Universal motor of similar dimensions.

In a paper by Byrne and Lacy⁽⁶⁾ in 1976 the fundamental principles of energy conversion in saturable variable-reluctance devices were presented and the basic construction of a 5 [kW], 2-phase, single-stack switched reluctance motor which exploited saturation to improve

performance was described briefly. Such a motor could rotate only in one direction.

Bausch and Rieke⁽⁷⁾ presented a brief description of various power electronic circuits for switched reluctance motor in a paper published in 1976.

In 1977 Koch⁽³²⁾ gave a basic, linear, theoretical treatment of a single-stack, 3-phase switched reluctance motor. The treatment was however seriously incomplete in that it failed to recognise the negative torque developed during part of the operating cycle and optimum modes of operation.

Finally Bausch and Rieke⁽³³⁾ have given in 1978 a further brief description of their 4-phase, 2-stack motor using their novel drive system and multiple saliencies to give low-speed running after the manner well known in stepping motors.

None of the published work gives a general consideration of machine geometry or the effect of various electrical and dimensional parameters on motor performance. In order to achieve high performance in a switched reluctance motor over a wide range of power and operating conditions, a broad understanding of the machine operation and behaviour must first be achieved. This, together with accurate mathematical modelling of the machine, would provide the necessary background for the design of a switched reluctance motor system which would be expected to be comparable with a dc motor system. These are the main objectives of this thesis.

The work of the thesis is presented in 9 chapters. A description of the machine, principles of operation, various switching circuits and an original study of the basic interactions of the main design parameters are presented in Chapter 2.

The analytical method for the estimation of minimum and maximum inductances, which are essential parameters for machine analysis and design, are given in Chapter 3.

The comprehensive machine analysis and speed control, when magnetic saturation of the iron and winding resistances are neglected, are established in Chapter 4.

Chapter 5 covers the design, measurement and analysis of performance of a series of experimental motors to meet a traction type of

torque-speed characteristic.

The mathematical model of the machine which takes into account magnetic saturation of the iron and a comparison of its accuracy against experimental results are presented in Chapter 6.

Chapter 7 establishes a design procedure based on the use of the non-linear mathematical model and the estimation of the minimum and maximum inductances.

Chapter 8 covers the design of a prototype rotor-position sensor and convertor for a voltage controlled drive and its measured performance.

Finally, the main conclusions of the thesis are summarised in Chapter 9.

CHAPTER 2

DESCRIPTION OF MACHINE PRINCIPLES OF OPERATION

STUDY OF BASIC DESIGN PARAMETERS

2.1 Introduction

The object of this chapter is to show how a machine with an extremely simple magnetic structure and excitation may be employed as a variable speed drive when supplied via controllable switching devices.

Having described the machine and switching circuits and principles of operation, a study of the basic interaction of the main design parameters of a doubly salient switched reluctance motor is presented. It appears that there is no comprehensive treatment of this subject in the literature. The necessary condition imposed on basic design parameters (stator and rotor pole number, stator and rotor pole arcs) are derived with respect to fundamental necessities for motor operation. Optimum conditions are considered and specific recommendations are given.

2.2 Basic elements of construction

The basic construction of the single-stack, cylindrical type switched reluctance motor is shown in Fig 2.1. The motor consists of a rotor, assembled on a shaft and mounted in bearings, and the stator assembly. The rotor possesses salient poles surrounded by the stator salient poles. The number of rotor poles is different from the number of stator poles. To minimise the effect of eddy-currents in the stator and rotor, the motor is constructed from thin steel laminations in the conventional manner.

Each stator pole holds a spool type winding (all windings are identical). Diametrically opposite pairs of pole windings are connected in series and each pair forms one phase winding. Each phase requires at least one switching device to control its supply. (The phase current flowing through the switching device and the winding is unidirectional.) The switching devices (normally semiconductor devices) are switched in

response to signals from a rotor-position sensor mounted on the shaft. An optical system comprising an infra-red emitter and a photo-transistor has been found suitable.

Thus the motor, rotor-position sensor and switching unit form a closed-loop system shown by block-diagram in Fig 2.2.

2.3 Idealised inductance variation

Fig 2.3 shows the geometry of the developed airgap of the machine. It is initially assumed that the iron of the machine is ideal (ie the permeability of iron $\mu_{Fe} = \infty$). With this assumption and the additional assumption that inductance varies piece-wise linearly against rotor angular displacement θ the diagram (a) in Fig 2.4 shows the variation of inductance of two successive phases against angle θ . The complete cycle of changing inductance occurs over $O'D'$ and corresponds to the angular rotation of the rotor through one rotor pole pitch. During that cycle the following typical regions of changing inductance may be observed:

- a) the region OA where no part of the rotor pole is under the stator pole (ie the inductance has a minimum value, L_0);
- b) The region AB where the leading edge of the rotor pole is under the stator pole (ie the slope of inductance, $\frac{dL}{d\theta}$, is + ve);
- c) the region BC where the arc of the rotor pole is fully overlapped by the stator, or vice versa, depending on the relative sizes of the rotor pole arc 'r' and stator pole arc 's' (ie the inductance has a maximum value, L_i);
- d) the region CD where the trailing edge of the rotor pole is under the stator pole (ie the slope of the inductance, $\frac{dL}{d\theta}$, is - ve).

The angle of complete cycle, $O'D'$, is given by

$$O'D' = \phi = \frac{2\pi}{N_r} \quad (2.1)$$

where N_r is number of rotor poles.
From Fig 2.4(a) it can be seen that

$$A'B' = C'D' = \min(r, s) \quad (2.2)$$

where r is rotor pole arc and
 s is stator pole arc

The angle $B'C'$ (commonly referred to as the 'dead zone') is

$$B'C' = |r - s| \quad (2.3)$$

Then the parameter k_d may be defined as the ratio of the dead zone to the smaller of the stator or rotor arcs, ie

$$k_d = \frac{|r - s|}{\min(r, s)} \quad (2.4)$$

Again from Fig 2.4(a)

$$O'A' = O'D' - (2A'B' + B'C') = \frac{2\pi}{N_r} - (2 + k_d) \min(r, s) \quad (2.5)$$

2.4 Basic principles of operation

In a switched reluctance machine the torque is produced purely by reluctance forces. As different phase windings are excited, the rotor moves in response to a reluctance torque, seeking the nearest stable equilibrium position. Since the numbers of stator and rotor poles are different, the rotor continues to rotate if the phases are excited in the appropriate pattern.

A feature of this type of reluctance motor is the *very small* mutual coupling between phase windings which enables the motor to be analysed under steady-state conditions by considering the action of one phase alone and using super-position. (It has been shown in Reference No 9 that the presence of mutual coupling reduces motor torque when the motor is excited with unidirectional currents.) Thus at any instant of operation the voltage, current, resistance and inductance of the phase winding are related by the equation

$$v = Ri + \frac{d}{dt} (Li) \quad (2.6)$$

In a reluctance machine the inductance varies with angular displacement (θ) of the rotor and hence with time. Consequently equation (2.6) becomes

$$v = Ri + i \frac{dL}{dt} + L \frac{di}{dt} \quad (2.7)$$

Hence the power into the winding at any instant is

$$P_e = vi = i^2 r + i^2 \frac{dL}{dt} + iL \frac{di}{dt} \quad (2.8)$$

The energy stored in a magnetic field is

$$W_m = \frac{1}{2} L i^2 \quad (2.9)$$

and the power transferred to the field is

$$P_m = \frac{dW_m}{dt} = \frac{1}{2} i^2 \frac{dL}{dt} + L i \frac{di}{dt} \quad (2.10)$$

Of the electrical power available, $i^2 r$ is dissipated as heat, P_m is transferred to the magnetic field and the remainder is available as mechanical work. Hence output power

$$P_{out} = P_e - P_m - i^2 r = \frac{1}{2} i^2 \frac{dL}{dt} = \frac{1}{2} i^2 \frac{dL}{d\theta} \frac{d\theta}{dt} \quad (2.11)$$

$\frac{d\theta}{dt}$ is instantaneous speed and hence torque

$$T(\theta) = \frac{1}{2} i^2 \frac{dL}{d\theta} \quad (2.12)$$

It is evident from expression (2.12) that the positive torque is developed if current flows through the phase winding when $\frac{dL}{d\theta}$ is + ve and retarding torque is developed if current flows when $\frac{dL}{d\theta}$ is - ve.

The phase windings of the machine considered in this work are excited with pulses of constant voltage (Fig 2.4(b)) and this is achieved by switching devices. The switching action can be described by two angles, θ_c and θ_{con} (Fig 2.4(b)).

θ_c is defined as the 'switch-on' angle, ie the angle between the leading edge of the rotor and the front edge of the stator pole of the considered phase. The case when $\theta_c < 0$ is referred to as 'early turn-on'.

θ_{con} is defined as the 'conduction' angle, ie the angle corresponding to a period when a switching device is in the 'on' state.

The 'switch-off' occurs after the rotor moves for an angle θ_{con} from angular position θ_c

$$\theta_{sw-off} = \theta_c + \theta_{con} \quad (2.13)$$

The next phase is switched on after the rotor moves through the angle ϵ in the direction which is opposite to the sequence of the phases.

$$\epsilon = \frac{\phi}{q} = \frac{2\pi}{qN_r} \quad (2.14)$$

The overlap angle of pulses of two successive phases is then

$$\theta_o = \theta_{con} - \epsilon \quad (2.15)$$

($\theta_o \leq 0$ corresponds to the case when there is no overlap.)

The current waveform is determined by equation (2.7). The machine equations and their solution are studied later in this work (Chapters 4 and 6). It is sufficient to say here that the resulting expression for the average torque over a cycle ϕ is given by

$$T = q \frac{V^2 \phi}{L_o} \left(\frac{s}{\phi}\right)^2 \frac{F}{\omega^2} \quad (2.16)$$

where F is a function of the dimensionless parameters $\frac{L_i}{L_o}$, k_d , $\frac{\theta_c}{s}$, $\frac{\theta_{con}}{s}$ and $\frac{\phi}{s}$. The expression (2.16) shows the nature of the torque/speed characteristics of the switched reluctance motor. Torque is seen to be inversely proportional to the square of the speed. Since

$$T \sim \frac{1}{\omega^2}$$

the torque/speed characteristics of the switched reluctance motor are of the same form as of the series dc motor.

According to the expression

$$\omega = V \left(\frac{s}{\phi} \right) \sqrt{q \frac{\phi}{L_0} \frac{F}{T}} = \text{const.} \cdot V \cdot \sqrt{F} \cdot \frac{1}{\sqrt{T}} \quad (2.17)$$

two basic methods of speed control are possible:

- a) speed control by varying the voltage V (control by voltage),
- b) speed control by varying θ_c and θ_{con} ie by varying F (control by switching angles).

The analysis of speed control is given in Chapter 4.

2.5 Switching circuits

After each conduction period during which the switching device is closed the stored magnetic energy in the phase winding must be removed in such a manner as to avoid very high winding voltages which would cause destructive breakdown of the semiconductor device.

The methods available for removing the stored energy from the phase winding may be broadly classified into two groups. Firstly, the energy can be simply wasted by switching the phase winding current into a resistance external to the motor. Secondly, the energy can be returned to the supply.

The first method is one of the simplest possible requiring only a diode and a resistor per phase and is used for applications where the efficiency of the machine is of secondary importance. (This method has been used by Blenkinsop¹ for a two-phase, 150W, 7000 $\frac{\text{rev}}{\text{min}}$ switched reluctance motor.) Fig 2.5 shows an example of the circuit dissipating the stored energy in a resistor (R_2). During the conduction period, diode D is reverse biased and no current flows in R_2 . When transistor TR*

* The treatment is sufficiently general that any form of switching device can be employed.

is switched off the collector voltage rises until D becomes forward biased and the winding current transfers into the free-wheeling resistance R_2 . The rate of change of flux-linkage during the free-wheel period is equal to the product of winding current and $(R_1 + R_2)$ and in order to achieve fast decay a high value of R_2 is desirable. However, the peak collector voltage is given by

$$V_{CE \text{ max}} = V + I_o R_2$$

(I_o is current in the winding at switch-off) and consequently, R_2 has to be chosen to give a good compromise between rate of decay and device voltage ratings. The efficiency of the motor is directly dependent upon R_2 .

The second method is used for applications where high motor efficiency is a requirement. Two circuits whereby the stored energy is returned to the supply are shown in Figs 2.6 and 2.7.

The circuit shown in Fig 2.6 requires two switches per phase. Opening transistors TR_1 and TR_2 the current continues to flow through the diodes D_1 and D_2 so that the stored magnetic energy is returned to the supply source. The rate of decay of flux-linkage is given by

$$\frac{d\psi}{dt} = -V - i R_1$$

The peak transistor voltage is

$$V_{CE \text{ max}} = V$$

Since the resistance of the phase winding (R_1) is small (for high efficiency) the flux decays almost linearly. This method gives a high efficiency for the drive but it requires two transistors per phase and involves the problem of different voltage levels of their emitters.

Fig 2.7 illustrates the use of an auxiliary (secondary) coil, wound in bifilar fashion with the main (primary) coil. The action of the circuit is such that when the transistor TR is in on-state the current flows through the primary coil, and when the transistor is switched off

the primary current decays rapidly to zero and in the same time induced emf establishes the current in the secondary coil in order to maintain the constant flux-linkage and stored magnetic field energy. The secondary current flows through the diode D and returns the energy to the supply.

The coefficient of mutual coupling between primary and secondary coils must be very high, otherwise the stored magnetic energy in leakage inductance would have a destructive effect on switching devices. The rate of decay of flux-linkage in the primary coil is

$$\frac{d\psi}{dt} = - \frac{N_1}{N_2} \left(V + \frac{N_1}{N_2} I_o R_2 \right)$$

where N_1/N_2 is primary/secondary turns ratio,

I_o is the current in the primary coil at switch-off.

The peak transistor voltage is

$$V_{CE \text{ max}} = V \left(1 + \frac{N_1}{N_2} \right) + \left(\frac{N_1}{N_2} \right)^2 I_o R_2$$

Since the resistances of phase windings, R_1 and R_2 , are small the peak transistor voltage is approximately equal to $V \left(1 + \frac{N_1}{N_2} \right)$ and can be controlled by altering the turns ratio. The flux decays almost linearly and is also controlled by turns ratio. However, in order to provide a high coefficient of mutual coupling and simple winding for manufacturing, the ratio $N_1/N_2 = 1$ is convenient.

This method uses a minimum number of switching devices but the use of an auxiliary winding results in a lower utilisation of the available winding space in the motor. The inevitable increase in winding volume is the price paid for simplicity in the drive circuits. The actual amount for extra space required is not as large as might at first be feared because the volumes of the windings are related to their rms currents (see Chapter 5). (It should be noted that V_{CE} is doubled.)

The cost penalty associated with a bifilar winding is more than offset by the cost reduction introduced by switching devices and therefore the use of bifilar winding in a switched reluctance motor is a good compromise between the utilisation of available winding space and the number of switching devices.

2.6 Derivation of necessary conditions for self-starting, symmetrical reversable performance

It is frequently required for industrial drives to have identical performance in both directions of rotation and to be self starting from any rotor position. These requirements impose the necessary conditions on basic design parameters.

The condition associated with the first requirement is straight-forward, ie

- i) machine must be symmetrical with respect to the rotor and stator pole axes

The conditions associated with the second requirement may be derived from Fig 2.4(a). These conditions are related to the production of starting torque at any angular position and are:

- ii) at least one phase must have $\frac{dL}{d\theta} + ve$ for any value of θ .
- iii) each phase must be excited at least over the angle ϵ when $\frac{dL}{d\theta}$ is positive.

The conditions (i) and (ii) are fulfilled by appropriate rotor and stator pole geometry, and condition (iii) is fulfilled by designing the rotor position sensor such that the conduction angle is at least equal to ϵ when the machine starts from rest.

2.6.1 Deductions from rotor and stator pole geometry

As the rotor rotates from any given starting point, of which there is a certain relationship of rotor and stator poles, it will come to another point at which this relationship is repeated. It can be seen that this will happen LCM times during a rotor angular displacement of 360° , where LCM is the least common multiple of the number of rotor poles N_r and number of stator poles N_s . Therefore it can also be stated that

$$\epsilon = \frac{2\pi}{\text{LCM}} \quad (2.18)$$

Combining (2.14) and (2.18)

$$\text{LCM} = q N_r \quad (2.19)$$

Equation (2.19) means that for a given q and N_r , a number of solutions can be obtained for N_s . The following consideration shows that only some of these solutions are valid.

- a) It has been stated above that the presence of mutual inductance between phases decreases the amount of torque produced. Hence, to reduce the amount of mutual inductance (ie to keep a simple '2-pole' flux-pattern), the number of rotor and stator poles should be even.
- b) From Fig 2.3, the interpolar arc on the rotor is $\phi - r$. The mid-point of region OA on Fig 2.4(a) will occur when the rotor interpolar axis is aligned with the stator pole axis. If, in this position, the length of the arc s is increased, there comes a point where the region of minimum inductance L_0 vanishes, ie when $s = \phi - r$. Since there will be some fringing in practice, this is the limiting condition for s and in general

$$s \leq \phi - r \quad (2.20)$$

- c) The condition (ii) can be expressed by

$$\min(r, s) \geq \epsilon \quad (2.21)$$

$$\text{(or } \phi \leq \frac{2\pi}{N_s} + \min(r, s),$$

$$\text{ie } \min(r, s) \geq 2\pi \frac{|N_s - N_r|}{N_r N_s})$$

- d) If N_s is an integral multiple of N_r , or vice versa, then $\text{LCM} = \max(N_s, N_r)$. Substituting this into equation (2.19) and then (2.21) gives $\min(r, s) \geq \frac{2\pi}{\max(N_s, N_r)}$. Since $2\pi/N_r$ is the rotor pole pitch, this condition can only be satisfied when the arc is equal to the pole pitch on the stator or rotor, a condition which is physically impossible. It follows, that to avoid this,

$$\text{LCM} > \max (N_r, N_s) \quad (2.22)$$

e) It will be considered in this study that

$$N_s > N_r \quad (2.23)$$

(The geometries with $N_s < N_r$ can be developed and are used in stepping motors. However, they are not considered in this work since they have small step angles and therefore raise the supply frequency with undesired effects on efficiency.)

The necessary conditions which must be fulfilled by the parameters considered can therefore be summarised as follows:

For any chosen values of the number of phases and the number of rotor poles, the number of stator poles is defined by

$$\text{LCM} (N_r, N_s) = q N_r > N_s > N_r \quad (2.24)$$

where N_r, N_s are even integers.

The pole arcs are governed by the conditions

$$\min (r, s) \geq \frac{2\pi}{q N_r} \quad (2.25)$$

$$s \leq \frac{2\pi}{N_r} - r \quad (2.26)$$

2.6.2 Practical implications of the conditions

From the last two expressions, the practical implications of the geometry can be seen. The limits for s can be derived as follows:

$$\text{When } s \text{ is larger than } r, r_{\min} = \frac{2\pi}{q N_r}$$

$$\text{Then } s_{\max} = \frac{2\pi}{N_r} - \frac{2\pi}{q N_r} = \frac{2\pi}{N_r} \left(1 - \frac{1}{q}\right) \quad (2.27)$$

When s is smaller than r ,

$$s_{\min} = \frac{2\pi}{q N_r} \quad (2.28)$$

The range of s is therefore

$$s_{\max} - s_{\min} = \frac{2\pi}{N_r} \left(1 - \frac{2}{q}\right) \quad (2.29)$$

Similarly the range of r can be shown to be

$$r_{\max} - r_{\min} = \frac{2\pi}{N_r} \left(1 - \frac{2}{q}\right) \quad (2.30)$$

ie both r and s have the same range although they are at the same time governed by $r + s \leq \frac{2\pi}{N_r}$ (Relation 2.20). It will be seen that the range increases with increasing q and decreases with increasing N_r .

These relationships may be shown diagrammatically as in Fig 2.8(a) where the limits of combinations of the values of r and s are denoted by the sides of the triangle XYZ. At point X (where the physical machine would contain the least amount of iron) the inductance variation has no dead zone (since $s = r$) and is of the form shown in Fig 2.8(b). As the geometry changes from the point represented by X along XY or XZ to Y or Z, a dead zone appears and the amount of minimum inductance period diminishes accordingly until, at Y or Z, the inductance has the form shown in Fig 2.8(c). Point Z corresponds to a machine with maximum winding space (as at X) and point Y to a machine with zero winding space (since stator pole arc = stator pole pitch when $s = s_{\max}$). The latter is not physically realisable but it should be noted that keeping r towards r_{\min} implies low rotor inertia, which might be useful if a fast response is required to a power input. A special case should be noted at point W where $s = r = \phi/2$. At this point, both the period of minimum inductance of Fig 2.8(b) and the dead zone of Fig 2.8(c) have vanished, as shown in Fig 2.8(d). Any geometry corresponding to a point inside the triangle will have an inductance pattern which will exhibit features of all three patterns shown, depending on the position of the point. The line of $s = r$ divides the triangle as shown into regions $s > r$ and $s < r$. Any two designs represented by points symmetrical about the line XW will have identical inductance profiles. The area where practical designs are to be found will be discussed in the next section.

2.7 Derivation for preferable conditions for design parameters

2.7.1 Rotor and stator pole arcs

One of the ways of reducing (or eliminating) retarding torque due to current flowing during the period of negative $dL/d\theta$ is to introduce a dead zone by making $r \neq s$. This poses the question of whether r or s should be the larger. Consider the two geometries shown in Fig 2.9 which differ only in that $r_1 = s_2$ and $r_2 = s_1$. From Fig 2.8(a) it will be seen that the two geometries will exhibit the same inductance profile. The two machines should therefore be capable of delivering the same output. However, it should be noted that the amount of winding space in motor 1 is smaller than that of motor 2 and hence would have a higher current density (which implies lower efficiency) and would be more difficult to manufacture. In addition, motor 1 would be heavier than motor 2 since there is a difference in the amount of iron given by

$$\begin{aligned} (r_1 N_r + s_1 N_s) - (r_2 N_r + s_2 N_s) &= (r_1 N_r + s_1 N_s) - (s_1 N_r + r_1 N_s) \\ &= r_1 (N_r - N_s) - s_1 (N_r - N_s) = (N_r - N_s) (r_1 - s_1) \end{aligned} \quad (2.31)$$

This difference vanishes at the cross-over point of $r_1 = s_1$. Hence, for the three reasons stated above, if a dead zone is required in the inductance curve,

$$r \geq s \quad (2.32)$$

Now referring back to Fig 2.8(a) it can be stated that practical designs will therefore lie in the lower part of the main triangle, ie will be in the minor triangle XWZ.

2.7.2 Number of rotor poles

The average torque over a cycle ϕ has been given by (2.16), ie

$$T = q \frac{V^2}{\mu_0 e N^2 \omega^2} \phi \left(\frac{s}{\phi}\right)^2 \frac{F}{P_0}$$

where F is a function of the dimensionless parameters

$$\frac{L_i}{L_o} (= \frac{P_i}{P_o}), k_d, \frac{\theta_c}{s}, \frac{\theta_{con}}{s} \text{ and } \frac{\phi}{s}$$

and P_o, P_i are normalised minimum and maximum permeances. If in this expression the only variable is P_o , then by reducing P_o the value of F increases and since $T \sim \frac{F}{P}$ the torque increases. Therefore it is desirable that normalised minimum permeance P_o has a small value. In Chapter 3 it is shown that if the airgap due to the minor rotor diameter is greater than a certain value, P_o mainly depends on the rotor interpolar arc $\phi - r$ since fringing effects become predominant in the value of inductance (the larger the $\phi - r$ the smaller the P_o).

$$(\phi - r)_{\max} = \phi - r_{\min} = \frac{2\pi}{N_r} - \frac{2\pi}{q N_r} = \frac{2\pi}{N_r} (1 - \frac{1}{q}) \quad (2.33)$$

Hence keeping N_r as small as possible (subject to the conditions previously derived) will give low values of P_o .

Another argument which supports such a choice of N_r is the fact that the switching frequency is directly proportional to N_r (see below). Hence, to reduce iron losses the number of rotor poles should be as small as possible.

2.8 Examples to illustrate the conclusions of 2.6 and 2.7

1. Combination $q = 2, N_r = 2$

$$\text{LCM} = q N_r = 2 \times 2 = 4$$

$$\text{LCM}(2, N_s) = 4 \therefore N_s = 4$$

However, condition (2.24) states that LCM must be greater than N_s . Since $\text{LCM} = 4 \nless N_s = 4$, the above combination does not satisfy the conditions.

2. Combination $q = 2, N_r = 4$

$$\text{LCM} = 2 \times 4 = 8$$

$$\text{LCM}(4, N_s) = 8 \therefore N_s = 8$$

Again $\text{LCM} = 8 \nless N_s = 8$ and the combination is not satisfactory.

3. Generally, any combination with $q = 2$ does not satisfy the conditions (self-starting, reversible machine with smooth rotor pole surface and with identical performance in both direction). Also, any combination with $N_r = 2$ is not satisfactory because any even value for N_s is a multiple of 2 and then condition (2.24) is not satisfied.

4. Combination $q = 3, N_r = 2$

$$\text{LCM} = 3 \times 2 = 6$$

$$\text{LCM}(2, N_s) = 6 \therefore N_s = 6$$

Again $\text{LCM} = 6 \nless N_s = 6$ and the combination is not satisfactory.

5. Combination $q = 3, N_r = 4$

$$\text{LCM} = 3 \times 4 = 12$$

$$\text{LCM}(4, N_s) = 12 \therefore N_s = 3, 6$$

According to (2.23) N_s should be greater than N_r (and N_s must be even). Thus only $N_s = 6$ satisfies this condition.

In this case $\text{LCM} = 12 > N_s = 6$ and the combination is satisfactory. Furthermore, relations (2.25), (2.26) and (2.32) must be satisfied:

$$s \leq \frac{2\pi}{4} - r$$

$$s \geq \frac{2\pi}{4 \times 3}$$

$r \geq s$ (sign '=' corresponds to the case without dead zone)

6. Combination $q = 4$, $N_r = 4$

$$\text{LCM} = 4 \times 4 = 16$$

$$\text{LCM}(4, N_s) = 16 \therefore N_s = 16$$

($N_s = 8$ does not satisfy because $\text{LCM}(4, 8) = 8$)

Again $\text{LCM} = 16 \nmid N_s = 16$ and combination does not satisfy.

7. Combination $q = 4$, $N_r = 6$

$$\text{LCM} = 4 \times 6 = 24$$

$$\text{LCM}(6, N_s) = 24 \therefore N_s = 8$$

Since $\text{LCM} = 24 > N_s = 8$, combination satisfies.

Furthermore the following must apply

$$s \leq \frac{2\pi}{6} - r$$

$$s > \frac{2\pi}{6 \times 4}$$

$r \geq s$ (sign '=' corresponds to case without dead zone).

Although the three phase machine requires the minimum number of switching devices the four phase machine provides better starting performance (see below). The possible combinations with bigger number of phases have no practical value since the number of switching devices are becoming exceedingly high. Therefore the attention should be concentrated on the following combinations

$N_r = 4$, $N_s = 6$ for 3 phase machines

$N_r = 6$, $N_s = 8$ for 4 phase machines.

2.9 Flux waveforms

Figs 2.10(b) to (f) illustrate examples of the flux waveforms in various parts of the magnetic circuit for a 3 phase, $6/4$ pole machine. The switching period of each phase is, from Fig 2.10(a)

$$\tau_{ph} = \frac{2\pi/N_r}{\frac{2\pi n}{60}} = \frac{60}{N_r n} \text{ [sec]} \quad (2.34)$$

and the switching period of the supply is

$$\tau_s = \frac{\varepsilon}{\frac{2\pi n}{60}} = \frac{60}{q N_r n} \text{ [sec]} \quad (2.35)$$

The period and form of the flux variations experienced by the iron in the machine varies between different parts of the magnetic circuit. This is a consequence of the use of unidirectional currents in the windings. The stator poles are subjected to unidirectional flux pulsations (the sense of which depend on the sense of the winding connection) of τ_{ph} as shown in 2.10(b). The flux pattern in the stator back iron varies with the position. The simplest way to illustrate this is to divide the back iron into sections bounded by pole centre lines. Assuming that the winding connections are 1,2,3 ... q on adjacent poles followed by 1', 2', ... q' on opposite poles (as in Fig 2.3), then the sections between the centre lines of poles 1 and 2, 2 and 3, 1' and 2', 2' and 3' will have flux waveforms of the type shown in Fig 2.10(c). The waveform has a period of τ_{ph} and a dc component, the sense of which will depend on the particular section being considered. The remaining sections, ie between the centre lines of poles 3 and 1', 3' and 1 can be seen, again from inspection, to have the type of waveform shown in Fig 2.10(d) which has a dc component with a ripple component of period τ_s . The rotor poles experience bidirectional pulses as shown in Fig 2.10(e), which have an overall period of $60/n$. The rotor core experiences bidirectional pulses of flux as shown in Fig 10(f), which again have an overall period of $60/n$ although the waveform is considerably more complex and contains higher order frequencies. This is the reason why the rotor is constructed of steel laminations and does not carry electrical conductors.

All of the above discussion is based on the assumption that the phase windings are connected in the same sense (ie 1,2,3, 1', 2', 3' reading around the stator). If one is reversed, say to give 1, 2', 3, 1', 2, 3', then the flux patterns will change and it has been shown in Reference No 10 that the general frequency of flux reversal in the magnetic circuit is increased quite considerably and this implies a substantial increase in iron loss.

For a four phase machine the same analysis may be carried out and the waveforms are shown in Figs 2.11(a) to (g) for a 4 phase, 8/6 pole combination with the windings connected 1,2,3,4, 1', 2', 3', 4'. Fig 2.11(a) shows the phase voltage pulses and 2.11(b) the stator pole fluxes. These correspond exactly to the 3-phase cases of 2.10(a) and 2.10(b). However the stator will have different waveforms occurring in the back iron. These are shown in Figs 2.11(c), (d) and (e) and have periods of $\frac{60}{N_r n}$, $\frac{60}{N_r n}$ and $\frac{60}{q N_r n}$ respectively. Since there are two different ways of connecting the four phases with regard to winding sense, there is a further set of waveforms possible. (It might seem at first glance that there are more than two possible combinations with four phases, but inspection will show that they all reduce to only two magnetically different patterns 1,2,3,4 and 1, 2', 3, 4'.) It has been shown in Reference No 10 that the general frequency of flux reversal in the magnetic circuit is increased quite considerably with the change in winding connection.

From above the following conclusion may be stated:

- a) The switching frequency and therefore iron loss rises with increasing the number of phases;
- b) The study of iron loss associated with these frequencies is exceedingly complex;
- c) There appears to be a definite advantage in keeping the winding sense of adjacent poles in the same direction since frequencies of flux reversals are then lower.

2.10 Number of phases

Although the iron losses (if significant) may be reduced by employing unusually thin laminations, this may not be compatible with conventional manufacturing processes. Therefore it may be confidently stated that the number of rotor poles and the number of phases must be kept as low as possible. (Reducing the number of phases may well keep down the cost of the associated commutator and power switching devices.)

The obvious choice is therefore to make $q = 3$ and hence $N_s = 6$ and $N_r = 4$. However, it has been found that the starting performance of a 3-phase machine is not entirely satisfactory for applications where the need for good starting performance is important. The reason for this can be deduced from Fig 2.4(a). Although the inductance waveforms are shown as being composed of straight lines, the actual curve will be different. If only the effect of flux fringing in the air is considered (and still considering the iron to be ideal), then the sharp corners will round off to give a much smoother pattern. This in turn means that $dL/d\theta$ will not be a constant, positive value over $A'B'$ but will have a peak value at the mid point of $A'B'$ and fall off to either side. The amount of overlap between phase inductances then becomes important since if $\frac{dL}{d\theta}$ has fallen to a value where insufficient torque is developed at a particular rotor angle, it is vital that the next phase is able to generate enough torque. The analysis for this is as follows.

If k_L is defined as the ratio of inductance overlap of two phases to the angle over which the inductance is changing, then from Fig 2.4(a)

$$k_L = \frac{A'B' - \epsilon}{A'B'} = \frac{\min(r, s) - \frac{2\pi}{qN_r} r}{\min(r, s)}$$

$$\text{ie } k_L = 1 - \frac{2\pi}{q N_r s} \text{ when } r > s \quad (2.36)$$

Now since values of N_r and s are to some extent dependent on q , the variation of k_L is best described by a diagram. Fig 2.12 shows the variation of k_L as a function of s , where s varies between the maximum and minimum values allowed by a combination of q and N_r . Curve (1) corresponds to $q = 3$, $N_r = 4$ and curve (2) corresponds to $q = 4$, $N_r = 6$.

It will be seen that higher values of k_L are achieved at relatively lower values of s for the 4-phase case. For a specified amount of overlap, the 4-phase machine can work much closer to s_{\min} , a condition which is beneficial for obtaining larger $dL/d\theta$. This being the case, the 4-phase machine allows greater flexibility in design and will have better starting performance.

If winding space is considered, then for an equal amount of winding space on 3-phase and 4-phase machines, the 4-phase machine allows this to be obtained at a point which provides greater overlap. Note the case where the winding space is required to be a minimum of 50% of the stator pole pitch. For 3-phase, this corresponds to 30° and for 4-phase to $22\frac{1}{2}^\circ$. Since the corresponding minimum values of stator pole arcs are 30° and 15° respectively, the 4-phase machine again shows advantages in that the design is more flexible.

2.11 Effect of grading the rotor pole profile

The idea of grading the rotor pole profile has already been exploited for a self starting-requirements of non-reversible 2-phase machine by P T Blenkinsop¹. In this section the topic will be considered more generally in the light of conditions for self-starting, symmetrical reversible performance.

Consider Fig 2.13(a) which shows a 3-phase, $6/2$ pole reluctance motor. The two rotor poles are graded as shown and produce the phase inductance curve of Fig 2.13(b). The total pole arc r is split into the main pole arc, r_m , and two equal starting poles, r_s . (The equality follows from the requirement of symmetry.) Thus

$$r = r_m + 2r_s \quad (2.37)$$

From Fig 2.13 it can be seen that

$$A'B' = G'H' = \min(r_s, s) \quad (2.38)$$

$$B'C' = F'G' = \begin{cases} r_s - s & (r_s > s) \\ 0 & (r_s \leq s) \end{cases} \quad (2.39)$$

$$C'D' = E'F' = \min(r_m, s) \quad (2.40)$$

$$D'E' = |r_m - s| \quad (2.41)$$

The relationships of Equations (2.14) and (2.20) are seen to be still valid, ie

$$\epsilon = \frac{\phi}{q} = \frac{2\pi}{q N_r} \text{ and } s \leq \phi - r$$

To provide forward torque at any rotor angle, at least one phase must have a positive $dL/d\theta$ for any value of θ . It will be seen from Fig 2.13 that this can only be achieved for realistically small angles of phase inductance overlap if the intermediate dead zones BC and FG vanish, otherwise the torque will fall to zero at some value of θ . (This might be avoided by making the phase inductance overlap angle very large, but this is not practicable.) Hence when these dead zones are made to vanish by making $r_s \leq s$, as in Fig 2.14, it can be stated that the condition to be fulfilled is

$$A'D' \geq \epsilon$$

ie

$$r_s + \min(r_m, s) \geq \frac{2\pi}{q N_r} \quad (2.42)$$

In general terms, the limits for r and s (Equations (2.27) to (2.30)) which were derived in Section 2.6.2 still apply, so the effect of adding a third variable r_s to extend the two dimensional shape of Fig 2.8(a) into a three dimensional one. The geometry of this shape is considerably more complex and is shown in Fig 2.15. Only the regions with $r \geq s$ are shown. In the same way as the inductance curves of Figs 2.8(b) to (d) correspond to particular points of the triangle of Fig 2.8(a), the inductance curves of Fig 2.16 correspond to specific points of the polyhedron of Fig 2.15. The inductance curves of Fig 2.16 are drawn for arbitrary, fixed values of r and s and the amount of main pole, r_m , is therefore the result of varying the starting pole, r_s .

The effect of these different gradings will not be discussed in detail since the effects on the inductance curves can be seen in Fig 2.16, but it is sufficient to note that if the intention of employing grading is to "stretch" $dL/d\theta$ over a longer period than is possible with a smooth rotor profile (ie by making $r - r_s > s$), then the case $r - 2r_s = s$ corresponds to the most effective value of r_s , as shown in Fig 2.16(d).

Employing the grading of rotor pole profile it appears that 3- or 4-phase machines with 6/2 and 8/2 or 8/4 pole combinations respectively, could be constructed as self-starting, symmetrical reversible machines. However, if we assume that $L_i - L_o$ is approximately constant, then (for the 6/2 and 8/2 or 8/4 pole combination) the average value of $dL/d\theta$ would fall to approximately 1/2 and 1/3 or 2/3 (see relation (2.42)) and therefore the phase currents would require to be increased by $\sqrt{2}$ and $\sqrt{3}$ or $\sqrt{1.5}$ for the same torque as the 6/4 and 8/6 pole combinations previously discussed. These higher current ratings imply a higher current density in the machine winding and a higher ratings of the switching devices. The only apparent advantage arises from reduced number of rotor poles - reduced switching frequency, but initial evaluation indicates that the net change will be disadvantageous.

However, one variant of this method of grading the rotor profile should not be dismissed - that of taking a pole combination which is already satisfactory without grading and applying grading to it. For example, if the 6/4 pole, 3-phase motor is considered, it has already been noted that the starting performance may not be acceptable for certain duties (because of lack of sufficient phase overlap). This overlap can be increased by grading the rotor pole profile so that the minimum points of the net starting torque curve are raised. Naturally this will be at the expense of reducing other parts of the torque curve (for the same current) and the overall effect would need to be carefully considered in the light of the particular application.

2.12 Conclusions

A switched reluctance motor of very simple construction suitable for variable speed operation has been described. It has no brushes, slip

rings, winding slots, or moving winding and its stator spool windings are excited from a constant dc voltage supply by means of suitable switching devices. The nature of the torque/speed characteristic is similar to that of the series dc motor.

Different switching circuits which provide excitation of the windings and removal of the stored energy from them after turn-off of the switching device have been described.

The conditions which are imposed on design parameters (stator and rotor pole number, stator and rotor pole arc) by the requirements for self-starting, symmetrical reversible performance have been established and it has been shown that two combinations of pole numbers and phases are superior to all others. These are 3-phase 6/4 pole and 4-phase 8/6 pole. The latter one provides better starting performance.

The inter-relationships between stator and rotor pole arcs and their ranges of values for given combinations of pole numbers and phases have been set out and fully discussed. Actual values for these arcs have not been recommended (except that the stator pole arc should be the smaller) since more comprehensive analysis is needed for their satisfactory choice (this follows in chapters below). The effects of grading the profile of 2-pole rotors has been examined but it has been shown that it does not yield any overall benefits. Grading of the rotors may provide self starting from any initial rotor position but at the expense of reducing average $dL/d\theta$ and hence reducing the torque at a given current.

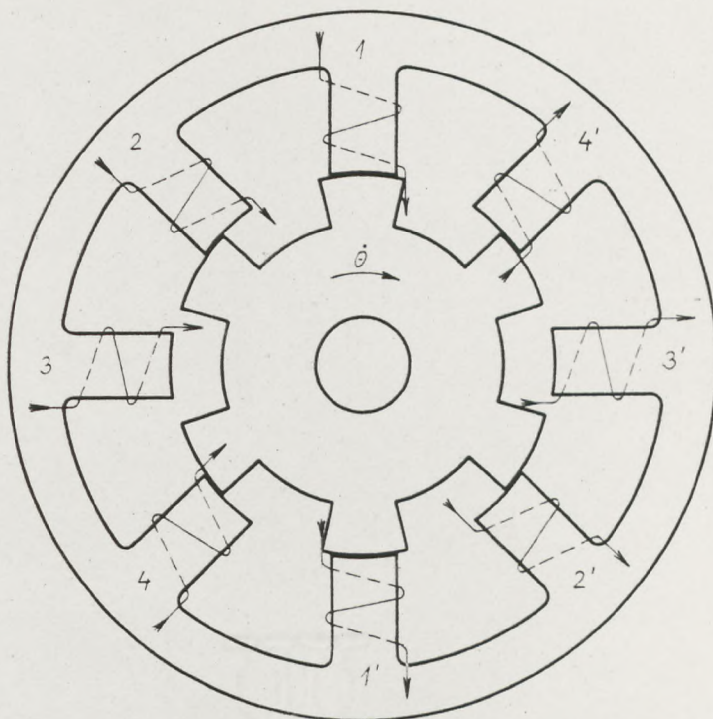


FIG 2.1 Basic construction of single-stack, cylindrical type switched reluctance machine

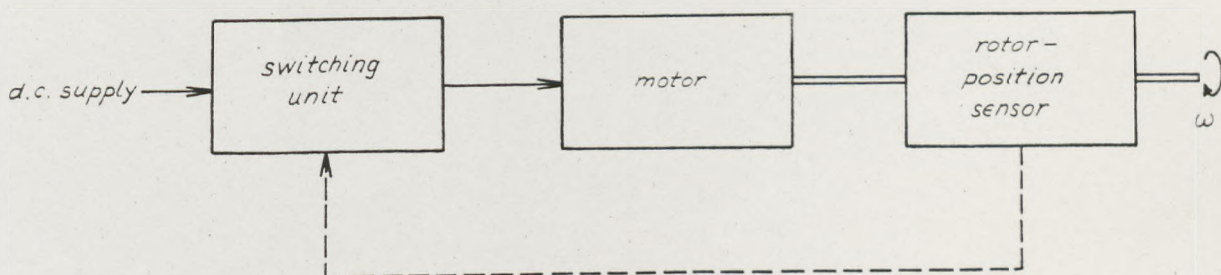


FIG 2.2 Block-diagram of switched reluctance machine

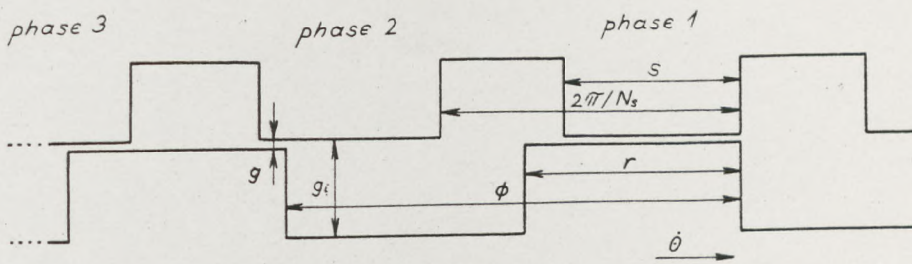


FIG 2.3 Geometry of developed airgap of machine

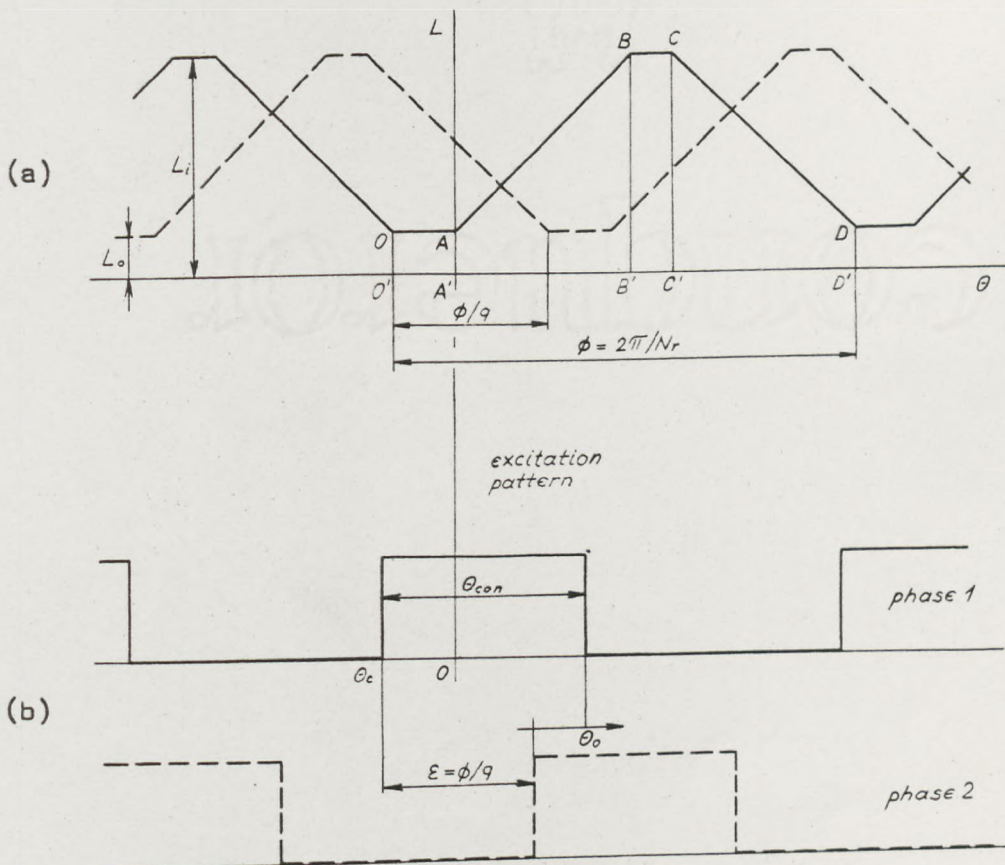


FIG 2.4 (a) Variation of inductance of two successive phases
 (b) Excitation pattern of two successive phases
 ——— phase 1
 - - - - phase 2

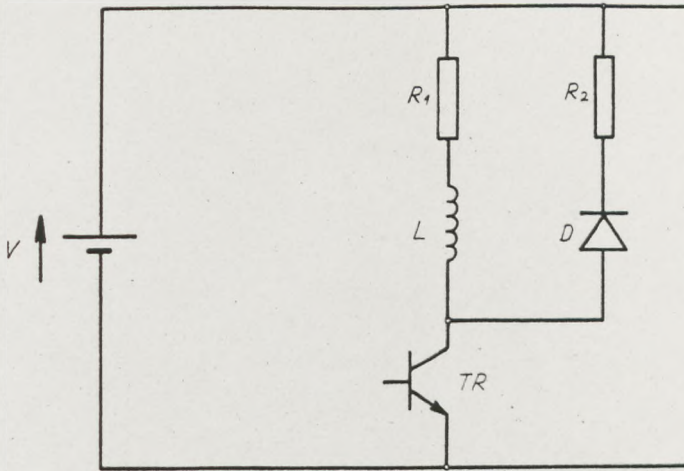


FIG 2.5 Switching circuit with dissipating resistor (R_2)

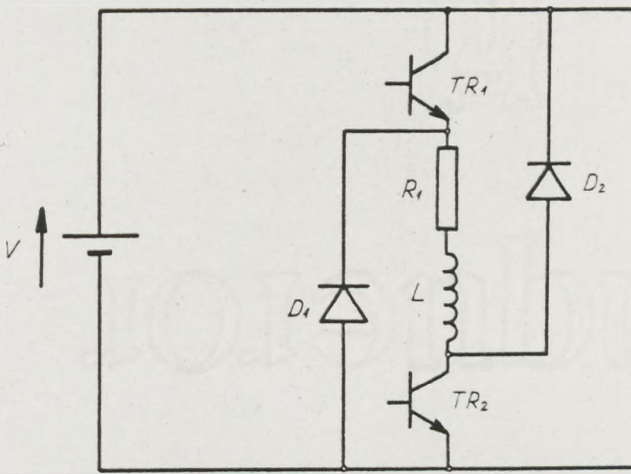


FIG 2.6 Switching circuit with two switches per phase

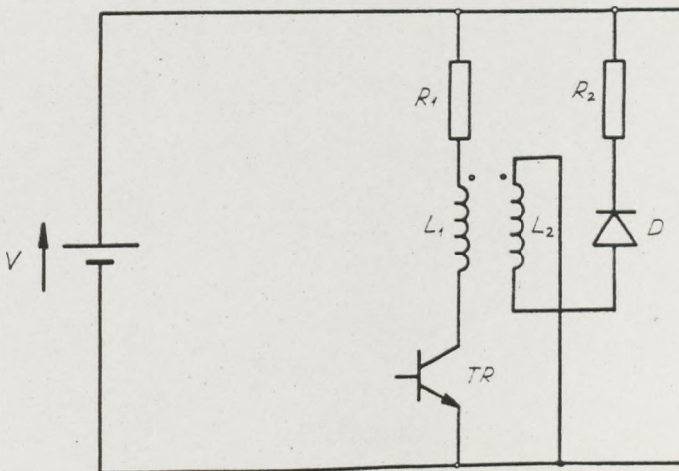


FIG 2.7 Switching circuit with bifilar winding

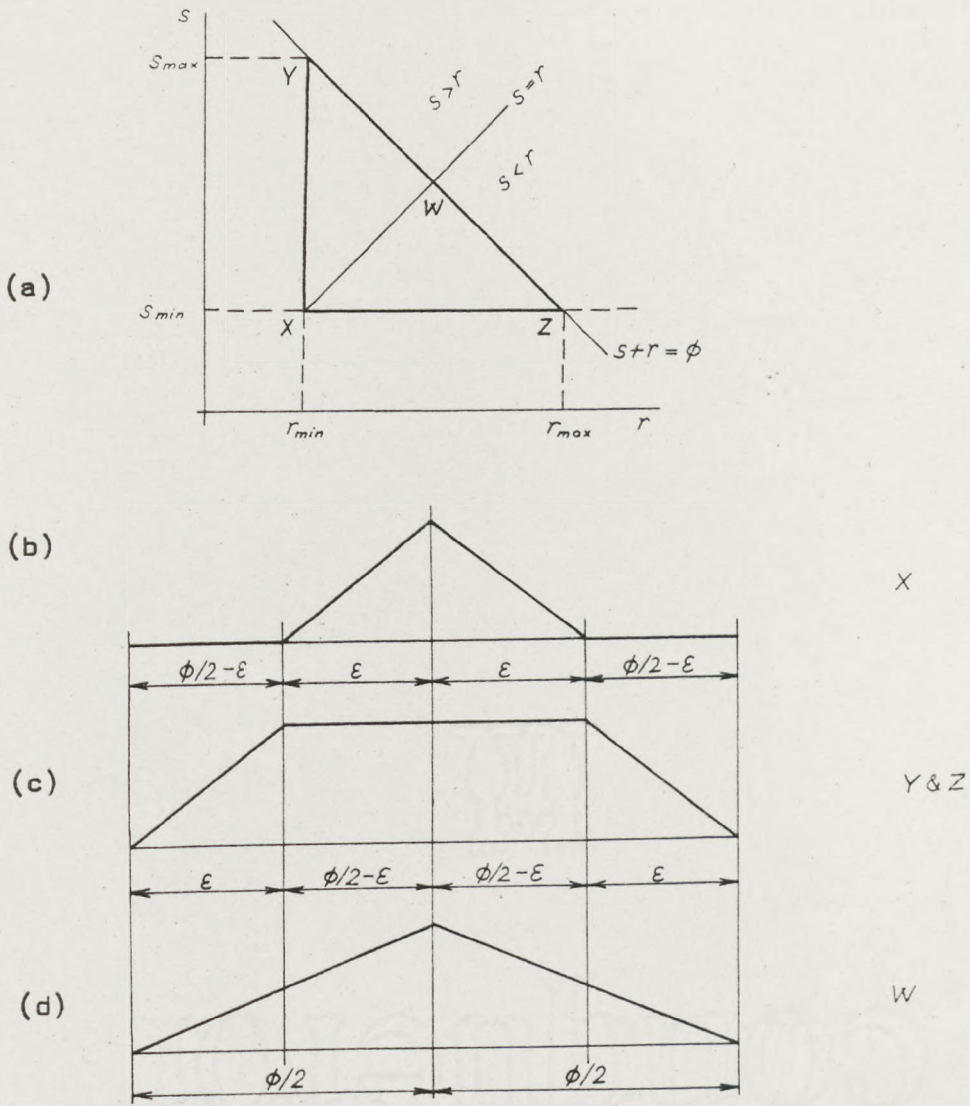


FIG 2.8(a) Boundaries of possible values of stator and rotor pole arcs
 (b,c,d) Limiting inductance profiles

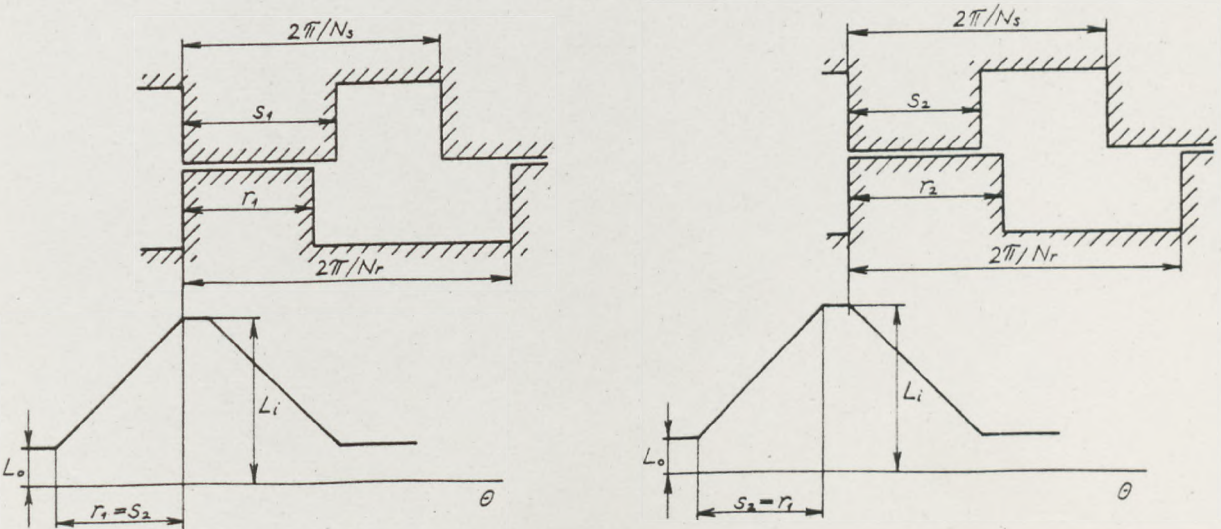


FIG 2.9 Geometries with same inductance profile

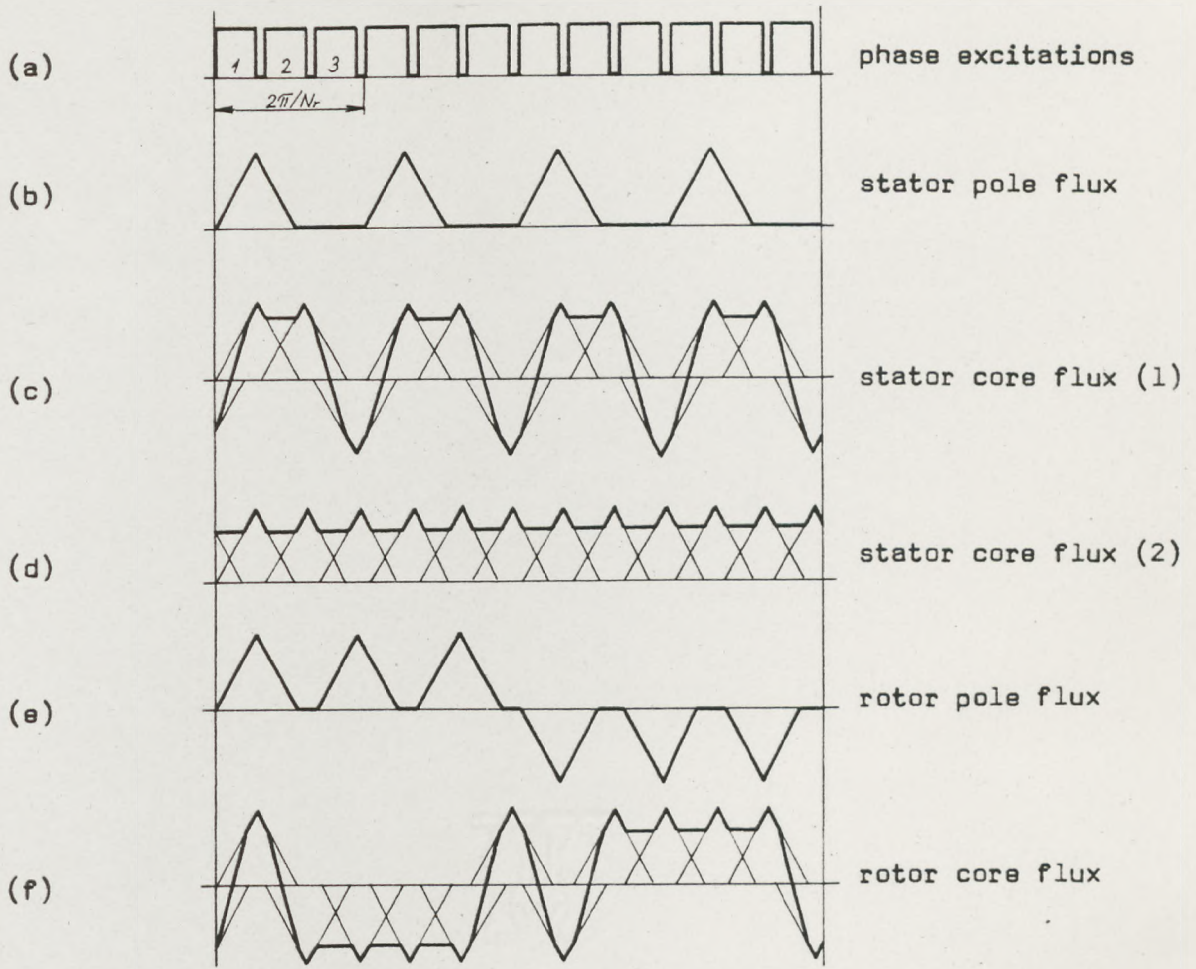


FIG 2.10 Flux waveforms for 3-phase machine

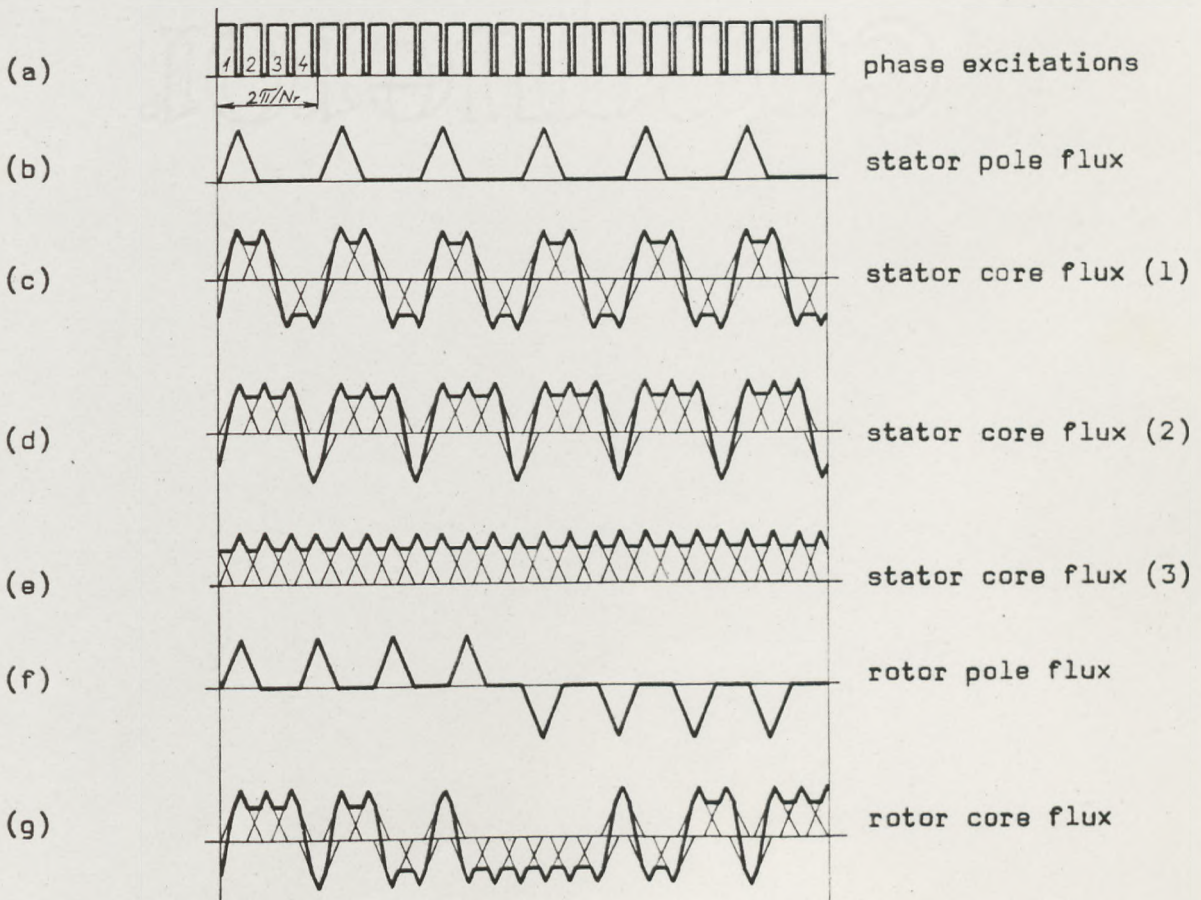


FIG 2.11 Flux waveforms for 4-phase machine

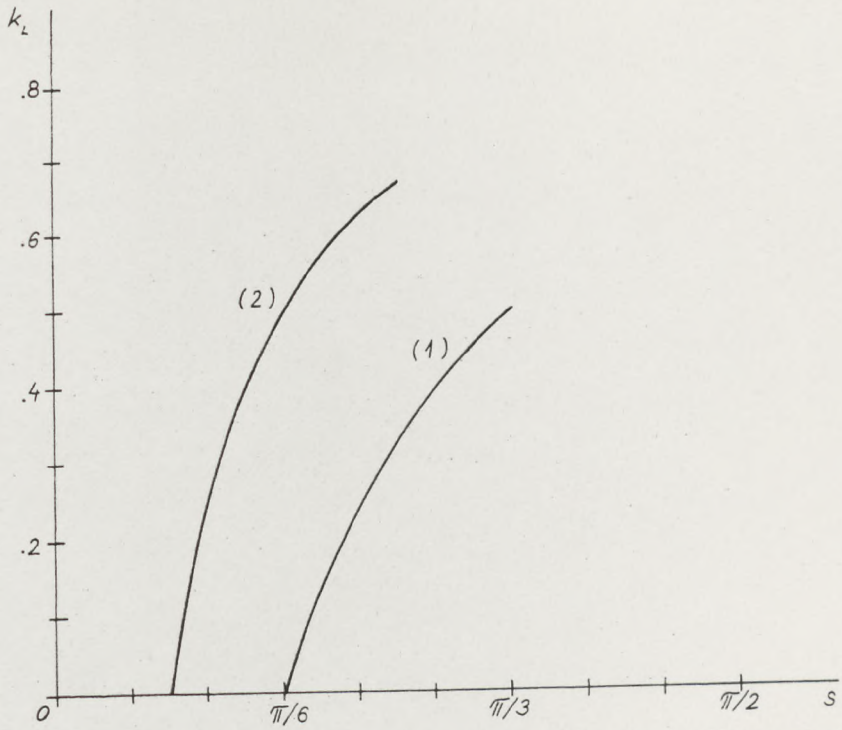


FIG 2.12 Variation of inductance overlap with stator pole arc

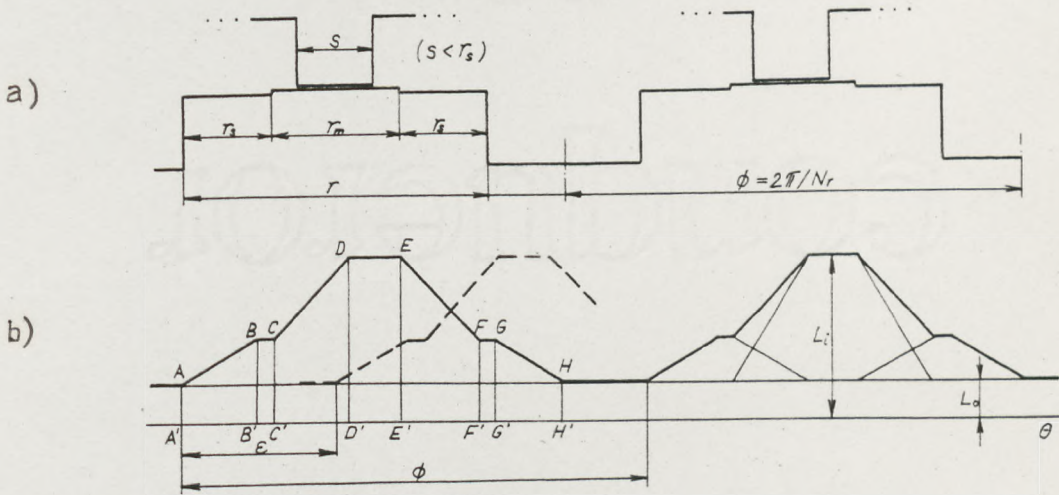


FIG 2.13 Graded rotor pole with $r_s > s$

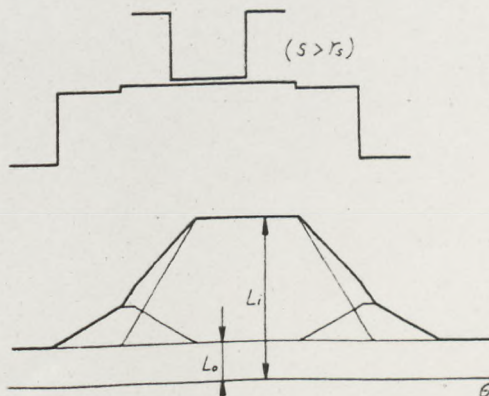
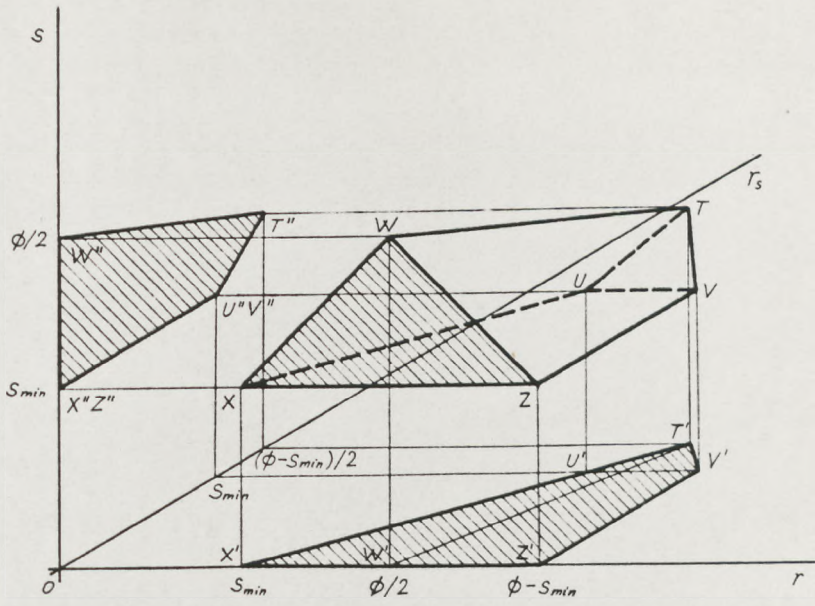
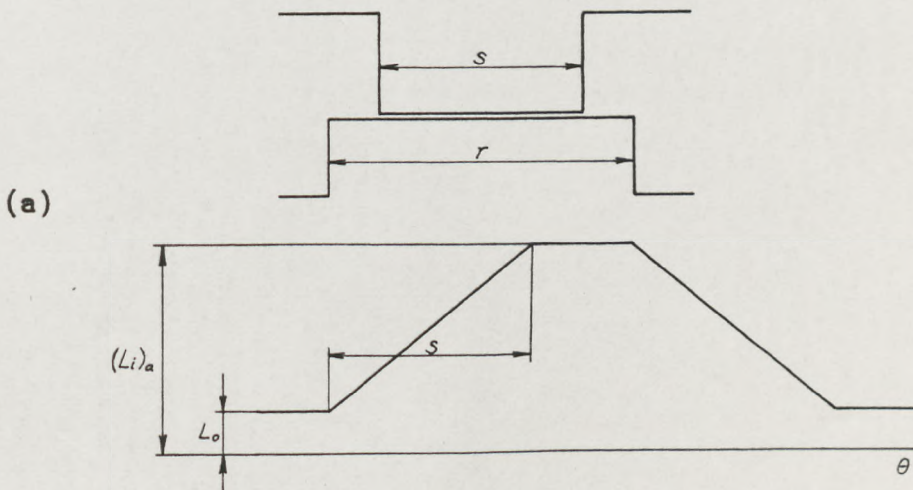


FIG 2.14 Graded rotor pole with $r_s < s$



$$\begin{aligned}
 s &> s_{\min} \\
 s + r &< \phi \\
 r &> s \\
 s &< r_s \\
 r - r_s &> s
 \end{aligned}$$

FIG 2.15 Boundaries of possible values of stator and rotor pole arcs and starting pole arc



continued

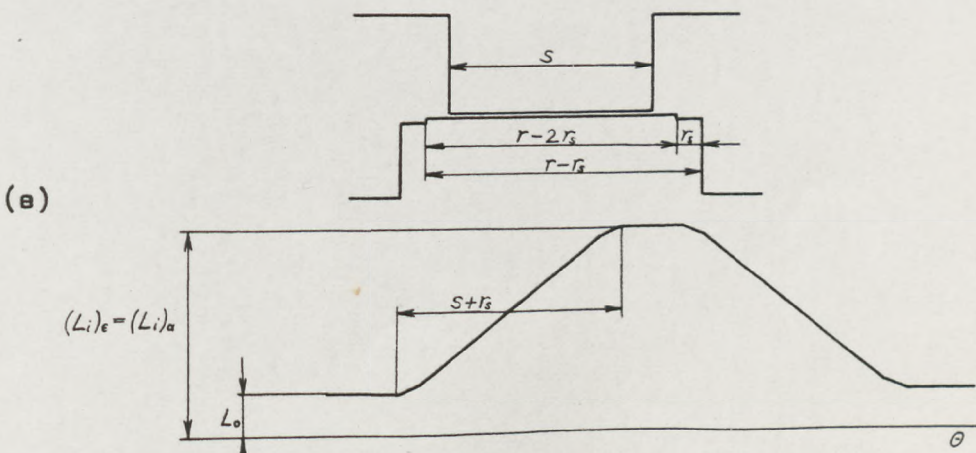
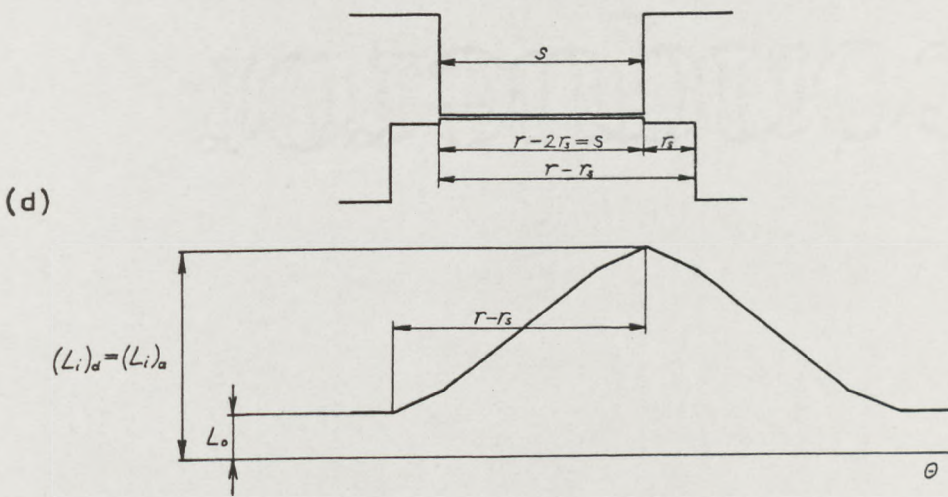
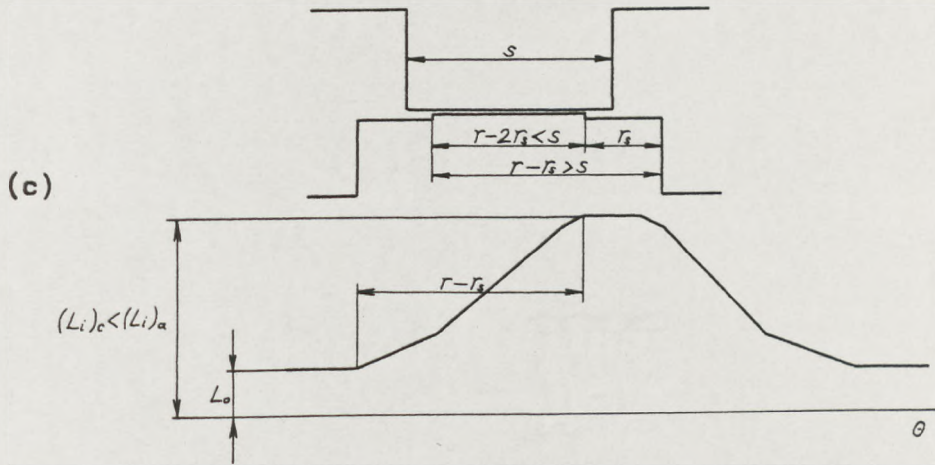
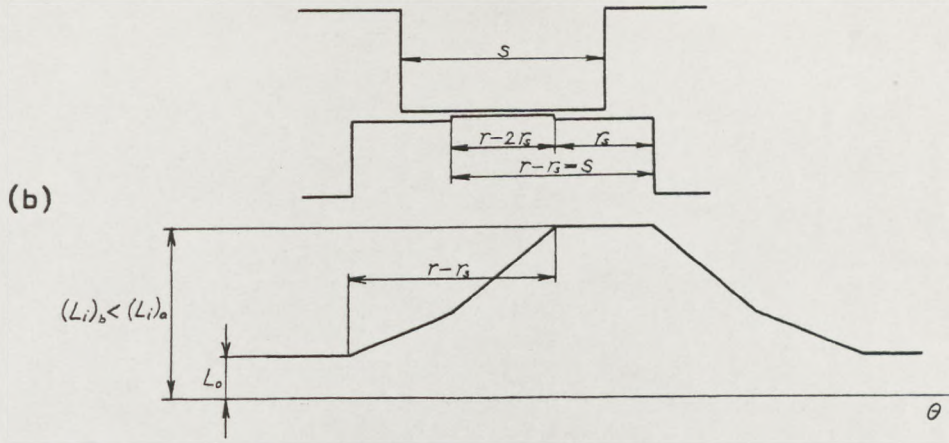


FIG 2.16 Gradings with various r_s

CHAPTER 3

ANALYTICAL ESTIMATION OF THE MINIMUM AND MAXIMUM INDUCTANCES OF A

DOUBLY-SALIENT MACHINE

3.1 Introduction

The minimum and maximum inductances corresponding to two extreme rotor positions, when the rotor interpolar pole axis is aligned with the axis of the excited pole and when the rotor pole axis is aligned with the axis of the excited pole, are very important parameters both in the linear analysis of the switched reluctance motor and in determining the behaviour under nonlinear conditions. It is therefore desirable to obtain a simple analytical estimation for calculating these parameters in terms of the geometric proportions of the machine in order to facilitate the optimisation of the motor design.

In the analysis which follows, a magnetic configuration of a switched reluctance motor having typical dimensional proportions, is considered and an analytical method of estimating the minimum and maximum inductances with the comparison between estimated and measured results are given.

From the results of the analysis a recommendation for a preferred rotor profile with respect to the minimum inductance value is presented.

3.2 General approach

A great deal of work has been done on analytically determining the magnetic permeance and force between toothed structures of stepping motors. Much of this springs from the work of F W Carter¹⁴ based on the Schwarz-Christoffel transformation. Some of Carter's unpublished work has been modified and used as a basis for a very comprehensive numerical analysis of identically double-slotted structures by

Mukherji and Neville¹⁵. Jones'¹³ solution, based on the Schwarz-Christoffel transformation, is for identical double-toothed structures where the gap is small compared to the tooth dimensions. Chai¹² has developed permeance formulae based on the assumption of the simple pattern of the field between toothed structures which consists of straight line segments and concentric circular arcs. It is important to note that Jones' and Chai's results for the permeance are in very good agreement when the air-gap length is small compared to the other dimensions.

However, all the methods mentioned above are based on the analysis of rectangular teeth and slots on the stator and rotor and neglect the distribution of the exciting winding on the teeth or assume it to be remote from the teeth. These assumptions may very often be justifiable in stepping motors, but in a switched reluctance motor having excitation windings on the stator poles (teeth) and where profiles of the stator and rotor poles (teeth) and interpolar spaces (slots) are not rectangular, the situation is much more complicated.

However, the fact that the air-gap in the switched reluctance motor is very small compared to the other dimensions, together with the above mentioned fact about the agreement of Jones' and Chai's results for permeance in a stepping motor, show that the assumption that field lines consist of straight line segments and circular arcs might be applied here as well.

Thus in the method for estimating the minimum inductance described below it is assumed that the magnetic permeability of the iron is infinite and that field lines inside the machine in the minimum inductance position consist of parallel straight line segments and concentric circular arcs which are perpendicular to the iron surface and along which integration is simple.

In the minimum inductance position, the air paths of the field lines are very long and the mmf drop in the iron is small compared to the mmf drop in the air. Therefore, the estimation of the minimum inductance given below is valid even for the case where the realistic situation in the iron is considered.

In the maximum inductance position the mmf drop in the iron is considerable (even in the case when iron is not saturated) in comparison with mmf drop in the air-gap because the air-gap length is small, and therefore must be taken into account. The saturation effect has to be taken into account.

The comparison between estimated and measured values of inductance is made for a motor with the following parameters:

- number of stator poles	$N_s = 8$
- number of rotor poles	$N_r = 6$
- stator pole arc	$s = 20^\circ$
- rotor pole arc	$r = 26^\circ$
- air-gap length	$g = 0.254 \text{ [mm]}$
- air-gap length of interpolar space	$g_i = 9 \text{ [mm]}$
- rotor diameter	$d = 75 \text{ [mm]}$
- stator outside diameter	$d_o = 140 \text{ [mm]}$
- back iron width	$c = 9.2 \text{ [mm]}$
- core length	$\ell = 76 \text{ [mm]}$
- number of turns per phase	$N = 290$

3.3 Estimation of the minimum inductance

Fig 3.1 shows a sketch of the field pattern of the magnetic configuration corresponding to the minimum inductance position (the axis of the rotor interpolar space is aligned with the axis of the excited pole). The figure represents typical dimensional proportions of the magnetic configuration of a switched reluctance motor. It is assumed that the field, inside the machine, is plane-parallel with respect to the plane of the figure and can therefore be considered in two dimensions. The field effects at the ends of the machine (in the third dimension) are considered separately. Since it is assumed that the magnetic permeability of iron is infinite, only the magnetic potentials of the stator poles of the excited phase are non zero. The field pattern is symmetrical with respect to the axis of the excited stator poles and with respect to the axis perpendicular to it. Therefore, it is sufficient to consider one quarter of the total field pattern and this is shown in Fig 3.1.

Assuming that the excited pole in Fig 3.1 has north polarity then the field map in the air space inside the machine may be divided into two parts: the first part contains the field lines which pass to the rotor and second one contains the field lines which do not.

The second group of lines consists of the lines which lead from the excited stator pole side to the stator back of core (path 1ℓ) and lines which lead from the stator pole side to the adjacent pole (path 2ℓ).

The first group of lines consists of the lines which lead from the stator pole side to the rotor pole surface (path $3r$), lines which lead from the stator pole side to the rotor pole side (path 4), lines which lead from the stator pole face to the rotor pole side (path 5) and lines which lead from the stator pole face to the rotor interpolar surface (path 6).

It has to be borne in mind that each of the field lines in the paths 1ℓ , 2ℓ and $3r$ is linked with a different number of turns. Such partial linkages have been neglected in the methods for analytical determination of inductances of doubly salient machines published so far. The lines of path 4, 5 and 6 are approximately linked with nearly all the turns and are assumed to link perfectly. In handling the partial linkages below, it is assumed that conductors are uniformly distributed over the winding cross section.

In order to allow an analytical solution, the field lines are approximated as follows:

It is clear from the path length and linked amp-turns that the flux-linkage of the path 2ℓ is very small in comparison with the flux-linkage of the paths 4, 5 and 6. This also applies to the flux-linkages of the path 1ℓ and the outer region of the path $3r$, which are small compared with the flux-linkages of the paths 4, 5, 6 and the inner region of the path $3r$, either because of the amount of amp-turns or because of the length of the field lines. Therefore, in calculating the total inductance, a large error will not be incurred even if a gross approximation is made to the mapping of the lines of path 2ℓ . These lines are represented with lines similar to the lines of the paths 1ℓ and $3r$. Thus the path 2ℓ may be associated with the paths 1ℓ and $3r$ forming together paths 1 and 3. The transition point O_e in Fig 3.2 is assumed to be at the mid-point of the coil

side. The analytical determination of the position of the point O_e is based on the condition that the ratio of the lengths of the lines from the point O_e is equal to the ratio of amp-turns linked by them. The results which are obtained by such rather extensive calculations show that point O_e lies very near to the mid-point of the pole side.* On the basis of this argument and the explanations given above about the values of the flux-linkages in the outer regions of the paths 1 and 3, the simple assumption that the point O_e is at the mid-point of the coil side is justified. Obviously, these approximations are justified for calculating the total inductance whereas for calculating separately the leakage inductance and the inductance between the stator and the rotor, it would not be justified.

Fig 3.2 shows the simplified field map inside the machine. In this figure it is assumed that:

- i) field lines of the path 1 consist of concentric circular arcs with the centre at the point C_1 ,
- ii) field lines of the path 3 consist of the concentric circular arcs with the centre at the point C_3 ,
- iii) the approximation for the lines of path 4 which is given below,
- iv) field lines of path 5 consist of concentric circular arcs with the center at the point C_5 , and
- v) field lines of path 6 consist of parallel straight line segments.

Points C_1 , C_3 , C_5 are chosen on the basis that approximated field lines are perpendicular or near to perpendicular at the iron surface and that this field form is preserved when the dimensions of the magnetic configuration are changed. The position of the transition point O_r is determined similarly to that of the transition point O_e . (This is shown below.)

Since the magnetic configuration in the minimum inductance position

* This is not true in general, but applies for the machine proportions considered here.

is symmetrical with respect to the pole axis and with respect to the axis perpendicular to it, then flux-linkage of one pole coil is

$$\Psi = 2(\psi_1 + \psi_3 + \psi_4 + \psi_5 + \psi_6)$$

where $\psi_1, \psi_3, \psi_4, \psi_5, \psi_6$ are flux-linkages of the paths 1, 3, 4, 5, 6 respectively. The total inductance of one phase is

$$L_o = 2 \frac{\Psi}{i}$$

because there are two poles per phase each of which has a coil with $N/2$ turns, where N is number of turns per phase.

$$\begin{aligned} L_o &= \frac{4}{i} (\psi_1 + \psi_3 + \psi_4 + \psi_5 + \psi_6) \\ &= 4 (L_1 + L_3 + L_4 + L_5 + L_6) \\ &= N^2 \mu_o \ell_F (P_1 + P_3 + P_4 + P_5 + P_6) \end{aligned} \quad (3.1)$$

$$= N^2 \mu_o \ell P_o \quad (3.2)$$

where,

$$P_j = L_j / \left[\mu_o \ell_F \left(\frac{N}{2} \right)^2 \right], \quad (j = 1, 3, 4, 5, 6)$$

ℓ_F is the effective core length (see below),

$P_o = \frac{\ell_F}{\ell} \sum_j P_j$ is the total normalised equivalent minimum permeance.

3.3.1 Parameters of the magnetic configuration

The magnetic configuration is described by the following set of parameters

- number of stator poles N_s ,
- number of rotor poles N_r ,
- stator pole arc s ,
- rotor pole arc r ,

- air-gap length g ,
- air-gap length of rotor interpolar space g_i ,
- rotor diameter d ,
- stator outside diameter d_o
- back iron width c ,
- core length l ,
- number of turns per phase N .

This set of parameters determines the coil dimensions as follows.

Although the filling coefficient of the stator interpolar space is not high when the pole winding profile is rectangular, that profile is technically simple. Any other profile is associated with winding difficulties and therefore a rectangular winding profile is assumed in the following analysis.

Using the above parameters, the remaining angles and dimensions in Fig 3.3 may be determined.

Rotor pole pitch

$$\phi = \frac{2\pi}{N_r} \quad (3.3)$$

Stator pole pitch

$$\delta = \frac{2\pi}{N_s} \quad (3.4)$$

Angle $H_1C_1E = \gamma$

$$\gamma = \frac{\pi}{2} - \frac{\delta}{4} \quad (3.5)$$

Stator pole width

$$2p = 2\left(\frac{d}{2} + g\right) \sin \frac{\gamma}{2} \quad (3.6)$$

and a half of stator pole width

$$p = \left(\frac{d}{2} + g\right) \sin \frac{\gamma}{2} \quad (3.7)$$

Coil width

$$w = \left(\frac{d}{2} + g\right) \tan \frac{\delta}{2} - p \quad (3.8)$$

Coil height may be determined from triangle $H_1 H_2 H_3$

$$v \approx \left[\frac{d_0}{2} - c - \frac{\frac{d}{2} + g}{\cos \frac{\delta}{2}} \right] \frac{1}{\cos \frac{\delta}{2}} \quad (3.9)$$

The lengths between marked points are

$$C_3 D = y$$

$$y = \left(\frac{d}{2} + g\right) - \frac{d}{2} \cos \frac{\phi-r}{2} \quad (3.10)$$

$$C_3 B = C_3 B_1 = h$$

$$h \approx \frac{d}{2} \sin \frac{\phi-r}{2} - p \quad (3.11)$$

$$C_3 A = BC_5 = b$$

$$b = \left(\frac{d}{2} + g\right) \cos \frac{s}{2} - \frac{d}{2} \cos \frac{\phi-r}{2} \quad (3.12)$$

$$DO_\ell = EO_\ell = q$$

$$q = \frac{v}{2} \quad (3.13)$$

$$C_1 E = u$$

$$u = \frac{w}{\tan \delta} \quad (3.14)$$

$$C_1 O_\ell = m$$

$$m = u + q \quad (3.15)$$

$$C_3 O_\ell = n \quad (3.15)$$

$$n = y + q \quad (3.16)$$

Normalising the dimensions with respect to the outside stator diameter gives

$$G = \frac{g}{d_o}, G_i = \frac{g_i}{d_o}, D = \frac{d}{d_o}, C = \frac{c}{d_o}, L_F = \frac{l_F}{d_o}$$

Then the normalised values P, W, V, Y, H, B, Q, U, M, N are

$$P = \left(\frac{D}{2} + G\right) \sin \frac{s}{2}$$

$$W = \left(\frac{D}{2} + G\right) \tan \frac{\delta}{2} - P$$

$$V = \left(\frac{1}{2} - C - \frac{\frac{D}{2} + G}{\cos \frac{\delta}{2}}\right) \cdot \frac{1}{\cos \frac{\delta}{2}}$$

$$Y = \frac{D}{2} + G - \frac{D}{2} \cos \frac{\phi-r}{2}$$

$$H = \frac{D}{2} \sin \frac{\phi-r}{2} - P$$

$$B = \left(\frac{D}{2} + G\right) \cos \frac{s}{2} - \frac{D}{2} \cos \frac{\phi-r}{2}$$

$$Q = \frac{V}{2}$$

$$U = \frac{W}{\tan \gamma}$$

$$M = U + Q$$

$$N = Y + Q$$

3.3.2 Calculation of minimum inductance components

a) Component L_1

Fig 3.4 shows detail of the magnetic configuration for flux-path 1 where the broken line represents the approximated back of core surface. The flux-linkage of path 1 is small in comparison with the flux-linkages of paths 3, 4, 5 and 6, because the linked amp-turns become smaller as the field lines are nearer to the corner between the back of core and the pole. This is taken to justify the approximation that in calculating this particular inductance the small empty space between the pole winding and the back of core may be considered filled with pole winding turns.

The elementary flux-path $l'l''$ is linked with

$$\frac{\text{area } C_1 l'' l' C_1}{\text{area } C_1 H_2 H_1 D} \left(\frac{Ni}{2}\right) \approx \frac{\frac{1}{2} \delta x \times x}{wv + \frac{1}{2} w u} \left(\frac{Ni}{2}\right) \text{ amp-turns}$$

The field on the elementary flux-path $l'l''$ is

$$H_x = \frac{1}{\delta x} \left(\frac{\frac{1}{2} \delta x \times x}{wv + \frac{1}{2} w u} \left(\frac{Ni}{2}\right) \right)$$

The elementary flux-linkage is

$$d\psi_x = \left(\frac{\frac{1}{2} \delta x \times x}{wv + \frac{1}{2} w u} \left(\frac{Ni}{2}\right) \right) \mu_0 H_x l_F dx$$

Hence, L_1 is

$$L_1 = \frac{\int_{(0)}^{(m)} d\psi_x}{i} = \mu_0 l_F \left(\frac{N}{2}\right)^2 \frac{\delta m^4}{4w^2(2v+u)^2} \quad (3.17)$$

or in the form of normalised equivalent permeance

$$P_1 = \frac{L_1 l}{\mu_0 l_F \left(\frac{N}{2}\right)^2} = \frac{\delta m^4}{4w^2(2v+u)^2} \quad (3.18)$$

For the machine defined by the parameters which are given above, $P_1 = 0.054 = 0.0249 P_0$. Consideration of the approximation of the above simple method indicates that the result is likely to be an

overestimate by perhaps 10%.

b) Component L_3

Fig 3.5 shows details of the magnetic configuration for flux-path 3. The amp-turns linked by field lines decrease and the length of the lines increases the further they are from line BB_1 . Thus the greater the radius of the line, the smaller the contribution of flux-line to the value of inductance component L_3 . This reasoning supports the approximation that the rotor pole surface may be represented by a straight line at right angle to the stator pole side through the point C_3 .

The elementary flux-path is linked with

$$\frac{wv - \text{area } D3''3'''D}{wv} \left(\frac{Ni}{2}\right) \approx \frac{wv + \text{area } D3'''3'C_3D - \text{area } C_33''3'C_3}{wv} \left(\frac{Ni}{2}\right)$$

$$= \frac{wv + xy - \frac{x^2\pi}{4}}{wv} \left(\frac{Ni}{2}\right) \text{ amp-turns}$$

The field on the elementary flux-path $3'3''$ is

$$H_x = \frac{1}{\frac{\pi}{2}x} \left(\frac{wv + xy - \frac{x^2\pi}{4}}{wv} \left(\frac{Ni}{2}\right) \right)$$

The elementary flux-linkage is

$$d\psi_x = \left(\frac{wv + xy - \frac{x^2\pi}{4}}{wv} \left(\frac{Ni}{2}\right) \right) \mu_0 H_x \ell_F dx$$

Hence, L_3 is

$$L_3 = \frac{\int (n)}{(h)} \frac{d\psi_x}{i} = \frac{2}{\pi} \left\{ 1n \frac{n}{h} + \frac{2(n-h)y}{wv} - \frac{(n^2-h^2)}{4(wv)^2} (\pi wv - 2y^2) - \frac{(n^3-h^3)y\pi}{6(wv)^2} + \frac{(n^4-h^4)\pi^2}{64(wv)^2} \right\} \mu_0 \ell_F \left(\frac{N}{2}\right)^2 \quad (3.19)$$

or in the form of normalised equivalent permeance

$$P_3 = \frac{L_3}{\mu_0 \ell_F \left(\frac{N}{2}\right)^2} = \frac{2}{\pi} \left\{ \ln \frac{N}{H} + \frac{2(N-H)Y}{WV} - \frac{(N^2 - H^2)}{4(WV)^2} (\pi WV - 2Y^2) \right. \\ \left. - \frac{(N^3 - H^3)Y\pi}{6(WV)^2} + \frac{(N^4 - H^4)\pi^2}{64(WV)^2} \right\} \quad (3.20)$$

For the machine defined by the parameters which are given above, $P_3 = 0.458 = 0.211 P_0$. The order of the likely error in the estimation with the above approximations is a 5% overestimate in the value of P_3 .

c) Component L_4

Fig 3.6 shows details of the magnetic configuration for flux-path 4 between the semi-broken lines B_1B and AA_1 . However, the field lines B_1B and AA_1 are not concentric circular arcs with centres C_3 and C_5 and therefore lines between them cannot be simple represented by concentric circular arcs with centres C_3 and C_5 . Therefore path 4 is approximated by the lines which consist of concentric circular arcs with centres A and B and parallel straight line segments which are perpendicular to the diagonal C_3C_5 and of length

$$f = 2b \cos (\widehat{C_3 AA'})$$

$$\text{Since } \widehat{C_3 AA'} = \widehat{AC_5 C_3} \text{ (because } C_3A \perp AC_5 \text{ and } A'A \perp C_3C_5) \\ = \widehat{ABC_3} \text{ (triangles } AC_5C_3 \text{ and } ABC_3 \text{ are similar)}$$

and $\widehat{ABC_3} \approx \frac{\phi - \tau}{2}$ (because AB is approximately perpendicular to BA_1), then

$$f = 2b \cos \frac{\phi - \tau}{2}$$

The radius $e = AB' = A'B$ is

$$e = f / \tan(\widehat{B'AB})$$

Since $\widehat{B'AB} = \widehat{B'AC_5} + \widehat{C_5 AB}$, $\widehat{B'AC_5} = \widehat{C_5 C_3 B}$ (angles between parallel sides)

and $C_5 \hat{C}_3 B = C_5 \hat{A} B$ (angles in rectangle) $\approx \frac{\phi-r}{2}$, ie $B'AB \approx 2 \frac{\phi-r}{2} = \phi-r$,
then $e = f/\tan(\phi-r)$

Further, $B' \hat{A} B_1 = \frac{\pi}{2} - B' \hat{A} C_5 = \frac{\pi}{2} - \frac{\phi-r}{2}$ and $A' \hat{B} A_1 = \frac{\pi}{2} - C_3 \hat{B} A' - \frac{\phi-r}{2} = \frac{\pi}{2} - (\phi-r)$

Since area $DB_1 D_1 D$ (Fig 3.3) is small in comparison with area $DEH_2 H_1 D$,
than it may be assumed that all field lines are linked with all amp-
turns.

The field on the elementary flux-path 4'4" is

$$H_x = \frac{1}{x \left(\frac{\pi}{2} - \frac{\phi-r}{2} \right) + f + (e-x) \left[\frac{\pi}{2} - (\phi-r) \right]} \left(\frac{Ni}{2} \right)$$

$$= \frac{1}{f + \left[\frac{\pi}{2} - (\phi-r) \right] e + \frac{\phi-r}{2} x} \left(\frac{Ni}{2} \right)$$

The elementary flux-linkage is

$$d\psi_x = \frac{N}{2} \mu_0 H_x \ell_F dx$$

Hence,

$$L_4 = \frac{\int_{(o)}^{(e)} d\psi_x}{i} = \mu_0 \ell_F \left(\frac{N}{2} \right)^2 \frac{2}{\phi-r} \ln \frac{2f + (\pi - \phi + r)e}{2f + (\pi - 2\phi + 2r)e}$$

Substituting for f and e

$$L_4 = \mu_0 \ell_F \left(\frac{N}{2} \right)^2 \frac{2}{\phi-r} \ln \frac{2\tan(\phi-r) + \pi - (\phi-r)}{2\tan(\phi-r) + \pi - 2(\phi-r)} \quad (3.21)$$

or in the form of normalised permeance

$$P_4 = \frac{L_4}{\mu_0 \ell_F \left(\frac{N}{2} \right)} = \frac{2}{\phi-r} \ln \frac{2\tan(\phi-r) + \pi - (\phi-r)}{2\tan(\phi-r) + \pi - 2(\phi-r)} \quad (3.22)$$

For the machine defined by parameters which are given above, $P_4 = 0.557$
 $= 0.257 P_o$. It is very difficult to give the order of likely error,
because the shapes of the field lines between lines $B_1 B$ and AA_1 are
very complex. The above approximation gives longer flux-lines than

actually occur and therefore the value of P_4 is underestimated. Consideration of other methods of representing the field which are not apparently as good as the above, but which clearly overestimate the permeance P_4 , indicates the error in the present method should not be worse than a 15% underestimate.

d) Components L_5 and L_6

Fig 3.7 shows the magnetic configuration of flux-paths 5 and 6. If the field lines of path 5 consist of concentric circular arcs with centre C_5 , and the field lines of path 6 consist of parallel straight line segments, then the transition point O_r on the stator pole surface, is determined from the condition mentioned above, ie the length of the circular arc (field line) $O_r O_1$ is equal to length of straight line segment $O_2 O_r$.

The angle which corresponds to the circular arc may be approximately taken to be $\pi/2 - (\phi-r)/2$. Therefore, the condition that $O_r O_1 = O_2 O_r$ is

$$t\left(\frac{\pi}{2} - \frac{\phi-r}{2}\right) = g_i \quad \therefore t = \frac{2 g_i}{\pi - (\phi-r)}$$

The field on the elementary flux path 5'5" is

$$H_x = \frac{1}{x\left(\frac{\pi}{2} - \frac{\phi-r}{2}\right)} \left(\frac{Ni}{2}\right)$$

and the elementary flux-linkage is

$$d\psi_x = \frac{N}{2} \mu_o H_x \ell_F dx$$

Hence,

$$L_5 = \frac{\int (t) d\psi_x}{i} = \mu_o \ell_F \left(\frac{N}{2}\right)^2 \frac{2 \ln \frac{t}{h}}{\pi - (\phi-r)}$$

Substituting for t

$$L_5 = \mu_o \ell_F \left(\frac{N}{2}\right)^2 \frac{2}{\pi - (\phi-r)} \ln \frac{2 g_i}{h[\pi - (\phi-r)]} \quad (3.23)$$

or in the form of normalised permeance

$$P_5 = \frac{L_5}{\mu_0 \ell_F \left(\frac{N}{2}\right)^2} = \frac{2}{\pi - (\phi - r)} \ln \frac{2 G_i}{H[\pi - (\phi - r)]} \quad (3.24)$$

The component L_6 is simply

$$L_6 = \mu_0 \ell_F \left(\frac{N}{2}\right)^2 \frac{p + h - t}{g_i}$$

and substituting for t

$$L_6 = \mu_0 \ell_F \left(\frac{N}{2}\right)^2 \left[\frac{p + h}{g_i} - \frac{2}{\pi - (\phi - r)} \right] \quad (3.25)$$

or in form of normalised permeance

$$P_6 = \frac{L_6}{\mu_0 \ell_F \left(\frac{N}{2}\right)^2} = \frac{p + h}{g_i} - \frac{2}{\pi - (\phi - r)} \quad (3.26)$$

For the machine defined by the parameters which are given above,

$P_5 = 0.474 = 0.218 P_0$ and $P_6 = 0.320 = 0.147 P_0$. The order of the likely error in the estimation of P_5 with the above approximation is a 6% overestimate in the value of P_5 .

3.3.3 Fringe flux at the ends of core Effective core length

The fringe flux at the end of core can be taken into account by introducing effective length. The effective length may be very roughly estimated by using the following method. Consider an axial cross-section. In Fig 3.8 stator and rotor are represented by a pair of opposing faces with flanks extending to infinity and with a fictitious uniform air-gap, g_F , the length of which is equal to the mean length of the lines (i), (ii), (iii), (iv) and (v) (Fig 3.3) (where the fringing is the most pronounced).

$$g_F = \frac{1}{5} \left[\frac{\pi}{2} n + \frac{\pi}{2} h + \left(\frac{\pi}{2} - \frac{\phi - r}{2} \right) h + g_i + g_i \right] \quad (3.27)$$

Approximately, it may be considered that the flux in the gap (Fig 3.8) becomes uniform at a short distance from the edge.

The model in Fig 3.8 is symmetrical about the axis ss and therefore, the permeance of that model is equal to one half of the permeance of the model shown in Fig 3.9.

In the model in Fig 3.9 the fringing field is unlimited, ie the problem involves an infinite fringe. Carter⁽¹⁴⁾ uses the Schwarz-Christoffel transformation to obtain an expression for fringe flux (effective core length) emphasizing that it is a matter of judgement how much of the computed fringe flux should be taken as effective. However, Carter's expressions for this case are very complex and are not suitable for simple analytical solution.

If the field line which leads from the point O_e (Fig 3.2) on the stator pole end to the rotor end is approximated by a semi-circle with the radius equals to n (see above), then the model in Fig 3.9 may be approximated by the model shown in Fig 3.10.

According to the Reference No 16 the effective core length which takes into account fringe flux for this model is

$$\ell_F = (\ell + 2n) - 2n\sigma = \ell + 2n(1-\sigma) \quad (3.28)$$

where σ is Carter's coefficient

$$\sigma = \frac{2}{\pi} \left\{ \arctan\left(\frac{2n}{g_F}\right) - \frac{g_F}{4n} \ln \left[1 + \left(\frac{2n}{g_F}\right)^2 \right] \right\} \quad (3.29)$$

For the machine defined by the parameters which are given above $g_F = 10.12$ [mm], $\sigma = 0.5089$, $\ell_F = 88.8$ [mm] which means that the fringing flux at the ends of core at the minimum inductance position is 16.5% of the total flux-linkage for $\ell/d=1.0$.

3.3.4 Comparison of estimated and measured results

Using the method presented above, the minimum inductance has been estimated for the switched reluctance motor with given parameters.

The estimated value (including the effect at the ends of core) is 17.5 [mH].

The measured value is 20.35 [mH]. (This value has been measured at a low current of 1[A] using the bifilar coil as a search coil (see Chapter 5), but it stays almost constant in the range between 1[A] and 10[A] (rated value).)

Taking the measured value as reference, the estimated value is 14% low. Some of the inductance components have been overestimated, others have been underestimated and although the errors in estimating the inductance components tend to balance out in the total inductance, this cancellation obviously cannot be complete and that is one of the reasons causing the difference between estimated and measured results. However, it is logical to assume that the main reason for the above discrepancy is the very rough estimation of fringe flux at the ends of core.

If the fringe flux at the ends of core is excluded, then the estimated value of minimum inductance is $17.5/(e_f/e) = 15.02$ [mH]. Unfortunately this value cannot be separately measured. The computed value of minimum inductance, which may be used as reference when the fringe flux at the ends of core is excluded, is obtained by using a sophisticated 2-dimensional numerical field solution based on boundary-integral method⁽³⁵⁾. This value is 14.63 [mH] which is 2.7% below the estimated value (15.02 [mH]). Such excellent agreement indicates that the value of minimum inductance, when the fringe flux at the ends of core is excluded, may be very accurately estimated using the simple analytical method. Similar agreement has been obtained for a 3-phase, 6/4 pole machine.

When Chai's method is used the error is 40% and this sufficiently illustrates the superiority of the presented method.

3.4 Recommendation for the rotor profile

It has already been stated in Chapter 2 that it is desirable for a high value of average output torque that the value of normalised

equivalent minimum permeance (P_o) is as small as possible. Assuming that the stator and rotor pole arcs of the machine with given stator and rotor pole number and stator and rotor diameters have been determined by linear optimisation with respect to certain requirements of performance, then P_o can only be reduced by increasing the rotor interpolar air-gap length g_i . A further benefit of increasing g_i is a reduced value of rotor inertia and hence improved speed of response.

From Fig 3.7 and the corresponding text, it may be observed that if g_i becomes equal to or greater than $g_{ic} = (p + h) \left(\frac{\pi}{2} - \frac{\phi-r}{2} \right)$, then the flux path 6 vanishes and P_o no longer depends on g_i . However, in that case the width of the rotor pole root becomes very small. If the condition is imposed that the maximum flux density in the roof of rotor pole must not be higher than the maximum flux density in the stator pole root, the edge which is parallel to rotor pole axis and at a distance p from it, is the limiting rotor pole edge (Fig 3.11). Therefore, the reduction of P_o is achieved by increasing of g_i with the rotor pole edge limited by the line $8NN_1$ (Fig 3.11), until g_i becomes equal to g_{ic} .

3.5 Estimation of the maximum inductance using B-H curve

In the maximum inductance position the mmf drop in the iron is considerable, even in the case when the iron is not saturated, in comparison with mmf drop in the air-gap (the air-gap length is very small compared with the rotor diameters, typically g is about $0.005d$). When the iron becomes saturated the mmf drop in the iron increases nonlinearly and may exceed the mmf drop in the air-gap. Therefore the mmf drop in the iron and the nonlinearity of B-H curve of iron must be taken into account for estimation of the maximum inductance.

To estimate the maximum inductance L_i by a simple analytical method the following assumptions are made:

- i) When a phase winding is excited the magnetic circuit is treated as a simple '2-pole' pattern (Fig 3.12);
- ii) There is no flux leakage, ie all flux passes from the stator to the rotor and back;
- iii) The flux is linked with all the turns;
- iv) The flux is uniformly distributed in the cross-section normal to the field lines.

In the maximum inductance position the field pattern is symmetrical about the axis of the excited phase and therefore only one half of the magnetic circuit, which carries one half of the total flux, need be considered. Further simplification is to split this half of the magnetic circuit into the following parts connected in the series:

- two stator poles (subscript 's') with
cross-section: $a_s = \frac{d}{2} \left(\sin \frac{s}{2} \right) \ell = 496.2 \text{ [mm}^2\text{]}$
- length : $\ell_s = 2 \left(\frac{d_0}{2} - c - \frac{d}{2} - g \right) = 44.9 \text{ [mm]}$

- two air-gaps (subscript 'g') with
cross-section*: $a_g = \left[\frac{1}{2} \left(\frac{d}{2} + g \right) s + (1 - \sigma) i \right] \ell = 531.1 \text{ [mm}^2\text{]}$
where, $i = \frac{1}{2} \frac{d}{2} (r-s)$
 $\sigma = \frac{2}{\pi} \left[\arctan \left(\frac{i}{g} \right) - \frac{g}{2i} \ln \left(1 + \left(\frac{i}{g} \right)^2 \right) \right]$
length : $\ell_g = 2g = 0.508 \text{ [mm]}$
- two rotor poles (subscript 'r') with
cross-section**: $a_r = a_g = 531.1 \text{ [mm}^2\text{]}$
length : $\ell_r = 2g_i = 18 \text{ [mm]}$
- rotor body (subscript 'b') with
cross-section : $a_b = \left(\frac{d}{2} - g_i \right) \ell = 2172 \text{ [mm}^2\text{]}$
length : $\ell_b = \frac{1}{2} \left(\frac{d}{2} - g_i \right) \pi = 44.8 \text{ [mm]}$
- stator yoke (subscript 'y') with
cross-section : $a_y = c\ell = 746.8 \text{ [mm}^2\text{]}$
length : $\ell_y = \frac{1}{2} (d_o - c) \pi = 204.5 \text{ [mm]}$

(The numerical results are related to the machine with the parameters given above.)

The mmf equation is

$$Ni = \frac{B_g}{\mu_0} \ell_g + H_s \ell_s + H_r \ell_r + H_b \ell_b + H_y \ell_y$$

Having given the value of flux-linkage, the values of flux densities B_g , B_s , B_r , B_b and B_y can be calculated ($B = \frac{\psi}{Na}$) and using the B-H curve of the appropriate steel the values for H_s , H_r , H_b and H_y can be found. Using the mmf equation the value of current corresponding to a given value of flux-linkage can be found and hence the maximum inductance is $L_i = \frac{\psi}{i}$. The normalised equivalent maximum permeance is given by

$$P_i = \frac{L_i}{\mu_0 \ell N^2}$$

* Due to fringing effects the effective cross-section in the air-gap is bigger than the stator pole cross-section. To make some allowance for this the air-gap cross-section is increased by introducing Carter's¹⁸ coefficient.

** It is assumed that the rotor pole cross-section is constant along the rotor pole and equal to effective cross-section in the air-gap (a_g).

Fig 3.13 shows the ψ -i curves at the maximum inductance position which are obtained by measurement, by 2-dimensional numerical field analysis and by using the above method. (The B-H curve also shown in Fig 3.13 has been obtained by measurements on a toroidal iron specimen.)

Bearing in mind that the above simple analytical method treats a very simplified field pattern, the error which is within 5% (in terms of inductance) is not so bad. In the nonsaturated region of the ψ -i curve the estimated and measured results are very close. Extremely good agreement between the measured ψ -i curve of maximum inductance position and the one obtained by using 2-dimensional numerical field analysis shows that the fringe flux at the ends of core in maximum inductance position is negligible compared with the flux within machine.

3.6 Conclusion

A method for the simple analytical estimation of the minimum and maximum inductances has been given. The estimation is valid even in the case where the realistic situation in the iron (saturation) is considered.

The method of estimation of the minimum inductance is based on the assumption that the field lines consist of circular arcs and straight line segments. The distribution of the winding is allowed for. The estimated value of minimum inductance, when the fringe flux at the ends of core is excluded, agrees very well with the result obtained by 2-dimensional numerical field solution (using boundary-integral method, the difference is 2.7%). An allowance based on a rough approximation for fringe flux at the ends of core has been made. The estimated value of total minimum inductance is 14% lower than measured value for $l/d = 1.0$.

In the maximum inductance position the machine is treated as a simple 2-pole pattern and it is assumed that the flux is linked with all turns and there is no flux leakage. The B-H curve of the iron is used in calculating the maximum inductance. The difference between measured and estimated values of the maximum inductance is within 5% in the saturated region of the ψ -i curve and is insignificant in the nonsaturated region.

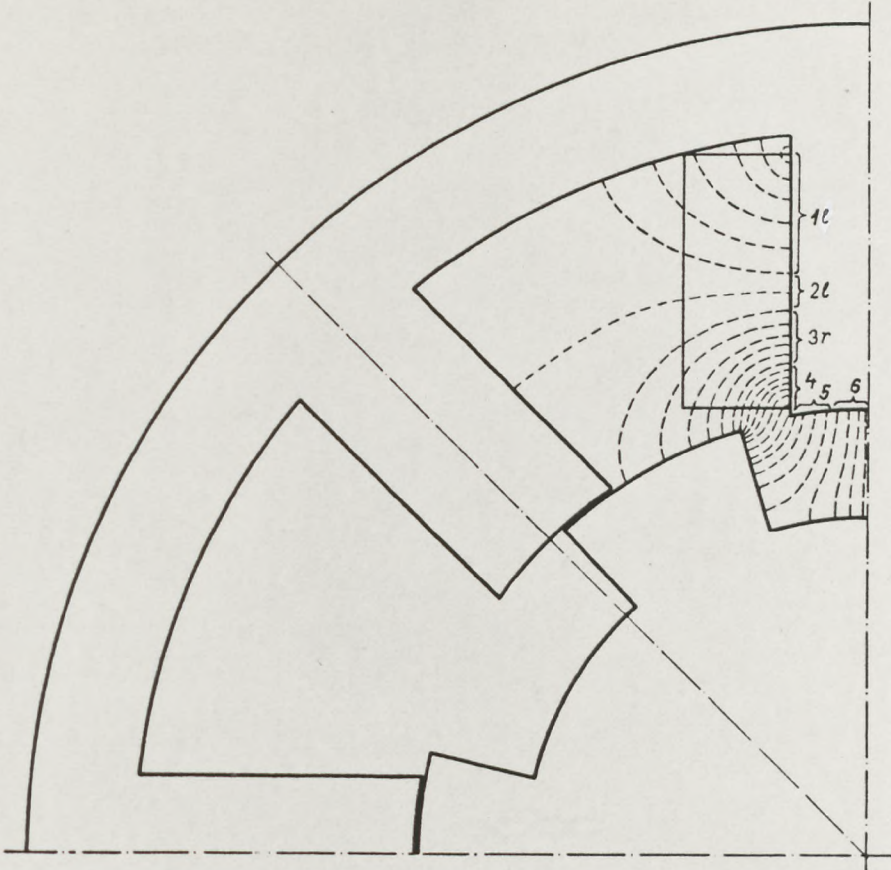


FIG 3.1 Sketch of the field pattern in minimum inductance position

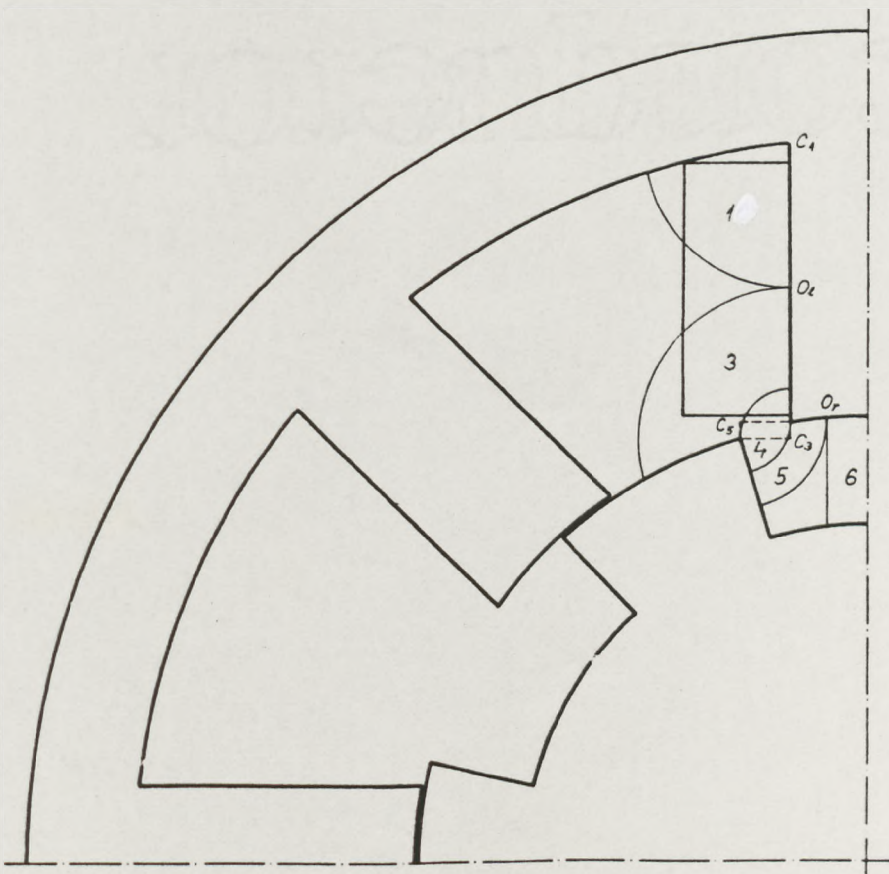


FIG 3.2 Approximated flux paths

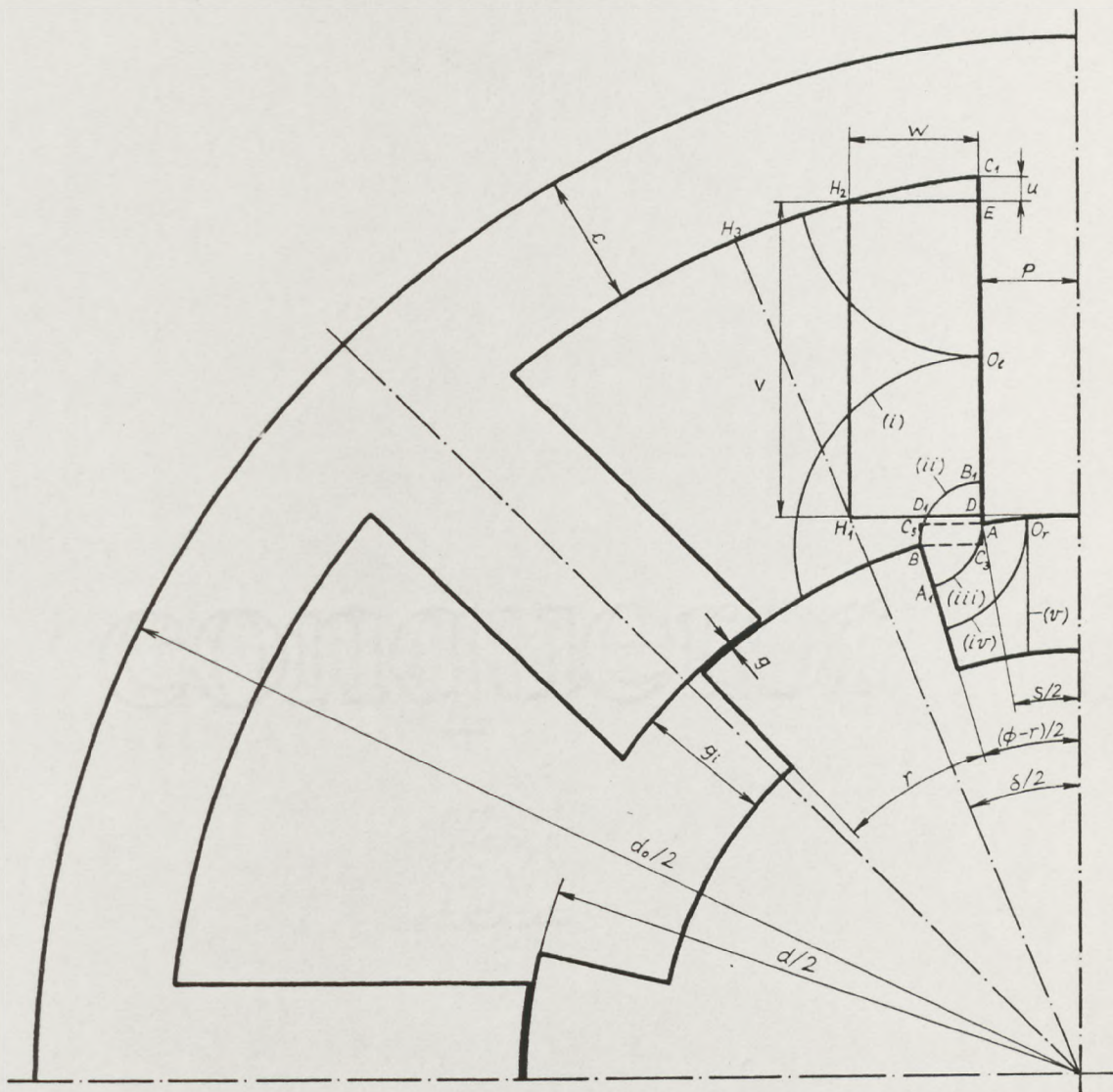


FIG 3.3 Dimensional description of magnetic configuration

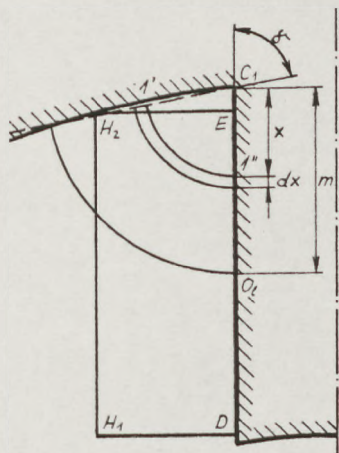


FIG 3.4 Detail with flux path 1

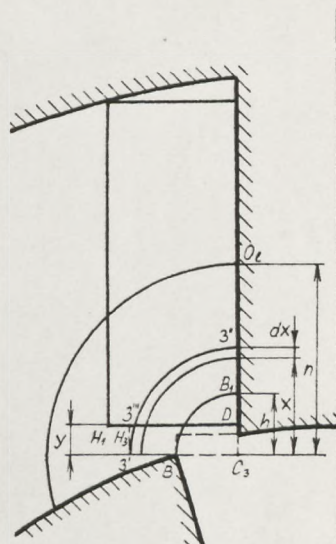


FIG 3.5 Detail with flux path 3

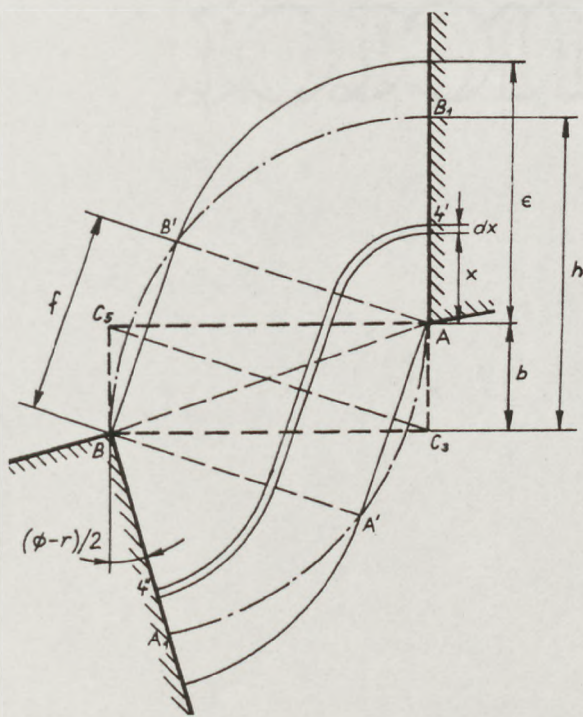


FIG 3.6 Detail with flux path 4

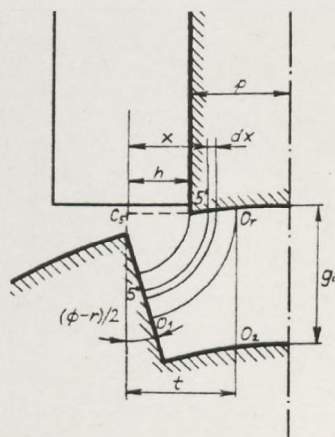


FIG 3.7 Detail with flux paths 5 and 6

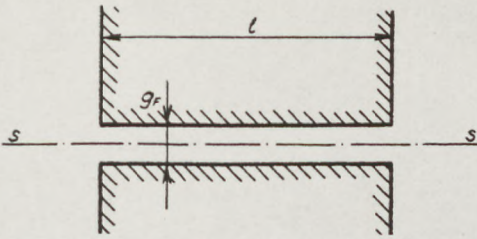


FIG 3.8 Axial model of magnetic configuration with fictitious air-gap

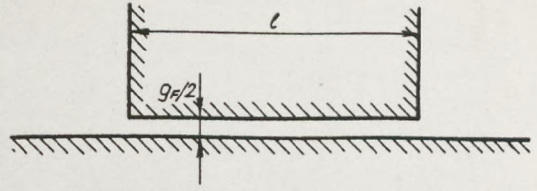


FIG 3.9 'Half'-equivalent of model with fictitious air-gap

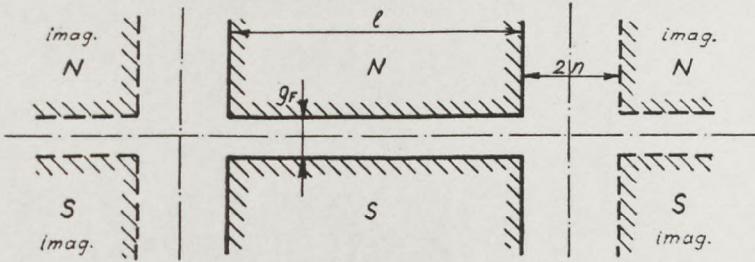


FIG 3.10 Approximation of model shown in FIG 3.8

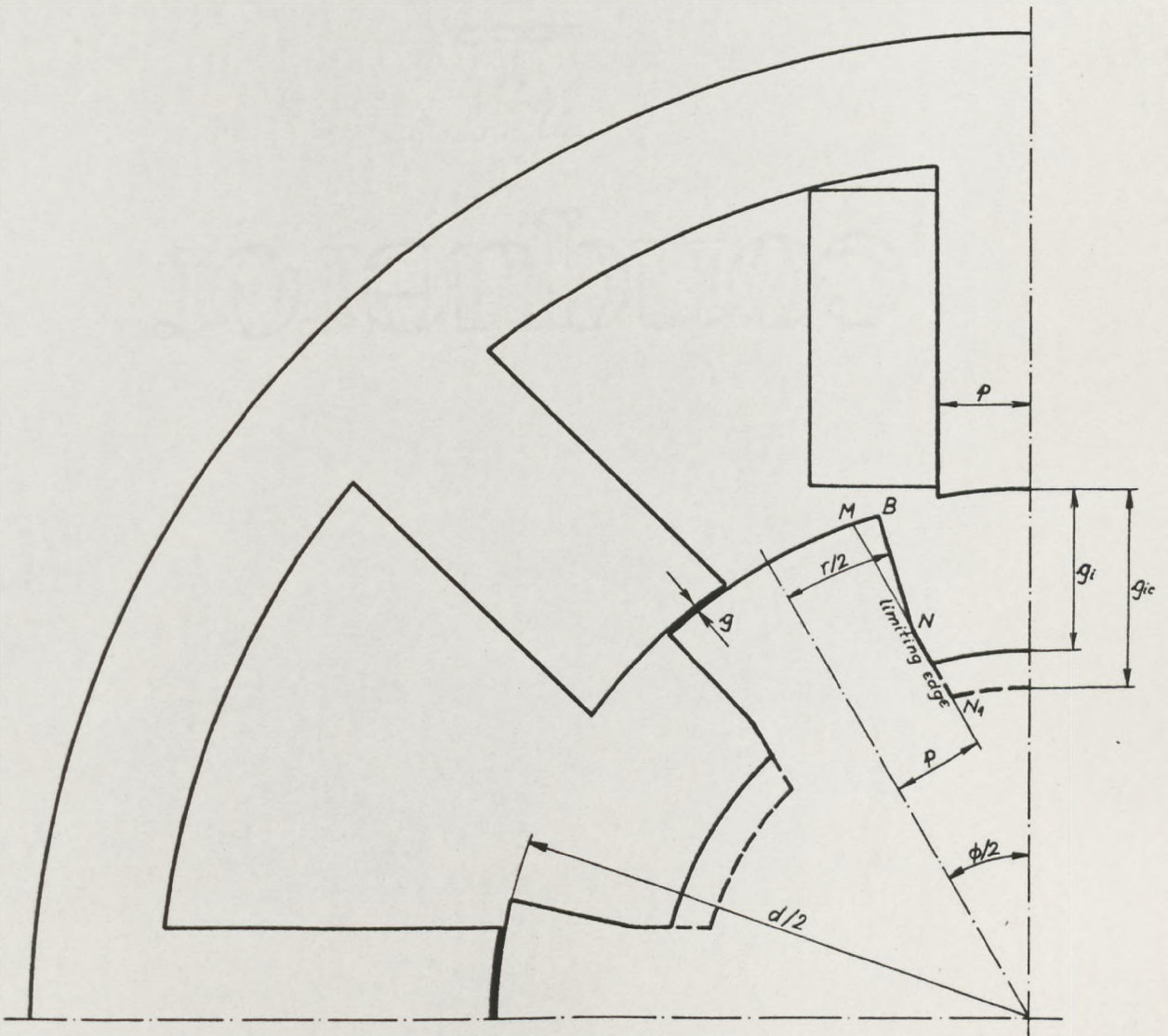


FIG 3.11 Recommendation for the rotor profile

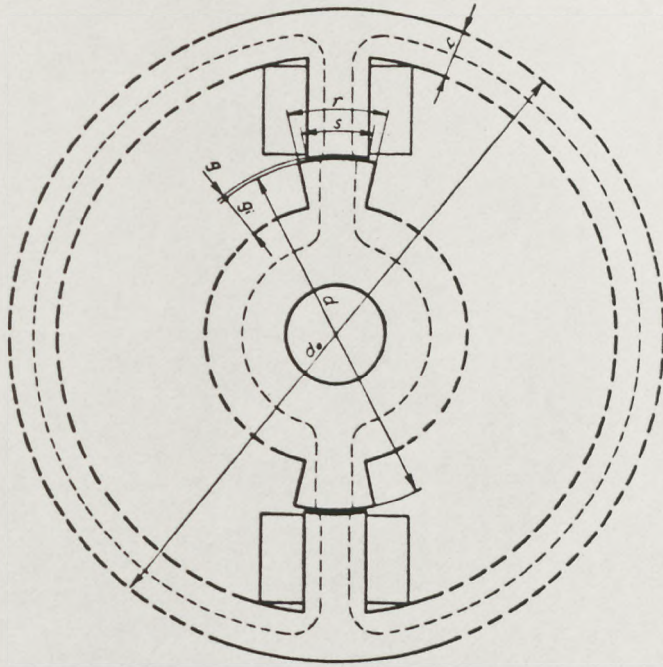


FIG 3.12 Simple '2-pole' pattern

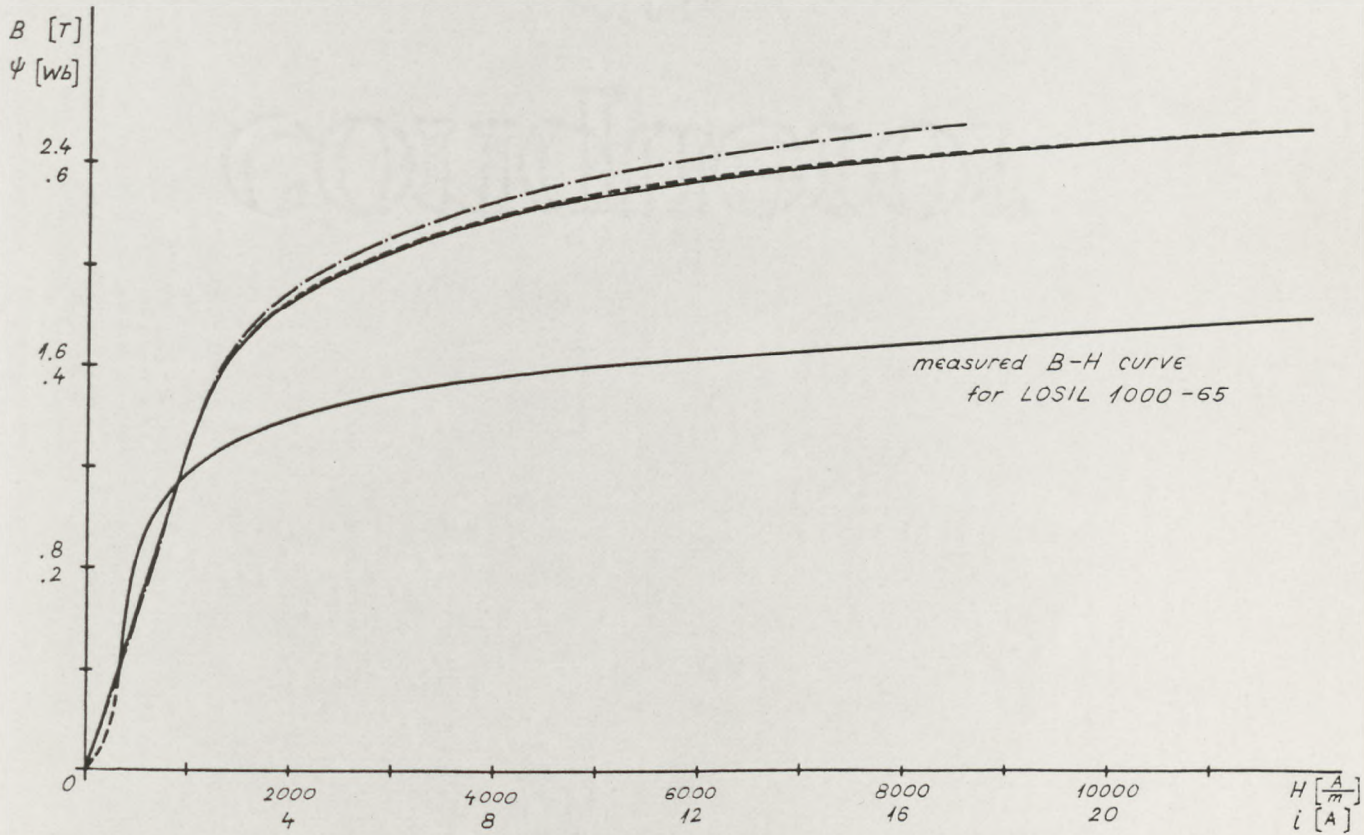


FIG 3.13 B-H curve and ψ -i curve in maximum inductance position

- measured
- computed by numerical field solution
- · - · - estimated by simple analytical method

CHAPTER 4

LINEAR ANALYSIS OF SWITCHED RELUCTANCE MOTOR

4.1 Introduction

In the preliminary analysis of a switched reluctance motor presented in this Chapter, it is convenient to treat the machine in a simple fashion. This treatment leads to a simple physical view of the behaviour of a switched reluctance motor and is achieved by ignoring: a) saturation of the iron (ie considering the function $\psi = f(i)$ to be linear) so that the differential equations become linear and it is possible to integrate them and obtain analytical solutions, and b) all power losses, since taking losses into account would make the preliminary analysis bulky and difficult to handle. In any case, iron losses would be difficult to calculate.

On the basis of these assumptions, the expressions for currents and torque are derived and two aspects of optimisation which involve the combined effect of the basic mechanical parameters and the controlling parameters of the motor are considered for both 4-phase and 3-phase motors.

The speed control of both a constant torque drive and a traction drive are presented using an original graphical method.

The regenerative mode of operation of a switched reluctance machine, which can be used for braking, is also considered.

4.2 Assumptions and approach to the analysis

In the analysis the following general assumptions are made:

- i) Inductances are independent on current;
- ii) All power losses are zero or insignificant, ie the following are negligible
 - a)* all resistances,

* These assumptions enable the analysis to be used for both the switching circuit with a bifilar winding (Fig 2.7) and that with the two switches per phase (Fig 2.6)

- b) iron losses,
 - c) friction and windage,
 - d) transistor (thyristor) and diode volt drops,
- iii)* Commutation of the switching devices and subsequent transfer of current from primary to secondary coil are instantaneous;
- iv)* The bifilar winding turns ratio is unity ($N_1/N_2 = 1$);
- v) The rotor angular velocity is constant, ie
 - a) steady-state operation is considered and
 - b) rotor inertia is large;
- vi) The inductance profile for the machine is defined by Fig 4.1.

Under these assumptions the machine can be represented by the basic circuit shown in Fig 4.2. The voltage equations describing the circuit are

$$+ V = \frac{d\psi}{dt}$$

or,

$$+ V = L \frac{di}{dt} + i \frac{dL}{dt}$$

In these equations the + ve sign corresponds to the state when the controlling switch S is closed and the - ve sign corresponds to the state when S is open.

These assumptions enable analytical expressions to be derived for the average torque and mean and rms primary and secondary currents in terms of the physical dimensions and electrical parameters of the motor. The calculation of average torque is based upon the change of system co-energy when the rotor moves through an angle equal to the rotor pole pitch ϕ .

* These assumptions enable the analysis to be used for both the switching circuit with a bifilar winding (Fig 2.7) and that with the two switches per phase (Fig 2.6)

Fig 4.3 shows the flux-linkage ψ plotted as a function of current for a system having a maximum inductance L_i and a minimum inductance L_o . If the system is excited with a constant current corresponding to point c then the change in co-energy, when the inductance changes from L_o to L_i , is given by the triangle oab. If, however, the current is not held constant, the trajectory of ψ -i is determined by the equation of the electrical circuit. Then the change in co-energy is given by the area enclosed by the trajectory which lies within hatched area. In the mathematical form the average torque per phase is given by

$$T = \frac{1}{\phi} \oint \psi di \quad (4.1)$$

From the expression (2.12) for instantaneous torque it is seen that when the current flows through the phase winding then positive torque is developed when $\frac{dL}{d\theta}$ is +ve and retarding torque is developed when $\frac{dL}{d\theta}$ is -ve. It would be ideal to supply the phase winding with current only during +ve $\frac{dL}{d\theta}$ period. However, since the circuit is inductive, the current cannot suddenly change and may even flow during the period when $\frac{dL}{d\theta}$ is -ve. Therefore to produce high torque from the motor this retarding torque should be reduced and positive torque increased.

The retarding torque can be reduced by two methods.

The first method is to introduce a dead zone in the inductance profile (ie the region k_d 's in Fig 4.1 where $\frac{dL}{d\theta} = 0$) so that the current is allowed to decay before the region of negative $\frac{dL}{d\theta}$ is reached.

The second method is also based on the reduction of the current before the region where $\frac{dL}{d\theta}$ becomes negative is reached. This is achieved if the switching device is turned off at an angle in advance of the dead zone region (commonly referred to as 'early turn-off'). Then the current will decay more rapidly since the rotational emf is forcing the current to decrease rather than increase and stored magnetic energy is converted into mechanical output.

The positive torque may be increased by two methods.

The first method is to increase the slope of the inductance profile, ie to increase $\frac{dL}{d\theta}$. This may be achieved by increasing the slope of inductance profile, ie the ratio

$$\frac{L_i - L_o}{s} (= \frac{1}{\phi} L_o \frac{\phi}{s} (\frac{L_i}{L_o} - 1)).$$

The second method is to turn on the switching device at an angle in advance of the region where $\frac{dL}{d\theta}$ is positive (commonly referred to as 'early turn-on'). This allows the current to rise rapidly before the region where $\frac{dL}{d\theta}$ is positive and thereby more positive torque can be produced.

Clearly, by introducing early turn-off some positive torque is lost. Also by early turn-on in the region where $\frac{dL}{d\theta}$ is negative some retarding torque is produced. Further, by introducing dead zone at given values of ϕ and s the region of minimum inductance is reduced. When the ratio

$$\frac{L_i - L_o}{s}$$

is increased the rotational emf ($i \frac{dL}{d\theta}$) increases and less current can be forced into the machine. In addition, the value of minimum inductance depends, among other parameters also, on dead zone coefficient k_d and the ratio ϕ/s (see Chapter 3).

From the above it becomes apparent that for the optimum choice of the machine parameters a comprehensive treatment involving the combined effects of many parameters has to be made.

The parameters to be considered are:

a defined as ratio $\frac{L_i}{L_o} (= \frac{P_i}{P_o})$

k_d (dead zone coefficient defined as ratio $\frac{r - s}{s}$)

$\frac{\phi}{s}$ ratio

k_c (early turn-on coefficient) defined in Fig 4.4(a)

k_e (early turn-off coefficient) defined in Fig 4.4(b)

4.3 Derivation of the expressions for torque and mean and rms primary and secondary currents

At this stage it is useful to normalise quantities as follows:

normalised angle	$\bar{\theta} = \frac{\theta}{s}$
normalised time	$\bar{t} = \frac{t}{\tau} = \bar{\theta} \text{ (where } \tau = \frac{s}{\omega}\text{)}$
normalised inductance	$\bar{L} = \frac{L}{L_i}$
normalised flux-linkage	$\bar{\Psi} = \frac{\Psi}{V\tau}$
normalised current	$\bar{i} = \frac{i}{(V\tau/L_i)}$

This simplifies the calculation of current waveform since a set of normalised waveforms may be computed which are, with appropriate scaling, applicable at any speed as shown below.

In Fig 4.5, which shows the inductance profile in normalised form, the switch-on and switch-off points are indicated. For convenience of analytical treatment, the inductance profile is divided into seven regions as indicated in Fig 4.5.

During the period when the switching device is on, the flux-linkage rises linearly with rate of rise $\frac{d\Psi}{dt} = V$, from zero to the peak value $V \frac{\theta_{con}}{\omega}$.

After turning off the switching device, the flux-linkage decays linearly with rate of decay $\frac{d\Psi}{dt} = -V$. Since the rate of rise is equal to the rate of decay the period of rise is equal to the period of decay. The sum of these two periods must not be greater than one cycle of changing inductance. (Otherwise the flux-linkage at the end of a cycle of changing of the inductance would not be zero and therefore the initial value of the flux-linkage at the beginning of the following cycle would not be zero. Thus values would increase steadily with successive cycles and in the ideal case, when winding resistances are zero the values of flux-linkage and current would increase to infinity.) From Fig 4.5

$$k_c + (1 - k_e) = k_e + k_d + x \leq \frac{1}{2} \frac{\phi}{s} \quad (4.2)$$

Hence,

$$x = k_c + 1 - 2k_e - k_d \quad (4.3)$$

If the switch-on point is in region 1 and flux-linkage decays to zero in region 6, then the following equations define the inductance, flux-linkage, current and the trajectories of flux-linkage/current in the normalised form.

Region 1: From Fig 4.5 the normalised inductance can be expressed in the following form

$$\bar{L}(\bar{t}_1) = \frac{1}{a} [1 + (a - 1) (k_{cl} - \bar{t}_1)]$$

Solving the equation $V = \frac{d\psi}{dt}$ in region 1 yields

$$\bar{\Psi}(\bar{t}_1) = \bar{t}_1 \quad (\text{from } 0 \text{ to } \bar{\Psi}_1 = k_{cl})$$

The current is given by

$$\bar{i}(\bar{t}_1) = \frac{a \bar{t}_1}{1 + (a - 1)(k_{cl} - \bar{t}_1)} \quad \text{from } 0 \text{ to } \bar{i}_1 = ak_{cl}$$

$$\bar{\Psi}(\bar{i}) = \frac{[1 + (a - 1)k_{cl}]\bar{i}}{a + (a - 1)\bar{i}}$$

$$\text{Region 2: } \bar{L}(\bar{t}_2) = \frac{1}{a}$$

$$\bar{\Psi}(\bar{t}_2) = \bar{t}_2 + k_{cl} \quad \text{from } \bar{\Psi}_1 = k_{cl} \text{ to } \bar{\Psi}_2 = k_c$$

$$\bar{i}(\bar{t}_2) = a(\bar{t}_2 + k_{cl}) \quad \text{from } \bar{i}_1 = ak_{cl} \text{ to } \bar{i}_2 = ak_c$$

$$\bar{\Psi}(\bar{i}) = \frac{\bar{i}}{a}$$

$$\text{Region 3: } \bar{L}(\bar{t}_3) = \frac{1}{a} [1 + (a - 1)\bar{t}_3]$$

$$\bar{\Psi}(\bar{t}_3) = \bar{t}_3 + k_c \quad \text{from } \bar{\Psi}_2 = k_c \text{ to } \bar{\Psi}_3 = 1 - k_e + k_c$$

$$\bar{i}(\bar{t}_3) = \frac{(\bar{t}_3 + k_c)a}{1 + (a - 1)\bar{t}_3} \quad \text{from } \bar{i}_2 = ak_c \text{ to } \bar{i}_3 = \frac{(1 - k_e + k_c)a}{a - k_e(a - 1)}$$

$$\bar{\Psi}(\bar{i}) = \frac{[1 - k_e(a - 1)]\bar{i}}{a - (a - 1)\bar{i}}$$

$$\text{Region 4: } \bar{L}(\bar{t}_4) = \frac{1}{a} [a + (a - 1)(\bar{t}_4 - k_e)]$$

$$\begin{aligned}\bar{\Psi}(\bar{t}_4) &= -\bar{t}_4 + 1 - k_e + k_c && \text{from } \bar{\Psi}_3 = 1 - k_e + k_c \text{ to } \bar{\Psi}_4 = 1 - 2k_e + k_c \\ \bar{i}(\bar{t}_4) &= \frac{(-\bar{t}_4 + 1 - k_e + k_c)a}{a + (a-1)(\bar{t}_4 - k_e)} && \text{from } \bar{i}_3 = \frac{(1 - k_e + k_c)a}{a - k_e(a-1)} \text{ to } \bar{i}_4 = 1 - 2k_e + k_c \\ \bar{\Psi}(\bar{i}) &= \frac{[a + (1 - 2k_e + k_c)(a-1)]\bar{i}}{a + (a-1)\bar{i}}\end{aligned}$$

$$\text{Region 5: } \bar{L}(\bar{t}_5) = 1$$

$$\begin{aligned}\bar{\Psi}(\bar{t}_5) &= -\bar{t}_5 + 1 - 2k_e + k_c && \text{from } \bar{\Psi}_4 = 1 - 2k_e + k_c \text{ to } \bar{\Psi}_5 = 1 - 2k_e + k_c - k_d \\ \bar{i}(\bar{t}_5) &= -\bar{t}_5 + 1 - 2k_e + k_c && \text{from } \bar{i}_4 = 1 - 2k_e + k_c \text{ to } \bar{i}_5 = 1 - 2k_e + k_c - k_d \\ \bar{\Psi}(\bar{i}) &= \bar{i}\end{aligned}$$

$$\text{Region 6: } \bar{L}(\bar{t}_6) = \frac{1}{a}[a - (a-1)\bar{t}_6]$$

$$\begin{aligned}\bar{\Psi}(\bar{t}_6) &= -\bar{t}_6 + 1 - 2k_e + k_c - k_d && \text{from } \bar{\Psi}_5 = 1 - 2k_e + k_c - k_d \text{ to } 0 \\ \bar{i}(\bar{t}_6) &= \frac{(-\bar{t}_6 + 1 - 2k_e + k_c - k_d)a}{a - (a-1)\bar{t}_6} && \text{from } \bar{i}_5 = 1 - 2k_e + k_c - k_d \text{ to } 0 \\ \bar{\Psi}(\bar{i}) &= \frac{[a - (a-1)(1 - 2k_e + k_c - k_d)]\bar{i}}{a - (a-1)\bar{i}}\end{aligned}$$

If the switch-on point is in Region 2, then it should be noted that $k_{c1} = 0$ in the above set of equations.

If the switch-on is in Region 3, $k_c < 0$.

If the flux-linkage and current decay to zero in Region 4, $x < -k_d$.

If the flux-linkage and current decay to zero in Region 5, $-k_d < x < 0$.

If the flux-linkage and current decay to zero in Region 7, $x > 1$ and

$$\begin{aligned}\bar{\Psi}(\bar{t}_7) &= k_c - 2k_e - k_d - \bar{t}_7 && \text{from } \bar{\Psi}_6 = k_c - 2k_e - k_d \text{ to } 0 \\ \bar{i}(\bar{t}_7) &= a(k_c - 2k_e - k_d - \bar{t}_7) && \text{from } \bar{i}_6 = a(k_c - 2k_e - k_d) \text{ to } 0 \\ \bar{\Psi}(\bar{i}) &= \frac{\bar{i}}{a}\end{aligned}$$

a) Expression for average torque

Substituting normalised values of \bar{i} and $\bar{\Psi}$ given above into (4.1) gives the expression for the average torque per phase

$$T = \frac{(V\bar{c})^2}{\phi L_o} F, \quad (4.4)$$

where

$$F = \frac{1}{\alpha} \oint \bar{\Psi} d\bar{i} = \sum_{j=1}^{\ell} F_j,$$

If $k_c > 0$ and $0 < x < 1$, then $\ell = 6$ and

$$F_1 = A, F_2 = B, F_3 = C, F_4 = D, F_5 = E, F_6 = G$$

If $k_c < 0$ and $0 < x < 1$, then $\ell = 6$ and

$$F_1 = 0, F_2 = 0, F_3 = H, F_4 = D, F_5 = E, F_6 = G$$

If $k_c > 0$ and $-1 - k_d < x < -k_d$, then $\ell = 4$ and

$$F_1 = A, F_2 = B, F_3 = C, F_4 = J$$

If $k_c > 0$ and $-k_d < x < 0$, then $\ell = 5$ and

$$F_1 = A, F_2 = B, F_3 = C, F_4 = D, F_5 = K$$

If $k_c > 0$ and $x > 1$, then $\ell = 7$ and

$$F_1 = 0, F_2 = B, F_3 = C, F_4 = D, F_5 = E, F_6 = L, F_7 = M$$

where

$$A = \frac{1 + (a-1)k_{c1}}{a-1} \left\{ -k_{c1} + \frac{1}{a-1} \ln [1 + (a-1)k_{c1}] \right\}$$

$$B = \frac{1}{2}(k_{c1}^2 - k_c^2)$$

$$C = \frac{1 - k_c(a-1)}{a-1} \left\{ (1 - k_e) \frac{1 - k_c(a-1)}{a - k_e(a-1)} - \frac{1}{a-1} \ln [a - k_e(a-1)] \right\}$$

$$D = \frac{a + (a-1)(1-2k_e+k_c)}{a-1} \left\{ \frac{k_e [a + (a-1)(1-2k_e+k_c)]}{a[a - k_e(a-1)]} + \frac{1}{a-1} \ln \frac{a - k_e(a-1)}{a} \right\}$$

$$E = \frac{k_d}{a} (1 - 2k_e + k_c - \frac{k_d}{2})$$

$$G = (1 - 2k_e + k_c - k_d - \frac{a}{a-1}) \left\{ \frac{1 - 2k_e + k_c - k_d}{a} + \frac{1}{a-1} \ln \frac{a - (a-1)(1-2k_e+k_c-k_d)}{a} \right\}$$

$$H = \frac{1 - k_c(a-1)}{a-1} \left\{ \frac{k_c + 1 - k_e}{a - k_e(a-1)} + \frac{1}{a-1} \ln \frac{1 - k_c(a-1)}{a - k_e(a-1)} \right\}$$

$$J = \frac{\alpha + (\alpha-1)(1-2k_e+k_c)}{\alpha-1} \left\{ \frac{1 - k_e + k_c}{\alpha - k_e(\alpha-1)} - \frac{1}{\alpha-1} \ln \frac{\alpha + (\alpha-1)(1-2k_e+k_c)}{\alpha - k_c(\alpha-1)} \right\}$$

$$K = \frac{1}{2\alpha} (1-2k_e+k_c)^2$$

$$L = (1-2k_e+k_c-k_d - \frac{\alpha}{\alpha-1}) \left\{ \frac{1 - (\alpha-1)(k_c-2k_e-k_d)}{\alpha} - \frac{1}{\alpha-1} \ln \alpha \right\}$$

$$M = \frac{1}{2}(k_c-2k_e-k_d)^2$$

b) Expressions for mean primary and secondary currents

The expression for primary mean current (average primary current in period $\frac{\phi}{\omega}$) is

$$I_{1m} = \frac{V\sqrt{2}}{L_o} \frac{s}{\phi} F_{1m} \tag{4.5}$$

If $k_c > 0$, then

$$F_{1m} = \frac{1}{\alpha} \int_0^{k_c} \bar{i} d\bar{t}_1 + \frac{1}{\alpha} \int_0^{k_c-k_c} \bar{i} d\bar{t}_2 + \frac{1}{\alpha} \int_0^{1-k_e} \bar{i} d\bar{t}_3 = A_m + B_m + C_m$$

If $k_c < 0$, then

$$F_{1m} = \frac{1}{\alpha} \int_{-k_c}^{1-k_e} \bar{i} d\bar{t}_3 = D_m$$

The expression for secondary mean current is

$$I_{2m} = \frac{V\sqrt{2}}{L_o} \frac{s}{\phi} F_{2m} \tag{4.6}$$

If $0 < x < 1$, then

$$F_{2m} = \frac{1}{\alpha} \int_0^{k_e} \bar{i} d\bar{t}_4 + \frac{1}{\alpha} \int_0^d \bar{i} d\bar{t}_5 + \frac{1}{\alpha} \int_0^x \bar{i} d\bar{t}_6 = E_m + G_m + H_m$$

If $-1 - k_d < x < -k_d$, then

$$F_{2m} = \frac{1}{\alpha} \int_0^{k_c+1-k_e} \bar{i} d\bar{t}_4 = J_m$$

If $-k_d < x_d < 0$, then

$$F_{2m} = \frac{1}{\alpha} \int_0^{k_e} \bar{i} d\bar{t}_4 + \frac{1}{\alpha} \int_0^{k_c+1-2k_e} \bar{i} d\bar{t}_5 = E_m + K_m$$

If $x > 1$, then

$$F_{2m} = \frac{1}{a} \int_0^{k_e} \bar{i}_d \bar{t}_4 + \frac{1}{a} \int_0^{k_d} \bar{i}_d \bar{t}_5 + \frac{1}{a} \int_0^1 \bar{i}_d \bar{t}_6 + \frac{1}{a} \int_0^{k_c - 2k_e - k_d} \bar{i}_d \bar{t}_7$$

$$= E_m + G_m + L_m + M_m$$

where

$$A_m = \frac{1 + (a-1)}{(a-1)^2} \ln [1 + (a-1)k_{cl}] - \frac{k_{cl}}{a-1}$$

$$B_m = \frac{k_c - k_{cl}^2}{2}$$

$$C_m = \frac{1 - k_e}{a-1} + \frac{k_c(a-1) - 1}{(a-1)^2} \ln [a - k_e(a-1)]$$

$$D_m = \frac{k_c + 1 - k_e}{a-1} + \frac{k_c(a-1) - 1}{(a-1)^2} \ln \frac{a - k_e(a-1)}{1 - k_c(a-1)}$$

$$E_m = - \frac{(k_c + 1 - 2k_e)(a-1) + a}{(a-1)^2} \ln \frac{a - (a-1)k_e}{a} - \frac{k_e}{a-1}$$

$$G_m = \frac{(k_c + 1 - 2k_e)k_d}{a} - \frac{k_d^2}{2a}$$

$$H_m = \frac{k_c + 1 - 2k_e - k_d}{a-1} + \frac{a - (a-1)(k_c + 1 - 2k_e - k_d)}{(a-1)^2} \ln \frac{a - (a-1)(k_c + 1 - 2k_e - k_d)}{a}$$

$$J_m = \frac{(k_c + 1 - 2k_e)(a-1) + a}{(a-1)^2} \ln \frac{a + (a-1)(k_c + 1 - 2k_e)}{a - (a-1)k_e}$$

$$K_m = \frac{(k_c + 1 - 2k_e)^2}{2a}$$

$$L_m = \frac{(k_c + 1 - 2k_e - k_d)(a-1) - a}{(a-1)^2} \ln a + \frac{a}{a-1}$$

$$M_m = \frac{(k_c - 2k_e - k_d)^2}{2}$$

c) Expressions for primary and secondary rms currents

The expression for primary rms current is

$$I_1 = \frac{V\sqrt{f}}{L_o} \sqrt{\frac{s}{\phi}} R_1 \quad (4.7)$$

If $k_c > 0$, then

$$R_1 = \sqrt{\left\{ \frac{1}{a^2} \int_0^{k_c} \bar{i}^2 d\bar{t}_1 + \frac{1}{a^2} \int_0^{c-k_c} \bar{i}^2 d\bar{t}_2 + \frac{1}{a^2} \int_0^{1-k_c} \bar{i}^2 d\bar{t}_3 \right\}}$$

$$= \sqrt{\{A_r + B_r + C_r\}}$$

If $k_c < 0$, then

$$R_1 = \sqrt{\left\{ \frac{1}{a^2} \int_{-k_c}^{1-k_c} \bar{i}^2 d\bar{t}_3 \right\}} = \sqrt{D_r}$$

The expression for secondary rms current is

$$I_2 = \frac{V\tau}{L_o} \sqrt{\frac{s}{\phi}} R_2 \quad (4.8)$$

If $0 < x < 1$, then

$$R_2 = \sqrt{\left\{ \frac{1}{a^2} \int_0^{k_e} \bar{i}^2 d\bar{t}_4 + \frac{1}{a^2} \int_0^{k_d} \bar{i}^2 d\bar{t}_5 + \frac{1}{a^2} \int_0^x \bar{i}^2 d\bar{t}_6 \right\}} = \sqrt{\{E_r + G_r + H_r\}}$$

If $-1 - k_d < x < -k_d$, then

$$R_2 = \sqrt{\left\{ \frac{1}{a^2} \int_0^{k_c+1-k_e} \bar{i}^2 d\bar{t}_4 \right\}} = \sqrt{J_r}$$

If $-k_d < x < 0$, then

$$R_2 = \sqrt{\left\{ \frac{1}{a^2} \int_0^{k_e} \bar{i}^2 d\bar{t}_4 + \frac{1}{a^2} \int_0^{k_c+1-2k_e} \bar{i}^2 d\bar{t}_5 \right\}} = \sqrt{\{E_r + K_r\}}$$

If $x > 1$, then

$$R_2 = \sqrt{\left\{ \frac{1}{a^2} \int_0^{k_e} \bar{i}^2 d\bar{t}_4 + \frac{1}{a^2} \int_0^{k_d} \bar{i}^2 d\bar{t}_5 + \frac{1}{a^2} \int_0^1 \bar{i}^2 d\bar{t}_6 \right.}$$

$$\left. + \frac{1}{a^2} \int_0^{k_c-2k_e-k_d} \bar{i}^2 d\bar{t}_7 \right\}} = \sqrt{\{E_r + G_r + L_r + M_r\}}$$

where

$$A_r = \frac{1}{(a-1)^3} \left\{ k_{cl}(a-1) [2 + k_{cl}(a-1)] - 2[1 + k_{cl}(a-1)] \ln [1 + k_{cl}(a-1)] \right\}$$

$$B_r = (k_c - k_{cl}) \left\{ \frac{(k_c - k_{cl})^2}{3} + k_c k_{cl} \right\}$$

$$C_r = \frac{1}{(a-1)^3} \left\{ (a-1)(1-k_e) \left[1 + \frac{(k_c(a-1)-1)^2}{a - (a-1)k_e} \right] + 2[k_c(a-1)-1] \ln [a - (a-1)k_e] \right\}$$

$$D_r = \frac{1}{(a-1)^3} \left\{ (a-1)(1-k_e) \left[1 + \frac{(k_c(a-1)-1)^2}{a - (a-1)k_e} \right] + (a-1)k_c \left[1 + \frac{(k_c(a-1)-1)^2}{1 - (a-1)k_c} \right] + 2[k_c(a-1)-1] \ln \frac{a - (a-1)k_e}{1 - (a-1)k_c} \right\}$$

$$E_r = \frac{1}{(a-1)^3} \left\{ (a-1)k_e \left[1 + \frac{((a-1)(k_c+1-2k_e)+a)^2}{(a - (a-1)k_e)a} \right] + 2[(a-1)(k_c+1-2k_e)+a] \ln \frac{a - (a-1)k_e}{a} \right\}$$

$$G_r = \frac{k_d}{a^2} \left\{ \frac{k_d^2}{3} + (k_c+1-2k_e)(k_c+1-2k_e-k_d) \right\}$$

$$H_r = \frac{1}{(a-1)^3} \left\{ (a-1)(k_c+1-2k_e-k_d) \left[1 + \frac{((a-1)(k_c+1-2k_e-k_d)-a)^2}{a(a - (a-1)(k_c+1-2k_e-k_d))} \right] - 2[(a-1)(k_c+1-2k_e-k_d)-a] \ln \frac{a - (a-1)(k_c+1-2k_e-k_d)}{a} \right\}$$

$$J_r = \frac{1}{(a-1)^3} \left\{ (a-1)(k_c+1-k_e) \left[1 + \frac{(a-1)(k_c+1-2k_e)+a}{a - (a-1)k_e} \right] - 2[(a-1)(k_c+1-2k_e)+a] \ln \frac{a + (a-1)(k_c+1-2k_e)}{a - (a-1)k_e} \right\}$$

$$K_r = \frac{(k_c+1-2k_e)^2}{3a^2}$$

$$L_r = \frac{1}{(a-1)^3} \left\{ (a-1) \left[1 + \frac{((a-1)(k_c+1-2k_e-k_d)-a)^2}{a} \right] + [(a-1)(k_c+1-2k_e-k_d)-a] \ln a \right\}$$

$$M_r = \frac{(k_c - 2k_a - k_d)^3}{3}$$

The expressions for torque and currents derived above are used in the analysis which follows.

4.4 Linear optimisation of a switched reluctance motor

Using the analytical expressions for torque and currents derived above it is possible to optimise the machine parameters.

Two aspects of linear optimisation will be considered here:

1. Optimisation of torque with respect to peak flux density at selected values of rotor diameter and core length which is equivalent to optimising with respect to the amount of active iron.
2. Optimisation of torque with respect to primary rms current at a given voltage which has direct bearing on the efficiency of the motor and is closely related to the device rating.

The basic purpose of this linear optimisation is to provide a physical view of the behaviour of the switched reluctance motor. Consequently, the effects of parameter variations have been depicted graphically and from these graphs an optimum set of parameters will be found.

4.4.1 Basic equations and constraints imposed upon parameters

Using expression (4.4), the total average torque of the switched reluctance motor is

$$T = q \frac{V^2 \phi}{L_o} \left(\frac{s}{\phi} \right)^2 \frac{F}{\omega} \quad (4.9)$$

In Chapter 3 the expression for minimum inductance has been given in the form

$$L_o = N^2 \mu_o \ell P_o \quad (4.10)$$

where N is number of turns per phase and

P_0 is the total normalised equivalent minimum permeance.

The torque is then

$$T = q \left(\frac{V}{N}\right)^2 \frac{\phi}{\mu_0 \ell P_0} \left(\frac{s}{\phi}\right)^2 \frac{F}{\omega^2} \quad (4.11)$$

where F is the function of α , k_d , k_{c1} , k_c , k_e and is given above.

According to Fig 4.5

$$k_c - k_{c1} = \frac{\phi}{s} - 2 - k_d$$

$$\therefore k_{c1} = k_c - \left(\frac{\phi}{s} - 2 - k_d\right)$$

Thus the parameter k_{c1} can be represented through the parameters $\frac{\phi}{s}$, k_c and k_d and the function F is now

$$F = f(\alpha, k_d, \phi/s, k_c, k_e) \quad (4.12)$$

Therefore F is a function of five parameters of the motor. These five dimensionless parameters may be classified into two groups:

- a) mechanical parameters: α , k_d , ϕ/s and
- b) controlling parameters: k_c , k_e .

The mechanical parameters represent design parameters of the motor which are constant for a given machine, and the controlling parameters may be used as speed-control parameters.

It is possible to impose constraints upon these parameters by considering the design and self-starting requirements of the motor.

1. The constraint imposed upon k_d has been given in Chapter 2, ie

$$s \leq \phi - r$$

$$\therefore 2 \leq \phi/s - \frac{(r-s)}{s}$$

$$\therefore k_d \leq \phi/s - 2$$

Thus

$$0 \leq k_d \leq \phi/s - 2 \quad (4.13)$$

2. The constraint imposed on ϕ/s has also been given in Chapter 2, i.e.

$$s \geq \frac{\phi}{q}$$

$\therefore \phi/s \leq q$

The lower limit on ϕ/s is given by relation (4.13) and thus

$$2 \leq \phi/s \leq q \quad (4.14)$$

3. The theoretical lower limit on $\alpha (= \frac{P_i}{P_o})$ is unity, corresponding to no rotor saliency and the output power is then equal to zero. The upper limit on α depends on the upper limit on P_i and the lower limit on P_o . The permeance P_i depends mainly on the air-gap length (g). In practice a minimum air-gap length will be imposed dependent upon the type of bearings used, the upper speed limit and the manufacturing tolerances. In Chapter 3 it has been shown that if the air-gap length of the rotor interpolar space is large enough, then the permeance P_o depends mainly on k_d and ϕ/s . The minimum value of P_o is obtained when $k_d = 0$ and $\phi/s = q$. (Taking these facts and the experience acquired from previously constructed switched reluctance motors into account, it is very optimistic to expect a value of more than 10 for α . However, it is interesting to consider what benefits, if any, might be obtained from higher values of α .)

4. The range of the parameter k_e is simple

$$0 \leq k_e \leq 1 \quad (4.15)$$

5. The range of k_c is determined by the maximum conduction

period* which is equal to $\frac{1}{2} \frac{\phi}{s}$ (see (4.2)) and by the value of the parameter k_e

$$0 \leq k_c + (1 - k_e) \leq \frac{1}{2} \frac{\phi}{s}$$

$$\therefore -1 + k_e \leq k_c \leq \frac{1}{2} \frac{\phi}{s} - 1 + k_e \quad (4.16)$$

4.4.2 Optimisation of torque with respect to peak flux density at selected values of rotor diameter and core length

The equation (4.11) shows that the torque is directly proportional to the function F which increases when the conduction angle $(k_c + 1 - k_e)s$ increases (see below). However, since the peak flux-linkage is directly proportional to the conduction angle, the question arises: Given a motor with fixed d and ℓ , what is the maximum torque that can be obtained for a given peak flux density \hat{B} ?

The expression for the peak flux-linkage per phase (stator pole) is

$$\hat{\Psi} = Vs \frac{k_c + 1 - k_e}{\omega} \quad (4.17)$$

$\hat{\Psi}$ may be approximately taken as the product of the number of turns per phase, peak flux density in stator pole root (where flux distribution is approximately uniform) and the cross-sectional area of the stator pole. This cross-sectional area may be approximately taken for parallel-sided stator poles as $\frac{d}{2} s\ell$. Thus equation (4.17) becomes

$$N \hat{B} \frac{d}{2} \ell s = Vs \frac{k_c + 1 - k_e}{\omega} \quad (4.18)$$

From expression (4.18)

$$\frac{V}{N} = \hat{B} \ell \frac{d}{2} \frac{\omega}{k_c + 1 - k_e} \quad (4.19)$$

Substituting (4.19) into (4.11)

* 'Conduction period' is commonly used to describe the period during which the switching device is in 'on' state

$$T = q \frac{\hat{B}^2}{\mu_0} \frac{d^2 \ell}{4} \frac{F}{(k_c + 1 - k_e)^2} \frac{\phi}{P_0} \left(\frac{s}{\phi}\right)^2 \quad (4.20)$$

In this expression the quantities d and ℓ determine size of the rotor, ϕ is the rotor pole pitch, and P_0 is the total normalised equivalent minimum permeance which depends upon the geometric proportions of the machine and the mechanical parameters k_d and ϕ/s .

It will now be shown that it is possible to select an optimum set of parameters α , k_d , ϕ/s , k_c , k_e which gives the maximum torque for given values of \hat{B} , d and ℓ .

Since P_0 depends on the number of the stator and rotor poles, ie on the number of phases, and this dependence cannot be expressed explicitly, the optimisation of the torque must be considered separately for different numbers of phases. Both 4-phase and 3-phase machines will be considered here. Let

$$\psi_1 = \frac{F}{(k_c + 1 - k_e)^2} \frac{\phi}{P_0} \left(\frac{s}{\phi}\right)^2 \quad (4.21)$$

then the torque is

$$T = q \frac{\hat{B}^2}{\mu_0} \frac{d^2 \ell}{4} \psi_1 \quad (4.22)$$

The values of the function ψ_1 have been computed for the parameters α , k_d , ϕ/s , k_c , k_e throughout the ranges given above and the significant results are depicted in Figs 4.6 to 4.10. The graphs in Figs 4.6, 4.7 show the dependence of the function ψ_1 on $k_c + 1 - k_e$, ϕ/s , k_d when $\alpha = 10$. These graphs relate to the 4-phase machine. The graphs in Figs 4.8, 4.9 show the same dependence but for the 3-phase machine.

Considering these graphs and those in Fig 4.10 (for 3 values of α) the following conclusions may be drawn.

1. By increasing the conduction region ($k_c + 1 - k_e$) to a certain value the forward (positive) torque is increased because the current during the positive region of $dL/d\theta$ is increased, but the

current during the negative region of $dL/d\theta$ is also increased. Therefore there is an optimum value of conduction region above which the increase in retarding torque becomes greater than the increase in forward torque. For the same reasons there is an optimum value of the parameter k_e .

2. By increasing the parameter ϕ/s (ie by decreasing s if the number of phases is unchanged) the region of the minimum inductance and the rate of change of the inductance are increased. The value of F increases and the value of P_0 decreases, thus tending to increase the value of ψ_1 . However, the function ψ_1 is also inversely proportional to $(\phi/s)^2$. There is therefore an optimum value of ϕ/s which is about 3.0 for both 4-phase and 3-phase motor. Some implications concerning the optimum value of ϕ/s are considered below.
3. By introducing a dead zone (ie by increasing k_d from 0) the value of ψ_1 is decreased. This means that increasing the dead zone (k_d) reduces the positive torque (by reducing the minimum inductance region) more than it reduces the retarding torque.
4. Fig 4.10 shows the effects of the variation of α on the function ψ_1 in an example in which the 4-phase machine has $\phi/s = 3$ and $k_d = 0$. It may be observed that in this case by increasing α from 6 to 10 the maximum value of ψ_1 is increased by 14%, and by increasing α from 10 to 14 the maximum value of ψ_1 is increased by 4.4%. Corresponding changes occur with other practical values of ϕ/s and k_d . This result shows that the contribution to the torque when α is increased above 10 is not so large as to justify technical difficulties associated with realising $\alpha > 10$.
5. Consideration of all the Figs 4.6 to 4.9 shows that the optimum values of k_e and $k_c + 1 - k_e$ (conduction region) are 0.9 and 1.2 respectively. Hence, the optimum k_c is 1.1. This means that the maximum torque at a given peak flux density is obtained at a quite large conduction angle. The implications of this results on the speed control of the motor will be discussed when speed control is being considered.

If α is given the value 10, then the optimum set of parameters is

$$k_d = 0.0, \phi/s = 3.0, k_c = 1.1, k_g = 0.9$$

which gives the maximum torque for a given peak flux density at a fixed rotor diameter and core length.

This set of parameters applies to both 4-phase and 3-phase motor.

Consider now the implications concerning the value $\phi/s = 3$ which is the value that maximises the function ψ_1 .

The value $\phi/s = 3$ is the upper limit for a 3-phase 6/4 pole machine which means that the overlap between phase inductances, which is relevant to starting performance, is $k_L = 0$ (see Chapter 2). As far as the linear analysis is concerned, where the diagram of instantaneous torque ($T(\theta) \Big|_{i=\text{const}} = \frac{1}{2} i^2 \frac{dL}{d\theta}$) is rectangular, this value is still acceptable. In the real situation due to rounded corners in the inductance profile a small amount of overlap when $\phi/s = 3$ still exists, but the value of the torque in this zone of overlap is small. A small improvement in starting performance may be achieved by introducing a dead zone when, due to the effects of fringing, the 'effective' stator pole arc is increased and therefore overlap is increased, but the value of ψ_1 is then decreased.

Larger improvements in starting performance may be achieved by decreasing ϕ/s (increasing s), but then the winding space is decreased.

In the case of a 4-phase 8/6 pole machine with $\phi/s = 3$ the coefficient of the overlap between phase inductances is $k_L = 0.25$ (see Chapter 2) and the starting performance is considerably improved. As has been stated in Chapter 2, this is the advantage of the 4-phase machine as compared with the 3-phase machine.

However, if the 3-phase and 4-phase machines have the same \hat{B} , d and ℓ , then the ratio of maximum developed torques, according to (4.22) and Figs 4.8(c) and 4.6(c), is

$$\frac{T(3)}{T(4)} = \frac{3\psi_1(3)}{4\psi_1(4)} = \frac{3 \times 0.0392}{4 \times 0.0237} = 1.24$$

Independent justification of the above statement is found in the following alternative approach.

The developed torque is given by

$$T = q \frac{1}{\phi} \int_0^{\phi} \left(\frac{1}{2} i^2 \frac{dL}{d\theta} \right) d\theta = \frac{q}{\phi} \int_0^{\phi} \frac{1}{2} i^2 \frac{L_i - L_o}{s} d\theta = \frac{q \mu_o \ell N^2 P_o (\alpha - 1)}{\phi s} \int_0^{\phi} i^2 d\theta$$

If the values of d , ℓ , V , ω and N are constant, α is given the value 10 and optimum values $k_d = 0.0$, $\phi/s = 3.0$, $k_c = 1.1$ and $k_e = 0.9$ are used for both 3-phase and 4-phase machines then the ratio of developed torques is

$$\begin{aligned} \frac{T^{(3)}}{T^{(4)}} &= \frac{\left(\frac{q P_o}{s \phi} \int_0^{\phi} i^2 d\theta \right)^{(3)}}{\left(\frac{q P_o}{s \phi} \int_0^{\phi} i^2 d\theta \right)^{(4)}} = \frac{3 \times P_o^{(3)}}{4 \times P_o^{(4)}} \frac{\left(\int_0^{\phi} i^2 d\theta \right)^{(3)}}{\left(\int_0^{\phi} i^2 d\theta \right)^{(4)}} \\ &= 0.33 \frac{P_o^{(3)}}{P_o^{(4)}} \frac{\left(\int_0^{\phi} i^2 d\theta \right)^{(3)}}{\left(\int_0^{\phi} i^2 d\theta \right)^{(4)}} \end{aligned}$$

The values of $P_o^{(3)}$ and $P_o^{(4)}$ for $k_d = 0.0$ and $\phi/s = 3.0$ can be calculated (see Chapter 2) and they are 1.6 and 1.8 respectively. Also, the integrals $\left(\int_0^{\phi} i^2 d\theta \right)^{(3)}$ and $\left(\int_0^{\phi} i^2 d\theta \right)^{(4)}$ can be calculated (eg graphically) for above values of α , k_d , ϕ/s , k_c , k_e and arbitrary values of d , ℓ , V , ω and N . The ratio of these integrals is evaluated to 12.0/2.9 and therefore

$$\frac{T^{(3)}}{T^{(4)}} = 0.33 \times \frac{1.6}{1.8} \times \frac{12.0}{2.9} = 1.23$$

The obtained result confirms the one given above.

Therefore if a high starting torque is not required from a drive, then

the linear analysis shows that the 3-phase motor has advantage as compared with the 4-phase motor with respect to developed torque.

4.4.3 Optimisation of torque with respect to primary rms current at a given voltage

Substituting (4.10) into (4.7) the expression for primary rms current becomes

$$I_1 = \frac{V}{N^2} \frac{s}{\mu_0 \ell P_0 \omega} \sqrt{\frac{s}{\phi}} R_1 \quad (4.23)$$

where R_1 is the function of α , k_d , ϕ/s , k_c , k_e and is given above. Hence,

$$\left(\frac{V}{N}\right)^2 = \frac{\mu_0 \ell P_0 \omega V I_1}{s \sqrt{\frac{s}{\phi}} R_1} \quad (4.24)$$

Substituting (4.24) into (4.11)

$$T = q \frac{V I_1}{\omega} \sqrt{\frac{s}{\phi}} \frac{F}{R_1} \quad (4.25)$$

In this expression the quantities V and I_1 determine the device ratings. It will now be shown that it is possible to select an optimum set of parameters α , k_d , ϕ/s , k_c , k_e which gives the maximum torque for given values of I_1 , V and ω .

Let

$$\Psi_2 = \sqrt{\frac{s}{\phi}} \frac{F}{R_1} \quad (4.26)$$

then the torque is

$$T = q \frac{V I_1}{\omega} \Psi_2 \quad (4.27)$$

The values of the function Ψ_2 have been computed for α , k_d , ϕ/s , k_c , k_e throughout the ranges given above and the results show that the highest values of Ψ_2 are obtained when the conduction region is maximum, i.e. $k_c + 1 - k_e = \frac{1}{2} \phi/s$. The effects of variation of α are the same as in the case of optimisation of Ψ_1 (see previous section). Therefore,

$\alpha = 10$ is taken as a realistic value.

The graphs in Fig 4.11 show the dependence of the function Ψ_2 on ϕ/s , k_d and k_e when $\alpha = 10$ and $k_c + 1 - k_e = \frac{1}{2} \phi/s$ for both 4-phase and 3-phase machines. It may be observed that maximum value of Ψ_2 is not particularly sensitive to k_d .

Since the value $\phi/s = 3$ is the upper limit for a 3-phase machine, the maximum value of Ψ_2 is obtained about $k_d = 0$ and $k_e = 0.7$. That value of Ψ_2 is only 2% less than absolute maximum (for $\alpha = 10$). For this reason and because of the fact that by taking $\phi/s = 3$ the starting performance of a 4-phase machine is considerably improved, the same values of ϕ/s , k_d and k_e may be taken as the optimum for a 4-phase machine.

For $\phi/s = 3$ and $k_e = 0.7$ the optimum conduction region is $k_c + 1 - k_e = \frac{3}{2}$, and hence $k_c = 1.2$.

If α is given the value 10, then the optimum set of parameters is

$$k_d = 0.0, \phi/s = 3.0, k_c = 1.2, k_e = 0.7$$

which gives the maximum torque for a given primary rms current at a fixed voltage.

This set of parameters applies to both 4-phase and 3-phase motors.

Comparison of these results for optimisation of torque for a given current with those previously obtained for the optimum torque for a given maximum flux density shows that the machine designed for maximum specific output will not then be operating at its maximum efficiency.

(This, of course, assumes linearity and negligible iron loss.)

4.5 Speed Control of a Switched Reluctance Motor

From equation (4.9)

$$\omega = V \frac{s}{\phi} \sqrt{q \frac{\phi}{L_o} \frac{F}{T}} \quad (4.28)$$

According to this expression two basic methods of speed control are possible:

- a) speed control by varying the voltage V (control by voltage),
- b) speed control by varying the switching angles, ie by varying the parameters k_c and k_e to change the value of F (control by switching angles).

The speed which corresponds to the operation at full voltage, torque and power is defined as base speed.

Fig 4.12 shows the torque/speed and power/speed characteristics of:

- A) a constant torque drive
- B) a traction drive

These two types of drive are considered below.

In the following analysis the expressions derived above are used for the average torque, output power, peak flux-linkage and primary rms current, ie

$$T = q \frac{V^2 \phi}{L_o} \left(\frac{s}{\phi}\right)^2 \frac{F}{\omega^2} \quad (4.29)$$

$$\hat{\psi} = Vs \frac{k_c + 1 - k_e}{\omega} \quad (4.30)$$

$$I_1 = \frac{Vs}{L_o} \sqrt{\frac{s}{\phi}} \frac{R_1}{\omega} \quad (4.31)$$

4.5.1 Speed control by voltage

For this type of control the dependence between voltage and speed for a given drive characteristic is determined by equation (4.29). In the region of constant torque this equation becomes

$$\text{const} = \frac{V^2}{\omega} \times \text{const}$$

$$\therefore V = \omega \times \text{const} \quad (4.32)$$

In this case $\hat{\psi}$ and I_1 (given by (4.30) and (4.31)) stay constant as the speed varies, in fact the current waveform remains exactly the same shape, changing only in frequency. Therefore, control by voltage naturally fulfills the requirements of speed control in the region of constant torque.

The full voltage corresponds to the base speed (ω_B) where the full torque and power are required (see Fig 4.12).

In a region of constant power the dependence between V and ω (from (4.29) is

$$\frac{\text{const}}{\omega} = \frac{V^2}{\omega} \times \text{const}$$

$$\therefore V = \sqrt{\omega} \times \text{const} \quad (4.33)$$

However, if the constant power region follows the constant torque region as shown in Fig 4.12(b) and if the voltage reaches the full value at base speed, then control by voltage in the constant power region cannot be achieved since the voltage cannot be increased further.

4.5.2 Speed control by switching angles

For this type of control the dependence between controlling parameters, k_c and k_e , and speed for a given load characteristic is determined by equation (4.29). However, since the controlling parameters in that equation are expressed implicitly in the function F , there is no analytical solution for k_c and k_e and therefore a graphical method is used.

For the purposes of this graphical method the 'control diagram' is introduced. This is represented in 3 quadrants of Decart's coordinate system.

In quadrant I the function F , (for optimum parameters $k_d = 0.0$, $\phi/s = 3.0$ and $\alpha = 10$) is plotted against conduction period, $k_c + 1 - k_e$, for various values of k_e .

In quadrant II the curve which represents the dependence between F and ω for a given load is plotted.

In quadrant IV the ordinate is speed, ω , and abscissa is conduction period, $k_c + 1 - k_e$. For a given motor operating at a given voltage, the peak flux-linkage is proportional to $\frac{k_c + 1 - k_e}{\omega}$ (see (4.30)) and therefore the ratio of the coordinates of a point in quadrant IV is proportional to $\hat{\psi}$.

Substituting the left hand side of the equation (4.29) with the known function $T(\omega)$ of a given load, the dependence between F and ω can be found analytically. The specific curve $F(\omega)$ can be determined providing that one pair of values of F (ie k_c and k_e) and ω is given. This pair of values is given by the requirement that a certain torque should be obtained at certain values of V , ω , k_c and k_e . The case when a motor is optimised with respect to peak flux density (see Section 4.4.2) and operates with full torque at a full voltage will be considered. (Analogous analysis can be made when a motor is optimised with respect to primary rms current, or operates at lower voltage.)

Having specified the curve $F(\omega)$ in quadrant II, the values of k_c and k_e at various values of ω can be found by transferring the corresponding values of F from quadrant II into quadrant I and requiring, for example, that the flux-linkage (and hence flux density) be held as small as possible, ie that the ratio of coordinates in quadrant IV ($\frac{k_c + 1 - k_e}{\omega}$) be held as small as possible.

Such a procedure is used below.

A) Constant torque drive

The dependence between F and ω (from (4.29) is

$$\text{const} = \frac{F}{\omega^2} \times \text{const}$$

$$\therefore F = \omega^2 \times \text{const} \quad (4.34)$$

When the torque is optimised with respect to \hat{B} , the optimum values of controlling parameters are $k_c = 1.1$ and $k_e = 0.9$. Therefore it is desirable that these values of k_c and k_e are used at base speed, ω_B , where the full torque and power are required. The point which corresponds to these values of k_c and k_e in quadrant II of diagram (a) in Fig 4.13 is marked by A, and the corresponding points in quadrant II and IV are marked by B and C respectively. The curve $F(\omega)$, which is determined by (4.34) and coordinates of point B, is plotted in quadrant II.

When the speed is reduced below base speed the values of F at various speeds are determined by the curve $F(\omega)$, and corresponding values of k_c and k_e are chosen in such a way as to give the smallest possible values of $\hat{\psi}$ (and hence \hat{B}).

The line of constant flux corresponding to $\hat{\psi}$ as at base speed is represented by direction OC in quadrant IV.

From quadrant IV of diagram (a) it is seen that $\hat{\psi}$ (and hence \hat{B}) increases above the value at base speed when ω decreases (by 8.5% at $\omega = 0.5 \omega_B$ and 21% at $\omega = 0.25 \omega_B$).

In order to find the variation of I_1 against ω the diagram (b) in Fig 4.13 is drawn. This diagram consists of 2 quadrants. In quadrant I the function R_1 (for $\alpha = 10$ and optimum values $k_d = 0.0$ and $\phi/s = 3.0$) is plotted against conduction period, $k_c + 1 - k_e$, for various values of k_e . In quadrant II the ordinate is R_1 and abscissa is ω and therefore their ratio is proportional to I_1 (see (4.31)). The line of constant current corresponding to base speed is represented by direction DE in quadrant II of diagram (b).

Transferring the corresponding values of ω , $k_c + 1 - k_e$ and k_e from diagram (a) to diagram (b) the values of R_1 and therefore the variations

of I_1 against speed can be found.

From quadrant II of diagram (b) it is seen that I_1 does not exceed the value at base speed when ω decreases.

The fact that \hat{B} increases above the value at base speed when ω decreases, is a very serious disadvantage for this method of control when compared with voltage control for a constant torque drive. In addition, the torque pulsations are increased when the conduction period becomes shorter.

B) Traction drive

In the constant torque region the dependence between F and ω (from (4.29)) is

$$\text{const} = \frac{F}{\omega^2} \times \text{const}$$

$$\therefore F = \omega^2 \times \text{const} \quad (4.35)$$

and in constant power region the dependence between F and ω (from (4.29)) is

$$\frac{\text{const}}{\omega} = \frac{F}{\omega^2} \times \text{const}$$

$$\therefore F = \omega \times \text{const} \quad (4.36)$$

When the torque is optimised with respect to \hat{B} , the optimum values of controlling parameters are $k_c = 1.1$ and $k_e = 0.9$. If these values of k_c and k_e are used at base speed then an increase of speed at constant power can be simply achieved by advancing the switch-on point (Fig 4.14), i.e. by increasing k_c , with a fixed switch-off point characterised by $k_e = 0.9$. However, the maximum top speed, ω_T , which can be achieved at constant power, is $\omega_T = 1.55 \omega_B$ because, due to the limiting value of the conduction period ($k_c + 1 - k_e < \frac{1}{2} \frac{\phi}{s} = 1.5$), the maximum value of F is the one at $k_c + 1 - k_e = 1.5$ and $k_e = 0.9$.

When the ratio ω_T/ω_B greater than 1.55 is required then the curve

$F(\omega)$ in constant power region is determined by (4.36) and pair of values $\omega = \omega_T$ and maximum F at $k_c + 1 - k_e = 1.5$ and $k_e = 0.9$. The control diagram, when $\omega_T = 3\omega_B$, is given in Fig 4.15. From all possible combinations of k_c and k_e at base speed, those which give the value of Ψ_1 nearest to the optimum one are chosen (see Section 4.4.2). According to Figs 4.6 and 4.8 such values of k_c and k_e are 0.8 and 0.9 respectively (the value of Ψ_1 is then about 10% less than the optimum value which can be used when the design is not constrained by the wide range of constant power speed control). The control between top and base speed can be simply achieved by controlling the switch-on point whilst retaining a fixed switch-off point ($k_e = 0.9$).

From diagrams (a) and (b) it is seen that both $\hat{\Psi}$ and I_1 decrease below the values at base speed when the speed increases from base to top speed. When the speed decreases below base speed only $\hat{\Psi}$ increases above the value at base speed.

It may therefore be concluded that control by switching angles is very suitable in the constant power region, while control by voltage is more suitable in the constant torque region. (In this respect it is exactly the same as the conventional d.c. motor, since control by switching angles is, in effect, control by flux.)

4.6 Regenerative Mode of Operation of Switched Reluctance Machine

If the switching angles are set so that, when the machine is rotating in the forward direction the retarding torque is greater than the positive (forward) torque, the machine operates as generator. Operation in the regenerative mode may be used for braking the switched reluctance motor, in which case the kinetic energy of the rotating inertias is transferred to the supply as the motor speed falls.

If the machine develops torque T_m when it rotates in forward direction, then it can regenerate with the same torque when it rotates in the same direction (provided that the rotor of the machine is supplied with the torque equal to T_m) with the same peak flux-linkage. To achieve this the switching angles are shifted by an angle equal to $(2k_e + k_d)s$ in the forward direction (ie switch-on and switch-off instants are each delayed for period equal to $(2k_e + k_d)\frac{s}{\omega}$). The current waveforms in

these two operating modes are symmetrical about the axis which corresponds to the axis of symmetry of the inductance profile which passes through maximum inductance. This is shown in Fig 4.16. It should be noted that in the regenerative mode of operation the secondary current is greater than the primary current (this fact may have to be borne in mind when considering the actual situation when the resistance of the coils are present).

4.7 Conclusions

The analytical expressions for the currents and torque of an 'ideal' switched reluctance motor have been derived and this has enabled optimisation involving the combined effect of several parameters (ratio ' L_i/L_o ', dead zone ' k_d ', ratio ' ϕ/s ', early turn-on coefficient ' k_c ', early turn-off coefficient ' k_e '). For realistic value $\alpha = 10$ the optimum parameters at which the motor produces maximum torque at a given speed and given values of the peak flux density, rotor diameter and core length, are: $k_d = 0$, $\phi/s = 3$, $k_c = 1.1$, $k_e = 0.9$. The optimum parameters at which the motor produces maximum torque at a given speed and fixed values of the primary rms current and voltage, are: $k_d = 0$, $\phi/s = 3$, $k_c = 1.2$, $k_e = 0.7$.

Speed control by varying the voltage and by varying the switching angles for a constant torque drive and a traction drive have been analysed. The analysis shows that voltage control is suitable for constant torque and switching angle control is suitable for constant power.

A prototype motor may now be built to determine actual behaviour and to test the value of this linear analysis.

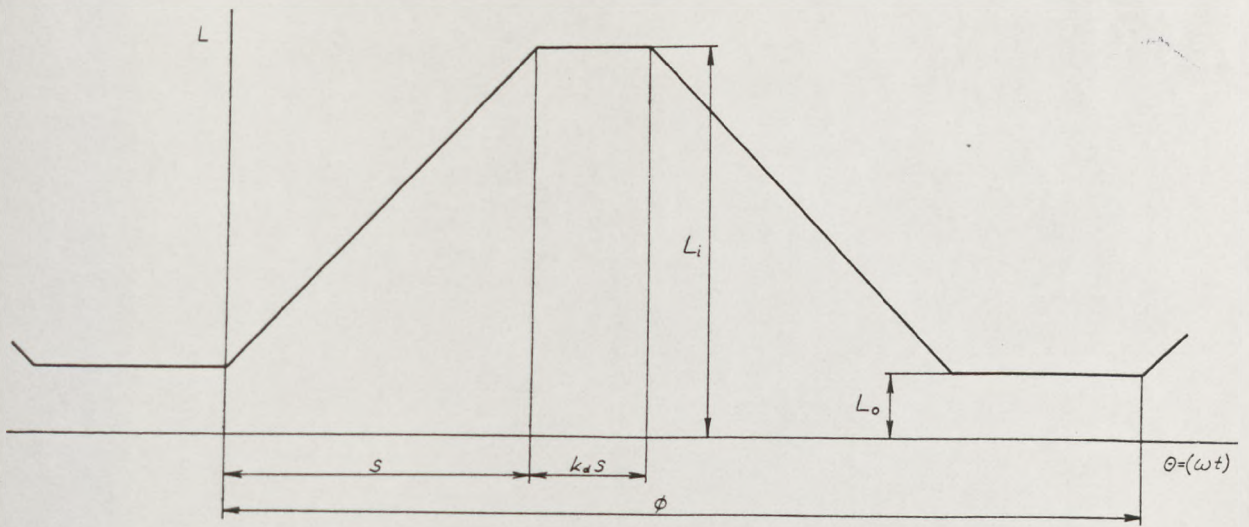


FIG 4.1 Inductance profile defined in terms of parameters L_o, L_i, s, k_d, ϕ

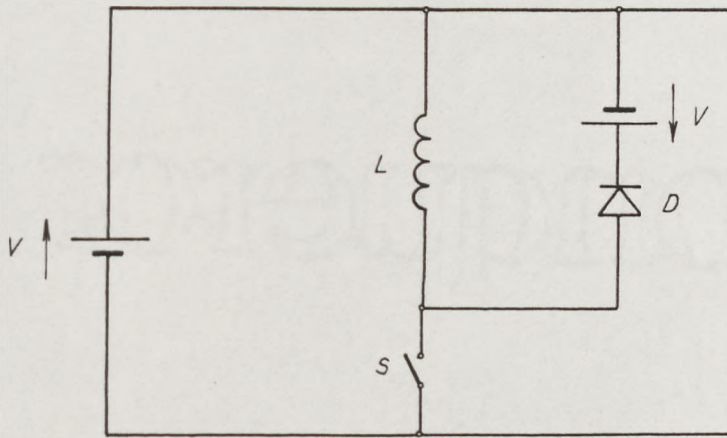


FIG 4.2 Basic machine circuit

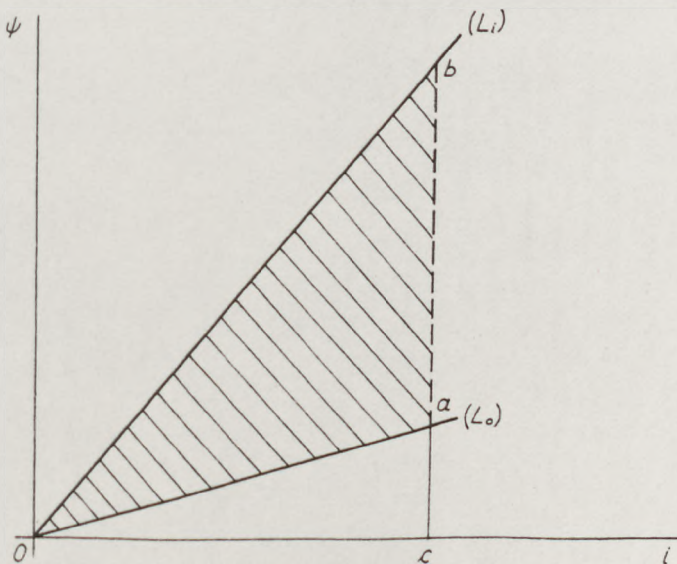


FIG 4.3 ψ - i diagram showing the change of system co-energy

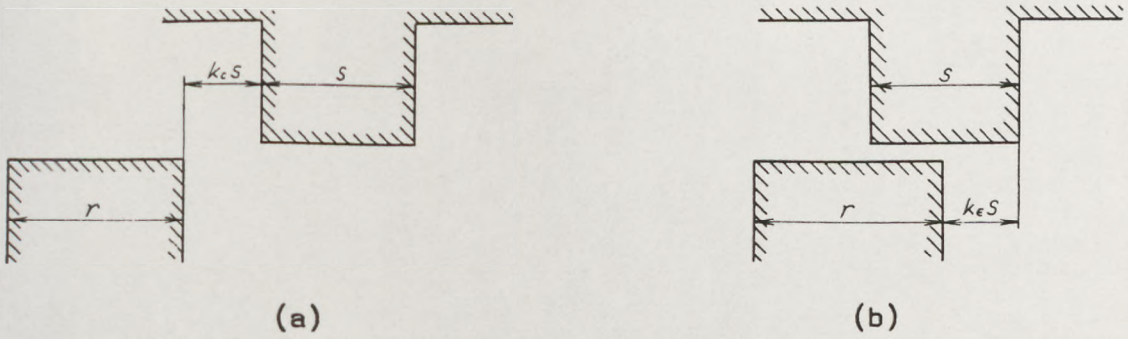


FIG 4.4 Definition of (a) early turn-on coefficient
(b) early turn-off coefficient

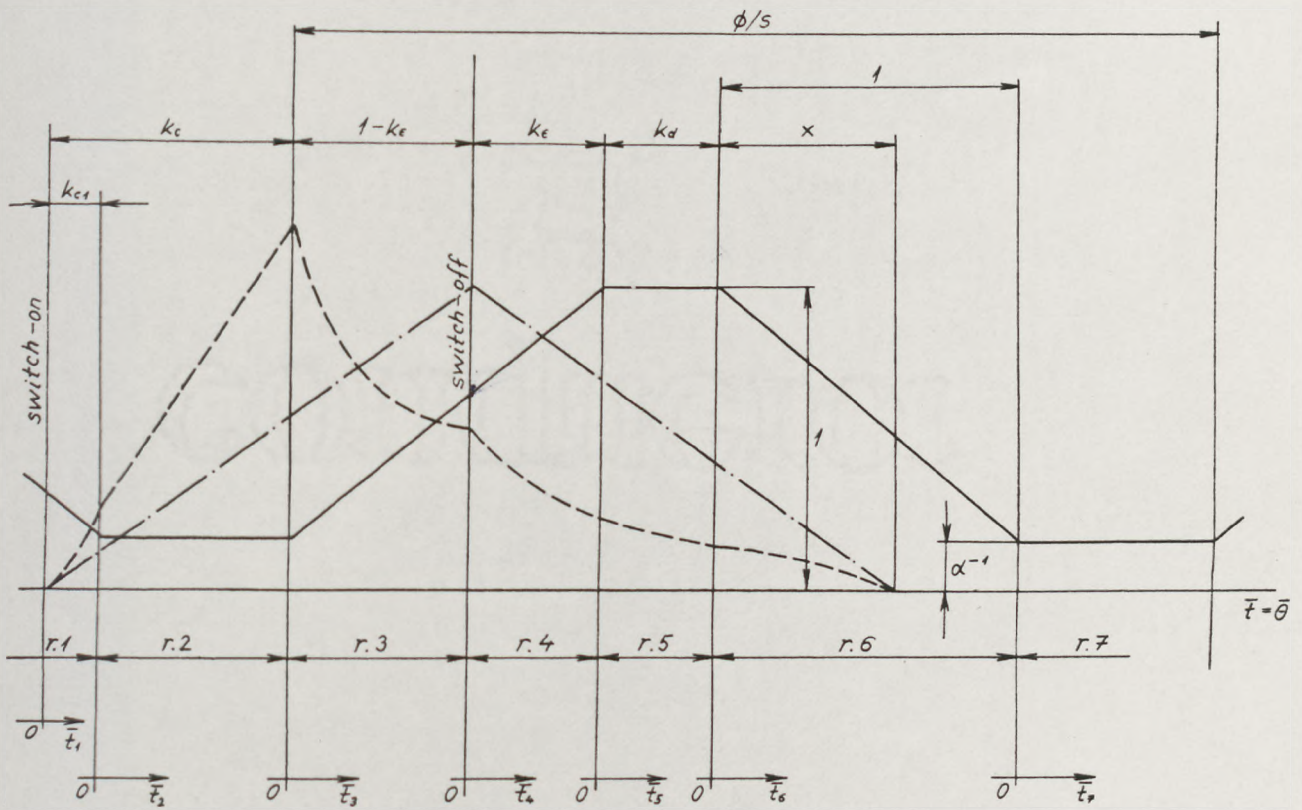


FIG 4.5 Normalised inductance profile with flux-linkage waveform (—) and current waveform (---)

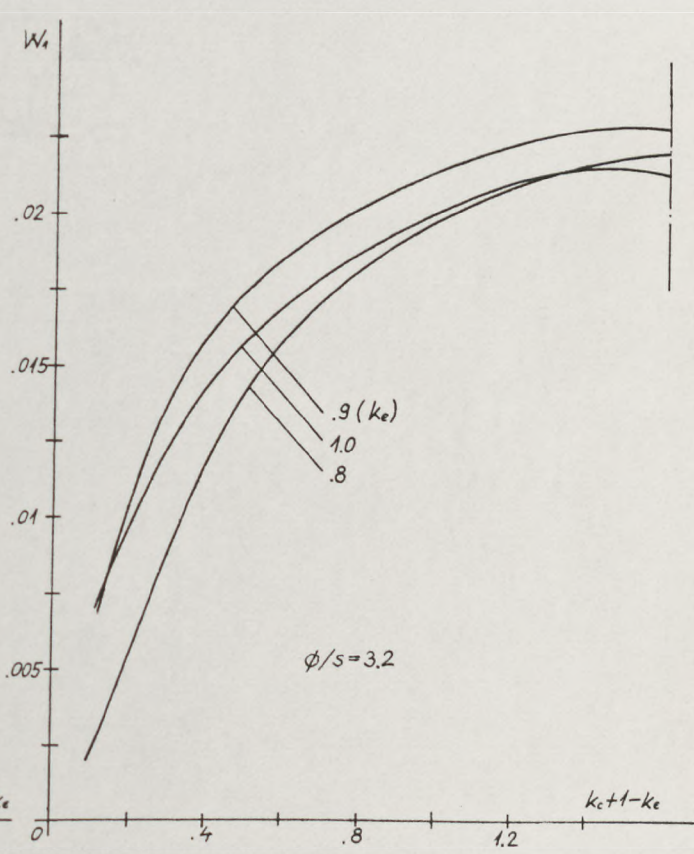
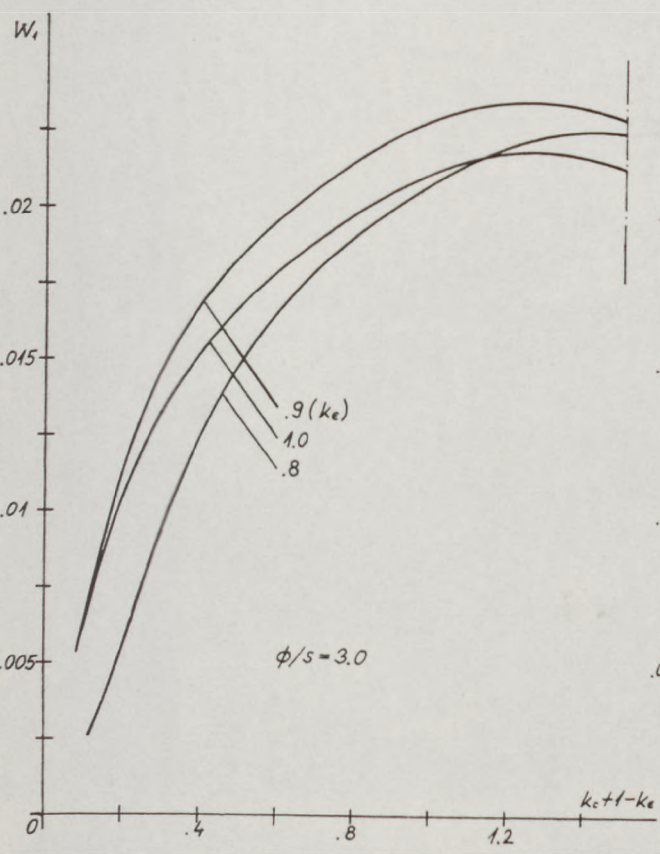
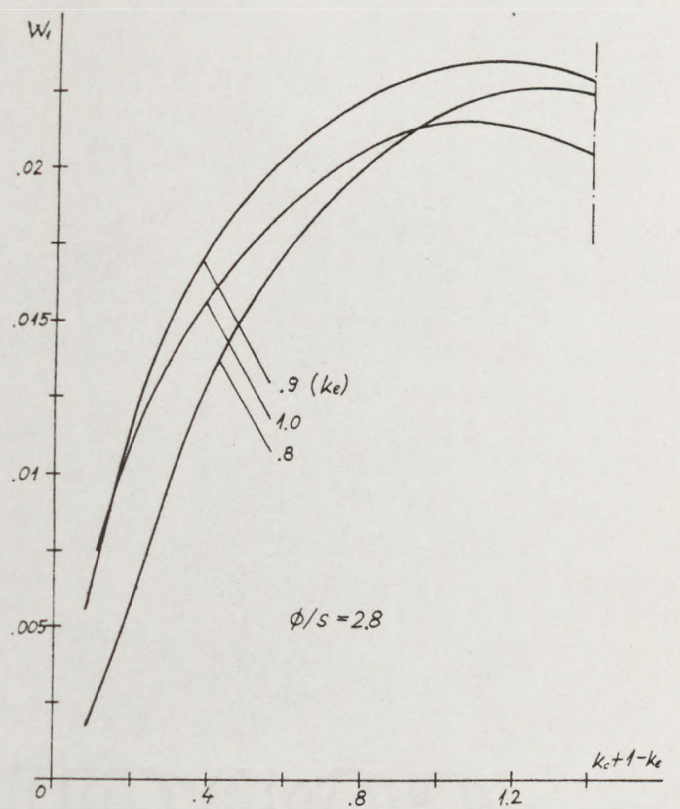
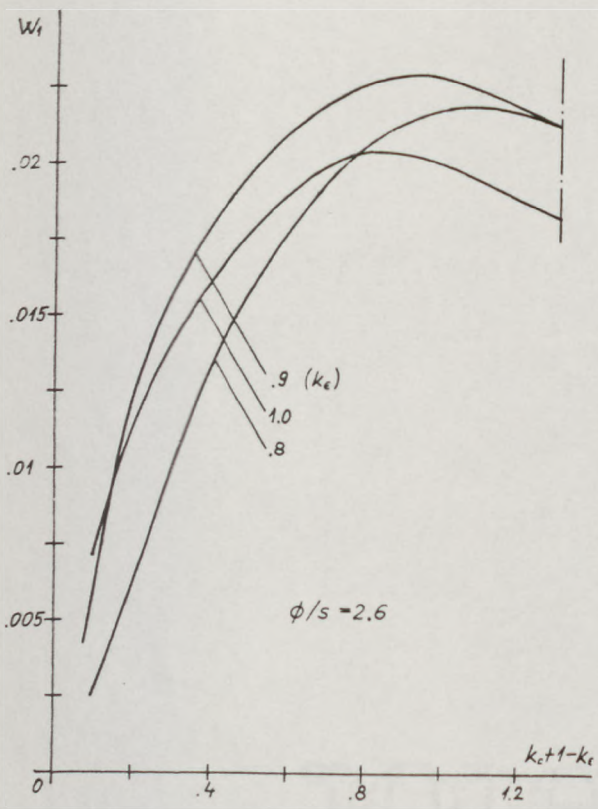


FIG 4.6 Variations of function W_1 at $\alpha = 10$, $k_d = 0.0$ for 4-phase machine

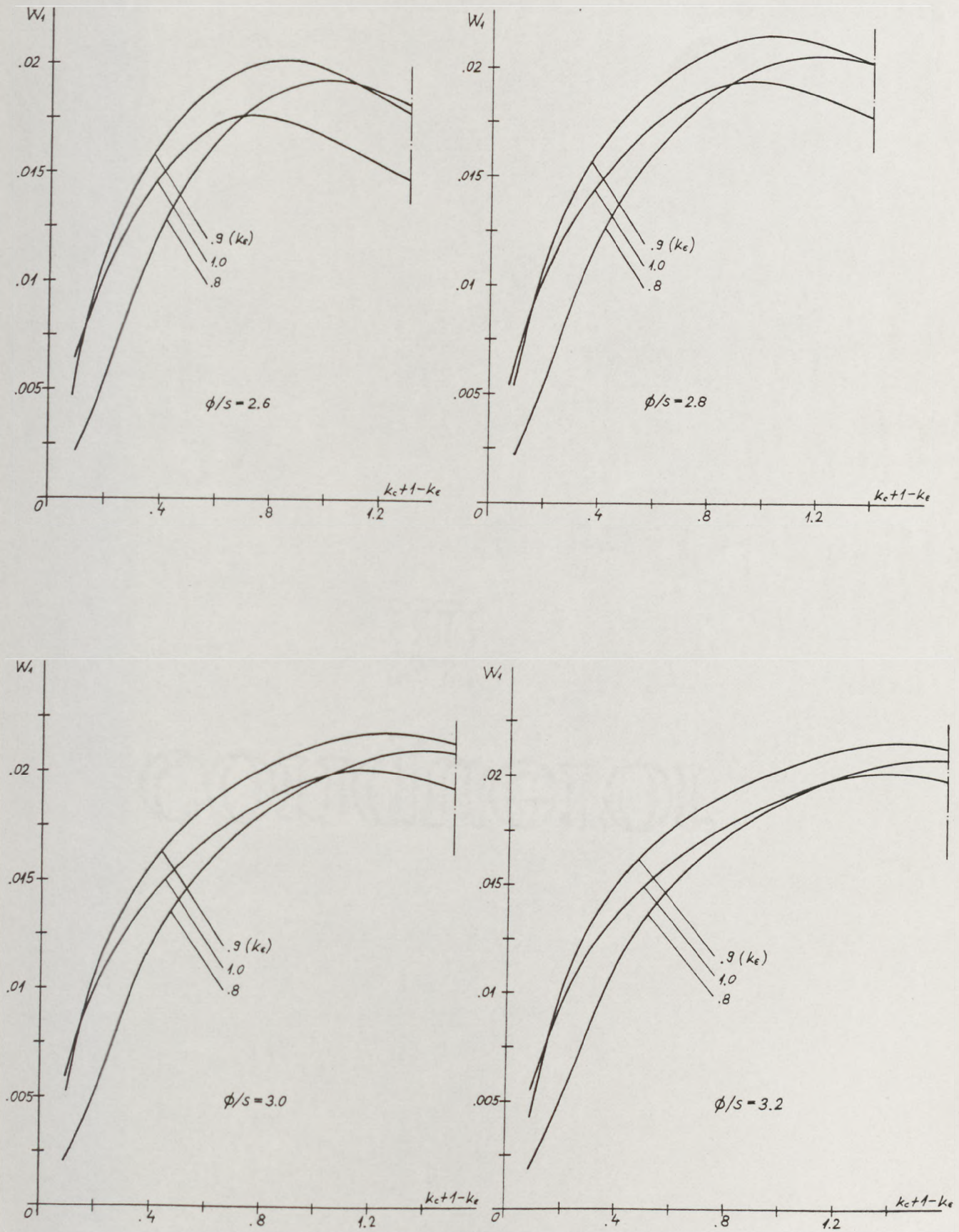


FIG 4.7 Variations of function W_1 at $\alpha = 10$, $k_D = 0.1$ for 4-phase machine

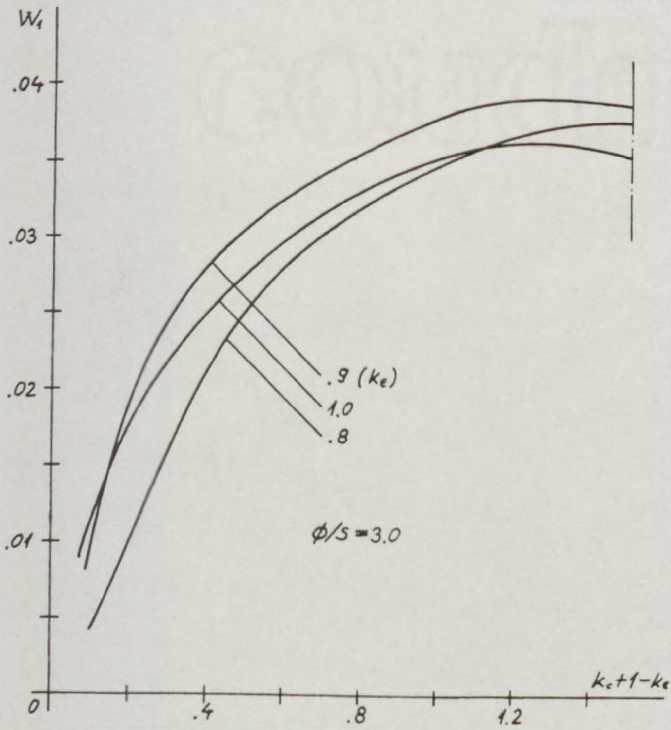
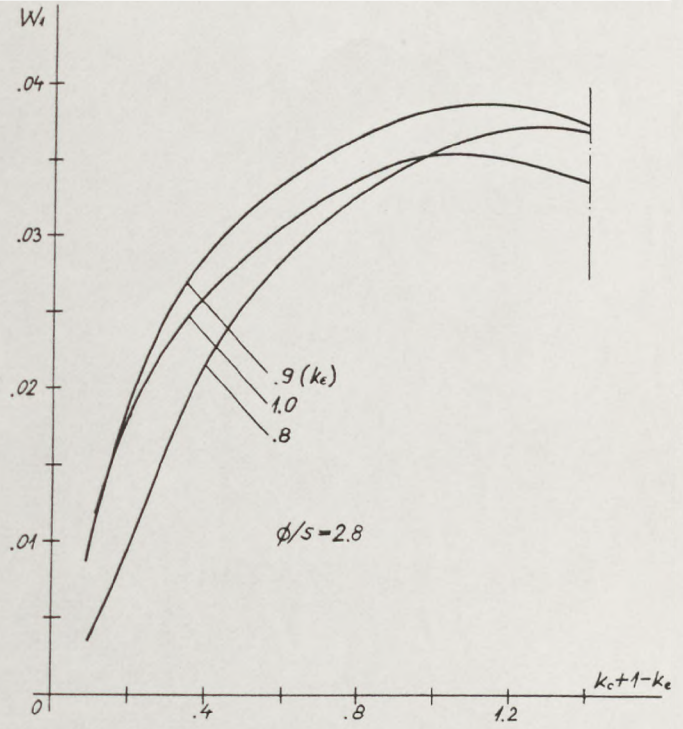
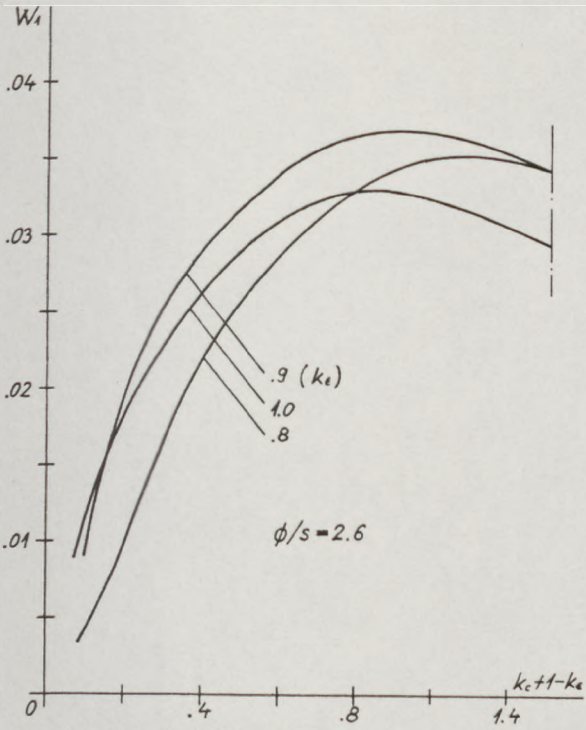


FIG 4.8 Variations of function W_1 at $\alpha = 10$, $k_D = 0.0$ for 3-phase machine

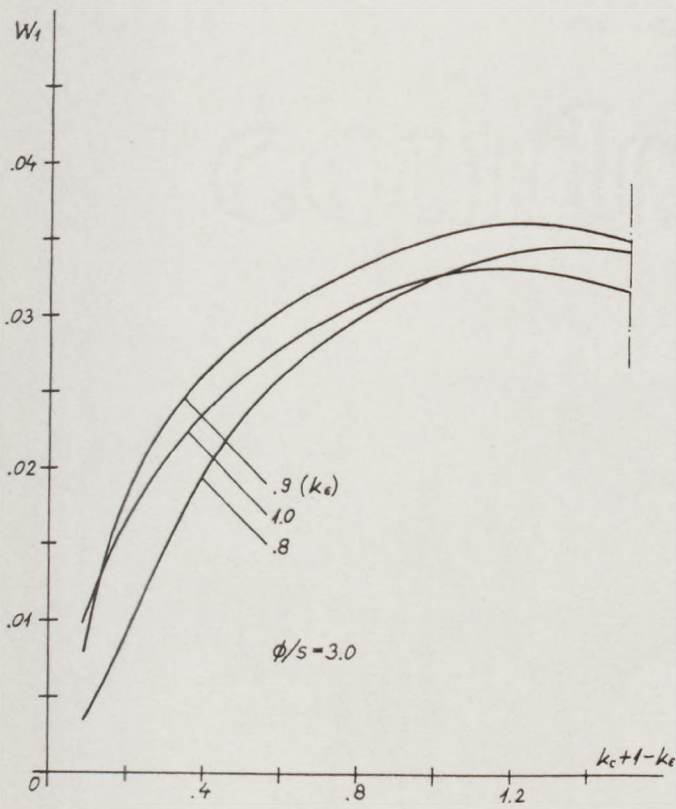
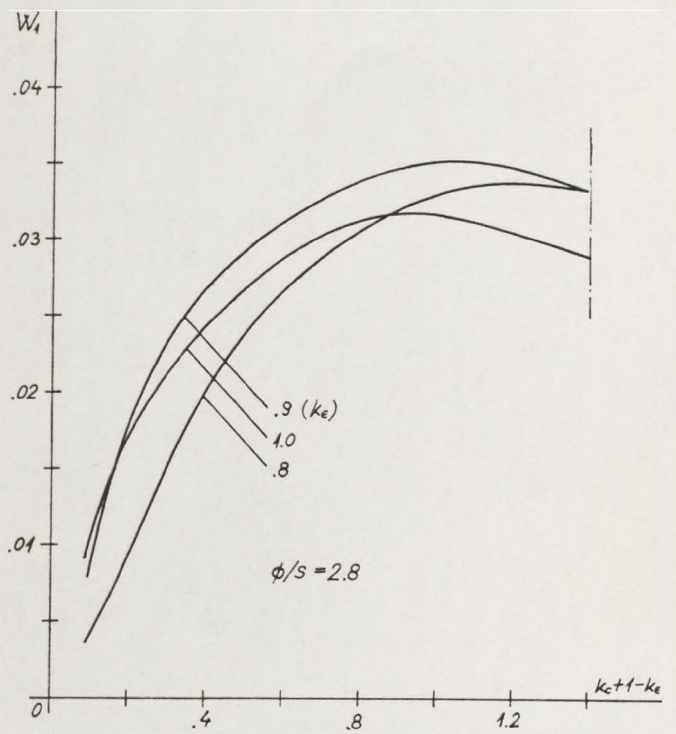
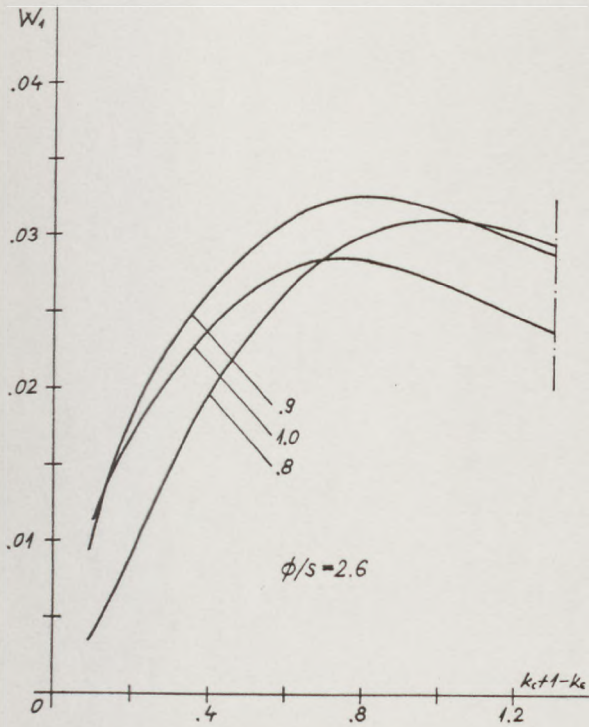


FIG 4.9 Variation of function W_1 at $\alpha = 10$, $k_d = 0.1$ for 3-phase machine

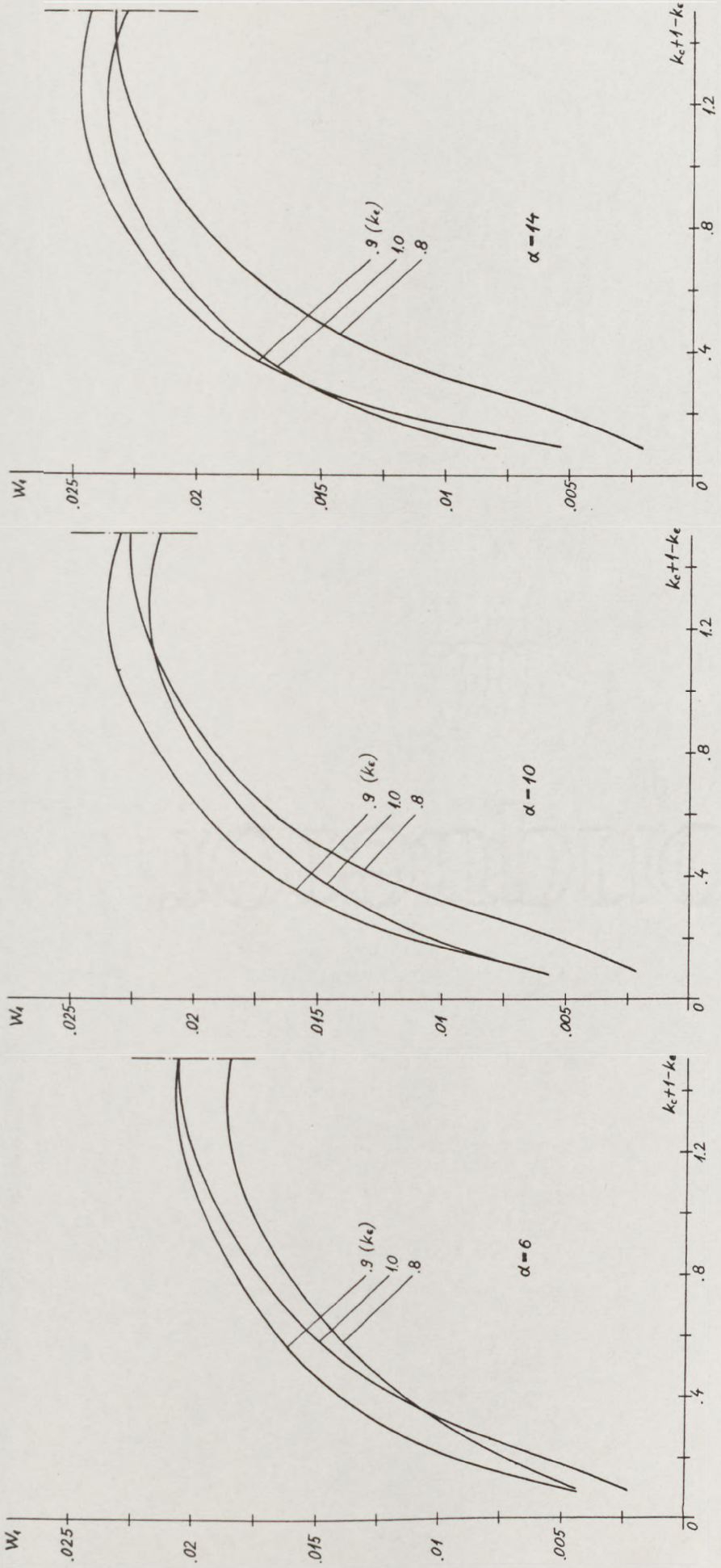


FIG 4.10 Variations of function W_1 at $k_D = 0.0, \phi/s = 3.0$ for 4-phase machine

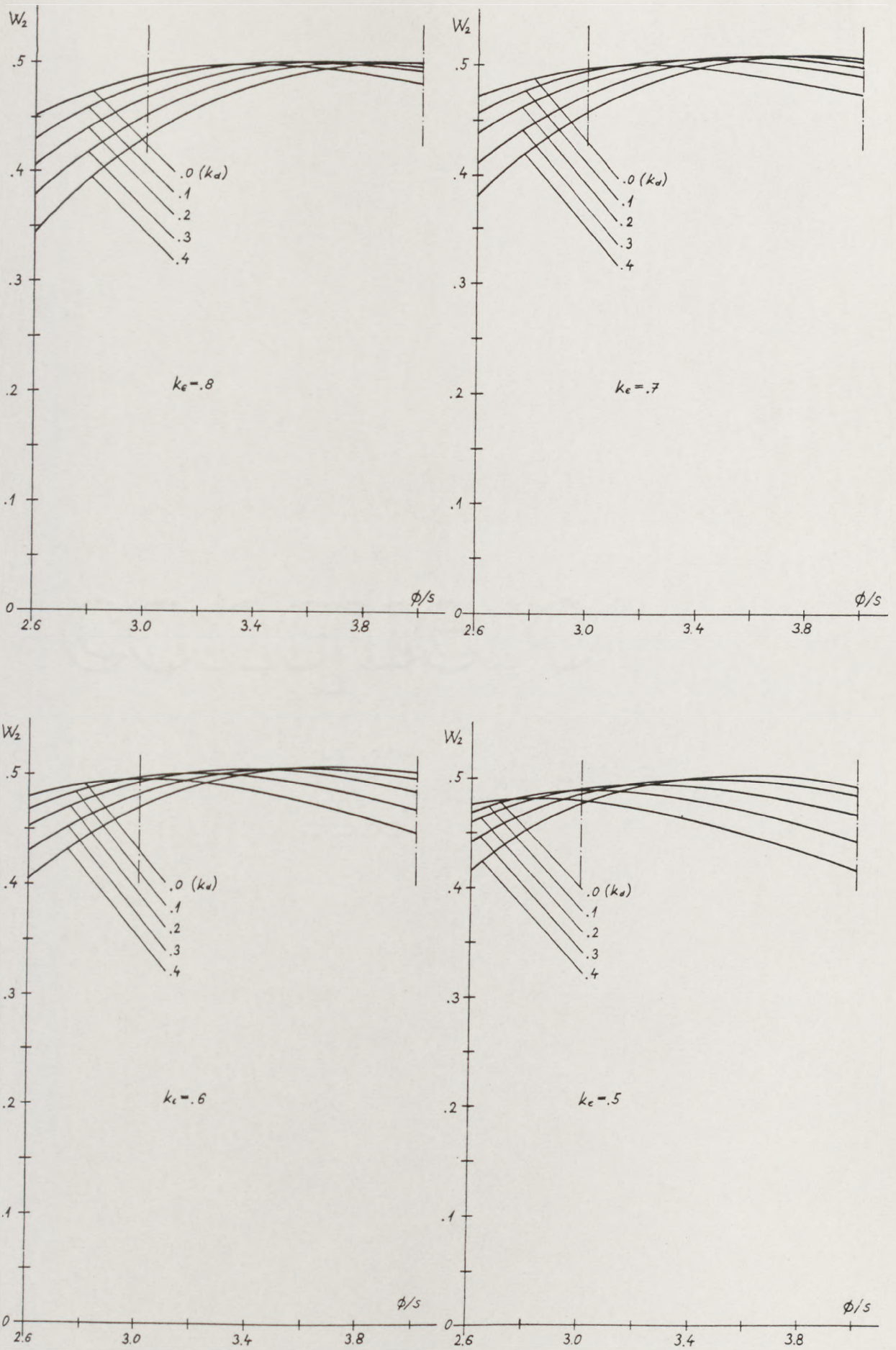


FIG 4.11 Variations of function W_2 at $\alpha = 10$ and $k_c + 1 - k_e = \frac{1}{2} \phi/s$

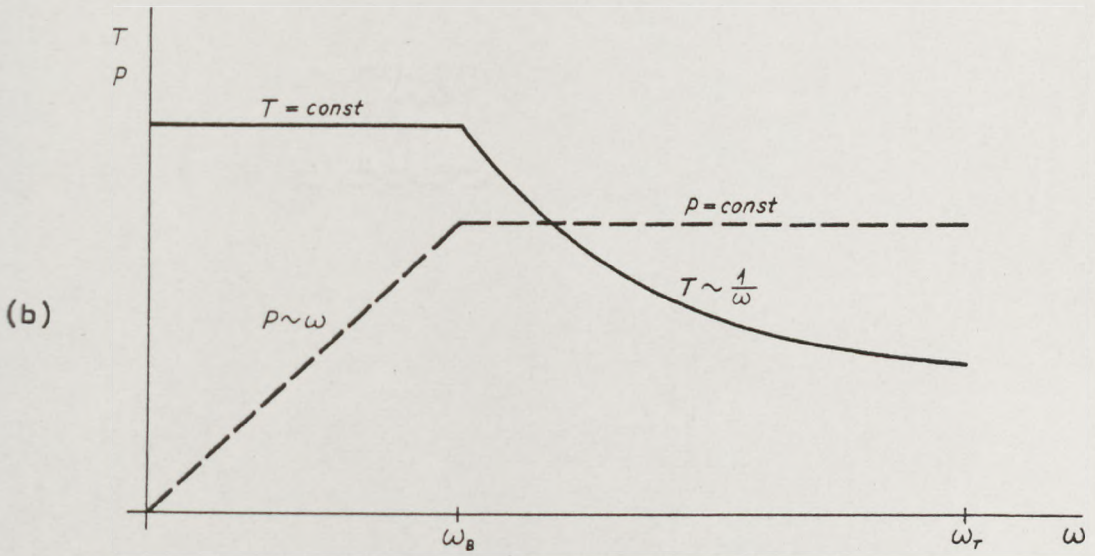
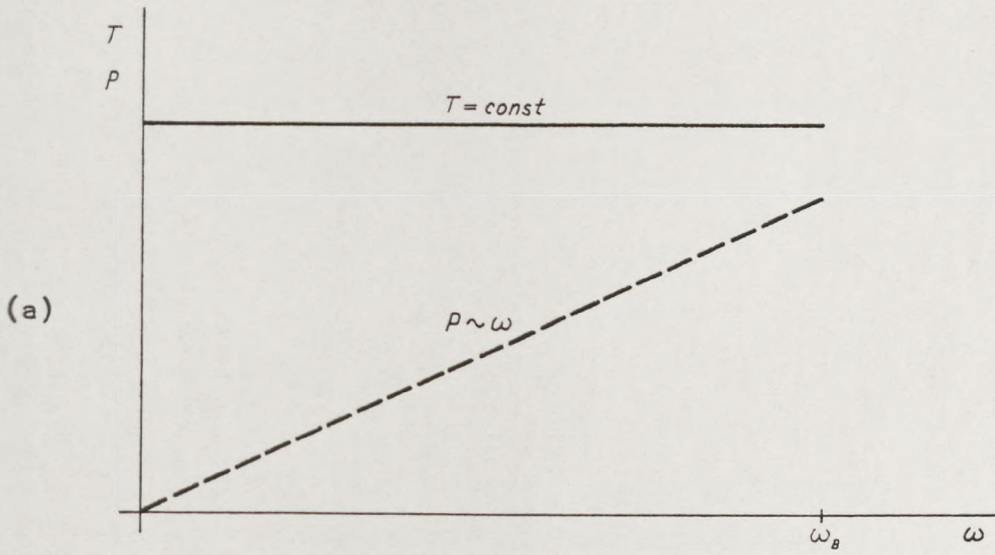


FIG 4.12 Torque/speed and power/speed characteristics for
 (a) a constant torque drive
 (b) a traction drive

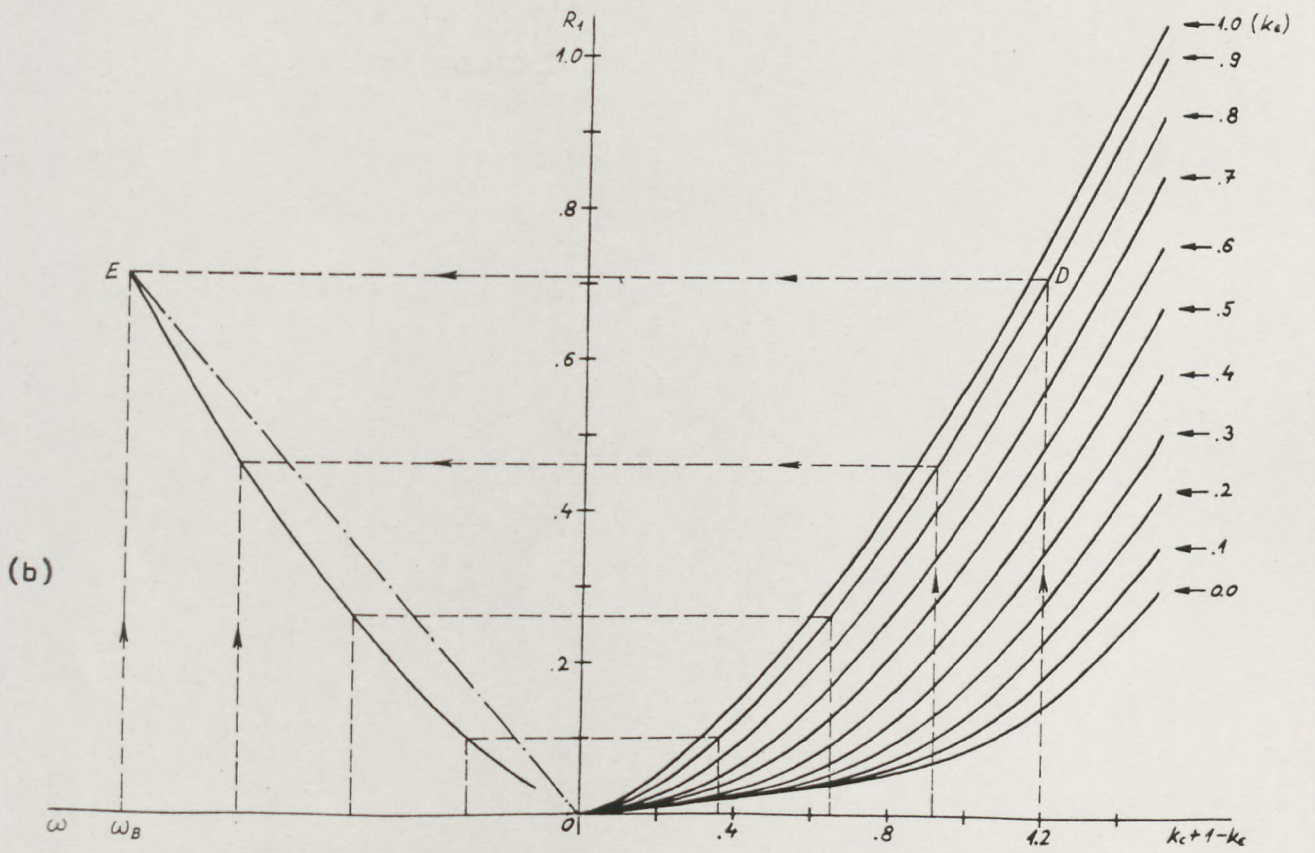
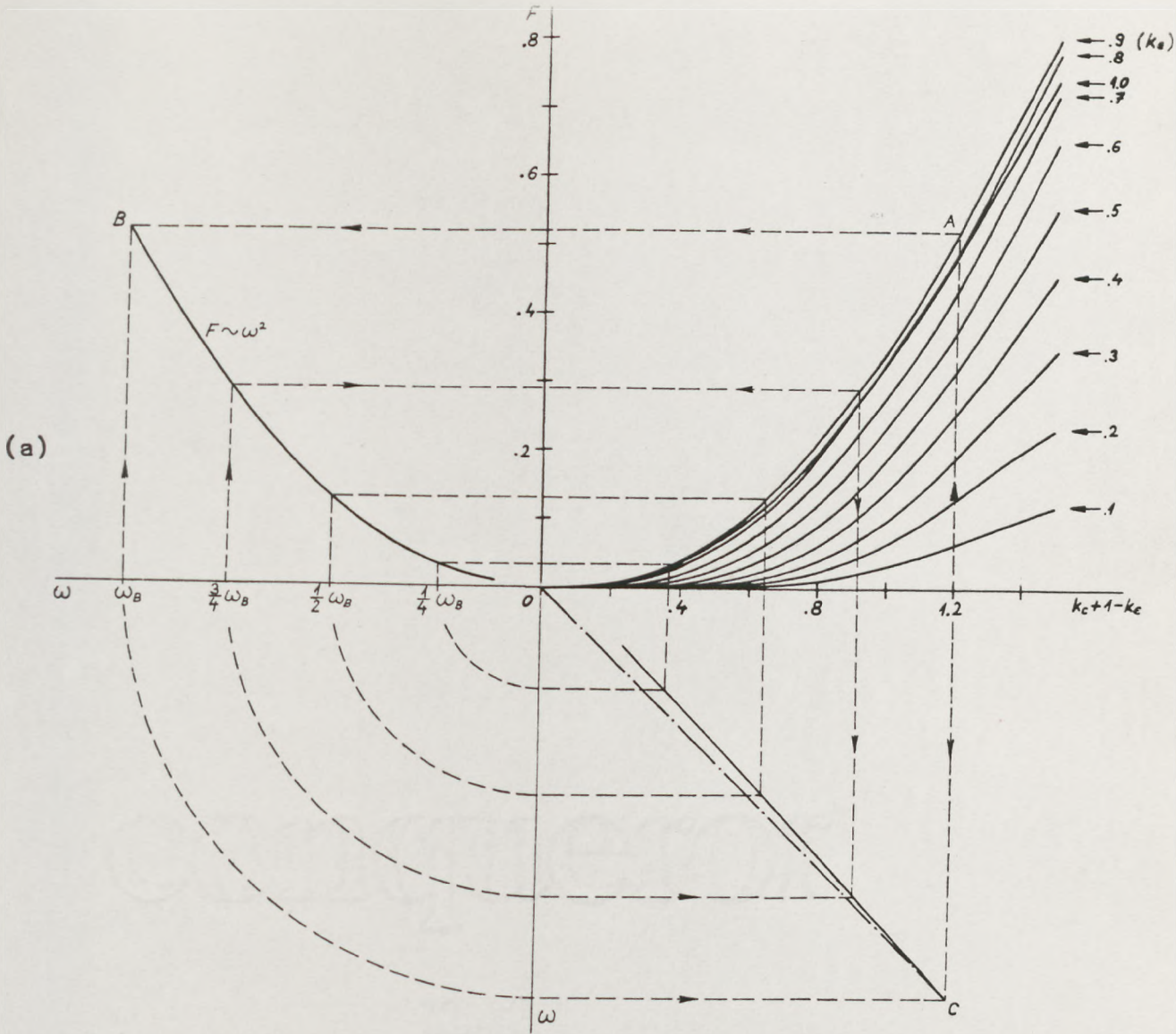


FIG 4.13 Control diagram for constant torque drive

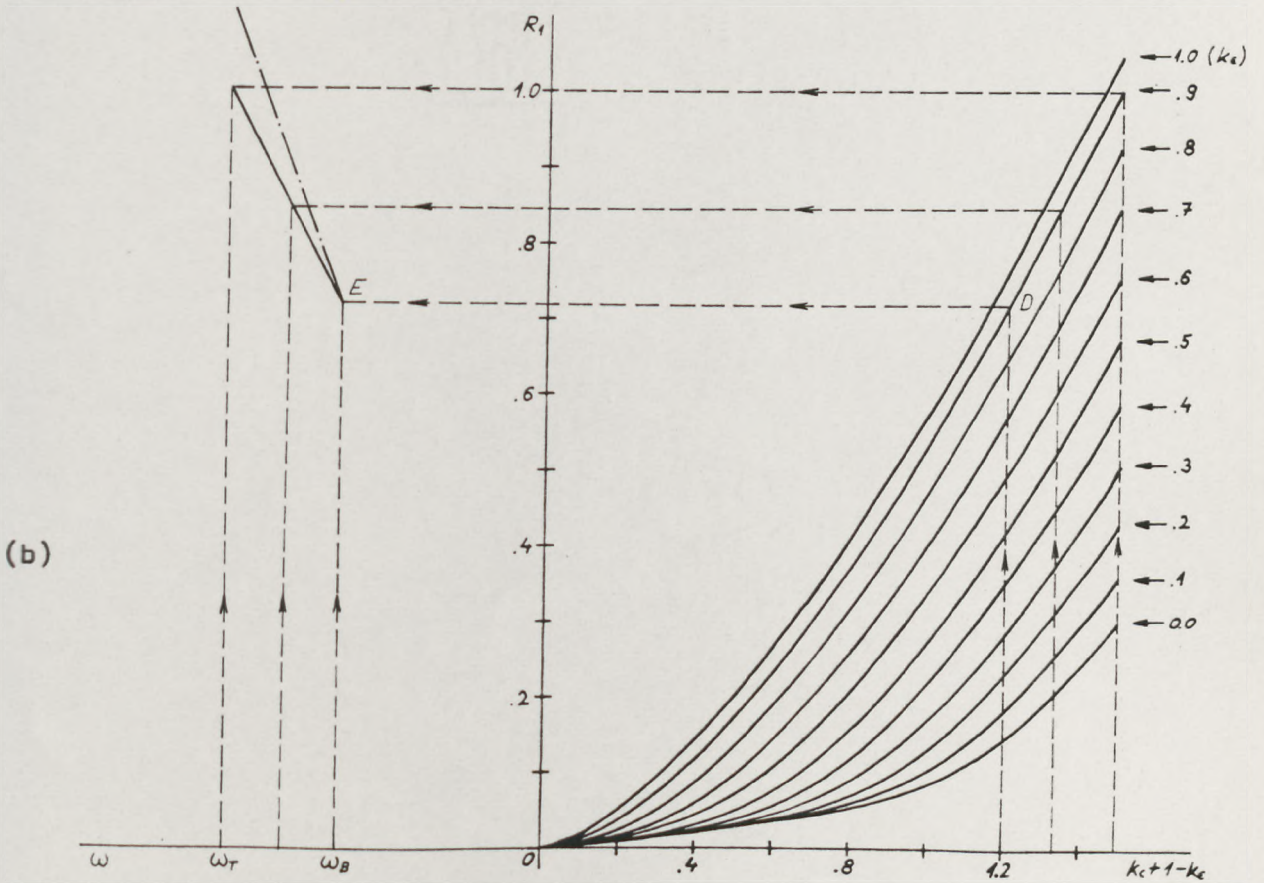
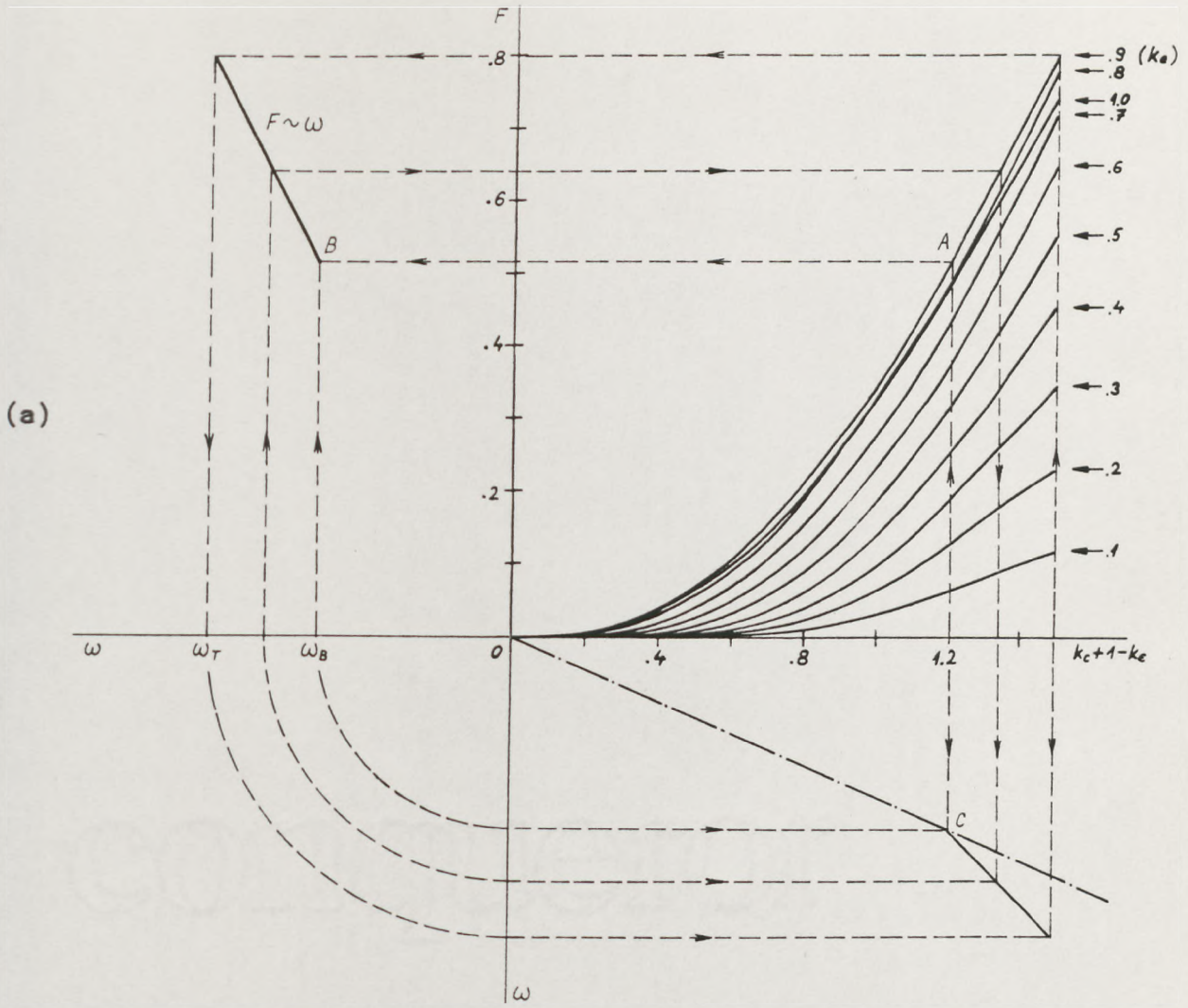


FIG 4.14 Control diagram in constant power region ($\omega_T/\omega_B \leq 1.55$)

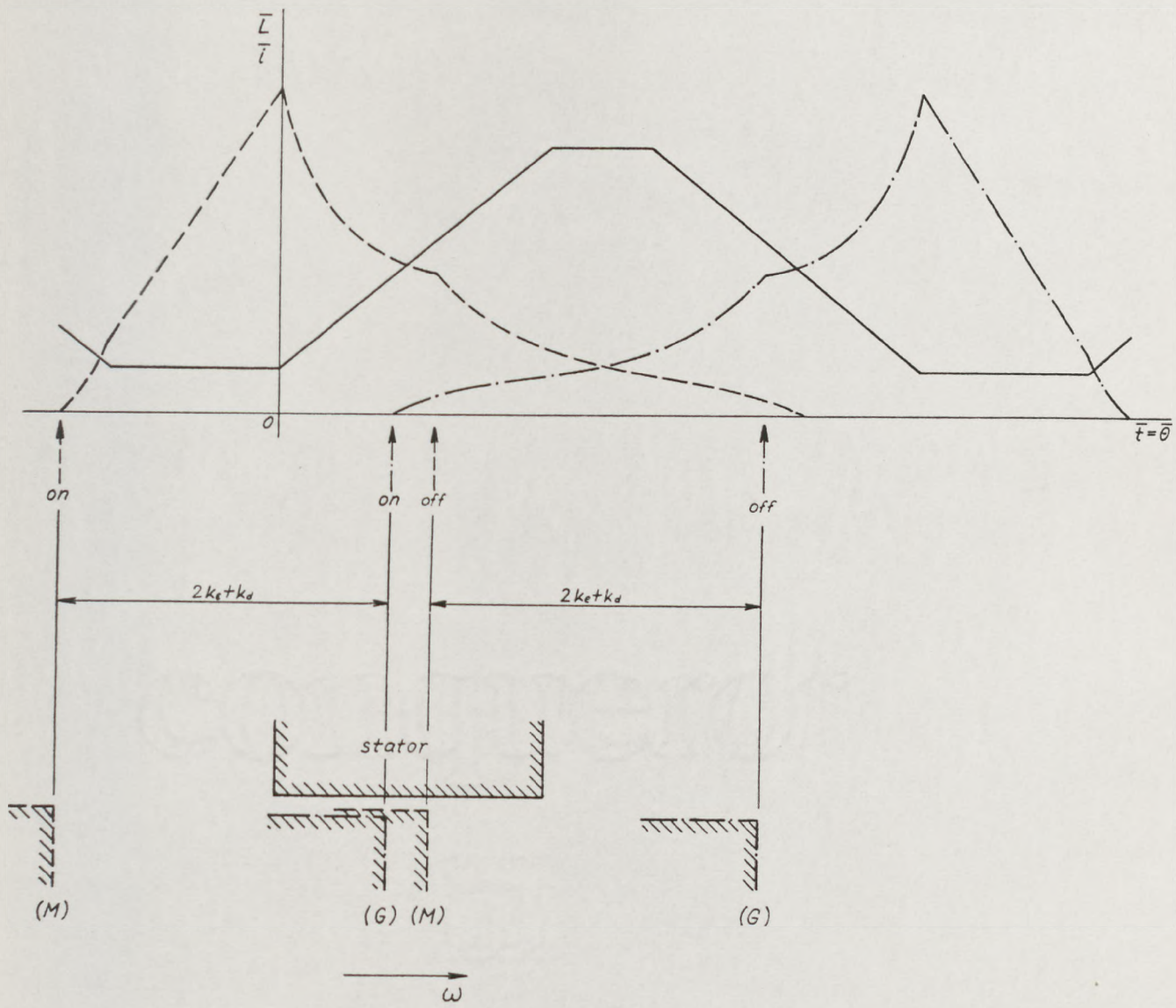


FIG 4.16 Motor (---) and regenerative (— · — · —) modes of operation

CHAPTER 5

DESIGN AND PERFORMANCE OF EXPERIMENTAL MOTORS

5.1 Introduction

This chapter covers the design, measurement and analysis of performance of a series of experimental switched reluctance motors to meet a traction type of torque-speed characteristic with an output power 0.75 [kW] over the range 750 to 2250 $\left[\frac{\text{rev}}{\text{min}}\right]$.

The design method is described first and it is based on theoretical knowledge presented in previous chapters.

Following the design procedure the detailed description of inductance, static torque and running performance measurements are presented and the obtained results are analysed with particular attention to saturation which is found to be very significant in this type of the machine.

Finally, to further clarify the effects of saturation a graphical method for prediction of current waveform using measured $\psi(\theta, i) \Big|_{\theta=\text{const}}$ curves but ignoring the winding resistance is demonstrated and the predicted current waveforms are compared with those obtained by linear analysis.

5.2 Design Philosophy of an Experimental Motor

In order to examine the behaviour of a switched reluctance motor it was convenient (particularly with relation to available power transistors) to construct an experimental motor to develop 0.75 [kW] over the range 750 to 2250 $\left[\frac{\text{rev}}{\text{min}}\right]$ with constant torque below 750 $\left[\frac{\text{rev}}{\text{min}}\right]$. The frame size of the motor was chosen to be that of the D90 three-phase induction motor rated at 0.75 [kW], at 1000 $\left[\frac{\text{rev}}{\text{min}}\right]$, so that it was not expected that the switched reluctance motor would be capable of a continuous rating of 0.75 [kW] at 750 $\left[\frac{\text{rev}}{\text{min}}\right]$, but this would correspond to a suitable maximum torque. Previous experience with other types of switched reluctance motors had shown this to be a reasonable objective.

In the light of considerations made in Chapters 2 and 4 it was decided to design the experimental motor as a 4-phase machine (since a 4-phase machine should give a larger torque at standstill than a 3-phase machine) and to introduce the bifilar winding which requires only one switching device per phase.

The details of the lamination geometry and the windings of the experimental switched reluctance motors, the design of which is presented below, are shown in Figs 5.1 and 5.2.

In order to see the effect of lamination material two motors with identical stators were built. The first motor D90M1 was constructed from Losil 1000-65 steel (a standard, low silicon steel used for small electric motors, lamination thickness 0.65 [mm]). The second motor D90M2 was constructed from Transil 315-35 steel (a low-loss steel usually employed for larger machines or those operating at higher frequencies, lamination thickness 0.35 [mm]). In order to study the effect of the rotor geometry, a series of modifications were made to the rotor of the D90M2 motor.

The results of these are presented below.

5.2.1 Stator pole arc and pole profile

According to linear analysis the optimum stator pole arc for a 4-phase machine is 20° . In addition this value gives a good compromise between the amount of overlap, k_L (starting torque), and the winding space (efficiency).

Parallel sided poles facilitate the insertion of former wound coils.

5.2.2 Rotor pole arc and pole profile

An initial arc of 26° , corresponding to $k_d = 0.3$, was chosen to allow for subsequent machining to find optimum rotor proportions. (The successive rotor modifications are shown in Fig 5.2.) The pole arc of 26° was used with radial-sided rotor poles for the D90M1 motor (Fig 5.1). The Rotor-1 of the D90M2 motor had parallel-sided poles again with the 26° arc and was subsequently machined to give the

Rotor-2 which had radial-sided poles with 26° arc (ie the D90M2-2 motor was identical in geometry with the D90M1 motor). The Rotor-3 retained the 26° rotor pole arc but had a reduced rotor minor diameter. This was subsequently machined to give Rotor-3b which had radial-sided poles with 25.5° and then Rotor-4 which had radial-sided poles with 24° arc. This smaller pole arc was machined without further narrowing of the rotor pole body as suggested in Section 3.4.

5.2.3 Back iron width

In order to make sure that the back iron, which forms the longest part of the magnetic circuit, is not highly saturated and hence to leave the stator pole as a critical cross-section, the back iron width, was chosen to be 50% wider than half of a stator pole width (because when more than one phase are switched on at the same time ($\theta_0 > 0$) some parts of the back iron carry more than a half the maximum stator pole flux).

5.2.4 Air-gap length

The experience with other types of switched reluctance motors had shown that the smaller the air-gap, the better the starting torque and running performance. This statement was confirmed also by linear analysis. While it was desirable to choose an air-gap which would be commercially realistic, at the same time it was desirable to explore the potential performance of the machine as fully as possible, ie to choose a minimum realistic air-gap. A compromise size of 0.25 [mm] was therefore chosen and maintained throughout the experimental work.

5.2.5 Stator outside diameter, rotor diameter and core length

In order to fit the available frame of the 'Brook Motors' D90 induction motor the outside diameter of the stator lamination was chosen to be the same as that of the induction motor, ie $d_o = 140$ [mm]. In the light of previous experience of the switched reluctance motor and in order to facilitate the comparison of performance the core length and rotor diameter were also chosen to be the same as that of the induction motor, ie $\ell = 76$ [mm] and $d = 75$ [mm]. (Hence the values of

$d^2 \ell$ of both the switched reluctance motor and induction motor are the same.)

5.2.6 Primary to secondary turns ratio

As has been mentioned in Chapter 2, a turns ratio 1:1 is the most convenient for use since it provides not only ease of manufacture but also the high coefficient of mutual coupling which is essential. The primary and secondary coils are wound in a bifilar manner.

5.2.7 Primary to secondary copper cross-sectional area

It is possible to minimise the copper loss by appropriately dividing the available cross-sectional area of the winding between the primary and secondary coils.

Let the subscripts 1 and 2 relate to the primary and secondary quantities respectively.

The total copper loss is

$$W = I_1^2 R_1 + I_2^2 R_2 = I_1^2 R_1 + (kI_1)^2 R_2$$

where k is defined as ratio of secondary and primary rms currents.

Assuming that turns ratio is 1:1, then

$$R_1 \sim \frac{1}{A_1} \text{ and } R_2 \sim \frac{1}{A_2}$$

where A_1 and A_2 are cross-sectional areas of the primary and secondary coils respectively.

If the cross-sectional area of the winding is constant, ie

$$A_w = A_1 + A_2 = C_w', \text{ then}$$

$$\therefore \frac{1}{R_1} + \frac{1}{R_2} = C_w$$

$$\therefore R_2 = \frac{1}{C_w - \frac{1}{R_1}}$$

$$\therefore W = I_1^2 R_1 + (kI_1)^2 \frac{1}{C_w - \frac{1}{R_1}}$$

$$\therefore \frac{\partial W}{\partial R_1} = I_1^2 \left[1 - \frac{k^2}{(R_1 C_w - 1)^2} \right]$$

For minimum loss, $\frac{\partial W}{\partial R_1} = 0$, ie

$$\frac{k}{R_1 C_w - 1} = \pm 1$$

Hence

$$R_1 = \frac{1+k}{C_w} \text{ or } R_1 = \frac{1-k}{C_w}$$

$$\text{Since } C_w = \frac{R_1 + R_2}{R_1 R_2}$$

$$\therefore R_1 = (1+k) \frac{R_1 R_2}{R_1 + R_2} \text{ or } R_1 = (1-k) \frac{R_1 R_2}{R_1 + R_2}$$

$$\therefore \frac{R_1}{R_2} = \pm k$$

Taking the positive solution only

$$\frac{R_1}{R_2} = \frac{I_2}{I_1}$$

$$\therefore \frac{A_1}{A_2} = \frac{I_1}{I_2},$$

ie for the minimum copper loss, the cross-sectional area of the winding should be split between primary and secondary coils as the ratio of primary and secondary rms currents.

It will be assumed, according to linear analysis that the ratio I_1/I_2 is about 2 at the operating conditions around base speed and full power.

5.2.8 Number of turns per phase

Having chosen the dimensions of the magnetic circuit, the number of turns per phase is deduced from the requirement that the machine should

develop constant power throughout the speed range from the base speed $n_B = 750 \left[\frac{\text{rev}}{\text{min}} \right]$ to the top speed $n_T = 2250 \left[\frac{\text{rev}}{\text{min}} \right]$ at constant supply voltage $V = 150 \text{ [V]}$.

The calculations are based on the requirement that the peak flux density at base speed and full torque (the most onerous condition) does not exceed value of $B_{\text{max}} = 2.0 \text{ [T]}$.

The corresponding control diagram for such a case is given in Fig 4.15 of Chapter 4. The diagram recommends that the conduction angle at top speed be fully open, i.e. $\theta_{\text{con}}^{(T)} = \frac{\phi}{2} = 30^\circ$, and at base speed $\theta_{\text{con}}^{(B)} = 18^\circ$.

The ratio of peak flux-linkages at base and top speed is given by

$$\frac{\hat{\psi}_B}{\hat{\psi}_T} = \frac{V \theta_{\text{con}}^{(B)} / \omega_B}{V \theta_{\text{con}}^{(T)} / \omega_T} = \frac{\omega_T}{\omega_B} \frac{\theta_{\text{con}}^{(B)}}{\theta_{\text{con}}^{(T)}}$$

and for $\omega_T / \omega_B = 3$ and $\theta_{\text{con}}^{(B)} / \theta_{\text{con}}^{(T)} = 30^\circ / 18^\circ$ it is equal to 1.67. This result is close to $\sqrt{\omega_T / \omega_B} = \sqrt{3}$ which indicates that the torque is approximately proportional to the square of the flux (since at constant power $T_B / T_T = \omega_T / \omega_B$).

The peak flux-linkage at top speed (neglecting winding resistance) is

$$\begin{aligned} \hat{\psi}_T &= V \frac{\theta_{\text{con}}^{(T)}}{\omega_T} \\ &= 150 \frac{\pi/6}{2250\pi/30} = 0.333 \text{ [Wb]} \end{aligned}$$

The peak flux-linkage at base speed is

$$\begin{aligned} \hat{\psi}_B &\approx \hat{\psi}_T \sqrt{\frac{\omega_T}{\omega_B}} \\ &= 0.333 \sqrt{\frac{2250}{750}} = 0.577 \text{ [Wb]} \end{aligned}$$

$\hat{\psi}_B$ may be taken to be approximately the product of the number of turns per phase, the maximum peak flux density in the stator pole root (where flux distribution is approximately uniform) and the cross-sectional area of the stator pole. This cross-sectional area is

$$A_{Fe} = \ell d \sin \frac{\theta}{2}$$

$$= 0.076 \times 0.075 \times \sin \frac{20^\circ}{2} = 9.9 \times 10^{-4} \text{ [m}^2\text{]}$$

and

$$\hat{\psi}_B = N B_{\max} A_{Fe}$$

$$\therefore N = \frac{\hat{\psi}_B}{B_{\max} A_{Fe}}$$

$$= \frac{0.577}{2 \times 9.9 \times 10^{-4}} \approx 290$$

ie each stator pole will have 145 turns.

5.2.9 Wire diameter

Having found the required number of turns the wire size can be selected. The cross-sectional area of the winding is given by an expression derived in Appendix 5A, ie

$$A_w = k_1 \left[\frac{d}{d_0} - k_2 \left(\frac{d}{d_0} \right)^2 \right] d_0^2$$

$$= 0.0597 \left[\frac{0.075}{0.140} - 1.328 \left(\frac{0.075}{0.140} \right)^2 \right] \times 0.14^2 = 1.8 \times 10^{-4} \text{ [m}^2\text{]}$$

The total cross-sectional area available for one turn of both primary and secondary coils is

$$a_w = \frac{A_w}{N/2} = \frac{1.8 \times 10^{-4}}{145} = 1.24 \times 10^{-6} \text{ [m}^2\text{]}$$

From Section 5.2.7 the ratio of the primary and secondary cross-sectional area per turn should be equal to the ratio of the primary and secondary rms currents, ie

$$a_1 + a_2 = a_w \text{ and } \frac{a_1}{a_2} = \frac{I_1}{I_2}$$

Assuming that the ratio of the primary and secondary currents is 2:1, then this condition is conveniently satisfied by winding the poles with 3 strands of the same wire gauge and connecting two in parallel

for the primary coil. The wire size which fills the winding area as completely as is practicable with the required number of turns is 0.50 [mm].

5.2.10 Primary and secondary coil resistances

The mean length of turn

$$l_1 = 2(\ell + Kd)$$

where K is defined in Appendix 5A.

The wire length per phase is therefore

$$Nl_1 = 2N(\ell + Kd)$$

The primary and secondary resistances per phase are then

$$R_1 = \rho \frac{2N(\ell + Kd)}{s_1}$$

$$R_2 = \rho \frac{2N(\ell + Kd)}{s_2}$$

where s_1 and s_2 are primary and secondary copper cross-sectional areas per each turn respectively.

For the D90 4-phase experimental motors these resistances are

$$R_1 = 2.8 [\Omega] \text{ and } R_2 = 5.6 [\Omega] \text{ at } 20^\circ\text{C.}$$

5.3 Motor Assembly

5.3.1 Stator assembly

The stator laminations were machined by milling and bonded together with epoxy-resin adhesive (Araldite) forming the stator core which was inserted in the preheated aluminium frame.

The primary and secondary coils for each pole were wound in bifilar manner forming a pole winding. The pole windings were inserted over the poles and held in place by slot covers. Although both ends of both coils on each phase were brought out to the terminal block, this

was for convenience in laboratory tests and would not be necessary in a commercial version, since many connections could be made internally.

5.3.2 Rotor assembly

The rotor laminations were machined by milling and bonded together with Araldite forming the rotor core which was pressed onto a mild steel shaft and mounted in between two ball bearings.

5.3.3 Rotor-position sensor

It is not necessary to describe its operation in detail in this chapter but it may be noted that it resolves rotor position to within 15° up to a speed of approximately $350 \left[\frac{\text{rev}}{\text{min}} \right]$ and, above that speed, resolves to 0.25° by means of a pulse counting technique.

5.3.4 Complete assembly

Fig 5.3 shows the component parts of the machine before assembly. The general simplicity of the machine and, in particular, the simplicity of the rotor should be noted. It had been decided to force ventilate the machine by the compressed air supply in the laboratory. The connections to the rear end-frame for the air line can be seen in Fig 5.3.

The design details of D9QM1 motor are given in Table 5.1.

A. LAMINATIONS

Material:	Losil	1000-65
Stator:	Pole No	8
	Pole Arc	20 ^o
	Window Area (Gross)	0.002213 m ²
	Iron Area	0.00876 m ²
Rotor:	Pole No	6
	Pole Arc	26 ^o
	Iron Area	0.00336 m ²
Core Length	0.0762 m	
Volume of Iron	742.7 x 10 ⁻⁶ m ³	
Weight (Calc)	5.79 kg	

B. WINDINGS

	PRIMARY COIL	SECONDARY COIL
Turns/Pole	145	145
Diameter	2 x 0.5mm	1 x 0.5mm
Enamel and Grade	Lewkanex Gr2	Lewkanex Gr2
Actual Cu Area/Coil Side	56.94mm ²	28.47mm ²
Resistance at 20 ^o C	2.82Ω	5.66Ω

C. INSULATION

Nomex liners without cuffs
Slot covers of a hard fibreglass material
Intercoil connections sleeved with acrylic sleeving
Stator not impregnated

TABLE 5.1 Design Details of D90M1 Motor

5.4 Inductances

5.4.1 Method of measurement

The inductance (or flux-linkage) is of great importance in the switched reluctance motor because its variation with rotor position characterises the whole behaviour of the motor and therefore its accurate evaluation is of significant importance. Unfortunately, its evaluation (whether by calculation or measurement) is complex task because of leakage paths, mutually coupled short-circuits (eddy-current paths) and particularly because of the non-linear characteristic of iron.

Among four different methods investigated in Reference No 1, the integration method, which uses a search coil, gives the most accurate results for inductance (provided that a good integrator is available and the search coil is very tightly coupled with the main coil), because it eliminates the effects of eddy-currents and winding resistance. In the case of the experimental motor the bifilar-wound secondary coil is ideally suited for use as a search coil, with a coupling coefficient very close to unity.

The integration method makes use of the fact that when a known steady dc current is reversed in a main (primary) coil, the integrated voltage of a closely coupled search (secondary) coil is a measure of the flux-linkage in the primary coil.

The equipment was connected as shown in Fig 5.4. The changeover switch S2 was incorporated to allow demagnetisation of the magnetic circuit of the motor before taking each reading. Before opening the switch S1 the current from the dc current supply must be decreased to zero. Switch S3 and the $1\text{[m}\Omega\text{]}$ resistor allowed the integrator to be reset before taking each reading.

Calibrated equipment combined with the use of an accurately calibrated digital voltmeter to measure the integrator output voltage, ensured that the overall accuracy of the measurements was about 1%.

5.4.2 Results of measurement

The photographs shown in Figs 5.5 to 5.7 show the ψ - i relationships when a primary coil of the D90M1 motor was supplied with ac current. Fig 5.5 was taken with the rotor in the minimum inductance position (L_0), the peak current set at 12[A]. No significant saturation can be observed. This is in sharp contrast with the ψ - i relationships shown in Fig 5.6, for which the rotor was in the maximum inductance position (L_i). Saturation occurs at approximately 2[A]. The extreme non-linearity of the system is seen in the 6[A] and 12[A] curves. Fig 5.7 shows the ψ - i relationships with the rotor in the mean position of L_0 and L_i . Saturation occurs at approximately 3[A].

The $\psi(\theta, i) \Big|_{\theta=\text{const}}$ curves of the motor obtained from measurements by the integration method are shown in Fig 5.8 for a variety of rotor angles. These can be replotted as $\psi(\theta, i) \Big|_{i=\text{const}}$ curves (Fig 5.9) or $L(\theta, i) \Big|_{i=\text{const}}$ curves (Fig 5.10).

The measurements of minimum and maximum inductances were repeated for each phase with each of the six rotor poles. The repeatability of readings showed that the symmetry of the machine was very good. (The maximum deviations were 1.5[%] and 1.1[%] at minimum and maximum inductance positions respectively.)

5.4.3 Observations on the shape of the $L(\theta, i) \Big|_{i=\text{const}}$ curves

The first effect to be observed is that of the large change in inductance with current at angles other than those near the centre of the minimum inductance region (eg when the current changes from 1 to 14[A] the maximum inductance changes from 166 to 44.6 [mH] respectively).

The second effect is related to the fringing flux between stator and rotor poles. The 'ideal' inductance curve can conveniently be considered as being composed of two components. The first component (Fig 5.11(a)) is a constant value, L_0 , which has been defined as the minimum inductance corresponding to the position when a rotor interpolar axis coincides with a stator pole axis (the value of L_0 has been estimated in Chapter 3). The second component (Fig 5.11(b)) depends only

on the inductance of the air-gap in the area of overlap between the poles. This component is rotor position dependent. The total ideal inductance curve is the sum of these two components (Fig 5.11(c)). The use of such a curve is explored in Chapter 7.

When the rotor is set to a position of minimum inductance, the fringing field from the excited stator pole is symmetrically distributed between two adjacent rotor poles. As the rotor moves in either direction, the fringing becomes non-uniform. Since the inductance is a non-linear function of fringing, the net effect is to increase the first component of the ideal inductance curve as the point of overlap approaches (Fig 5.11(d)). As soon as overlap occurs the pole surfaces over which fringing takes place is reduced (because the flux in the air-gap is considered to be a separate component) so the first component of inductance falls from the peak which it has reached at 0° . At the position where the poles are aligned ($\theta = s$) fringing is still present so the first component of the ideal inductance curve is increased by that amount. The shape of the curve between $\theta = 0$ and $\theta = s$ is deduced from measured results. The total of the components is shown in Fig 5.11(e). Note that the slope of the actual curve is rather less than the constant value of the ideal curve in the region $0 < \theta < s$. On the other hand, the change in inductance during the nonoverlap period will give rise to torque production in this region. (This is confirmed by static torque tests - see below.)

When a dead zone is introduced, the initial part of the curve is unchanged (compare Figs 5.11(g) and (i)). At $\theta = s$, there is an increase in inductance because of the shorter fringing paths to the rear of the rotor pole face (compare Figs 5.11(h) and (j)). The inductance will continue to rise until the symmetrical position $\theta = s + \frac{r-s}{2}$ is reached (Fig 5.11(f)). It will be seen by comparing Figs 5.11(e) and (f) that the introduction of a dead zone has effectively increased the slope of the $L(\theta, i) \Big|_{i=\text{const}}$ curve, at least towards its peak, if not at lower values.

Due to the fringing the 'effective' stator pole arc is altered. If, for arbitrary comparison, the distance between 105% L_0 and 95% L_i is measured on various curves (Fig 5.10), the 20° stator pole arc appears

to be:

$$\text{at } 1[A], s_{\text{eff}} = 21.1^\circ$$

$$\text{at } 4[A], s_{\text{eff}} = 18.9^\circ$$

$$\text{at } 14[A], s_{\text{eff}} = 16.1^\circ$$

This indicates that at higher currents the 'effective' stator pole arc decreases, ie the effective dead zone increases, and therefore the initially chosen dead zone may need to be reduced in order to balance the increase due to the fringing.

5.4.4 Observations on the shape of the $\psi(\theta, i)|_{\theta=\text{const}}$ curves

Several important points may be noted from a study of the $\psi(\theta, i)|_{\theta=\text{const}}$ curves of Fig 5.8.

- i) The curves below 2[A] are linear, ie there is neither main circuit nor local saturation.
- ii) Consider the curve which corresponds to maximum inductance position ($\theta=23^\circ$). In this position there is no 'local saturation', hence the non-linearity in the curve is due to 'main magnetic circuit saturation' which becomes significant at 300 [mWb]. It therefore follows that to see effects of local saturation in isolation from main magnetic circuit saturation, the curves below 300 [mWb] must be studied.
- iii) It can be observed that local saturation has its greatest effect at small overlap angles. If the linear parts of these curves are projected on the 300 [mWb] line, the extra current required because of local saturation can be measured.
 - at 8° curve, 0.6 [A]
 - at 5° curve, 1.85 [A]
 - at 2° curve, 2.2 [A]

5.4.5 Comparison of motors

Motor	L_o [mH]		L_i [mH]		α	
	1 [A]	14 [A]	1 [A]	14 [A]	1 [A]	14 [A]
D90M1	20.4	21.0	166	42.6	8.16	2.03
D90M2-1	21.9	22.0	181	40.8	8.28	1.85
D90M2-2	21.5	22.0	180	40.8	8.37	1.85
D90M2-3	20.7	20.9	183	40.5	8.84	1.94
D90M2-3b	20.3	20.5	181	40.3	8.94	1.97
D90M2-4	19.8	19.9	180	40.2	9.09	2.02

TABLE 5.2 Summary of Inductance Measurement on the Six Motors

Table 5.2 shows the results for minimum and maximum inductances, at the extremes of the current range, for the tested motors.

The change in the ratio α (defined as L_i/L_o) illustrates the effect of saturation in the motors and indicates the need for a non-linear approach to the problem. The gradual increase in α with the changes to the rotor geometry are evident. It can be seen that the biggest reduction in L_o is obtained by reducing the rotor minor diameter to a value such that little or no flux enters this part of the rotor. The benefits are seen in the increased values of α and the consequent improvements in performance are recorded in the following sections. (This has confirmed the recommendation for the rotor profile given in Chapter 3.)

Since the D90M1 and D90M2-2 had identical magnetic geometry, the significant difference in the inductance results may be attributed to the differences in the lamination steels. The Transil steel gives a small increase in α in the unsaturated condition (2.6%) but it also gives a significant reduction in α when highly saturated (8.9%). This effect is due to the shapes of the B-H curves for the steels.

5.4.6 Mutual inductances

By supplying the primary coil of one phase and connecting the integrator to the secondary coil of another, the mutual inductance between phases may be measured. Table 5.3 shows the results of such measurements.

Mutual	Rotor Angle	I = 1 [A]	I = 6 [A]	I = 14 [A]
M_{ab} [mH]	0.5°	2.35 (6.7)	1.75 (5.7)	1.75 (6.7)
M_{ad} [mH]	45.5°	4.30 (12.3)	2.75 (8.9)	2.34 (8.9)
M_{ac} [mH]	8.0°	0 (0)	0.11 (0.1)	0.10 (0.3)

TABLE 5.3 Mutual Inductances Between Phases of D90M2-3 Motor

From the geometry of the machine, it would be expected that M_{ab} and M_{ad} would be equal and much larger than M_{ac} . The measured variations in M_{ab} and M_{ad} probably arise because the values are so small that they are difficult to measure accurately.

The inductances shown are the maximum mutual inductance for any rotor position (the average mutual inductance being much smaller) and the numbers in parentheses are the mutual inductances as a percentage of the corresponding self inductances at that rotor angle and current. The small values justify the decision, made early in the work, to ignore mutual inductances.

5.5 Static Torque

The 'static torque' is that torque developed when the rotor is stationary and is a function of rotor position and excitation current. The dependence on angle is very important as the smallest torque occurring at any angle may limit the ability of the motor to start from rest. (In contrast it is the average torque which determines the motor rating when it is running.)

5.5.1 Method of measurement and test results

The static torque developed by the motors has been recorded as a function of rotor position and excitation current. The method used is as follows. With the rotor of the test motor locked, a known, direct current is passed through the primary winding of one phase and the torque is measured on a calibrated balance. By successively re-setting the rotor in different positions, the torque/rotor angle curves may be built up. Figs 5.12 and 5.14 show the static torque curves for the D90M1 and D90M2-2 motors respectively. The static torque curves for the D90M2-2 and D90M2-3 are identical. Fig 5.13 shows the curves for the D90M2-1 motor, and Fig 5.15 shows the curves for the D90M2-4 motor.

5.5.2 Observations from the static torque curves

The two features of the static torque curves which are of most interest for starting performance are the ' ϵ -torque' value and the peak/mean torque ratio. (The ϵ -torque, T_ϵ , is defined as the maximum torque which can be developed throughout the angle ϵ with a given current. The angle ϵ has already been defined in Chapter 2 as $360/(qN_p)$. For the 4-phase machine it is 15° .) If the specification for the drive system requires constant torque from base speed down to standstill, the ϵ -torque value effectively determines the rating of the machine. For example, a machine rated at 0.75 [kW] at a base speed of $750 \left[\frac{\text{rev}}{\text{min}} \right]$ must develop 9.55 [Nm] . This value of torque is defined as the 'base torque'. Having a transducer with a simple angular resolution in the starting mode of operation (ϵ degrees), then unless the value of ϵ -torque exceeds this base torque at a given current the rating of the machine must be reduced or the current rating of the drive system must be increased. For the D90M1 motor the ϵ -torque (9.55 [Nm]) is produced at current equal to 14 [A] .

The peak/average torque ratio, on the other hand, will determine the smoothness of the drive when pulling away from the standstill condition, the lower the ratio the smoother the drive.

The effect of saturation of the magnetic circuit can be seen particularly at high currents when the rotor overlaps the stator pole by more than 5° .

It is the increasing saturation with increasing overlap, for a given current, which reduces the torque.

The beneficial effect of fringing can be seen in that it widens the torque curves, especially at high saturation levels.

5.5.3 Comparison of motors

The comparison is made in the light of the above comments.

The comparison of Figs 5.12 and 5.14 shows that the D90M1 motor with standard steel develops more torque than the D90M2-2 motor with low-loss steel (compare inductances).

The comparison of the D90M2-1 motor with parallel-sided rotor poles with the D90M2-2 motor with radial-sided rotor poles (Figs 5.13 and 5.14 respectively) shows that there is no significant difference between two motors. The static torque curve of the D90M2-3 motor with reduced rotor minor diameter is identical to the static torque curve of the D90M2-2 motor.

The comparison of the curves for the D90M2-3b motor with a reduced rotor pole arc (Fig 5.15) with the curves of the previous versions shows that a slight increase in the ϵ -torque is achieved at 14[A]. Further reduction of the pole arc (to 24° on the D90M2-4) gives no improvement.

Therefore it can be taken that the optimum rotor pole arc (for highest starting torque) lies in the region of 24° to 25.5°.

5.6 Running Performance: Base Speed to Top Speed

5.6.1 Equipment and methods

The motors were tested on the test rig which consists of a dynamometer with field current control for varying the load, an appropriate transistor switching and control unit (converter) and suitable shunts,

meters, etc. The layout of the equipment in the laboratory is shown in Fig 5.16 and the details are summarised below.

Converter

This was designed for experimental purposes. It consists of a 3-phase bridge rectifier with smoothing capacitors, switching unit (Darlington MJ10001 power transistors are used for the main switching devices) and control unit which incorporates all the electronic logic to control the switch-on and switch-off angles to $\frac{1}{4}$ (these angles being set independently).

Supply voltage

The motor was supplied by dc voltage obtained from the 3-phase bridge rectifier. This dc voltage was measured on a high quality digital voltmeter.

Mean supply current

This was measured on a calibrated shunt and moving coil ammeter (0.25% accuracy).

Peak current

High frequency co-axial shunts were connected in series with the primary and secondary coils of one phase and an oscilloscope was used to display the current waveform. The peak value of the current was recorded from the oscilloscope. The accuracy of this method is limited by the oscilloscope display.

R.M.S. current

The waveforms of currents of particular interest were recorded in one of two ways:

- i) A camera was used to photograph the waveform on the oscilloscope. The accuracy of this method is limited by the oscilloscope

display and the optical accuracy of the camera.

- ii) A more accurate but much more time consuming method is to record the waveform digitally in a transient recorder and to hard copy via a X-Y plotter.

From either of these two methods, the rms current may be determined graphically by measuring the current at several intervals on the waveform.

Torque

This was measured as the reaction of the dynamometer stator. The calibration was first checked and the accuracy estimated as 0.5% at full scale deflection.

Speed

This was measured by frequency meter counting pulses at a convenient part of the logic.

5.6.2 Test results

The full load performance of the D90M1 motor at base speed is summarised below:

Supply voltage (V)	150 [V]
Speed (n)	750 $\left[\frac{\text{rev}}{\text{min}}\right]$
Switch-on angle (θ_c)	-10.75 [$^\circ$]
Conduction-angle (θ_{con})	18.5 [$^\circ$]
Phase overlap angle (θ_o)	3.5 [$^\circ$]
Mean supply current ($I_{\text{m tot}}$)	9.0 [A]
Peak supply current (I_{tot})	18.0 [A]
Peak phase current (\hat{I})	12.5 [A]
R.m.s. primary current (I_1)	5.1 [A]
R.m.s. secondary current (I_2)	1.4 [A]
Torque (T)	9.55 [Nm]
Power output (P_{out})	750 [W]

$$\begin{aligned} \text{Power input } (P_{in} = V I_{m \text{ tot}}) & 1350 \text{ [W]} \\ \text{Efficiency* } (\eta = \frac{P_{out}}{P_{in}}) & 55.6 \text{ [\%]} \end{aligned}$$

To estimate copper loss the primary and secondary resistances were measured at operating temperature and they are $R_1 = 3.8 \text{ } [\Omega]$ and $R_2 = 7.57 \text{ } [\Omega]$.

Hence,

$$\begin{aligned} \text{Copper loss} &= 4(I_1^2 R_1 + I_2^2 R_2) = 4(5.1^2 \times 3.8 + 1.4^2 \times 7.57) = 396 + 59 \\ &= 455 \text{ [W]} \end{aligned}$$

The estimated device losses (snubbing circuits, main transistors and diodes) are 60 [W].

Hence,

$$\text{Iron loss} = P_{in} - (P_{out} + 455 + 60) = 85 \text{ [W]}$$

The error in estimating the iron loss using this method can be very large because even a relatively small error in estimating copper-loss (using the graphical method). Device losses may also cause a large error in estimating the iron loss because it is relatively small.

As was to be expected, the iR drop of this motor is relatively large and this is reflected in the copper loss and hence low motor efficiency. This is a general characteristic of small power motors and the effect is greatly diminished with increasing motor size (when per-unit resistance is much smaller). The copper loss at base speed could be reduced by altering the ratio primary/secondary copper cross-sectional area to be approximately equal to the optimum value (I_1/I_2), ie about 4:1, rather than chosen ratio 2:1. In that case dominant primary copper loss would be reduced and this would reduce total copper loss by about 7.5% and hence improve the efficiency to 58.1%.

The performance of the motor over its speed range above base speed is summarised in Fig 5.17. The individual points are marked with switch-on/conduction angles and measured efficiency.

When the motor is not working near its output limit, there is normally a range of switching angles which gives the required output. The

* This efficiency takes into account device losses.

switching angles corresponding to marked points in Fig 5.17 are around the optimum. It can be seen that the higher the speed (at constant output power) the earlier is the switch-on point and longer conduction angle. (This has already been stated in linear analysis - Section 4.5.2.).

For the sake of security against error in the converter unit the maximum conduction angle was kept below 30° . Therefore the full power at the top speed was not quite used.

The efficiency against speed curves for constant power output are shown in Fig 5.18.

The primary and secondary current waveforms for various speeds and output powers, corresponding to the points A, B, C, D, E and F in Fig 5.17, are shown in Fig 5.19. It can be seen that at base speed the rate of rise of the current increases before the switch-off point. This effect is more pronounced at larger loads. This indicates that saturation increases the current rapidly as the poles overlap.

The peak value of current at base speed ($12.5 [A]$) is close to that required to produce the base-speed torque at standstill ($14 [A]$). This means that the switching devices are being worked almost equally hard in these two conditions.

5.6.3 Comparison of motors

Table 5.4 shows the performance, at base and top speed, of the tested motors. The comparison between D90M1 and D90M2-2 motors, which have the same lamination geometry but different lamination steel, shows that the differences at base speed are very small, but the efficiency of the D90M2-2 motor is superior at top speed. In quantitative terms, the iron loss in the superior steel is smaller than in the standard steel and this results in an improvement in efficiency, particularly at top speed, which indicates that iron loss at top speed is bigger than at base speed. The benefits resulting from the use of this steel would be even greater in a larger machine where the ratio of iron loss to copper loss is greater.

Motor	$L_i/L_o i=1A$ $\times 10^{-3} H$		$L_i/L_o i=14A$ $\times 10^{-3} H$	$T_\varepsilon i=14A$ Nm	base speed $n_B=750 \frac{rev}{min}$			top speed $n_T=2250 \frac{rev}{min}$		
					θ_c/θ_{con}	P_{out} W	η %	θ_c/θ_{con}	P_{out} W	η %
D90M1	166/20.4	42.6/21.0	9.55	-10.75/18.5	750	55.6	-22.5/27.5	711	69	
D90M2-1	181/21.9	40.8/22.0	9.1	-11.25/18.75	750	56	-22.5/27.5	650	76	
D90M2-2	180/21.5	40.8/22.0	9.2	-10.75/18.5	750	56	-22.0/27.5	671	75	
D90M2-3	183/20.7	40.5/20.9	9.2	-10.50/18.5	750	57	-22.5/27.5	727	75	
D90M2-3b	181/20.3	40.3/20.5	9.3	-10.00/18.75	750	57	-22.75/27.5	746	77	
D90M2-4	180/19.8	40.2/19.9	9.3	- 8.75/18.75	750	59	-19.50/27.5	749	79	

TABLE 5.4 Summary of Performance of the Six Motors at Supply Voltage 150 [V]

The comparison of the D90M2-1 to -4 with different rotor lamination geometry shows that the D90M2-4 motor with 24° rotor pole arc and 'preferred' rotor pole geometry (defined in Chapter 3) gives the optimum performance both in running (Fig 5.20) and in starting conditions.

5.7 Graphical Prediction of Current Waveform

It is possible to graphically derive the current waveforms from the $\psi(\theta, i)|_{\theta=\text{const}}$ curves provided the function $\psi = f(\theta)$, for a given speed and switching angles, is known. This function is obtained by integrating the differential equations which describe the basic machine circuit in steady-state operation

$$+ V = Ri + \omega \frac{d\psi(\theta, i)}{d\theta}$$

In this form the solution cannot be obtained analytically and the numerical methods are necessary.

However, if the resistance is assumed to be zero then the equations become

$$\frac{d\psi}{d\theta} = + \frac{V}{\omega}$$

The flux-linkage obtained from this equation is a simple linear function of θ , and it is shown by the thick line in Fig 5.21 for the experimental full load condition at base speed $n = 750 \frac{\text{rev}}{\text{min}}$, $V = 150 \text{ [V]}$, $\theta_c = 10.75^\circ$ and $\theta_{\text{con}} = 18.5^\circ$. By projecting points from this curve onto the $\psi(\theta, i)|_{\theta=\text{const}}$ of Fig 5.8 at corresponding values of θ , the current waveform shown by the full line in Fig 5.21 is obtained. It is appropriate to compare this current waveform with the one obtained by linear analysis at the same operating conditions, because both are derived assuming that the winding resistance is zero and therefore both have the same flux-linkage waveform. The direct comparison of these waveforms shows the effect of saturation in the iron on the current waveform.

At base speed the ψ - i trajectory passes through the highly non-linear regions of $\psi(\theta, i)|_{\theta=\text{const}}$ curves (in these regions the values of inductance depend on the current) and this results in highly saturated current waveform. Therefore the linear predictions of current waveform even using widely different values of α are very far from the one which accounts the saturation effect (see Fig 5.21).

Using the same procedure the current waveform for the experimental full power condition near the top speed $n = 2195 \left[\frac{\text{rev}}{\text{min}} \right]$, $V = 150 \text{ [V]}$, $\theta_c = -22.5^\circ$ and $\theta_{\text{con}} = 27.5^\circ$, can be obtained. This is shown by full line in Fig 5.22.

At high speed the ψ - i trajectory does not pass through highly non-linear regions of the $\psi(\theta, i)|_{\theta=\text{const}}$ curves (the values of inductance do not change very much with current) and therefore the current waveform is much closer, than at base speed, to the one predicted by linear analysis when $\alpha = 8$ (this value of α corresponds to the linear region of $\psi(\theta, i)|_{\theta=23^\circ}$ curve of Fig 5.8).

Although the graphical prediction of the current waveform presented above ignores the effect of winding resistance the comparison between 'linear' and 'non-linear' current waveforms shows clearly the deficiency of the linear analysis as a means for quantitative analysis of the machine.

The comparison between graphically predicted current waveforms and the corresponding current waveforms obtained by measurements shows that the winding resistance has a high effect on the current waveform - compare Fig 5.21. with 5.19 (D) and Fig 5.22 with 5.19(F). (In Chapter 6 the effect of the inclusion of the resistance term will be demonstrated.)

5.8 Conclusions

It has been shown in this chapter that a practical switched reluctance motor can be built to meet the design requirements of $0.75 \left[\frac{\text{kW}}{\text{min}} \right]$ over the range 750 to 2250 $\left[\frac{\text{rev}}{\text{min}} \right]$ with constant torque below 750 $\left[\frac{\text{rev}}{\text{min}} \right]$. The design of the motor was based on the theoretical knowledge presented in previous chapters with the main dimensions of a commercial

induction motor (D90, 0.75 kW, 1000 $\frac{\text{rev}}{\text{min}}$).

The experimental results, which have been fully discussed, have demonstrated the real potential of this type of the motor. Saturation has been found to be very significant and consequently the method of linear analysis has been found to be unsatisfactory as a means for quantitative analysis of the machine. The method of non-linear analysis developed to meet this situation is described in the next chapter.

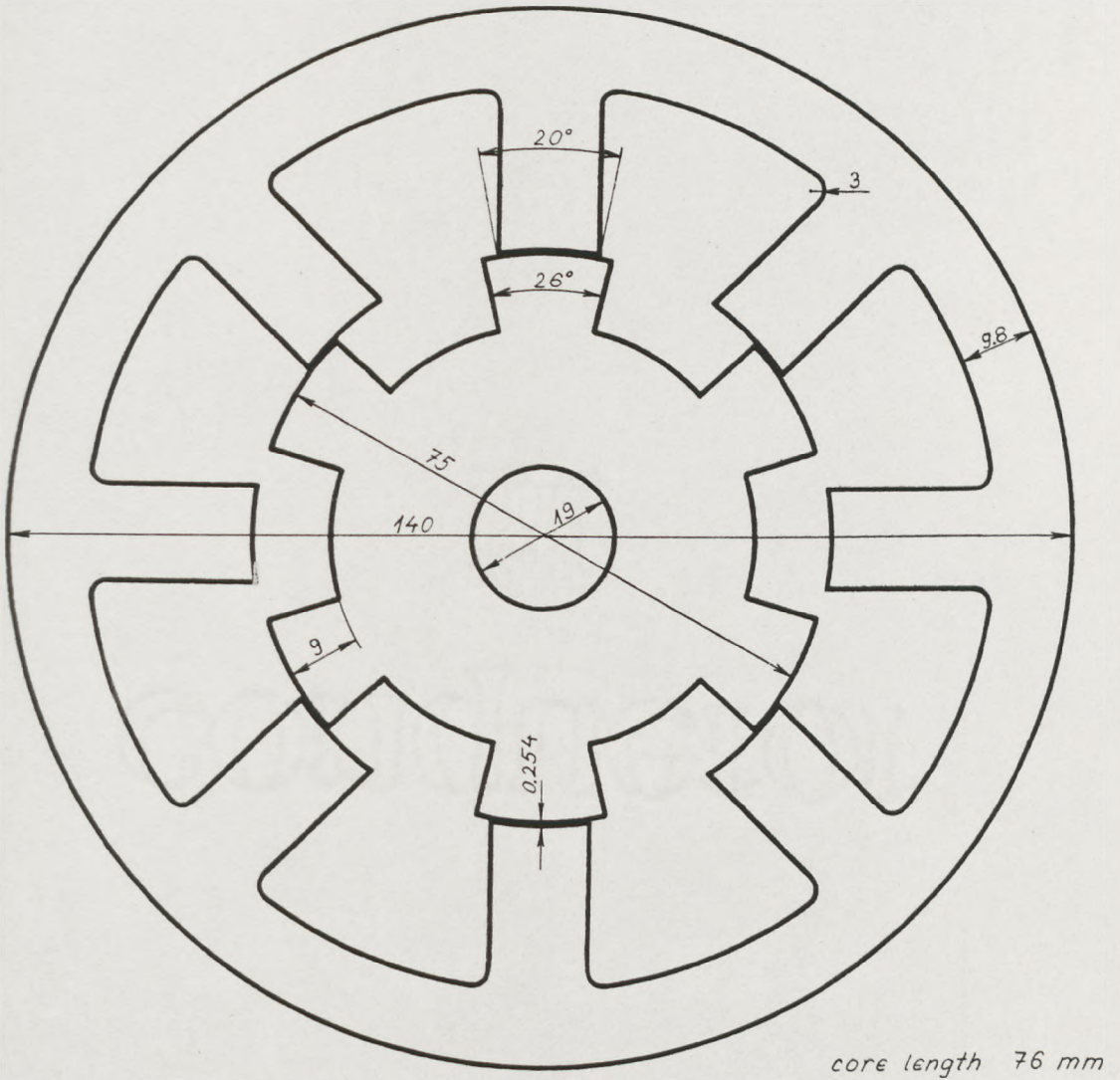


FIG 5.1 Stator and rotor laminations of D90M1 motor

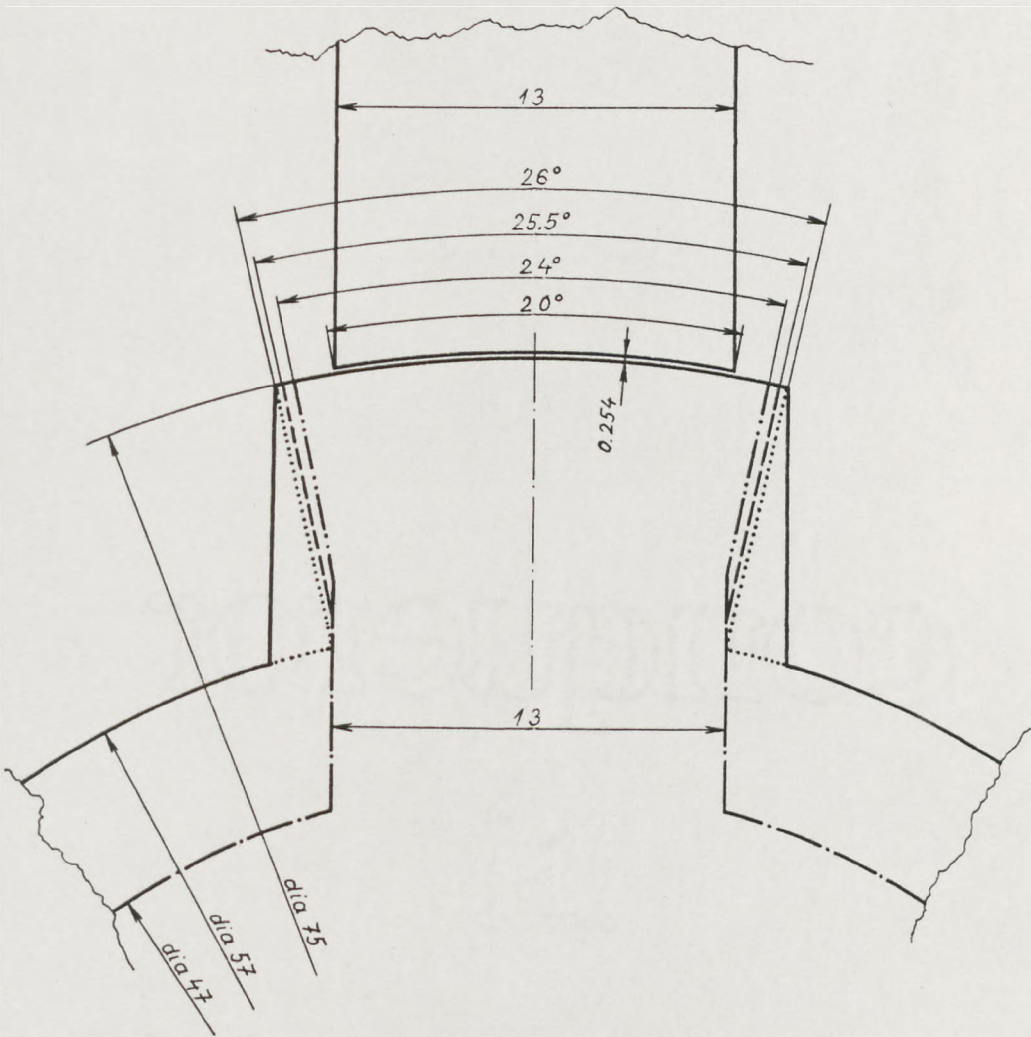
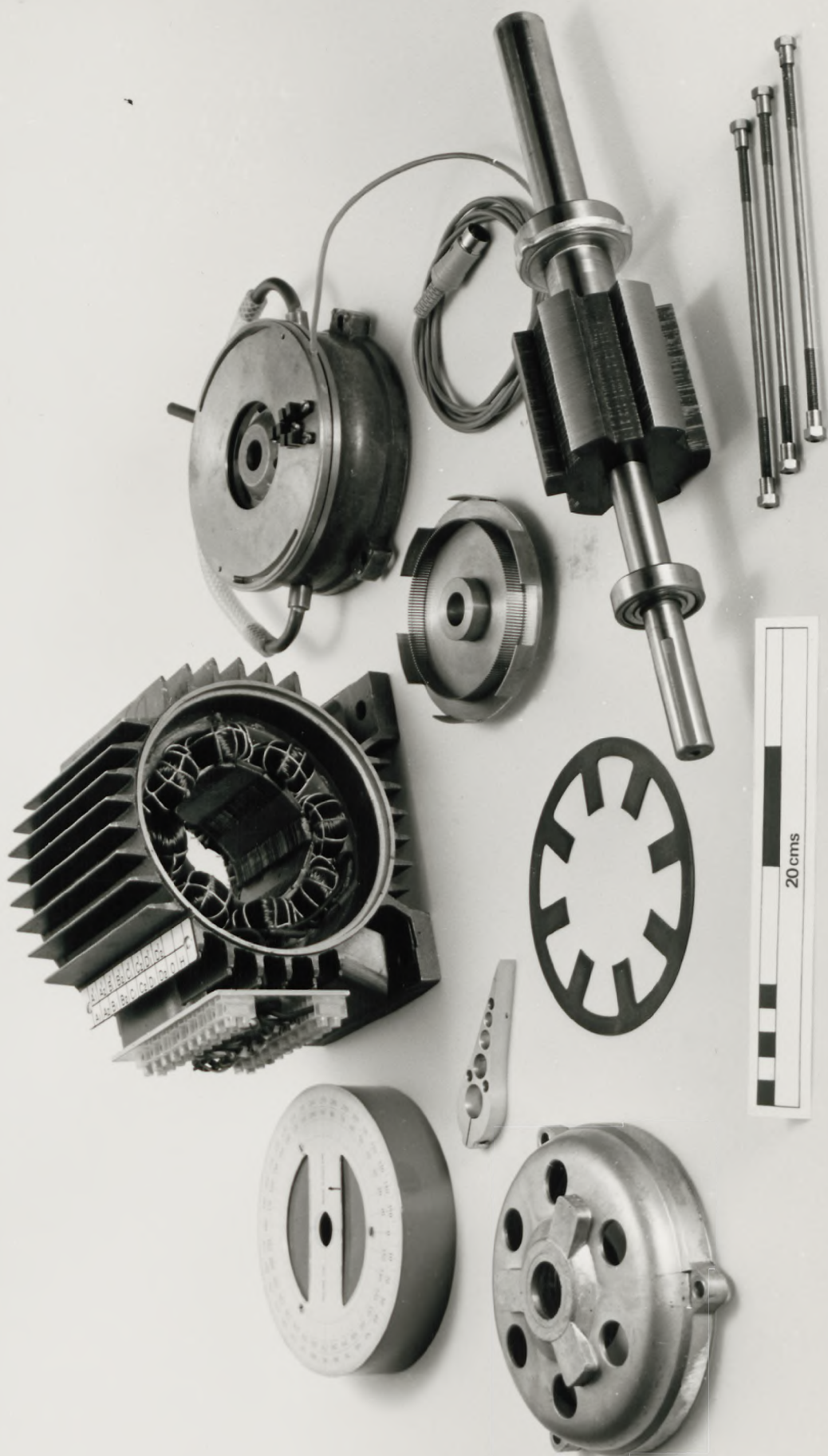


FIG 5.2 Detail of stator and rotor laminations of D90M2 motor

- Rotor 1 (parallel-sided poles, $r = 26^\circ$)
- Rotor 2 (radial-sided poles, $r = 26^\circ$)
- Rotor 3 (radial-sided poles, $r = 26^\circ$,
reduced rotor minor diameter)
- Rotor 3b (as Rotor 3 but $r = 25.5^\circ$)
- Rotor 4 (as Rotor 3 but $r = 24^\circ$)

FIG 5.3 Component parts of D90M1 machine



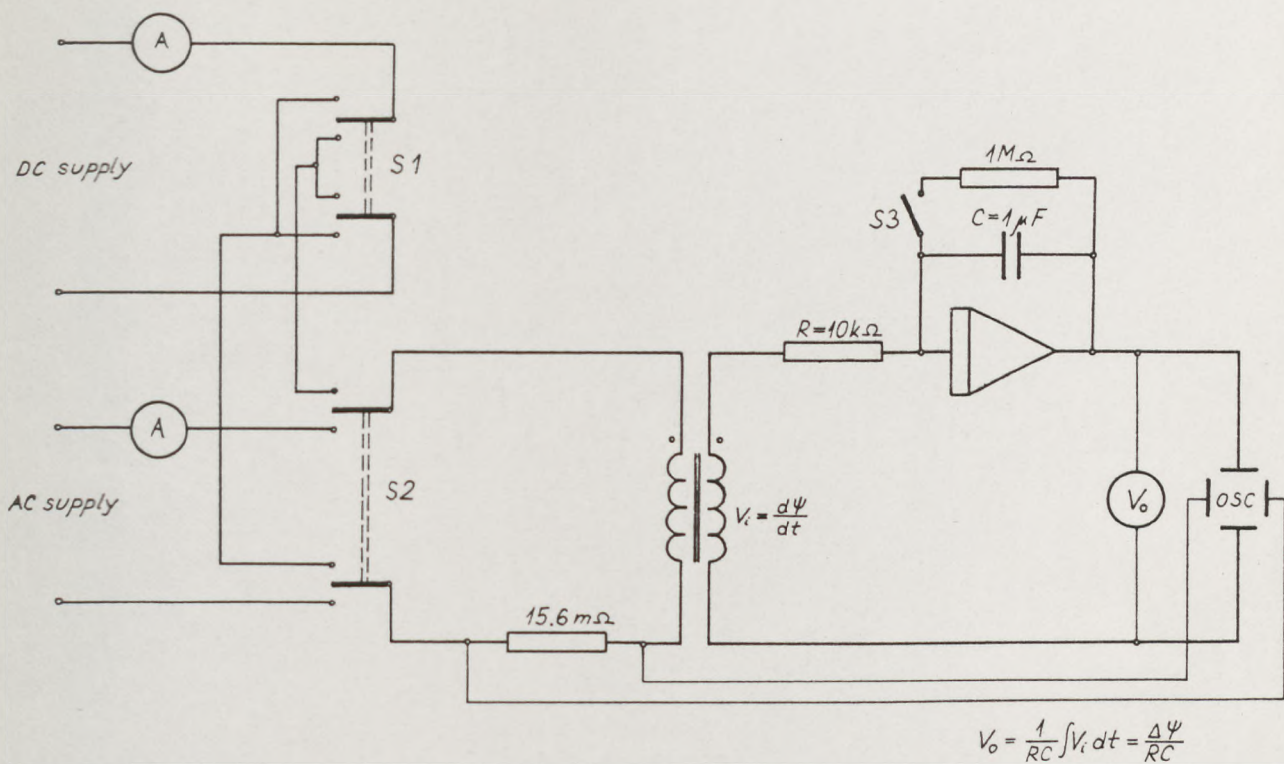


FIG 5.4 Circuit diagram for integration method of inductance measurement

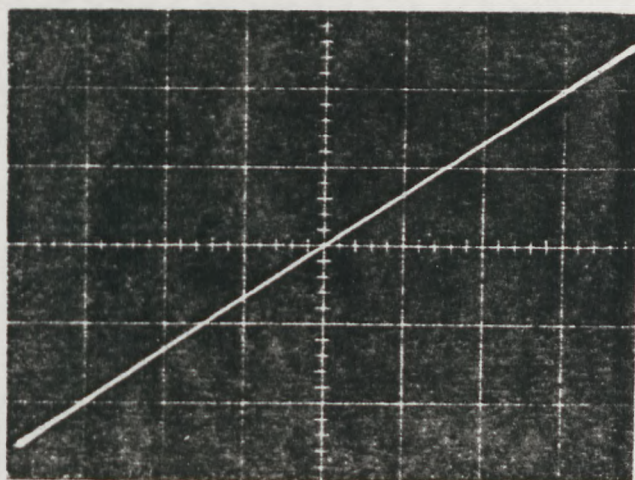


FIG 5.5 ψ - i relationship with AC excitation
 Motor: D90M1
 Rotor position: -7° (minimum inductance)
 Scale: Y-axis 0.1 Wb/div
 X-axis 3.117 Wb/div

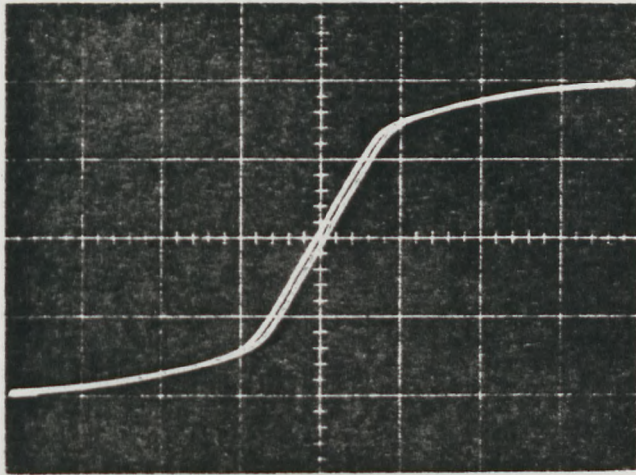
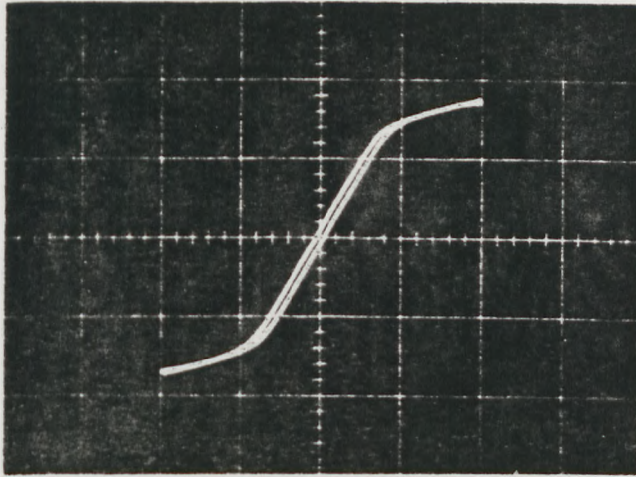
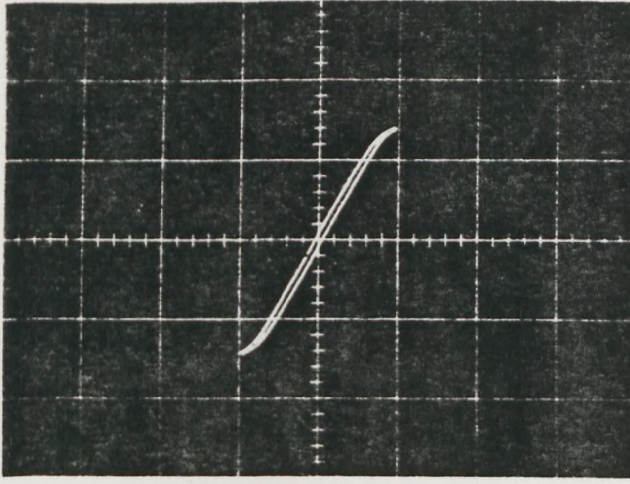


FIG 5.6 ψ - i relationship with AC excitation
Motor: D90M1
Rotor position: $+23^\circ$ (maximum inductance)
Scale: Y-axis 0.3 Wb/div
X-axis 3.117 Wb/div

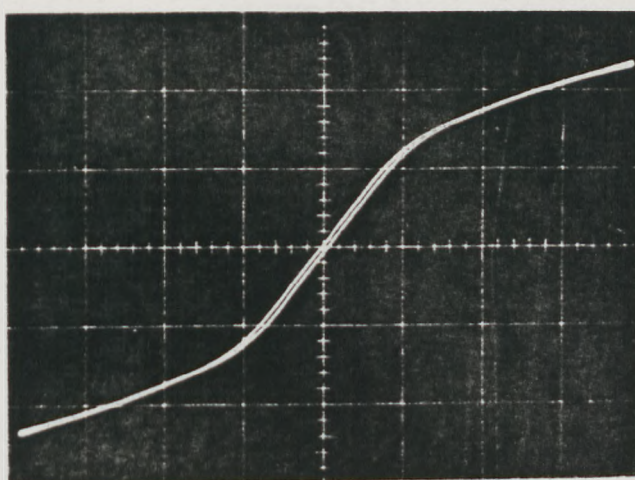
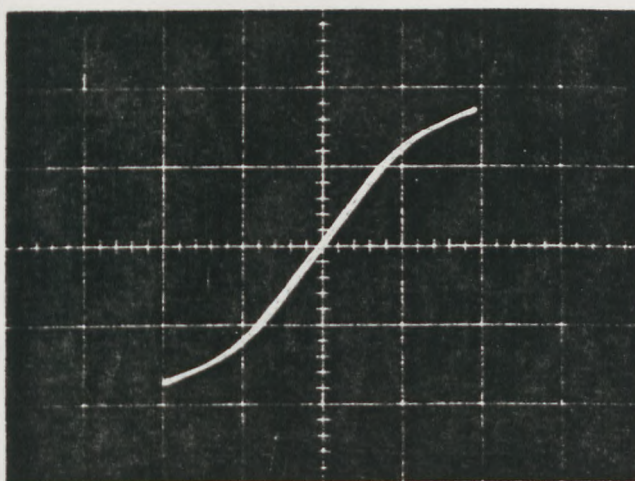
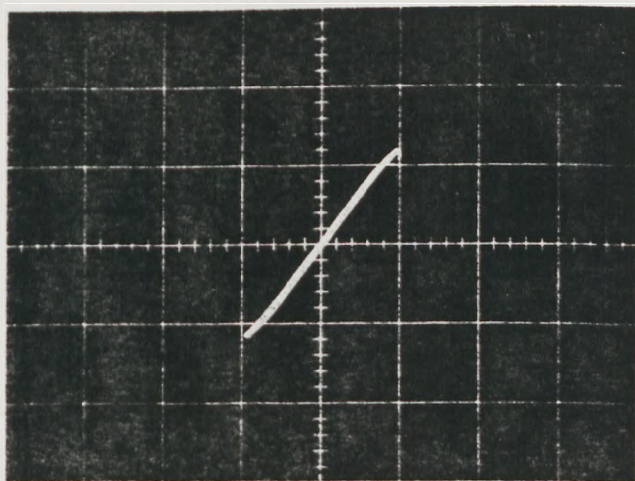


FIG 5.7 Ψ - i relationship with AC excitation

Motor: D90M1

Rotor position: $+8^\circ$ (mean position)

Scale: Y-axis 0.2 Wb/div

X-axis 3.117 A/div

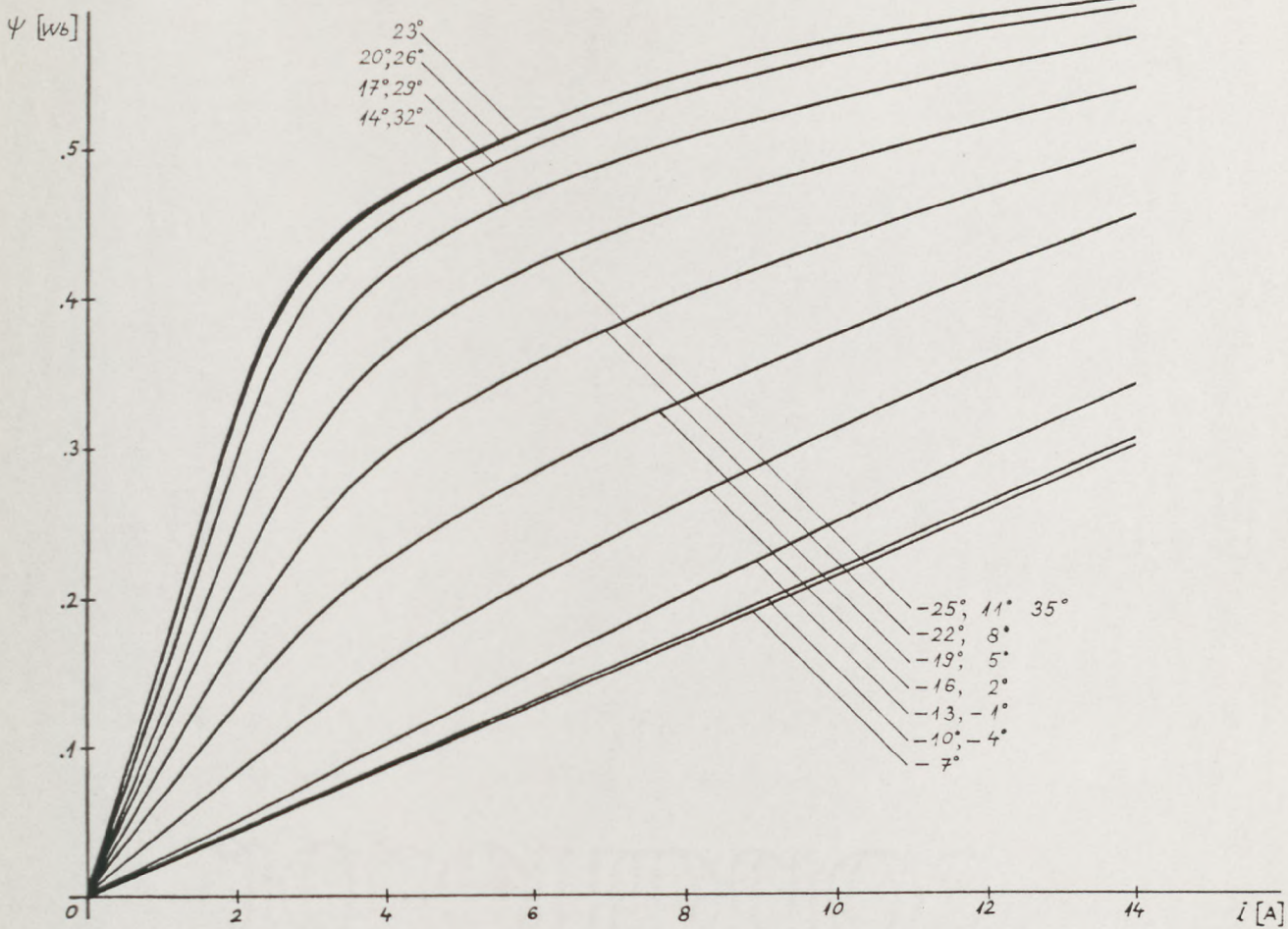


FIG 5.8 $\psi(\theta, i) |_{\theta=\text{const}}$ curves measured by integration method
Motor: D90M1

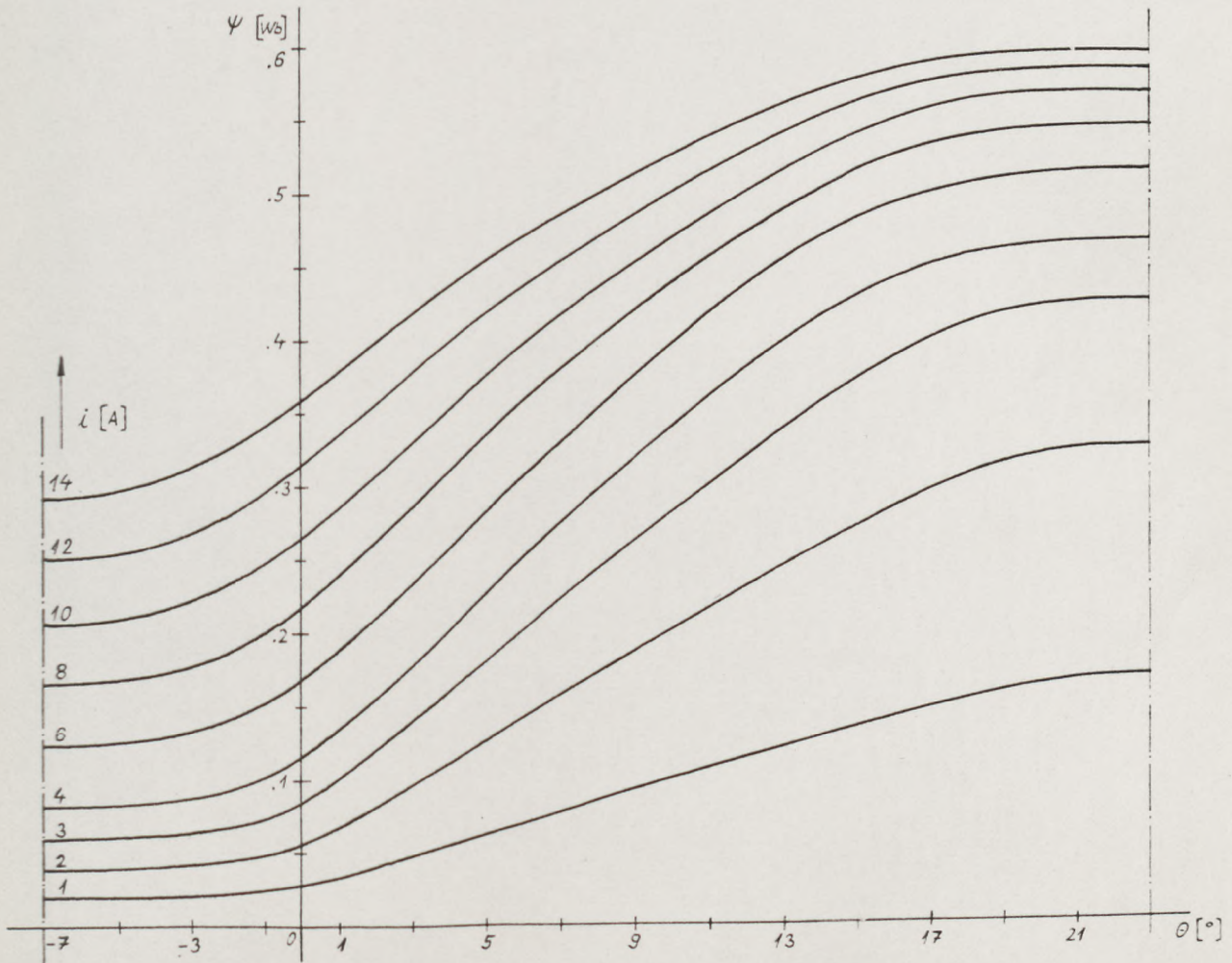


FIG 5.9 $\psi(\theta, i) |_{i=\text{const}}$ curves derived from Fig 5.8

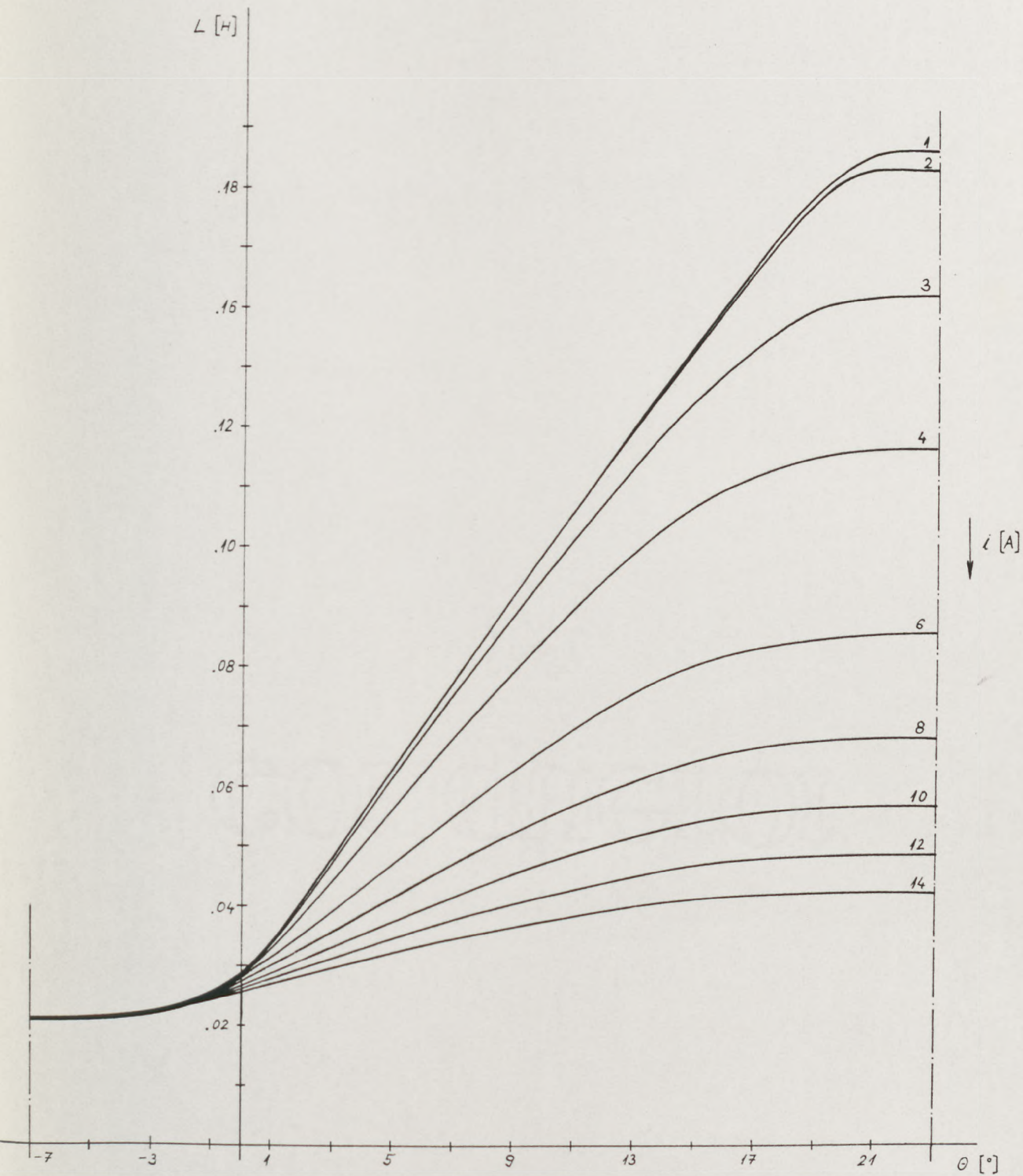
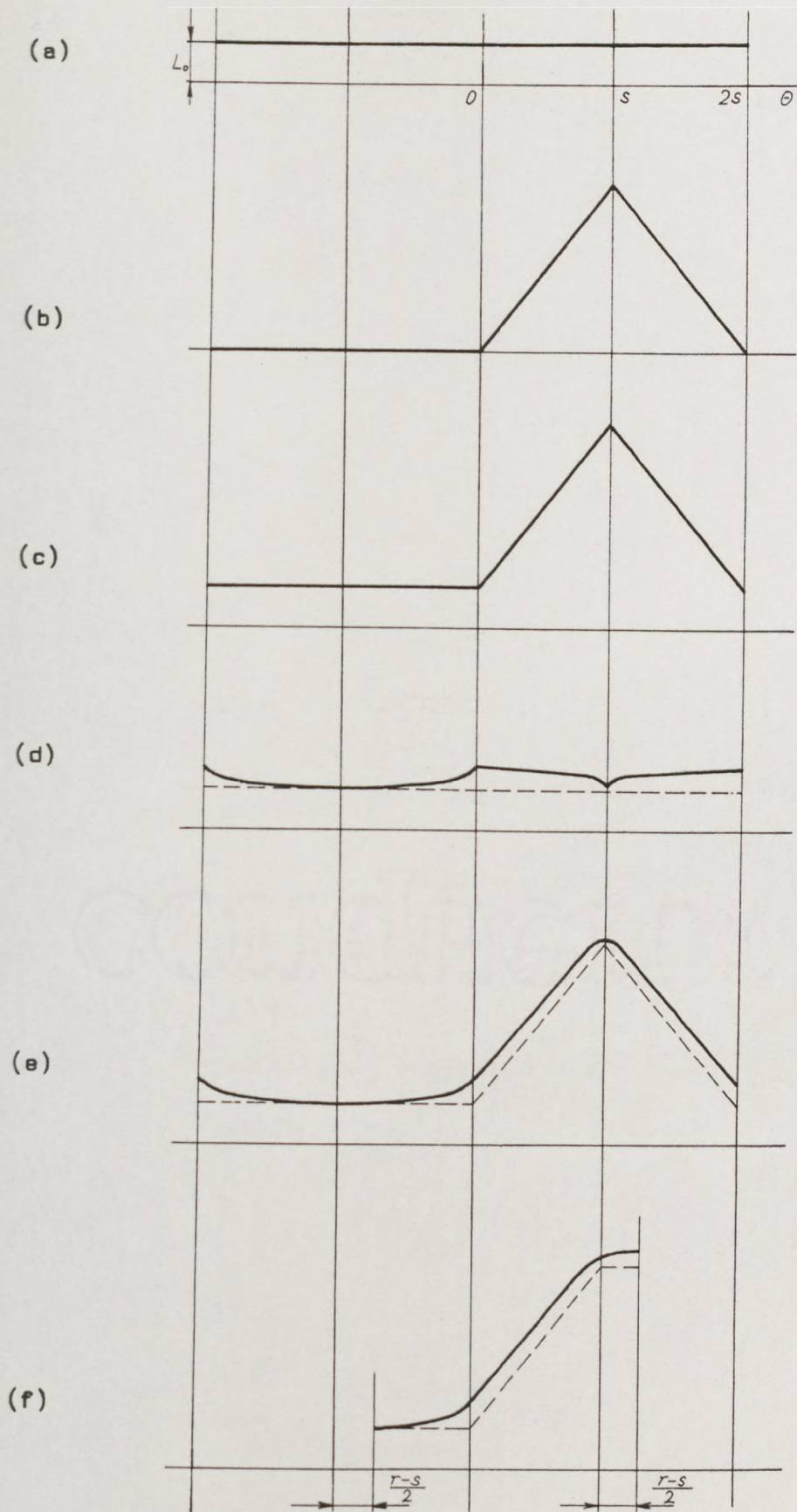


FIG 5.10 $L(\theta, i) |_{i=\text{const}}$ curves derived from Fig 5.8



Continued

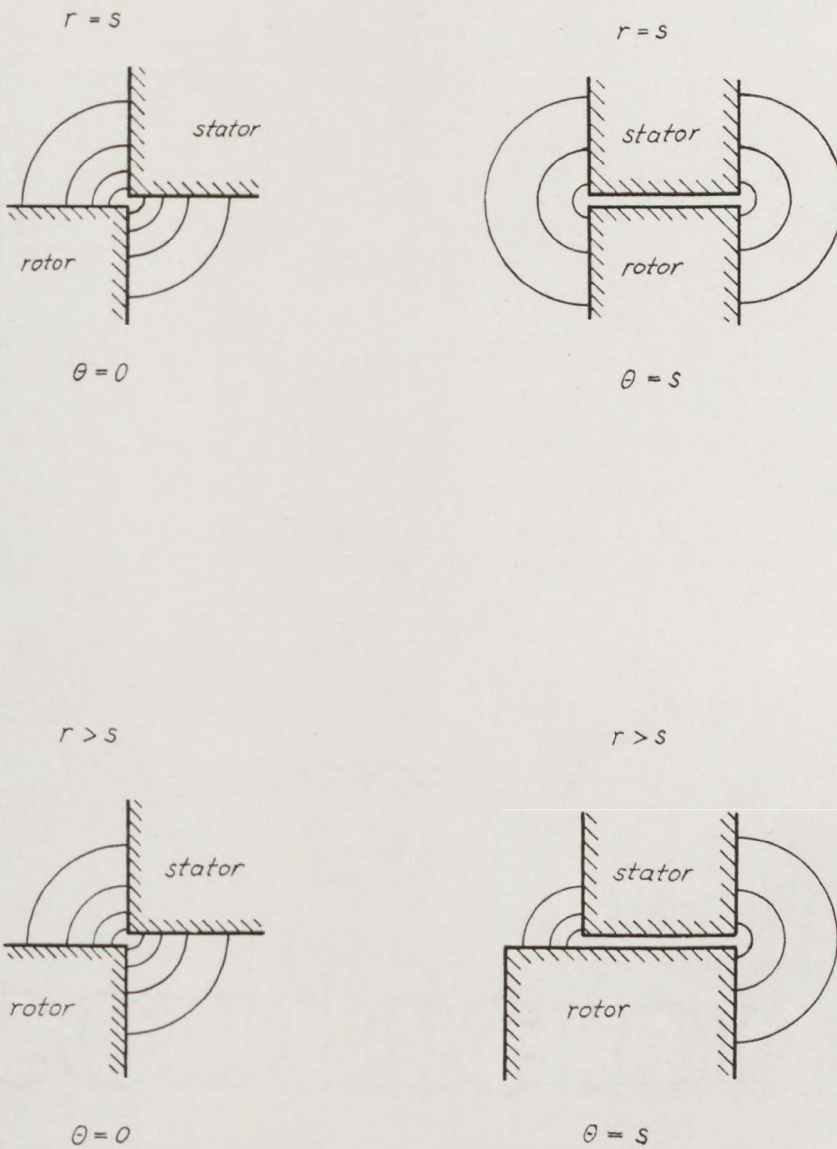


FIG 5.11 Effect of fringing flux on $L(\theta, i)|_{i=\text{const}}$ curve

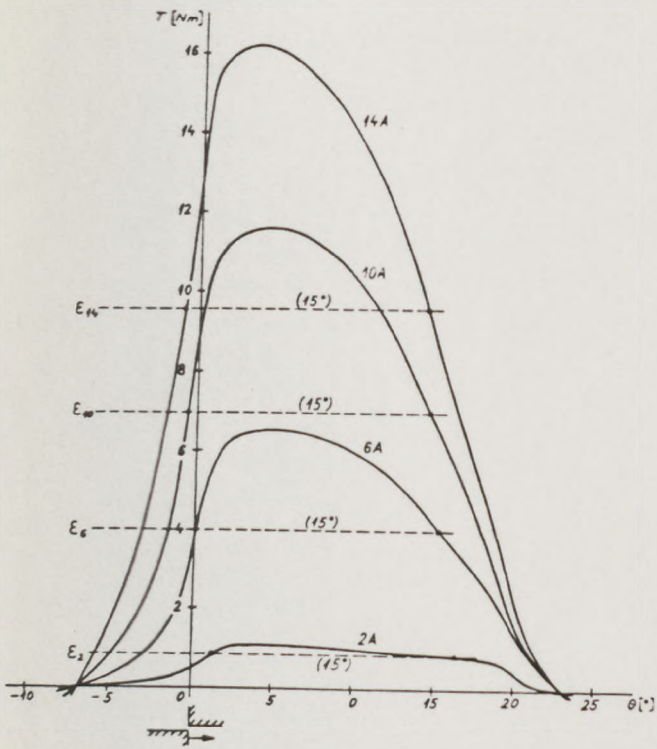


FIG 5.12 Static torque curves of D90M1 motor

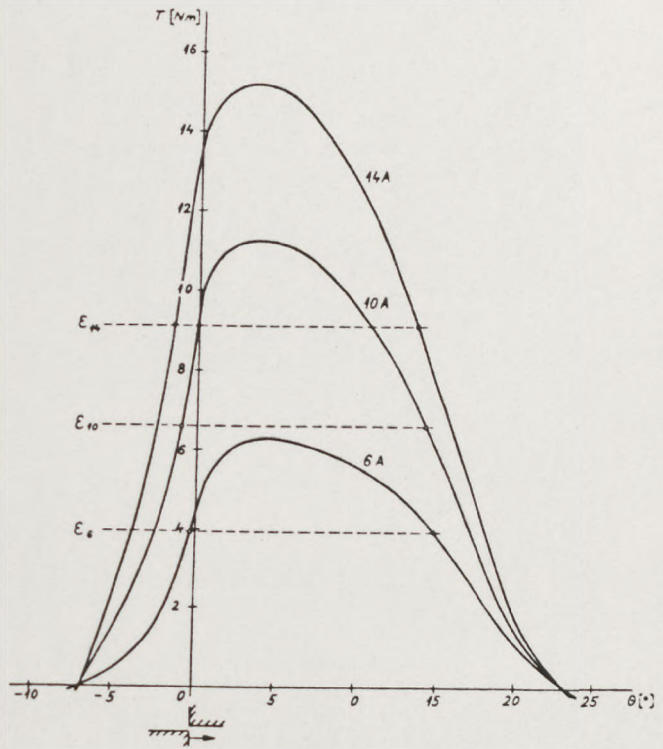


FIG 5.13 Static torque curves of D90M2-1 motor

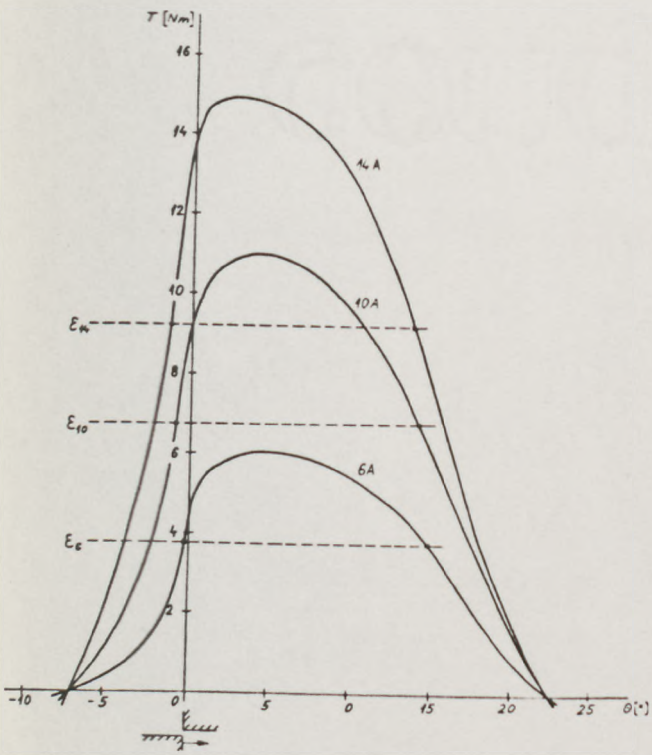


FIG 5.14 Static torque curves of D90M2-2 and D90M2-3 motors

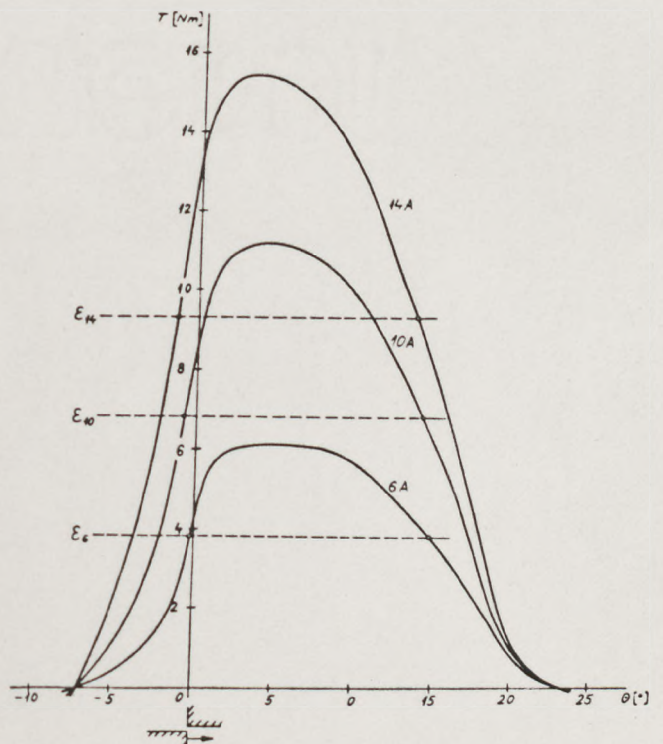
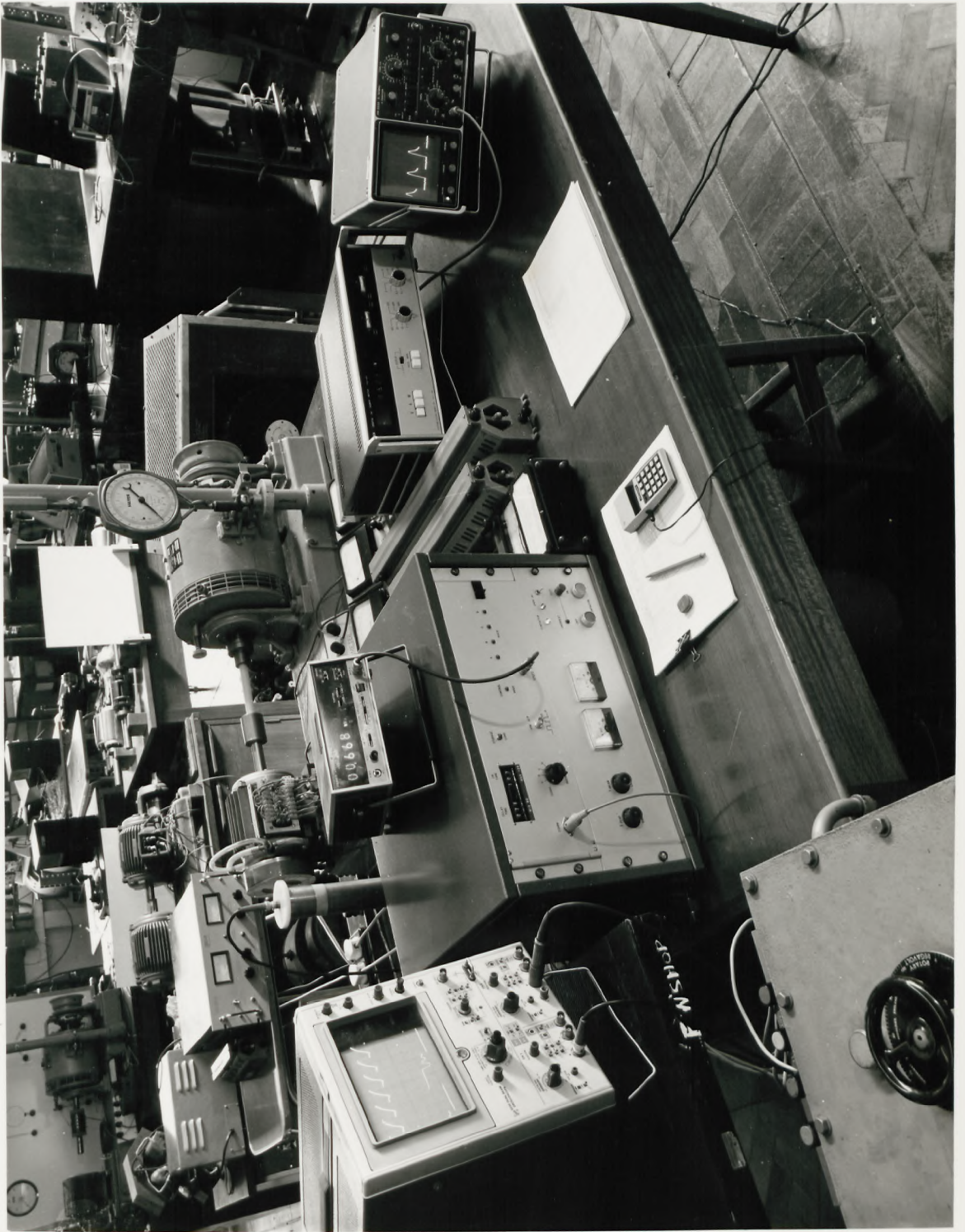


FIG 5.15 Static torque curves of D90M2-3b and D90M2-4 motors

FIG 5.16 Test equipment for D90 motors



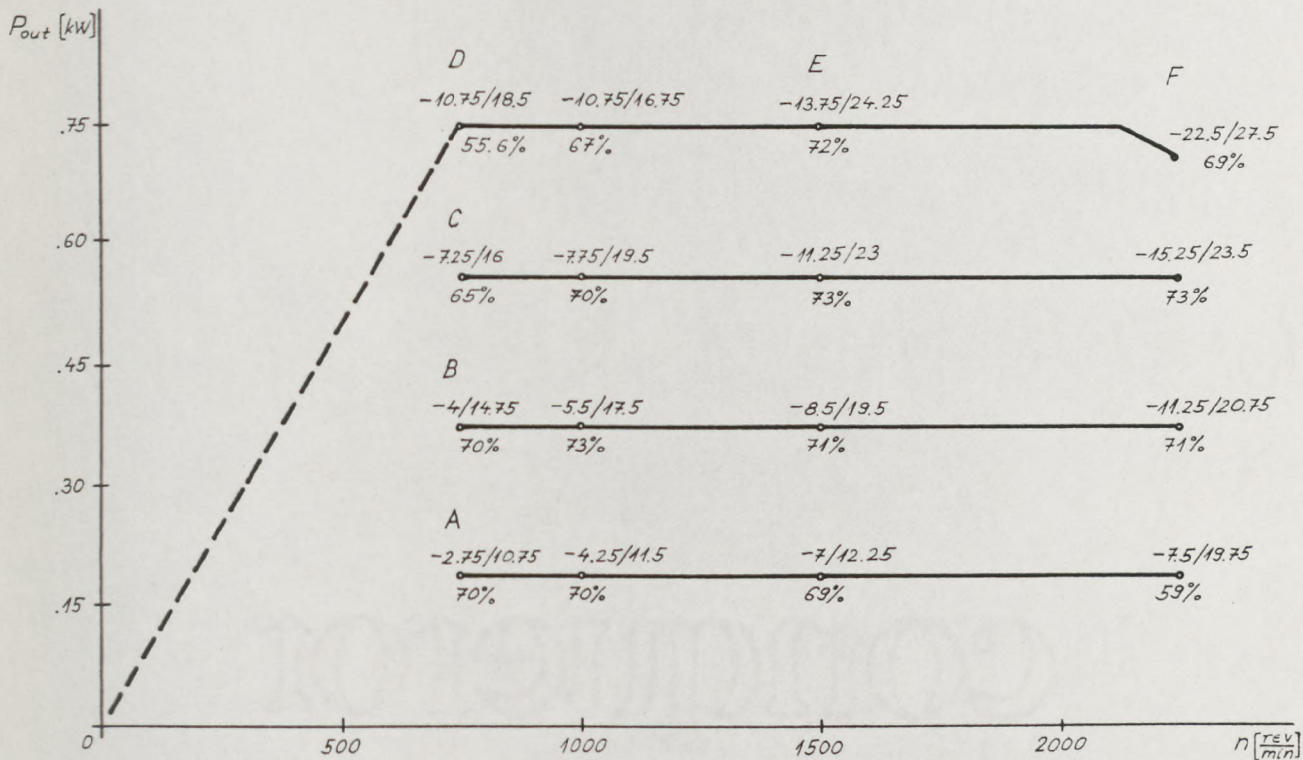


FIG 5.17 Running performance of D90M1 motor
Supply voltage: 150 [V]

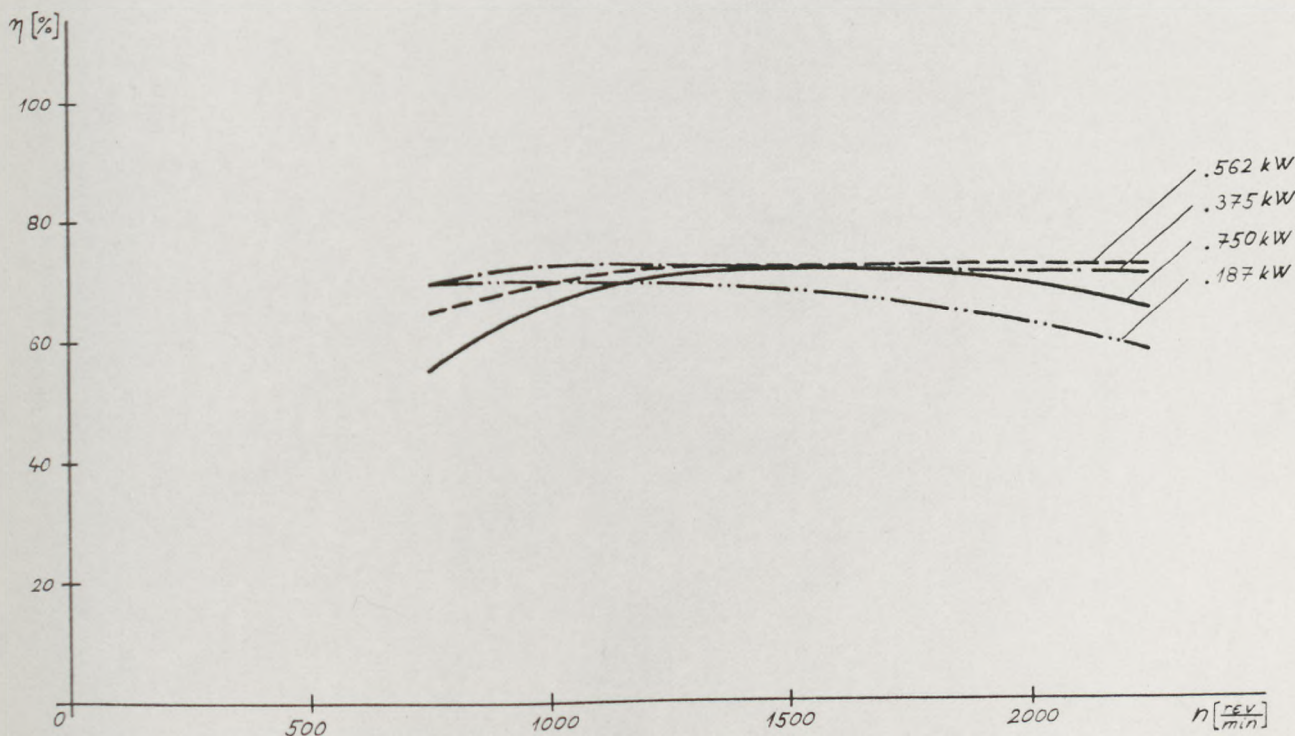
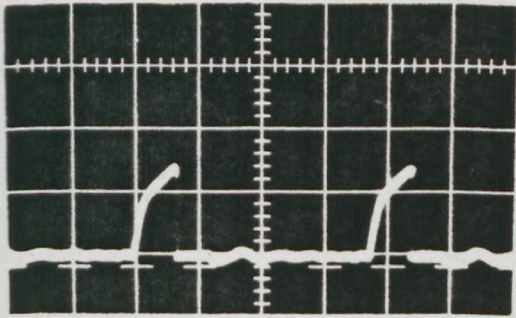
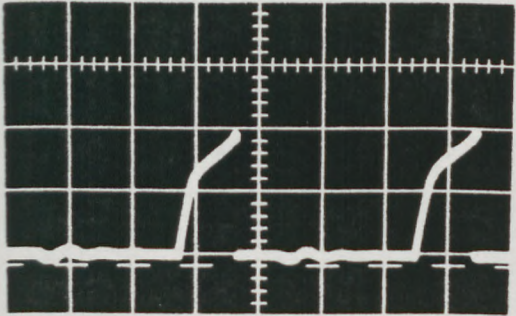
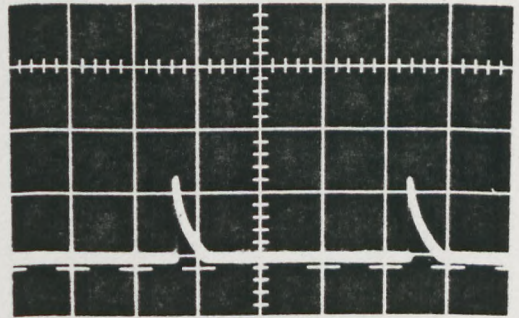


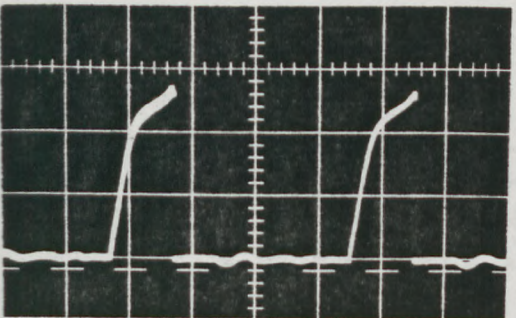
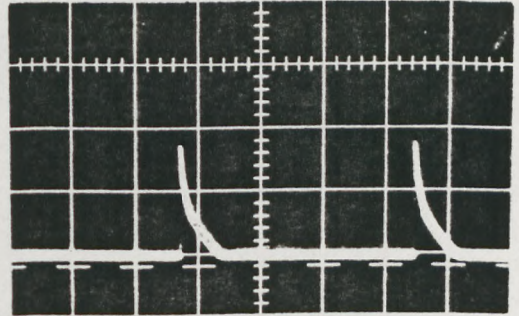
FIG 5.18 $\eta(n) |_{P_{out=const}}$ curves of D90M1 motor
Supply voltage: 150 [V]



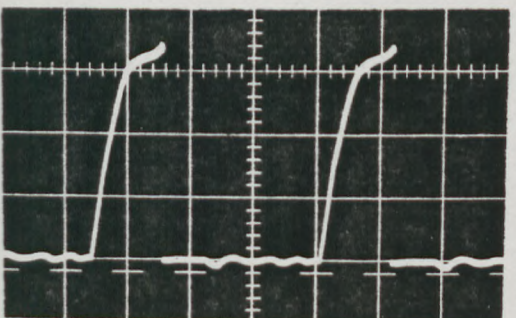
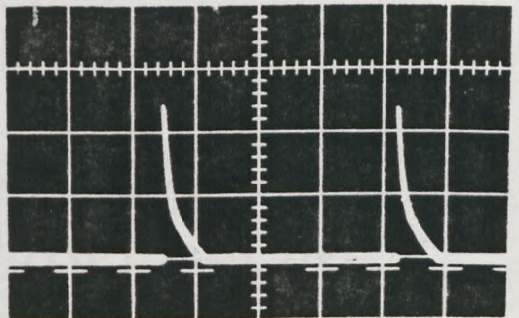
A



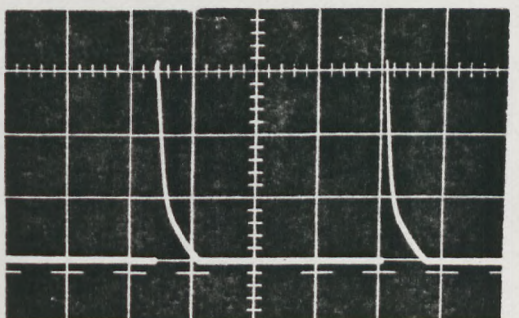
B



C



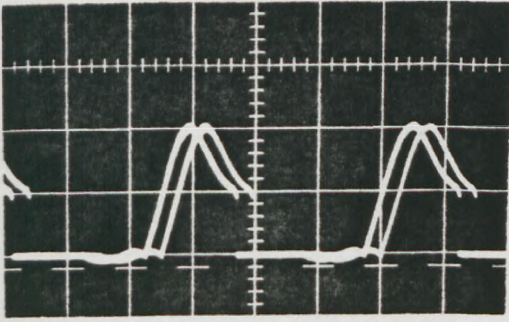
D



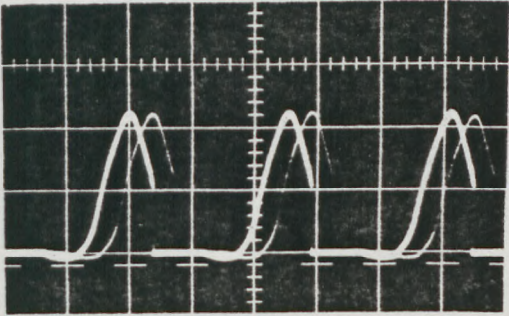
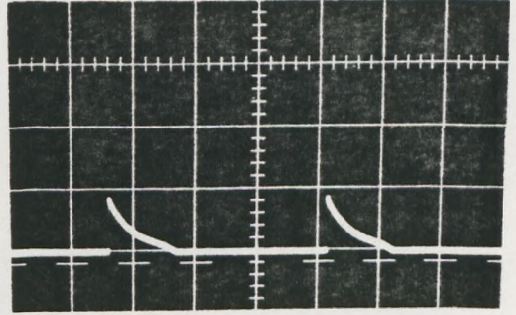
Scale: Y-axis $3.38 \frac{A}{div}$

t-axis $2 \frac{msec}{div}$

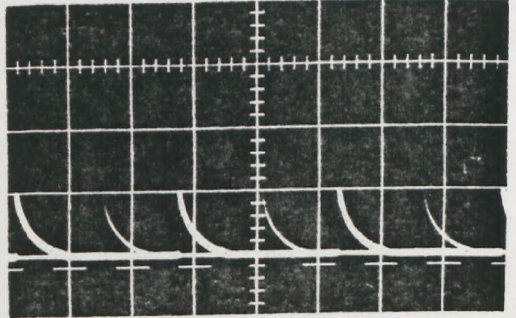
Continued



E



F



Scale: Y-axis $3.38 \frac{A}{div}$

t-axis $1 \frac{msec}{div}$

FIG 5.19 Primary and secondary current waveforms
(Points A and F refer to Fig 5.17)

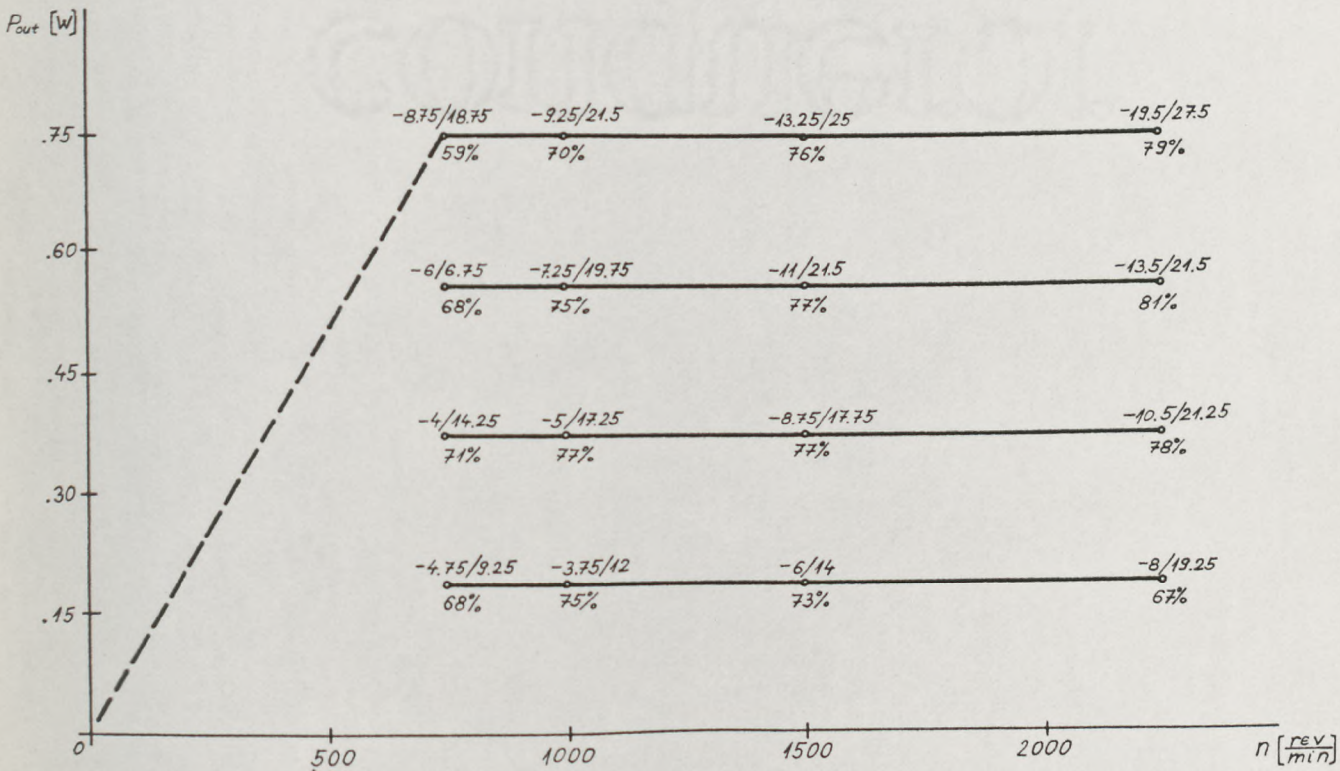


FIG 5.20 Running performance of D90M2-4 motor
Supply voltage: 150 [V]

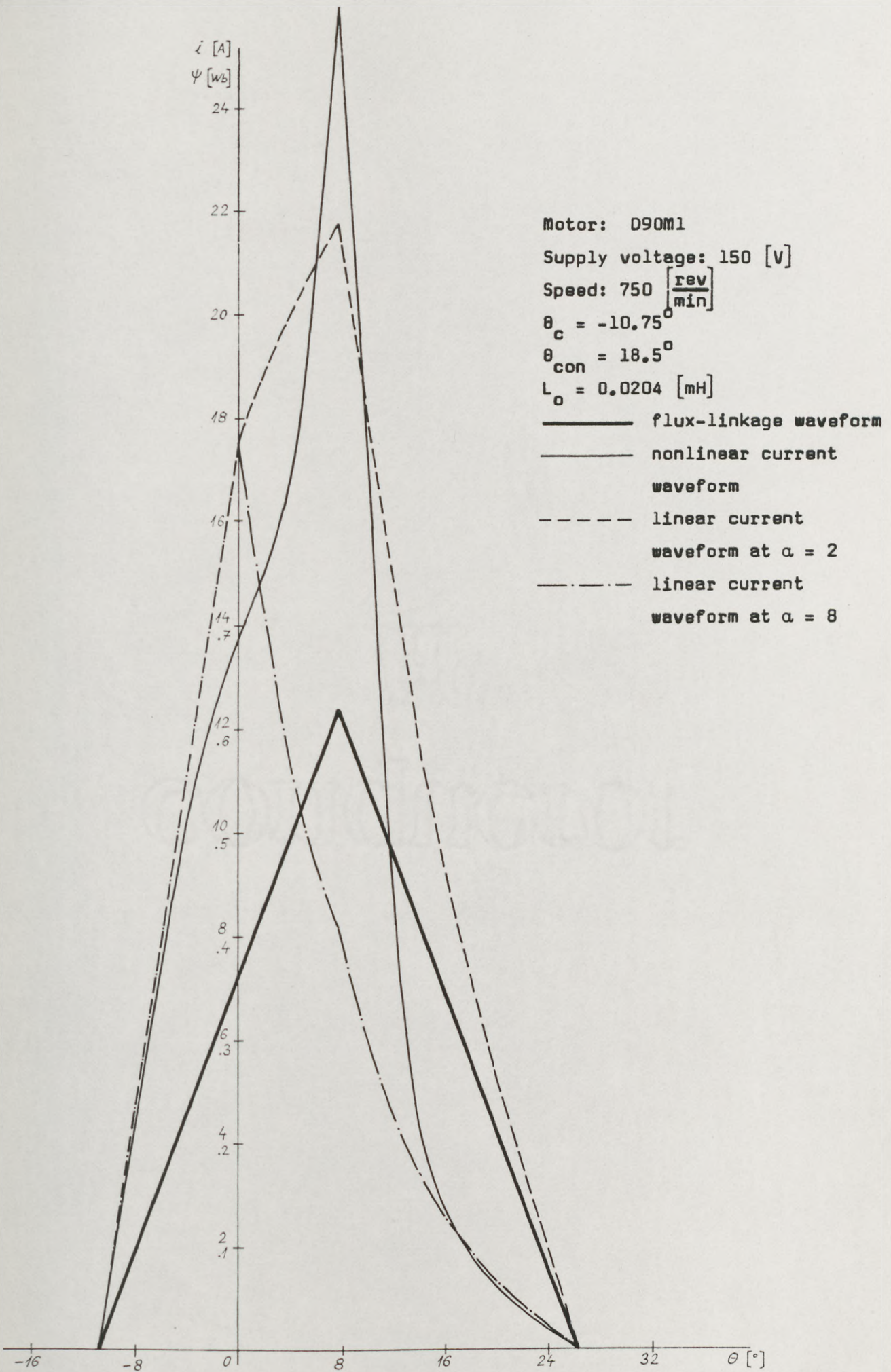


FIG 5.21 Linear and nonlinear current waveforms at zero winding resistance

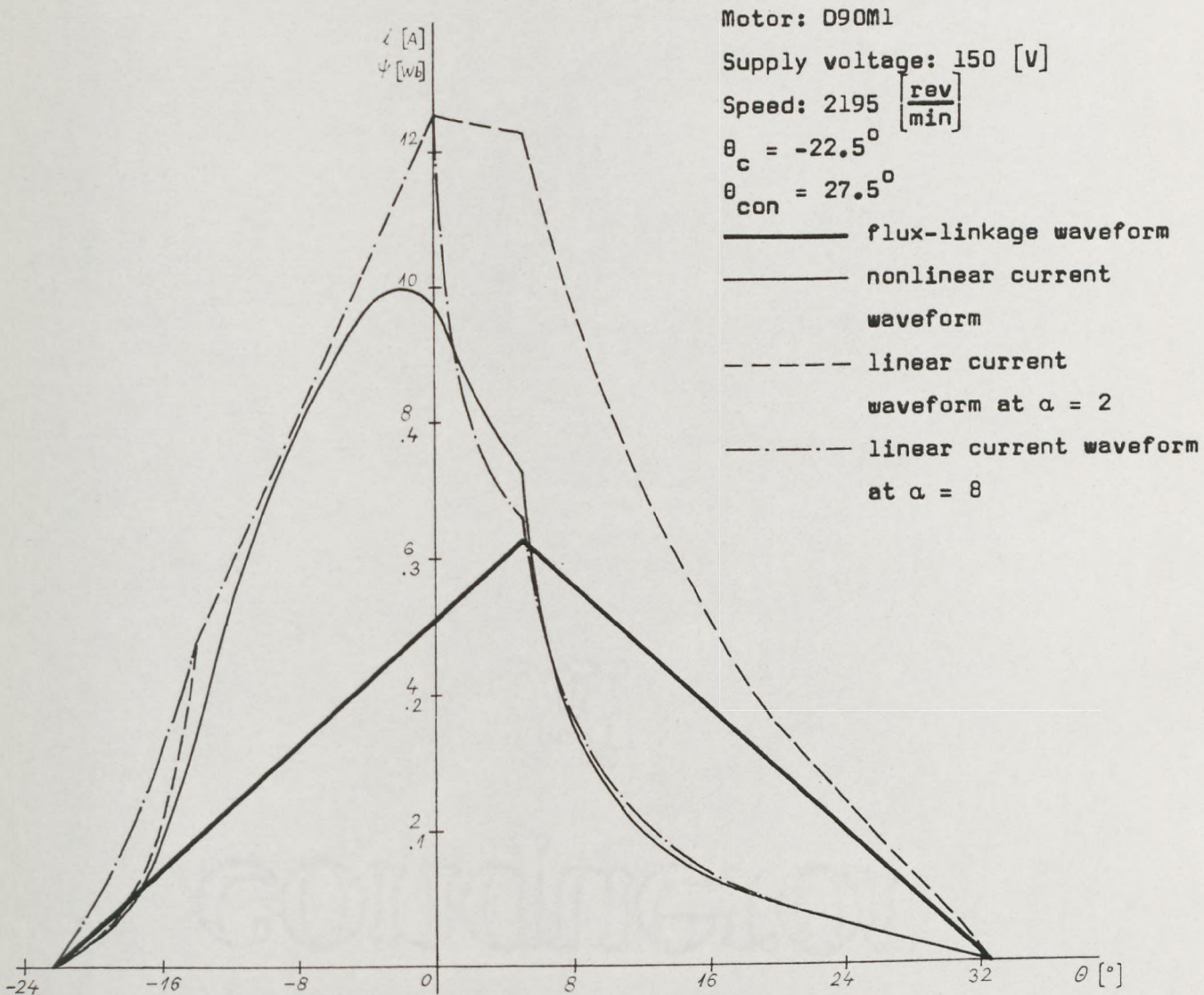


FIG 5.22 Linear and nonlinear current waveforms at zero winding resistance

APPENDIX 5A

Fig 5A.1 shows the section of the stator between two adjacent pole axes. It is possible to establish an expression for cross-sectional area of the winding in terms of d_o , d , s , $\delta (= \frac{2\pi}{N_s})$. Assuming that the stator pole sides are parallel, winding cross-sectional area fills the maximum rectangular profile and back iron width is 50% wider than half of a stator pole width, then

$$SA \approx \frac{d}{2} \frac{s}{2}$$

$$c = \frac{3}{2} SA \approx \frac{3}{2} \frac{d}{2} \frac{s}{2}$$

$$AF \approx \frac{d}{2} \sin \frac{\delta-s}{2}$$

$$\hat{B}\hat{A}F = \frac{\delta}{2}$$

$$AB = AF / \cos \hat{B}\hat{A}F$$

$$BE = \frac{d_o}{2} - OB - c = \frac{d_o}{2} - \frac{d}{2} \cos \frac{s}{2} / \cos \frac{\delta}{2} - \frac{3}{2} \frac{d}{2} \frac{s}{2}$$

$$BC \approx BE / \cos \frac{\delta}{4}$$

Cross-sectional area per one side of the winding is

$$A_w = AB \times BC = K_1 (\Omega - K_2 \Omega^2) d_o^2 \quad (5A.1)$$

where

$$\Omega = \frac{d}{d_o}$$

$$K_1 = \frac{1}{4} \frac{\sin \frac{\delta-s}{2}}{\cos \frac{\delta}{2} \cos \frac{\delta}{4}} \quad \text{and}$$

$$K_2 = \frac{\cos \frac{s}{2}}{\cos \frac{\delta}{2}} + \frac{3}{4} s$$

If $s = 20^\circ$ and $\delta = 45^\circ$, then $K_1 = 0.0597$, $K_2 = 1.328$ and

$$A_w = 0.0597 (\Omega - 1.328\Omega^2) d_o^2$$

The maximum cross-sectional area of the winding is obtained when $\Omega = 0.376$.

The winding resistance is a function of d_o , d , s , N_s , ℓ , N as follows

$$R \sim \frac{N\ell_1}{A_w/N} = N^2 \frac{\ell_1}{A_w} = N^2 \frac{2(\ell + Kd)}{K_1(\Omega - K_2\Omega^2)d_o^2} = N^2 \frac{2}{d_o} \frac{(\frac{\ell}{d} + K\Omega)}{K_1(\Omega - K_2\Omega^2)} \quad (5A.2)$$

where K is defined as $\frac{\text{mean end winding length}}{\text{rotor diameter}}$

$$K \approx \frac{\frac{s+\delta}{2} \frac{d}{2} \frac{\pi}{2}}{d} = \frac{\pi}{8} (s+\delta) \quad (\text{see Fig 5A.2})$$

If $s = 20^\circ$ and $\delta = 45^\circ$, then $K = 0.445$ and

$$R \sim N^2 \frac{2}{d_o} \frac{(\frac{\ell}{d} + 0.445\Omega)}{0.0597(\Omega - 1.328\Omega^2)}$$

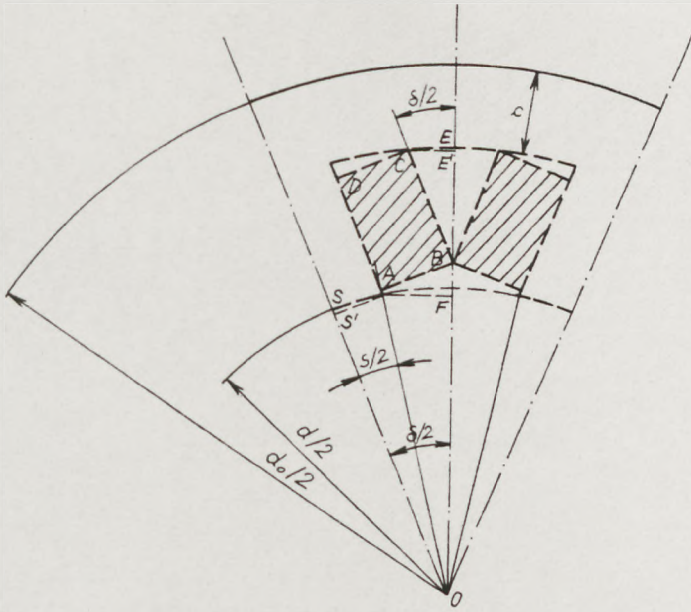


FIG 5A.1 Cross-sectional area of winding

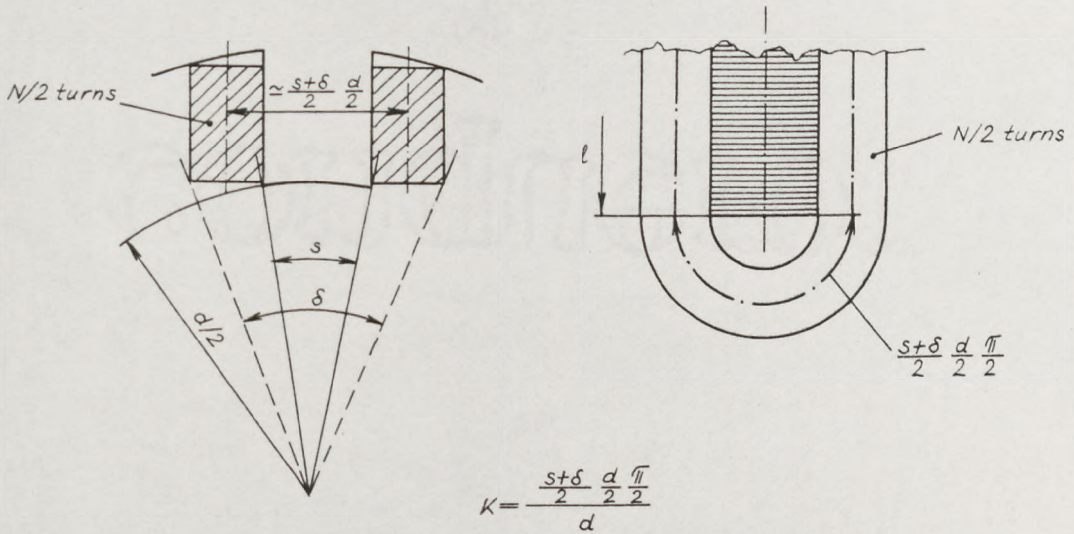


FIG 5A.2 Definition of coefficient K

CHAPTER 6

NON-LINEAR MODEL OF DOUBLY-SALIENT RELUCTANCE MOTOR

6.1 Introduction

The experimental work presented in Chapter 5 indicates the severity of saturation in the magnetic circuit. Consequently the representation of the machine by the equations of the linear analysis (Chapter 4) does not provide a satisfactory means for calculating the performance of the machine. In addition the presence of the resistances of the phase windings which have been neglected in the linear analysis are of great importance for accurately representing the machine by a mathematical model.

The importance of an accurate mathematical model lies in its use in:

- a) using measured inductance or flux-linkage data to enable detailed examination of behaviour over a wide variety of simulated operating conditions without limitations associated with drive circuits, transducers or instrumentation;
- b) using basic measured data modified as required to test the sensitivity of performance to hypothetical design changes;
- c) using data computed by field analysis, enabling, for example, purely computational studies of design to be made to meet specified performance requirements.

In this chapter the various previously published methods for computing motor performance from non-linear magnetic data are reviewed and tested against the present requirements. They are found to be unsatisfactory and a new method for accurately calculating the performance of the doubly-salient reluctance motor from flux-linkage/current/rotor position data is described. The new method is more accurate and uses less input data than previously known procedures and is computationally efficient.

Direct comparison is made between computed performance and measured results from the experimental 4-phase motor D90M1 described in Chapter 5. (The computer model can however be used for a motor with any number of phases, stator and rotor poles.)

6.2 Model Equations

The model equations describing the behaviour of a machine become non-linear when magnetic saturation is included. The flux-linkage/rotor angle relationships cannot, in general, be taken either as linear or as simple sinusoidal functions.

The terms which take into account the effect of mutual inductance are neglected in the machine equations. (It has been found by experimental measurements that mutual inductances are very small and therefore can be neglected.)

The iron losses are not accounted for in this model since their calculation is difficult even in those machines where current and flux are sinusoidal functions of time. For the motor where current waveforms are discontinuous and where flux densities vary widely throughout the machine, an analytical treatment of such losses is beyond the scope of this work. For the experimental machine used in this work the iron losses are small.

An allowance for friction and windage losses is made in the model but for the present machine they are very small compared with the output torque and are neglected.

The basic machine circuit is shown in Fig 6.1. In this figure L represents the inductance of one phase winding of the motor and is a non-linear function of θ and i .

The voltage equations describing the circuit in Fig 6.1 are:

$$+ V = Ri + \frac{d\psi(\theta, i)}{dt} \quad (6.1)$$

In these equations the +ve sign corresponds to the state when the

controlling switch S is closed and $V = V_S$, $R = R_1$, and the -ve sign corresponds to the state when S is open and $V = V_R$, $R = R_1 + R_2'$. The equations (6.1) can be expressed in the following alternative forms, the choice depending on the method used for handling the non-linear data.

$$\frac{di}{dt} = \frac{1}{\frac{\partial \psi}{\partial i}(\theta, i)} \left\{ \begin{array}{l} + V - Ri - \omega \frac{\partial \psi}{\partial \theta}(\theta, i) \\ - V - Ri - \omega \frac{\partial \psi}{\partial \theta}(\theta, i) \end{array} \right\} \quad (6.2)$$

$$\frac{di}{dt} = \frac{1}{\ell(\theta, i)} \left\{ \begin{array}{l} + V - \left[R + \omega \frac{\partial L}{\partial \theta}(\theta, i) \right] i \\ - V - \left[R + \omega \frac{\partial L}{\partial \theta}(\theta, i) \right] i \end{array} \right\} \quad (6.3)$$

$$\frac{di}{dt} = \frac{1}{L(\theta, i)} \left\{ \begin{array}{l} + V - \left[R + \omega \frac{dL(\theta, i)}{d\theta} \right] i \\ - V - \left[R + \omega \frac{dL(\theta, i)}{d\theta} \right] i \end{array} \right\} \quad (6.4)$$

The mechanical equations are

$$\frac{d\theta}{dt} = \omega \quad (6.5)$$

$$\frac{d\omega}{dt} = \frac{1}{J} \left\{ T(\theta, i) - T_{mech} \right\} \quad (6.6)$$

The dependence of the parameters of these equations upon both current and angle requires the use of numerical integration methods and before the model equations can be solved they must be represented for all values θ and i . In addition, the action of the rotor position sensor (commutator) in controlling the switch S has to be described in terms suitable for the numerical solution.

In this work only steady-state operation is considered. It has been shown¹ even for a small two-phase reluctance motor that variation in instantaneous speed over a cycle is insignificant down to very low speeds and this result allows a constant speed version of the model to be used in steady-state operating conditions.

6.3 Review of Known Methods

Since the model requires flux-linkage or inductance to be known at all values of both θ and i , some means of translating the discrete measurements into continuous functions is required.

Singh²⁴ used equations in the form (6.3). The functions $\ell(\theta, i)$, $L(\theta, i)$ and $T(\theta, i)$ were measured and approximated by fundamental cosinusoidal components in θ and by linear functions in i , the derivatives $\frac{\partial L}{\partial \theta}(\theta, i)$ being obtained analytically.

$$L(\theta, i) = (L_{00} - L_{01} i) + (L_{20} - L_{21} i) \cos n\theta$$

$$\ell(\theta, i) = (\ell_{00} - \ell_{01} i) + (\ell_{20} - \ell_{21} i) \cos n\theta$$

where $L(\theta, i)$ is average inductance $L(\theta, i) = \frac{\Psi(\theta, i)}{i}$

$$\ell(\theta, i) \text{ is incremental inductance } \ell(\theta, i) = \frac{\delta \Psi}{\delta i},$$

n is number of poles per phase

Having approximated the measured function $\ell(\theta, i)$ by an analytical function, the functions $L(\theta, i)$ and $T(\theta, i)$ could have been found analytically as $L(\theta, i) = \left\{ \int_0^i \ell(\theta, i) di \right\} / i$ and $T(\theta, i) = \partial \int_0^i L(\theta, i) i di / \partial \theta$ thus avoiding the measurement of T and L . The probable reason why this was not done is the poor approximation for $\ell(\theta, i)$. Particular disadvantages of this method are: for a switched reluctance motor the large pole-arc to air-gap ratio leads to an inductance function which is far from sinusoidal and representation by the fundamental component of θ leads to considerable inaccuracy; the relationship between inductance and current is far from a linear function.

Pickup and Tipping^{25,26} used equations in the form (6.2). Flux-linkage was measured at equally spaced angles and currents (19 x 7 readings). In their first method the function $\Psi(\theta, i)$ was approximated by polynomials in both θ and i

$$\Psi(\theta, i) = \sum_{r=0}^k \left\{ (A_{1r} i + A_{3r} i^3 + \dots + A_{jr} i^j) (n\theta)^r \right\}$$

The coefficients A_{1r}, \dots, A_{jr} were determined using a modification of the least square method.

In their second method the function $\Psi(\theta, i)$ was approximated by Fourier cosine series in θ and a polynomial in i

$$\Psi(\theta, i) = \sum_{r=0}^k \left\{ (B_{1r} i + B_{3r} i^3 + \dots + B_{jr} i^j) \cos(rn\theta) \right\}$$

The derivatives $\frac{\partial \Psi}{\partial \theta}(\theta, i)$ and $\frac{\partial \Psi}{\partial i}(\theta, i)$ and torque $T(\theta, i) = \partial \int_0^i \Psi(\theta, i) di / \partial \theta$ were then found analytically.

Byrne and Dwyer²⁷ also used the equation in form (6.2). Flux-linkage $\Psi(\theta, i)$ was measured at equally spaced angles and currents (18 x 10 readings). The curves $\Psi(\theta, i)|_{\theta=\text{const}}$ were each fitted by a sum of three exponentials.

$$\Psi(\theta, i) = a_0 i + a_1 \{1 - \exp(-\alpha_1 i)\} + a_2 \{1 - \exp(-\alpha_2 i)\} + a_3 \{1 - \exp(-\alpha_3 i)\}$$

The coefficients $\alpha_1 = 0.3$, $\alpha_2 = 0.1$ and $\alpha_3 = 0.03$ were used and the coefficients a_0, a_1, a_2, a_3 were determined by the linear least squares method. The values of

$$\frac{\partial \Psi}{\partial i}(\theta, i)|_{\theta=\text{const}} \quad \text{and} \quad \int_0^i \Psi(\theta, i) di |_{\theta=\text{const}}$$

were obtained analytically and values of $\frac{\partial \Psi}{\partial \theta}(\theta, i)|_{i=\text{const}}$ and

$$T(\theta, i) = \partial \int_0^i \Psi(\theta, i) di / \partial \theta |_{i=\text{const}}$$

were obtained numerically. The intermediate values of $\frac{\partial \Psi}{\partial i}(\theta, i)$, $\frac{\partial \Psi}{\partial \theta}(\theta, i)$ and $T(\theta, i)$ were found by linear interpolation in θ and i .

Blenkinsop¹ has used the equation in form (6.4) with the inductance $L(\theta, i)$ measured at equally spaced angles and unequally spaced currents (for stepped air-gap 37 x 7 readings). Then using polynomial fitting for the curves $L(\theta, i)|_{\theta=\text{const}}$ more values of $L(\theta, i)$ at equally spaced currents were obtained. The values of coenergy $\Psi'(\theta, i) = \int_0^i L(\theta, i) i di |_{\theta=\text{const}}$ were found analytically, and the values of

$$\frac{dL(\theta, i)}{d\theta} |_{i=\text{const}} \quad \text{and} \quad T(\theta, i) = \frac{\partial \Psi'(\theta, i)}{\partial \theta} |_{i=\text{const}}$$

were obtained numerically. The intermediate values of $L(\theta, i)$, $\frac{dL(\theta, i)}{d\theta}$ and $T(\theta, i)$ were found by linear interpolation in θ and i .

Acarnley⁹ used equations in the form (6.3) with the incremental inductance $\ell(\theta, i)$ measured at equally spaced angles and currents. The function $\ell(\theta, i)$ was approximated by polynomials in i and by Fourier series in θ . Then the inductance $L(\theta, i)$ was found analytically as $L(\theta, i) = \int_0^i \ell(\theta, i) di/i$. The derivative $\frac{\partial L}{\partial \theta}(\theta, i)$ and torque $T(\theta, i) = \partial \int_0^i L(\theta, i) di / \partial \theta$ were then obtained analytically.

The common disadvantage in all these reviewed methods is that they use voltage equations in form (6.2), (6.3) or (6.4) which contain coefficients $\frac{\partial \psi}{\partial i}(\theta, i)$, $\frac{\partial \psi}{\partial \theta}(\theta, i)$, $\frac{\partial L}{\partial \theta}(\theta, i)$ or $\frac{dL(\theta, i)}{d\theta}$. The errors introduced by fitting the curves $\psi(\theta, i)$ or $L(\theta, i)$, which alternate +ve or -ve with respect to the measured curves, are significantly increased by the process of differentiation. Also, the amount of data required in these methods is large for highly saturated machines which directly increases the computing time required for producing the data by numerical field analysis and the time required to make the measurements.

The difficulties in obtaining accurate values for the differential of a function specified only by tabulated points are demonstrated below using Blenkinsop's method to calculate the performance of the experimental motor D90M1 operating in very saturated conditions (150 [V], 0.75 [kW] 750 $\left[\frac{\text{rev}}{\text{min}} \right]$). The program took data in the form of inductance measurements for 16 values of rotor angle (every 2°) and for 10 values of current (0.0, 1.0, 2.0, 3.0, 4.0, 6.0, 8.0, 11.0, 14.0, 18.0 [A]). The curves $L(\theta, i)|_{\theta=\text{const}}$ were fitted with polynomials of 5th order.

Figs 6.2, 6.3, 6.4 show how an apparently good polynomial fit of inductance $L(\theta, i)$ with current i can give rise to significant errors in the differentiation with respect to θ (ie in evaluating $\frac{dL(\theta, i)}{d\theta} \Big|_{i=\text{const}}$).

Improvement in accuracy may be achieved by increasing the amount of data (ie current readings) but the benefits are not found to be as great as expected. Similarly, increasing the order of the polynomial does not yield any significant benefit.

The errors introduced by fitting the curves $L(\theta, i)|_{\theta=\text{const}}$ with p -th order polynomials in i are compensated in the process of integration

$$\begin{aligned} \Psi'(\theta, i) &= \int_0^i L(\theta, i) di \\ &= \int_0^i (a_0 + a_1 i + \dots + a_p i^p) di = \\ &= \frac{a_0 i^2}{2} + \frac{a_1 i^3}{3} + \dots + \frac{a_p i^{p+2}}{p+2} \end{aligned}$$

so that the torque $T(\theta, i) = \left. \frac{\partial \Psi'(\theta, i)}{\partial \theta} \right|_{i=\text{const}}$ is not seriously in error (Fig 6.5).

The computed current waveform is in good agreement with the measured one until high degrees of saturation are reached. However, the polynomial fitting of $L(\theta, i) \Big|_{\theta=\text{const}}$ introduces serious errors at high flux densities (Fig 6.6). The flux-linkage continues to increase in value for a tenth of a cycle following switch-off and the calculated average torque is 29% high. The error in the rate of decay of current results in a large error in the input power (48% low) and the combined errors results in an apparent efficiency of 137%. (The efficiency has been computed using expression

$$\eta = \frac{\text{output power}}{(\text{power transferred by primary current}) - (\text{returned power})} \cdot)$$

6.4 New Improved Method

The essential feature of the new method described below is that, unlike the methods described above it is based on using non-linear differential equations which do not require the evaluation of the differential coefficients and consequently the results are more accurate and require less input data.

6.4.1 Voltage equations

Using voltage equations in the form

$$\frac{d\Psi(\theta, i)}{dt} = \pm V - R i \quad (6.7)$$

eliminates $\frac{\partial \Psi}{\partial \theta}(\theta, i)$ and $\frac{\partial \Psi}{\partial i}(\theta, i)$ as coefficients with the inevitable problem of error amplification. An additional advantage is that, in general, the maximum rate of change of flux-linkage is not so rapid as the maximum rate of change of, for example, current, so that the step

length in the integration of the model equations can be relatively long with consequential saving in computing time.

6.4.2 Method of solution

The given data defining the magnetic nature of the machine are stored as a $N_\theta \times N_i$ table of values of $\psi(\theta, i)$ (see Appendix 6A). It is very desirable that the number of values to be specified be as small as possible and it has been found that the curves of $\psi(\theta, i)|_{\theta=\text{const}}$ (being monotonic and having as a family their maximum rates of change in the same region of i) can be represented with sufficient accuracy and considerable economy by using unequally spaced values of current. This is illustrated in Fig 6.7. A quadratic interpolation method has been found to be very effective in deriving intermediate values of flux-linkage (see below). However the curves $\psi(\theta, i)|_{i=\text{const}}$ are not monotonic (being cyclic) so that the quadratic interpolation cannot be simply applied, and as a family do not lend themselves so readily to economy of the specifying data. Equally spaced angles have therefore, been used in the table of input data $\psi(\theta, i)$ and simple linear interpolation in deriving intermediate values of ψ . The choice of the number of elements in the input table $\psi(\theta, i)$ is given below.

The solution of equations (6.7) to obtain current waveforms and the motor performance requires the magnetic behaviour of the motor to be defined in the form of a table $i(\theta, \psi)$ to enable the value of i to be updated after each step of the numerical integration of the model equations (ie after each integration step to find a new value of ψ , it is necessary to find the corresponding current which is then inserted in the right hand side of equations (6.7)). It may be that the supposed difficulty in generating this table is the reason why equations (6.7) have not been used before. This table $i(\theta, \psi)$ (with a sufficient number of equally spaced angles and flux-linkages to ensure sufficiently accurate interpolation) is obtained by inverting the input table. The values of $i(\theta, \psi)|_{\theta=\text{const}}$ at equally spaced flux-linkages may be found by using quadratic interpolation through three successive points (see below).

The intermediate values of $i(\theta, \psi)$ required in the course of numerical integration of the model equations are found by linear interpolation in θ and quadratic interpolation in ψ . Also the intermediate values of $\psi(\theta, i)|_{\theta=\text{const}}$ required in the course of computation of $T(\theta, i)|_{i=\text{const}}$ are found by quadratic interpolation in i .

6.4.3 Production of Table $i(\theta, \psi)$

Quadratic interpolation

The table of values $i(\theta, \psi)$ at equally spaced angles and flux-linkages is obtained by inverting the input table $\psi(\theta, i)$. (Equal spacing is used to provide simple identification of intermediate values of angle and flux-linkage in the process of numerical integration of model equations.)

The values of $i(\theta, \psi)|_{\theta=\text{const}}$ at equally spaced flux-linkages are found by using quadratic interpolation through three successive tabulated points. Although many different types of interpolation may be suitable, quadratic interpolation is used because of the good fitting of segments of the magnetisation curve with suitably chosen segments of parabolae.

Consider three tabulated points P_I, P_{I+1}, P_{I+2} on measured curve $\psi(\theta, i)|_{\theta=\text{const}}$ (Fig 6.8). The parabola

$$i = A\psi^2 + B\psi + C \quad (6.8)$$

is determined by these three points. The coefficients A, B, C are obtained by substituting the coordinates of points P_I, P_{I+1}, P_{I+2} in equation of parabola (6.8).

$$i_I = A\psi_I^2 + B\psi_I + C$$

$$i_{I+1} = A\psi_{I+1}^2 + B\psi_{I+1} + C \quad (6.9)$$

$$i_{I+2} = A\psi_{I+2}^2 + B\psi_{I+2} + C$$

Solving system (6.9), coefficients A, B, C of the parabola are

$$\begin{aligned}
 A &= \frac{1}{\psi_{I+2} - \psi_{I+1}} \left\{ \frac{i_{I+2} - i_I}{\psi_{I+2} - \psi_I} - \frac{i_{I+1} - i_I}{\psi_{I+1} - \psi_I} \right\} \\
 B &= \frac{i_{I+1} - i_I}{\psi_{I+1} - \psi_I} - A(\psi_{I+1} + \psi_I) \\
 C &= i_I - A\psi_I^2 - B\psi_I
 \end{aligned} \tag{6.10}$$

For any value of ψ , the value of i on the parabola is given by

$$i = (\psi - \psi_I) \left\{ A(\psi - \psi_{I+1}) + \frac{i_{I+1} - i_I}{\psi_{I+1} - \psi_I} \right\} + i_I \tag{6.11}$$

Three successive tabulated points P_I, P_{I+1}, P_{I+2} can be chosen so that given value of flux-linkage lies between P_I and P_{I+1} (zone I) or between points P_{I+1} and P_{I+2} (zone II). In order to decide which zone is preferred for interpolation, the fitting error may be estimated in each case. Consider, for example, the smooth curve $\psi(\theta, i)$ for $\theta = 23^\circ$ of experimental machine D90M1 and interpolate the value of current corresponding to $\psi = 0.535$ [Wb]. (This is the region where largest error is expected.)

Firstly take three successive tabulated points so that $\psi_I < \psi < \psi_{I+1}$. These are

$$P_I \quad (i_I = 6[A], \quad \psi_I = 0.513 \text{ [Wb]})$$

$$P_{I+1} \quad (i_{I+1} = 9[A], \quad \psi_{I+1} = 0.558 \text{ [Wb]})$$

$$P_{I+2} \quad (i_{I+2} = 14[A], \quad \psi_{I+2} = 0.596 \text{ [Wb]})$$

Using equations (6.10) and (6.11) the value of current at $\psi = 0.535$ [Wb] is $i = 7.153$ [A]. The reading from the curve is $i = 7.3$ [A] and the difference is $(7.153 - 7.3) 100/7.3 = -2\%$.

Now take three successive tabulated points so that $\psi_{I+1} < \psi < \psi_{I+2}$. These are

$$P_I \quad (i_I = 4[A], \quad \psi_I = 0.465 [\text{wb}])$$

$$P_{I+1} \quad (i_{I+1} = 6[A], \quad \psi_{I+1} = 0.513 [\text{wb}])$$

$$P_{I+2} \quad (i_{I+2} = 9[A], \quad \psi_{I+2} = 0.558 [\text{wb}])$$

Using equations (6.10) and (6.11) the value of current at $\psi = 0.535$ [wb] is $i = 7.33$ [A]. The difference between interpolated value and reading from the curve is $(7.33-7.3) 100/7.3 = + 0.41 \%$. If the linear interpolation is used then the interpolated value of current corresponding to $\psi = 0.535$ [wb] is $i = 7.47$ [A] i.e. + 2.33% greater than the reading from the smoothed curve.

These results show the superiority of placing ψ in zone II of parabola (so that $\psi_{I+1} < \psi < \psi_{I+2}$). For interpolation in the first interval specified by the limiting point $(0,0)$ (as P_{I+1}) and $(i_1, \psi_{k,1})$ (as P_{I+2}), (where $k = 1, \dots, N_\theta'$), the dummy point (as P_I) must be defined. Since the point $(i_1, \psi_{k,1})$ lies in the linear part of curve $\psi(\theta, i) \Big|_{\theta=\text{const}} (-i_1, -\psi_{k,1})$ may be taken as the dummy point. Thus, using this fast and very accurate method, the table $i(\theta, \psi)$ which is the inverse of the input table $\psi(\theta, i)$ is obtained. (The corresponding curves are shown in Fig 6.9.)

6.4.4 Numerical solution of the model equations

The computer program representing the machine model has been written so that it can be used for different machine circuits providing that they can be represented by the basic machine circuit shown in Fig 6.1.

In the case of a machine with a bifilar winding having a primary/secondary turns ratio 1:1 and operating under steady state conditions ($\omega=\text{const}$), the equations (6.7) become

'S' closed ($V = V_s - V_T$, $R = R_1$):

$$\frac{d\psi(\theta, i)}{d\theta} = (V_s - V_T - R_1 i_1) / \left(\frac{180}{\pi} \omega\right) [\text{wb}/^\circ] \quad (6.12a)$$

'S' open ($V = V_s + V_D$, $R = R_2$):

$$\frac{d\psi(\theta, i)}{d\theta} = (-V_s - V_D - R_2 i_2) / \left(\frac{180}{\pi} \omega \right) [\text{Wb/}^\circ] \quad (6.12b)$$

where R_1 and R_2 are the primary and secondary coil resistances;

V_T is transistor saturation voltage; (It has been found experimentally that $V_T \approx 0.8 + 0.2 i_1$ [V].)

V_D is diode forward drop of voltage ($V_D \approx 1$ [V]);

V_s is d.c. supply voltage.

The differential equations are solved by the Runge-Kutta fourth-order method, the values of the flux-linkage and current being found after each step of integration.

The procedure of integration is shown below. Let θ , $\psi(\theta)$, $i(\theta, \psi)$ be the values at the beginning of the integration step and let f be the differential of ψ with respect to θ (ie the right hand side of equations 6.12a and 6.12b, then

1. Auxiliary variable $A_1 = h_\theta \times f(\theta, \psi)$,
2. Using the table $i(\theta, \psi)$ and quadratic interpolation find $i(\theta + \frac{h_\theta}{2}, \psi + \frac{A_1}{2})$,
3. Auxiliary variable $A_2 = h_\theta \times f(\theta + \frac{h_\theta}{2}, \psi + \frac{A_1}{2})$,
4. Using the table $i(\theta, \psi)$ and quadratic interpolation find $i(\theta + \frac{h_\theta}{2}, \psi + \frac{A_2}{2})$,
5. Auxiliary variable $A_3 = h_\theta \times f(\theta + \frac{h_\theta}{2}, \psi + \frac{A_2}{2})$,
6. Using the table $i(\theta, \psi)$ and quadratic interpolation find $i(\theta + h_\theta, \psi + A_3)$,
7. Auxiliary variable $A_4 = h_\theta \times f(\theta + h_\theta, \psi + A_3)$,

8. The new value of ψ at the end of the integration step is given by weighted mean of the auxiliary variable $\psi = \psi(\theta + h_\theta) = \frac{1}{6} \{A_1 + 2(A_2 + A_3) + A_4\}$
9. Using the table $i(\theta, \psi)$ and quadratic interpolation find the value of current at the end of integration step $i = i(\theta + h_\theta, \psi)$. The initial condition for ψ and i on switch-on is zero but the program allows incomplete commutation when flux and current at the end of the cycle may be non-zero. In that case the final value of i is re-inserted as the initial condition and the integration repeated. When the initial and final value of current are within a specified error the integration is completed.

The following quantities are computed throughout the cycle

$$\begin{aligned}
 S_1 &= - \sum_{j=1}^{n_s} \frac{(\psi_j + \psi_{j-1})}{2} (i_j - i_{j-1}) \\
 S_2 &= h_\theta \sum_{j=1}^{n_s} \frac{\psi_j + \psi_{j-1}}{2} \\
 S_3 &= h_\theta \sum_{j=1}^{n_s} \frac{i_j + i_{j-1}}{2} \\
 S_4 &= h_\theta \sum_{j=1}^{n_s} \left(\frac{i_j + i_{j-1}}{2} \right)^2 \\
 S_5 &= h_\theta \sum_{j=1}^{n_s} \frac{i_j + i_{j-1}}{2} \\
 S_6 &= h_\theta \sum_{j=1}^{n_s} \left(\frac{i_j + i_{j-1}}{2} \right)^2
 \end{aligned}
 \left. \begin{array}{l} \\ \\ \\ \\ \\ \end{array} \right\} \begin{array}{l} \text{either 'S' closed or open} \\ \\ \text{'S' closed} \\ \\ \text{'S' open} \end{array}$$

where n_s is number of steps of integration,

h_θ is integration step length [°].

From these variables the following output data can be obtained,

Total co-energy change per cycle: $W' = q S_1$

Average torque per complete cycle: $T = W' / (2\pi/N_r)$

Output power:	$P_{out} = \omega T$
Average stator flux-linkage:	$\psi_m = q S_2 / (360/N_r)$
Power transferred by primary current:	$P_1 = q S_3 V_s / (360/N_r)$
Power returned to supply:	$P_2 = q S_5 V_s / (360/N_r)$
Efficiency:	$\eta = \frac{P_{out}}{P_1 - P_2}$
Copper loss in primary coil:	$I_1^2 R_1 = q S_4 R_1 / (360/N_r)$
Copper loss in secondary coil:	$I_2^2 R_2 = q S_6 R_2 / (360/N_r)$

After each step the instantaneous value of total current as the sum of the instantaneous values of current of each phase is computed

$$i_{tot} = \sum_{p=1}^q i_p$$

The rms and mean values of the total current are computed throughout the cycle

$$I_{tot} = \sqrt{\frac{h_\theta}{360/N_r} \sum_{j=1}^{n_s} \left(\frac{i_{tot j} + i_{tot j-1}}{2} \right)^2}$$

$$I_{m tot} = q (S_3 - S_5) / (360/N_r)$$

The rms of the a.c. component of the total current is computed as

$$I_{ac tot} = \sqrt{I_{tot}^2 - I_{m tot}^2}$$

6.4.5 Computation of instantaneous torque

In order to compute the torque $T(\theta, i)$ the table of co-energies $\Psi'(\theta, i)$ is required. $\Psi'(\theta, i) = \int_0^i \psi(\theta, i) di \Big|_{\theta=\text{const}}$ is found numerically using trapezoidal integration. (An increased number of values of $\psi(\theta, i)$ at equally spaced currents are computed using the method of quadratic interpolation.) The torque

$$T(\theta, i) = \frac{\partial \Psi'(\theta, i)}{\partial \theta}$$

is obtained by numerical differentiation using Stirling's interpolation formula. The differentiation requires the forming of a difference table in θ at each value of i from the stored co-energy data. Table 6.1 shows the formation of a difference table up to and including fifth differences. Using this table the odd-order, mean central differences are computed

$$\delta_m^{(2p+1)}(\theta_k, i) = \frac{\delta_{k+\frac{1}{2}}^{(2p+1)} + \delta_{k-\frac{1}{2}}^{(2p+1)}}{2}, \quad p = 0, 1, 2$$

and then

$$T(\theta_k, i)|_{i=\text{const}} = \frac{1}{h_\theta} \left\{ \delta_m^{(1)}(\theta_k, i) - \frac{1}{6} \delta_m^{(3)}(\theta_k, i) + \frac{1}{30} \delta_m^{(5)}(\theta_k, i) \right\}$$

$$W'(\theta_1, i)$$

⋮

$$W'(\theta_{k-3}, i)$$

$$\delta_{k-\frac{5}{2}}^{(1)}$$

$$W'(\theta_{k-2}, i)$$

$$\delta_{k-2}^{(2)}$$

$$\delta_{k-\frac{3}{2}}^{(1)}$$

$$\delta_{k-\frac{3}{2}}^{(3)}$$

$$W'(\theta_{k-1}, i)$$

$$\delta_{k-1}^{(2)}$$

$$\delta_{k-1}^{(4)}$$

$$\delta_{k-\frac{1}{2}}^{(1)}$$

$$\delta_{k-\frac{1}{2}}^{(3)}$$

$$\delta_{k-\frac{1}{2}}^{(5)}$$

$$W'(\theta_k, i)$$

$$\delta_k^{(2)}$$

$$\delta_k^{(4)}$$

$$\delta_{k+\frac{1}{2}}^{(1)}$$

$$\delta_{k+\frac{1}{2}}^{(3)}$$

$$\delta_{k+\frac{1}{2}}^{(5)}$$

$$W'(\theta_{k+1}, i)$$

$$\delta_{k+1}^{(2)}$$

$$\delta_{k+1}^{(4)}$$

$$\delta_{k+\frac{3}{2}}^{(1)}$$

$$\delta_{k+\frac{3}{2}}^{(3)}$$

$$W'(\theta_{k+2}, i)$$

$$\delta_{k+2}^{(2)}$$

$$\delta_{k+\frac{5}{2}}^{(1)}$$

$$W'(\theta_{k+3}, i)$$

⋮

$$W'(\theta_N, i)$$

TABLE 6.1 Difference Table

6.4.6 The program arrangement

It was decided to solve the non-linear model with a suite of three programs:

- program for torque computation,
- program for production of table $i(\theta, \psi)$,
- program for computation of running performance

The nonlinear flux-linkage/rotor angle/current data are stored in the form of a table $\psi(\theta, i)$.

The first program uses the table $\psi(\theta, i)$ as input data (see Appendix 6A) and gives results for the torque in the form of a table $T(\theta, i)$.

The second program also uses the table $\psi(\theta, i)$ as input data and produces an inverse table $i(\theta, \psi)$ (see Appendix 6B) which is then stored for further use in the third program.

The third program is arranged so that the bulk of the motor data is held internally. This program uses the table $i(\theta, \psi)$ as input data and, for specified supply voltage (V_s), speed (n) and switching angles (θ_c and θ_o) (see Appendix 6C), calculates the following items of the running performance:

- average values of torque, output power, input power, primary current, secondary current, flux-linkage,
- rms values of primary current, secondary current, total current, ac component of total current, copper losses,
- efficiency,
- peak values of flux-linkage primary and secondary currents.

The computing time of these programs are 3, 2 and 3 seconds, respectively. (An ICL1906A computer has been used.)

6.4.7 Choice of number of elements in input table $\psi(\theta, i)$

The number of elements in the input table $\psi(\theta, i)$ (each element being one measurement or field solution of flux-linkage against rotor position and current) has a direct influence on the accuracy of

computed results. Therefore the number of these elements, necessary for good agreement between computed and measured results, is deduced from the comparison of these results.

The comparison is made with data from the experimental machine D90M1 in four cases when the measured values of flux-linkage are taken at:

- i) every $2[^\circ]$ and every $1[A]$ (from 1 to $14[A]$),
the total number of readings is 224^* ;
- ii) every $2[^\circ]$ and at 1, 2, 3, 4, 6, 9 and $14[A]$;
the total number of readings is 112;
- iii) every $3[^\circ]$ and at 1, 2, 3, 4, 6, 9 and $14[A]$,
the total number of readings is 77;
- iv) every $4[^\circ]$ and at 1, 2, 3, 4, 6, 9 and $14[A]$,
the total number of readings is 56.

No difference can be observed between computed results for static torque of the first two cases and the same is true of the running performance. This means that 112 readings give equally good results as 224 readings.

For the third case, when the number of readings is 77, the difference between computed results for static torque of the first two cases and the third case is less than 1%, and the computed results for running performance are the same as in the previous case.

In the fourth case the number of elements is 56 and although computed results of static torque are good at individual points (Fig 6.10) these points are too widely spaced to allow correct interpolation and therefore do not allow accurate prediction of the starting torque at any rotor position. The computed results of running performance are still in very good agreement with the previous three cases (see Table

* In the case of symmetrical inductance waveform the number of angles specified in table i(θ, ψ) is $N_\theta' = 2 N_\theta + 1$ where N_θ is number of angle measurement points. If angular increment between measured points is $\Delta\theta$ then $N_\theta' = \frac{\phi}{\Delta\theta} + 1$.

6.2).

	Torque	Efficiency	Peak Current	Mean current per phase	Primary rms current per phase
	Nm	%	A	A	A
Cases: i, ii, iii	9.61	57.5	12.4	8.76	5.29
Case: iv	9.65	57.6	12.2	8.77	5.30

TABLE 6.2 Comparison between computed results of running performance for different numbers of elements in Table $\psi(\theta, i)$

The third case is accepted as optimal giving very good accuracy with a relatively small number of readings in the input table $\psi(\theta, i)$.

Fig 6.11 shows the distribution of current values at which the values of flux-linkage in the input table are specified (see also Appendix 6A).

6.4.8 Choice of number of integration steps

The integration step length, h_{θ} , used in the numerical integration of the model equations in steady state operating conditions is a compromise between accuracy and computing time.

In order to see how the step length affects the accuracy of computed results, the comparison has been made between computed current waveforms of the experimental machine D90M1 at $h_{\theta} = 0.125^{\circ}$ and $h_{\theta} = 0.25^{\circ}$ at several conduction angles (since the accuracy of the current waveform is dependent on the number of steps within the region where the current has a value different from zero). No significant difference has been observed when θ_{con} is decreased to the value $\phi/6 (= 10^{\circ})$. Below this value of θ_{con} the difference between computed current waveforms, with the two values of h_{θ} given above, becomes apparent. Thus, for example, at $\theta_{con} = 6^{\circ}$ the difference in mean values of current is 2% and at $\theta_{con} = 3^{\circ}$ this difference is 5%.

Therefore the $h_{\theta} = 0.25^{\circ}$ (number of steps of integration $n_s = \frac{\phi}{h_{\theta}} = 240$)

is sufficiently small to produce high accuracy because it is unlikely that values of θ_{con} less than $\phi/6$ will be used.

6.4.9 Comparison between computed and measured results

The model D90M1 is used for the presentation of the comparison between computed and measured results. Fig 6.12 shows the excellent degree of agreement achieved for torque at four different currents 2, 6, 10 and 14 [A], (14 [A] is the current which produces rated torque in the stall condition and thus the highest degree of saturation is encountered at this current).

The comparison for the running performance is made for a wide range of operating conditions at rated voltage including the constant power range from base speed to 3 X base speed at full power and the constant speed range from 1/4 of full power to full power.

The winding resistances were corrected for temperature rise.

The computed and measured performance (output power, input power, efficiency) and their differences at six different operating conditions are shown in Table 6.3.

Fig 6.13 shows computed and measured current waveforms* at 150 V, $750 \left[\frac{\text{rev}}{\text{min}} \right]$, $\theta_c = -10.75^\circ$, $\theta_{con} = 18.5^\circ$. The measured current waveform was recorded using a co-axial shunt and a digital transient recorder. The stored waveform from the recorder was plotted using an Y-t plotter. A known dc current was used for direct calibration.

The agreement between computed and measured running performance is very good at lower speeds but at higher speeds a significant discrepancy arises. Assuming that measurement errors are small this discrepancy is attributed to the following reasons.

* The effect of the winding resistances of the experimental D90M1 motor on the current waveform can be seen by direct comparison between waveform represented by broken line in Fig 6.13 and waveform represented by full line in Fig 5.20.

v_s	n	θ_c	θ_{con}		P_{out}	P_{in}	
v	$\frac{rev}{min}$	$^\circ$	$^\circ$		W	W	$\%$
150	750	-10.75	18.50	computed	755	1313	57.5
				measured	750	1350	55.6
				difference	+0.7%	-2.8%	+1.9
150	750	- 7.25	16.00	computed	546	829	65.8
				measured	555	855	65.0
				difference	-1.6%	-3.0%	+0.8
150	750	- 4.00	14.75	computed	356	493	72.3
				measured	375	534	70.0
				difference	-5.0%	-7.7%	+2.3
150	750	- 2.75	10.75	computed	185	247	74.9
				measured	188	270	70.0
				difference	-1.6%	-8.5%	+4.9
150	1500	-13.75	24.25	computed	747	967	77.2
				measured	744	1035	72.0
				difference	+0.4%	-6.6%	+5.2
150	2195	-22.50	27.50	computed	835	1147	72.8
				measured	729	1065	68.5
				difference	+14.5%	+7.7%	+4.3

TABLE 6.3 Comparison between computed and measured results

- i) There may be a switching time delay associated with the optical heads. The angular delay is directly proportional to the speed. At speed $2195 \left[\frac{\text{rev}}{\text{min}} \right]$ the delay of 0.75° in θ_c is sufficient to compensate the above difference in P_{out} .
- ii) The effect of the snubbing circuits* is not included in the computer model and their effect on the current waveform is to reduce the peak of the secondary current and as a consequence the power returned to the supply is reduced. The snubbing circuit power loss is proportional to frequency (speed).
- iii) The iron losses are not included in the computer model and these depend on the frequency of flux reversals in the different core paths and on their differing flux densities.

Similar agreement has been obtained for the other tested machines.

6.5 Conclusions

The methods for predicting the performance of doubly-salient reluctance motors from computed or measured $\psi(\theta, i)$ data have been reviewed and basic weaknesses under highly saturated conditions have been identified. The model equations have been reformulated in a more suitable form which avoids the use of differentials of the input data $\psi(\theta, i)$ but which necessitates the generation of an inverse table of data $i(\theta, \psi)$. This is efficiently achieved using quadratic interpolation and at the same time allows the specification of unequally spaced currents and hence the minimum quantity of input data.

Given the non-linear flux-linkage/rotor angle/current data and the constant speed, supply voltage, switching angles and winding resistances, the new model computes the torque $T(\theta, i) \Big|_{i=\text{const}}$ and the

* Snubbing circuits are resistor/capacitor networks connected across the main transistors to suppress voltage spikes and to reduce switching losses - see Chapter 8.

running performance of machine (average torque, output power, input power, efficiency, mean flux-linkage, rms of phase current, rms of total current, ripple of total current).

Good agreement between computed and measured results has been demonstrated. Although other authors have not given full details of the accuracy of their methods, it appears from what has been published that the new method described above is superior.

A paper describing the new computational method presented in this chapter has been published in the Proceedings IEE, May 1979, pp 393-398.

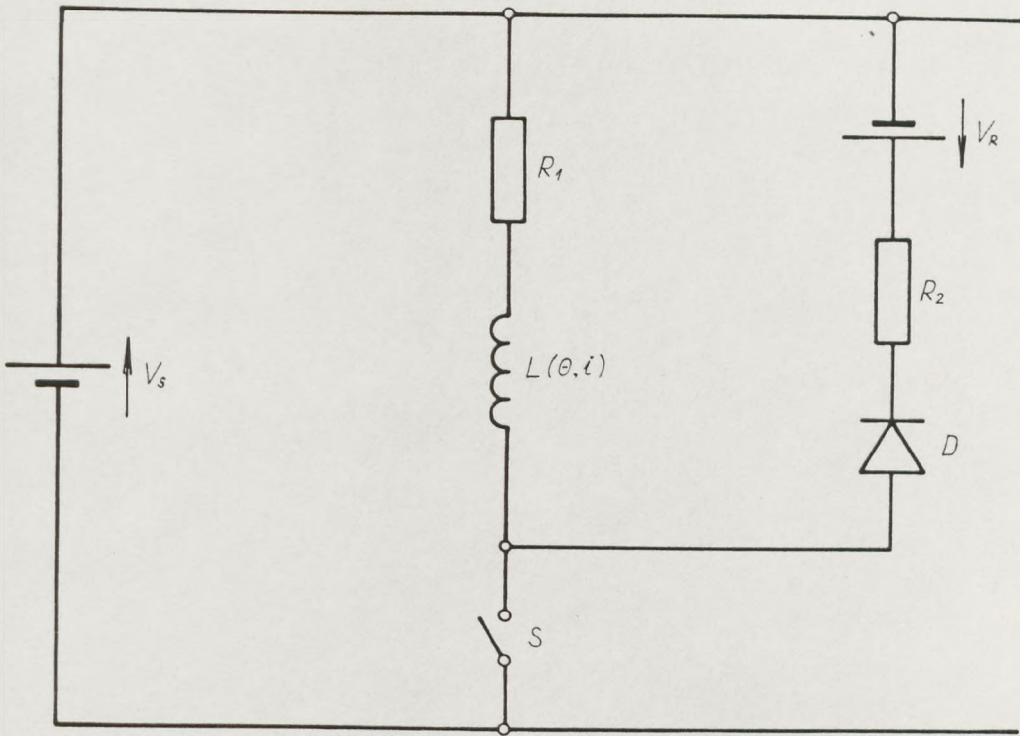


FIG 6.1 Basic machine circuit

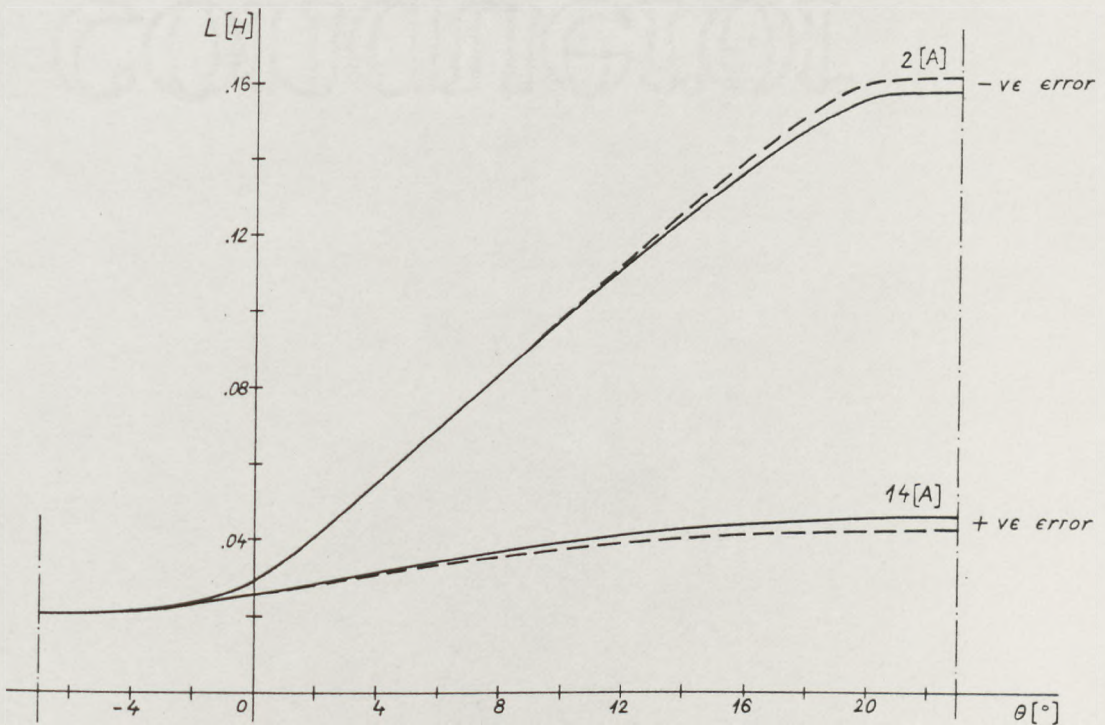


FIG 6.2 Inductance vs angle

———— fitted by polynomial in i

----- measured

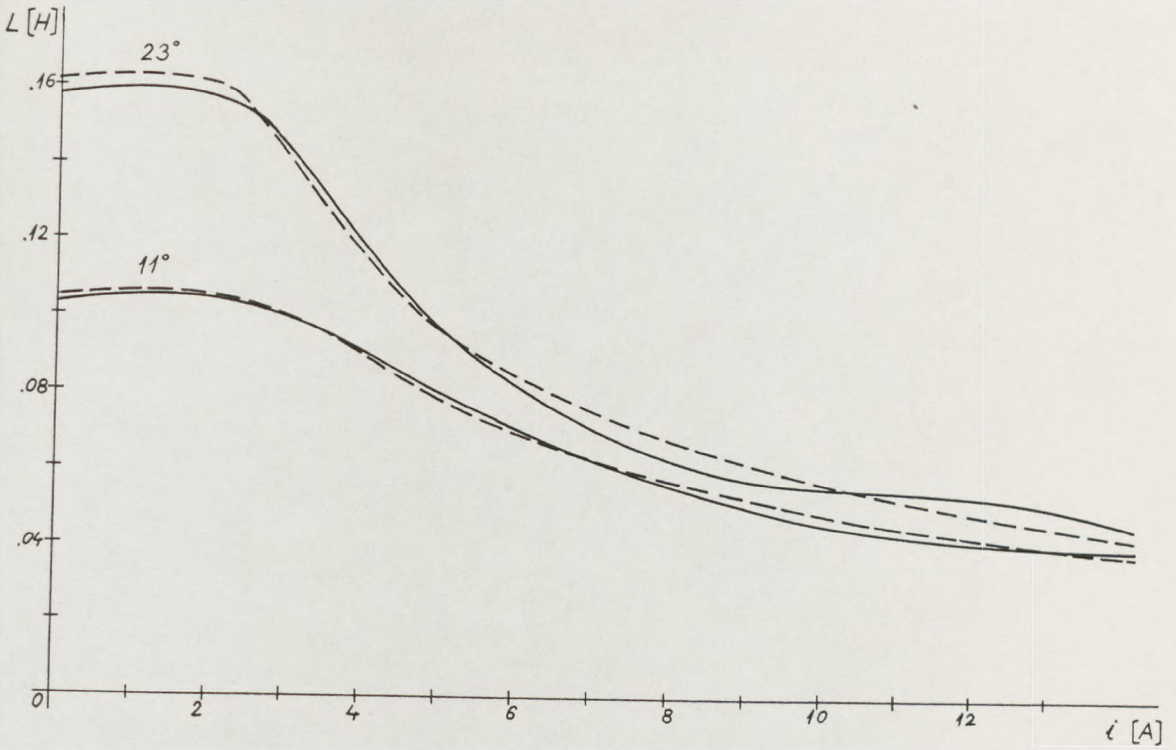


FIG 6.3 Inductance vs current

—— fitted by polynomial in i
 - - - - measured

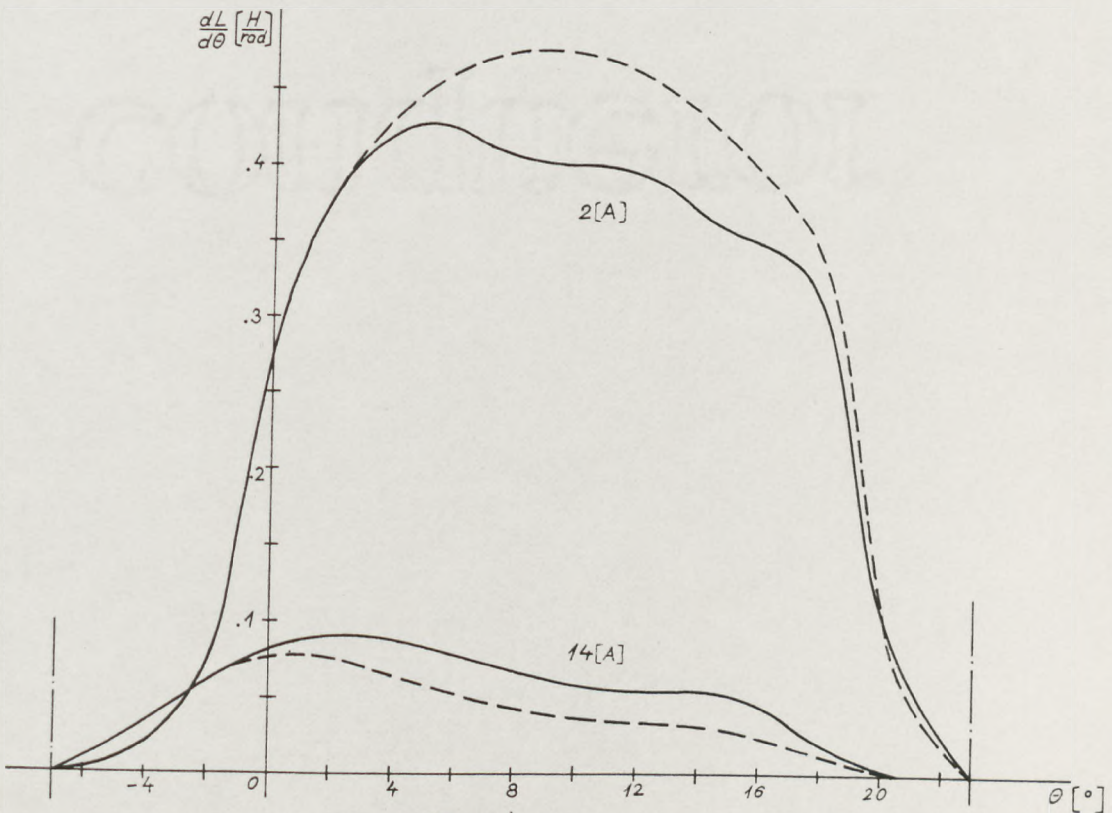


FIG 6.4 Derivative $\left. \frac{dL(\theta, i)}{d\theta} \right|_{i=\text{const}}$ vs angle

—— corresponds to fitted inductance curve
 - - - - corresponds to measured inductance curve

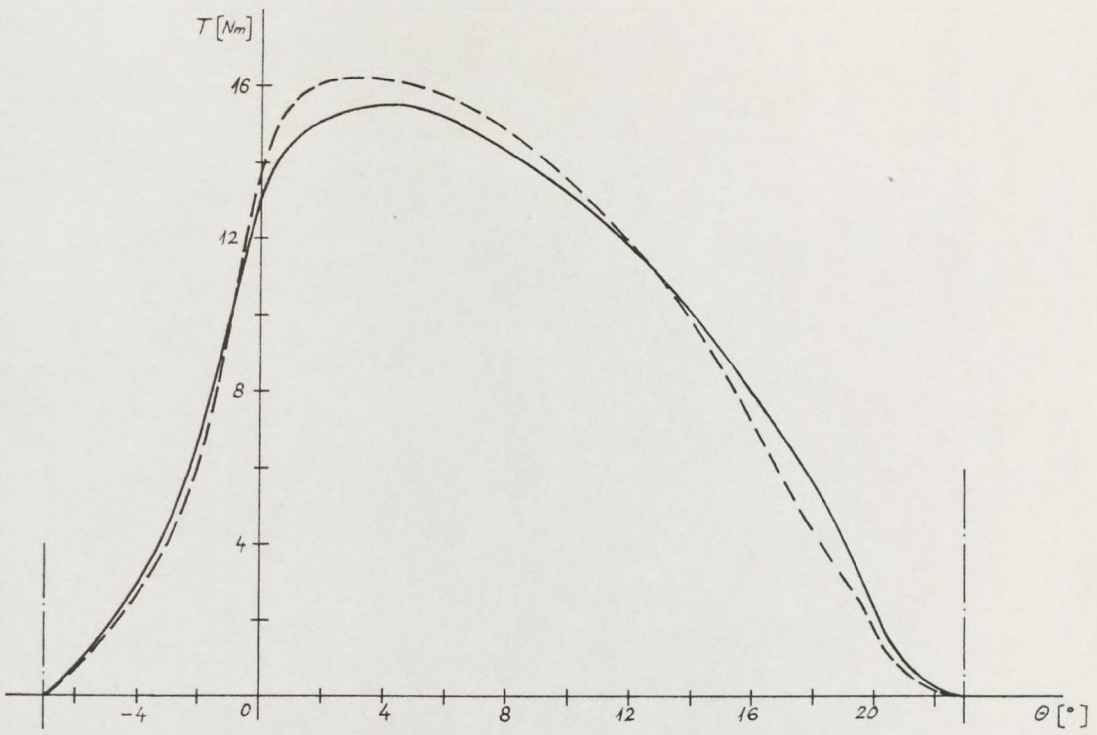


FIG 6.5 Static torque curve at 14 [A]

———— computed by Blenkinsop's method
 - - - - - measured

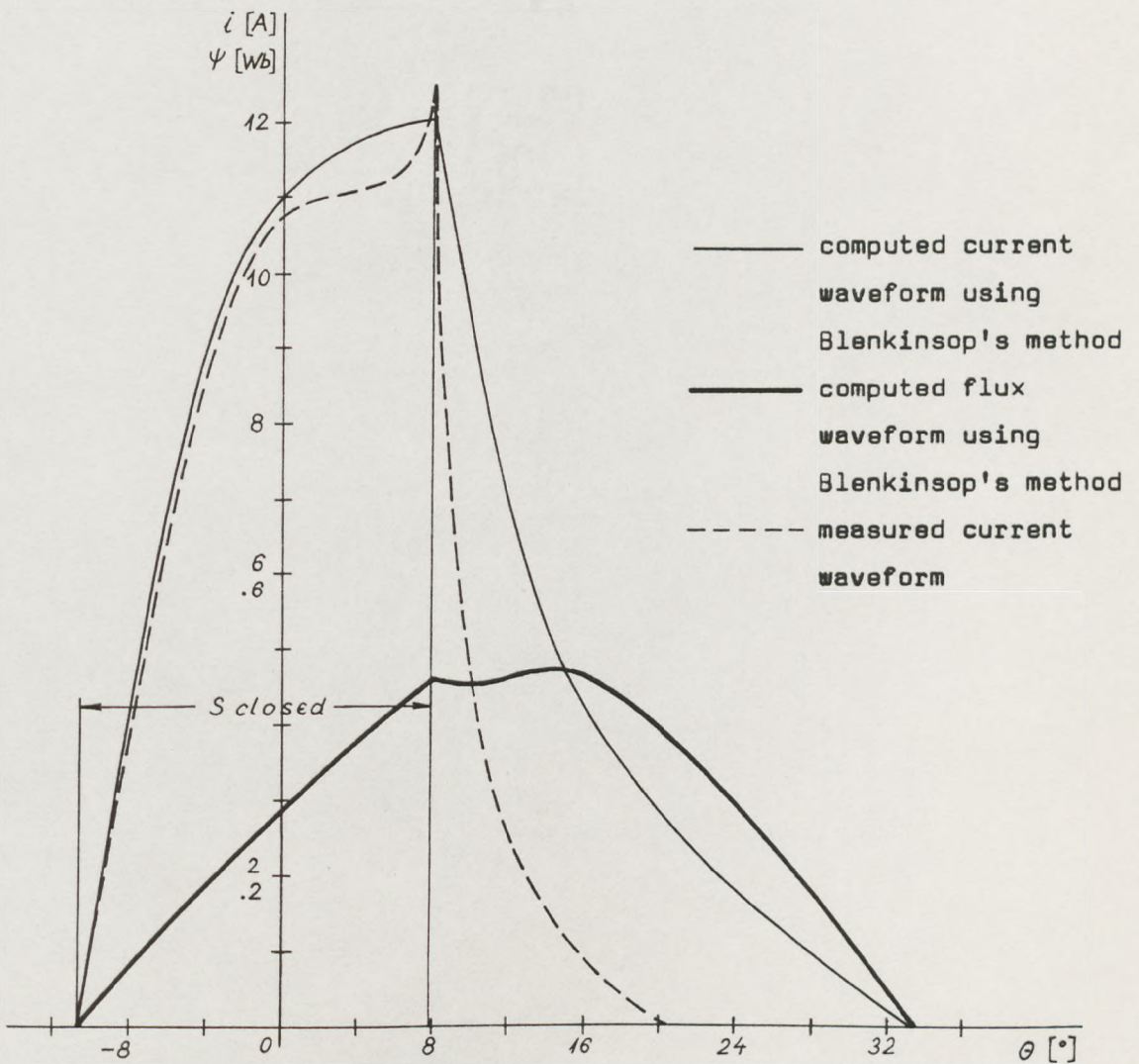


FIG 6.6 Current and flux waveforms

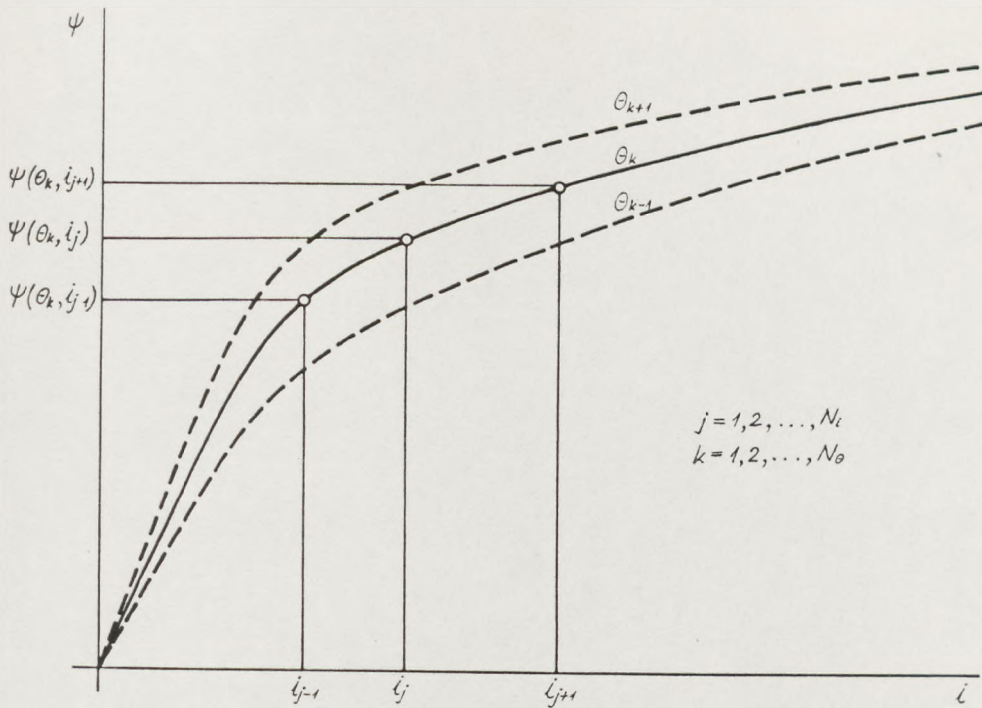


FIG 6.7 Flux-linkage as a function of current for 3 different rotor angles, illustrating the use of unequally spaced current values for tabulating the data

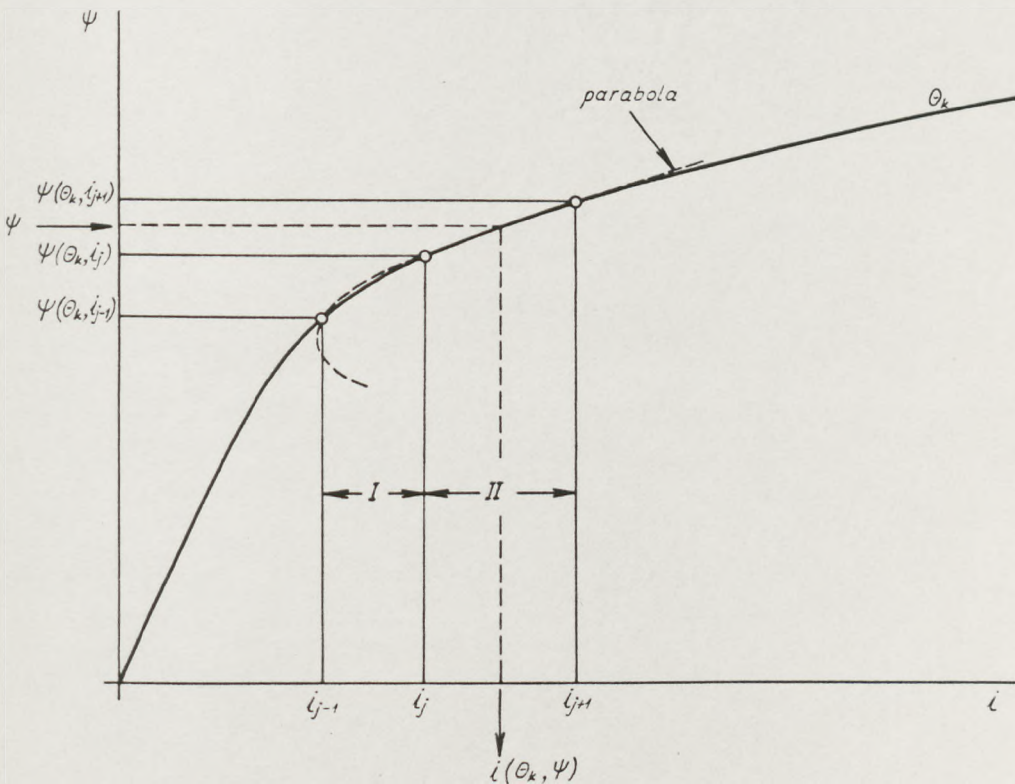


FIG 6.8 $\psi(\theta, i) |_{\theta=\text{const}}$ curve illustrating the use of quadratic interpolation to find current i corresponding to a flux-linkage ψ using 3 tabulated points

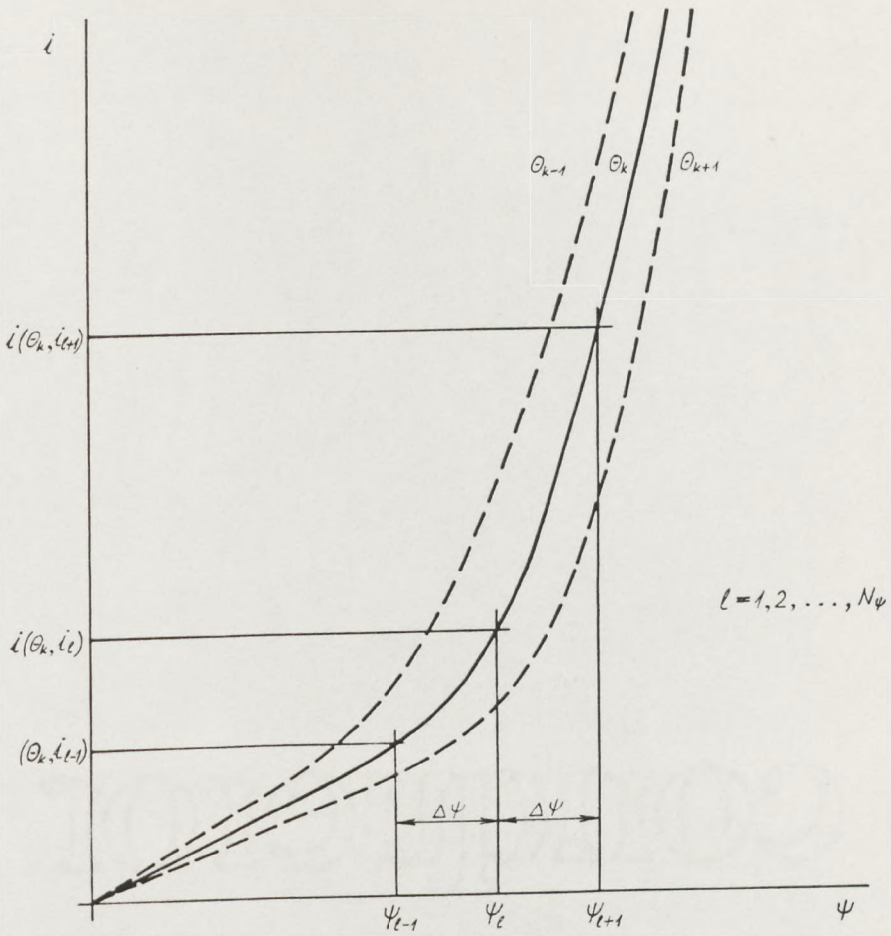


FIG 6.9 $i(\theta, \psi) |_{\theta=\text{const}}$ curves. These are the derived inverse functions of those shown in FIG 6.7

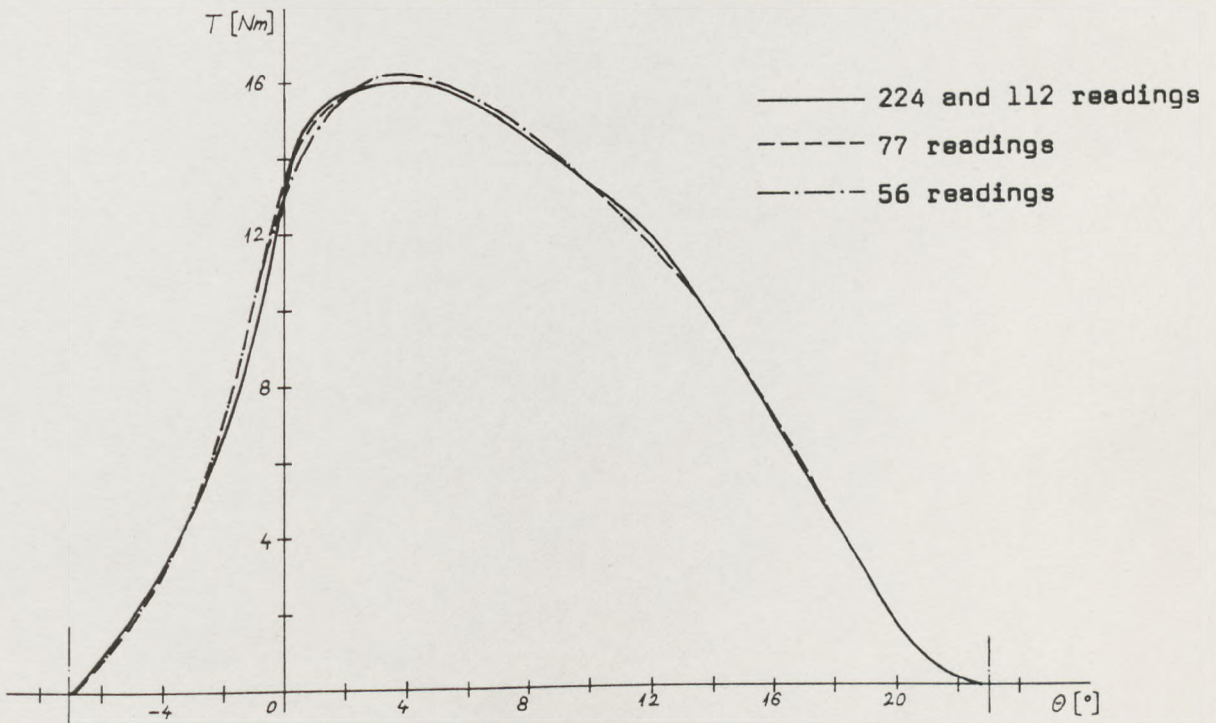


FIG 6.10 Torque/angle curves for various numbers of readings in input $\psi(\theta, i)$ table

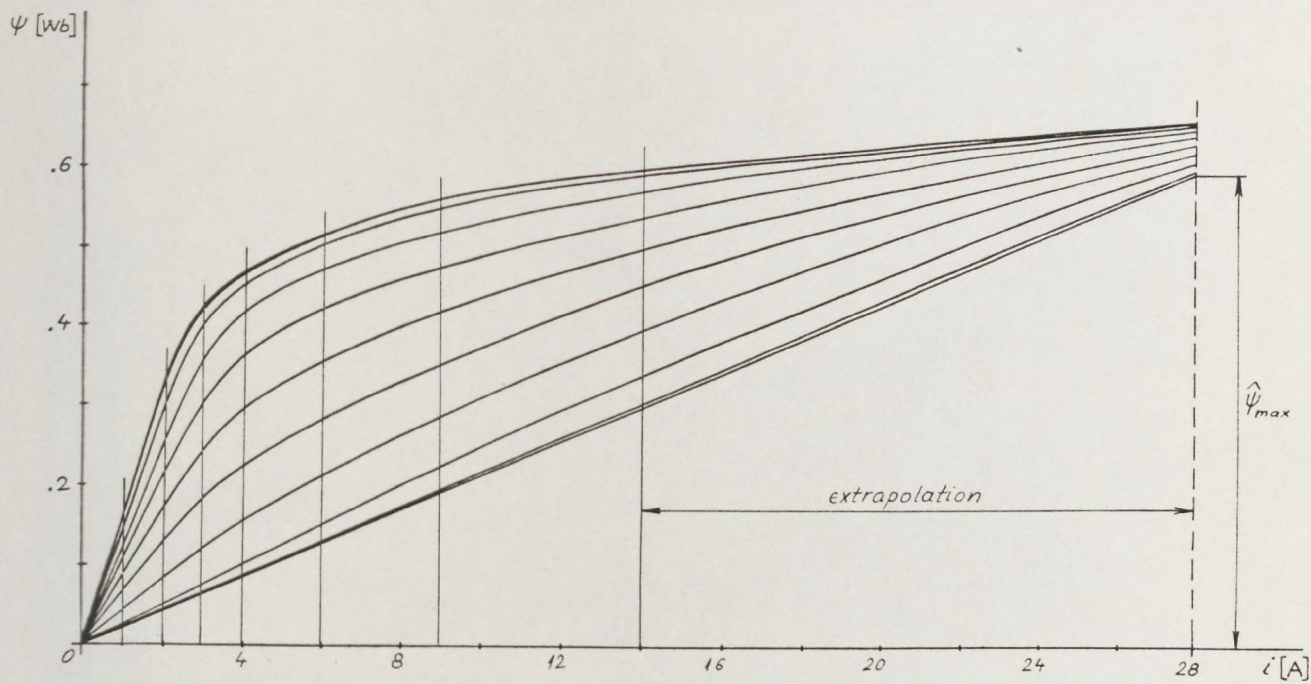


FIG 6.11 Flux-linkage/rotor angle/current data

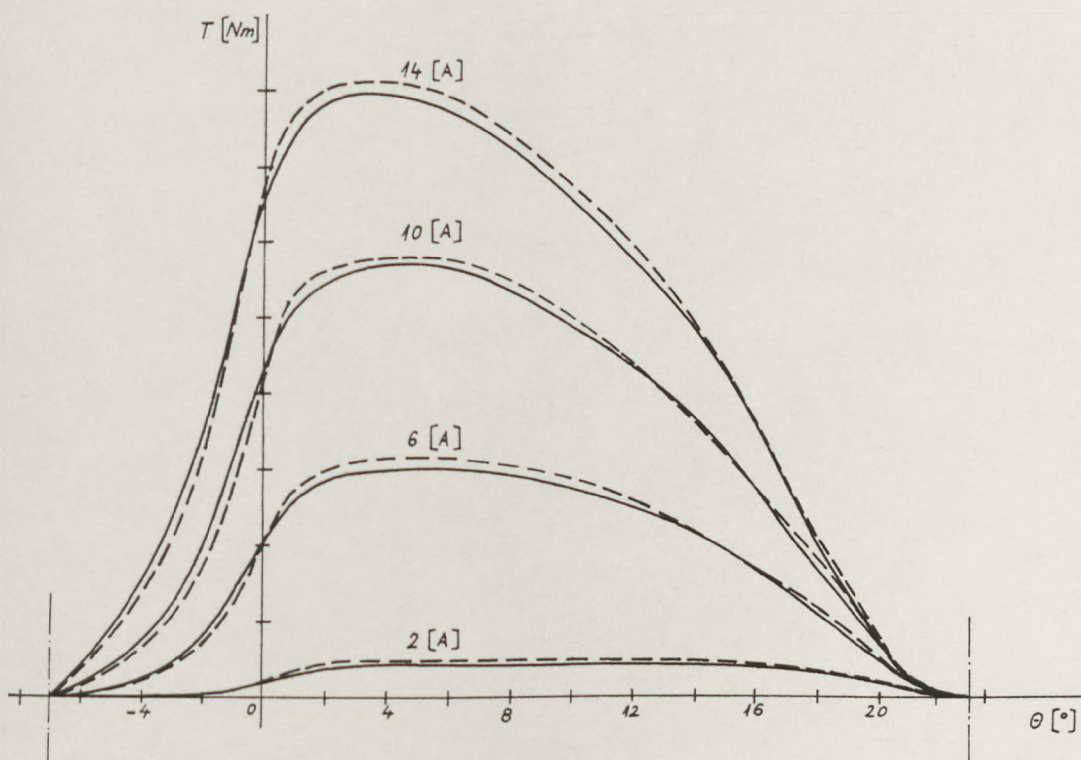


FIG 6.12 Static torque curves

— computed
 - - - measured

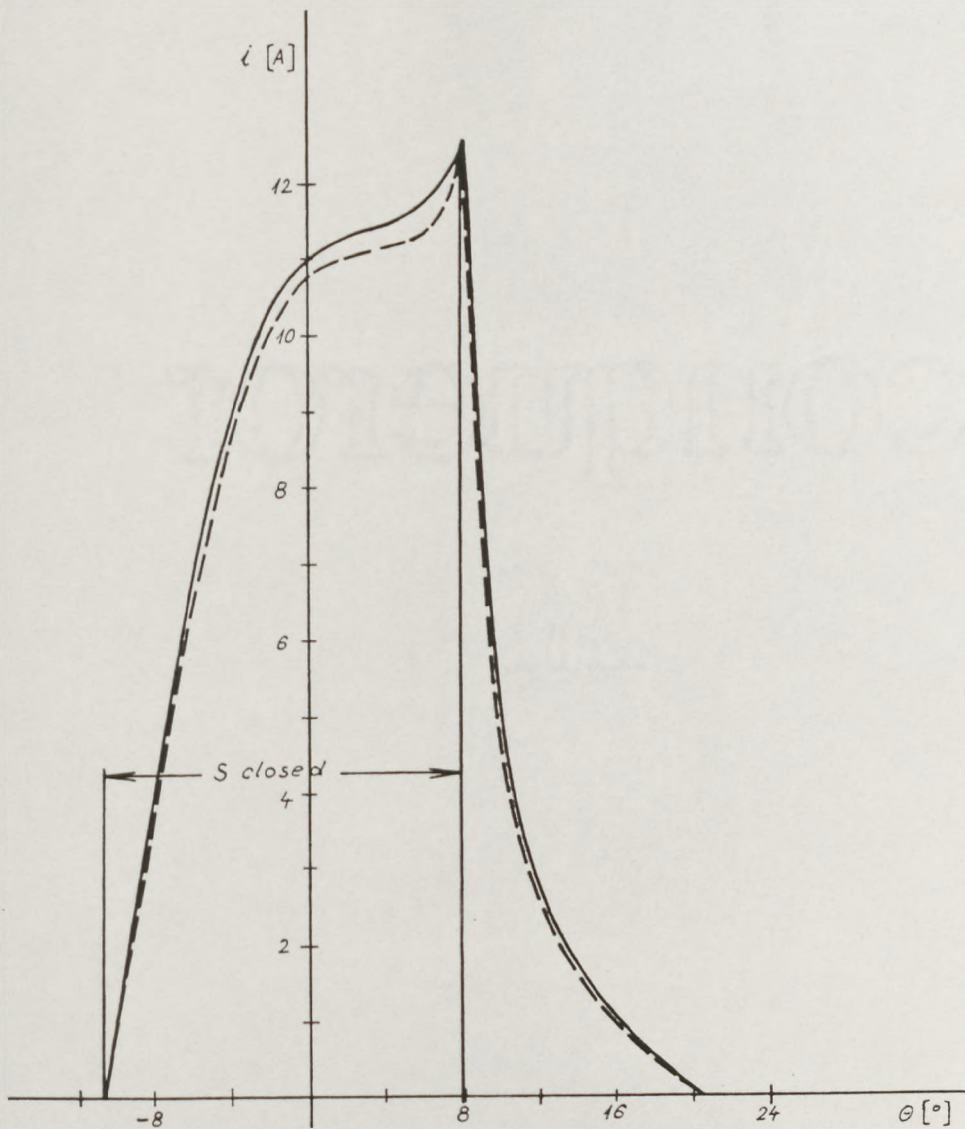


FIG 6.13 Current waveform
 ——— computed
 - - - - measured

Appendix 6A

Table $\Psi(\theta, i)$

N_{θ}'	N_i'	θ_{\min}	$\Delta\theta$	i_{\max}	h_i	Δi
N_p	N_g	i_{N_i}'	$\hat{\Psi}_{\max}$			
i_1	i_2	.	.	.	i_{N_i}	i_{N_i}'
$\Psi_{1,1}$	$\Psi_{1,2}$.	.	.	Ψ_{1,N_i}	Ψ_{1,N_i}'
$\Psi_{2,1}$	$\Psi_{2,2}$.	.	.	Ψ_{2,N_i}	Ψ_{2,N_i}'
.
.
$\Psi_{N_{\theta},1}$	$\Psi_{N_{\theta},2}$.	.	.	Ψ_{N_{θ},N_i}	Ψ_{N_{θ},N_i}'

where

- N_{θ}' [NTHET]* is number of angles specified in table (in the case of symmetrical inductance waveform $N_{\theta}' = 2N_{\theta} + 1$, where N_{θ} is number of angle measurement points);
- N_i' [NCURR] is number of currents specified in table ($N_i' = N_i + 1$, where N_i is number of current measurement points);
- θ_{\min} [THETHMIN] is angle of first entry in the input data with respect to the angle reference (zero reference corresponds to aligned leading edges);
- $\Delta\theta$ [THETINC] is angular increment between tabular points;
- i_{\max} [CMAX] is maximum current for which results will be required ($i_{\max} < i_{N_i}$);

* Variable names in square brackets are those which are used in computer program.

- h_i [XINC] is increment of current used for the integration along the flux-linkage/current curve to find the co-energy. (i_{\max}/h_i must be an integer and should be around 30);
- Δi [CSTEP] is interval in current between points at which torque is calculated ($\Delta i/h_i$ must be an integer);
- N_p [NPRL] is number of ' Δi 's which will appear between current values at which the results are printed;
- N_g [NPRG] is number of ' Δi 's which will appear between current values at which the results are plotted;
- $\hat{\psi}_{\max}$ [FM] is the maximum allowed value of flux-linkage, ie
- $$\hat{\psi}_{\max} = V \frac{\phi/2}{\omega_T} \sqrt{\frac{\omega_T}{\omega_B}}$$
- $i_{N_1'}$ [CURMAX] is value of current usually corresponding to extrapolation point. (The quadratic interpolation is used in the program and therefore an extra current point is required. It is more economic if the whole current measuring region is exploited in the results and therefore this extra current point can be obtained by extrapolating curves $\psi(\theta, i)|_{\theta=\text{const}}$.) The value of $i_{N_1'}$ may be obtained assuming that curves flux-linkage/current corresponding to minimum inductance position is linear up to $\hat{\psi}_{\max}$. Then $i_{N_1'} = \hat{\psi}_{\max}/L_0$;
- $i_1, i_2, \dots, i_{N_1'}$ [CUR] are the values of current at which values of flux-linkage are measured ($i_1 > 0$);

$\psi_{k,j}$ [FL] ($k = 1, 2, \dots, N_{\theta}'$; $j = 1, 2, \dots, N_{\psi}'$) are values of flux-linkage specified in the table.

Appendix 6B

Table $i(\theta, \psi)$

N_{θ}'	N_{ψ}	$\Delta\theta$	$\Delta\psi$	θ_{\min}	$i_{N_{\theta}'}$	$\hat{\psi}_{\max}$
ψ_1	ψ_2	.	.	.	$\psi_{N_{\psi}}$	

$i_{1,1}$	$i_{1,2}$.	.	.	$i_{1,N_{\psi}}$	
$i_{2,1}$	$i_{2,2}$.	.	.	$i_{2,N_{\psi}}$	
.	
.	
.	
$i_{N_{\theta}',1}$	$i_{N_{\theta}',2}$.	.	.	$i_{N_{\theta}',N_{\psi}}$	

$\Delta\psi$ [FINC] is flux-linkage increment between tabular points;

N_{ψ} [NFLUX] is number of flux-linkage values specified in table ($N_{\psi} = \frac{\hat{\psi}_{\max}}{\Delta\psi} + 2$ and should be around 10);

$\psi_1, \psi_2, \dots, \psi_{N_{\psi}}$ [VFLUX] are the values of current at which values of current are calculated ($\psi_{N_{\psi}} = \hat{\psi}_{\max}$);

$i_{k,1}$ [VCUR] ($k=1,2,\dots,N_{\theta}'$; $\ell=1,2,\dots,N_{\psi}$) are computed values of current.

Appendix 6CInput data for the program for computation of running performance

Using appropriate instruction the program will read data from stored table $i(\theta, \psi)$ (see Appendix 6.B). In addition the following data must be specified.

IDMOT	ITC	NC		
s	R_1	R_2	VIH	VIL
INTEX	V_s	θ_o	n	
$(\theta_c)_1$	$(\theta_c)_2$.	.	$(\theta_c)_{NC}$

where

IDMOT		identifies the motor;
ITC		identifies the type of switching circuit (ITC = 1-sw. circ. with bifilar winding and transistor, ITC = 2-sw. circ. with two transistors, ITC = 3-sw. circ. with bifilar winding and thyristor);
NC		is number of switching-on angles at which program is run;
$(\theta_c)_1, (\theta_c)_2, \dots, (\theta_c)_{NC}$	[THETC]	are switching-on angles;
s	[S]	is stator pole arc;
R_1, R_2	[RS, RSERT]	are winding resistances (R_1 corresponds closed 'S' and R_2 corresponds to open 'S');
VIH, VIL		are upper and lower current limits for simulation of hysteretic current limit;

INTEX consists of eight letter characters (INTERNAL or EXTERNAL*);

V_s [VS] is d.c. supply voltage;

θ_o [THETO] is overlap angle of two phases ($\theta_o = \theta_{con} - \epsilon$);

n [SPEED] is speed.

* If the characters INTERNAL are used then the data stored internally are used. If the characters EXTERNAL are used then the program will demand additional data in the form:

N_s N_r LCM q TR
 FW_1 FW_2 FW_3 FW_4 FW_5 FW_6

where

N_s [NS] is number of stator poles;

N_r [NR] is number of rotor poles;

LCM is least common multiple of N_s and N_r ;

q [NPH] is number of phases;

TR [ERTRAT] is turns ratio (primary/secondary) of bifilar winding (for switching circuit without bifilar winding TR = 1)

FW_1, \dots, FW_6 are coefficients of fifth-order polynomial used for fitting of friction and windage losses in function of speed ω . If these losses are neglected then these coefficients are zero.

CHAPTER 7

APPLICATION OF THE NON-LINEAR MATHEMATICAL MODEL

7.1 Introduction

The importance of the non-linear mathematical model presented in the previous chapter lies in its application in those areas of investigation where it is inconvenient to use or to build experimental machines. This importance is demonstrated in this chapter in the following applications:

- a) Searching for the optimum switching angles with respect to efficiency, which give the required output power for a given voltage and speed;
- b) Finding the current needed for producing base torque at standstill;
- c) Investigating the effects of changes of the number of turns on the performance of the motor;
- d) Developing a design procedure.

In this last application the understanding built up in earlier chapters is brought to bear upon the development of a design method. The resulting procedure is based on an approximate analytical method for producing the $\psi(\theta, i)$ table and on the use of the non-linear mathematical model.

7.2 Searching for the Optimum Switching Angles using Computed Results

It has already been shown in Chapters 4 and 5 that, when the motor is not working near its output limit, there is normally a range of switching angles (θ_c and θ_{con}) which gives the required output power. A general analytical relationship between a range of switching angles and power for a given voltage and speed cannot be defined explicitly in terms of θ_c and θ_{con} even in the simple linear treatment of the

switched reluctance machine (see Section 4.5.2) and therefore a graphical method is used.

It will now be shown how it is possible graphically using computed results, to select the optimum switching angles (say, with respect to efficiency) which give the required output power for a given voltage and speed. (The procedure, given below, is demonstrated using the measured $\psi(\theta, i)$ data of the D90M2-4 motor when the required power is 0.75 [kW], $V = 150$ [V], $n_B = 750$ $\left[\frac{\text{rev}}{\text{min}}\right]$ and $n_T = 2250$ $\left[\frac{\text{rev}}{\text{min}}\right]$.)

The values of the output power computed at various combinations of switching angles at base and top speed are plotted in Fig 7.1(a) as families of curves $P_{\text{out}}(\theta_c, \theta_{\text{con}}) \Big|_{\theta_{\text{con}} = \text{const}}$ for the corresponding speeds. From the crossing points of these curves with the line representing constant output power (0.75 [kW]) the pairs of switching angles are found and are represented in the diagram θ_{con} vs θ_c by the curve $\theta_{\text{con}}(\theta_c)$ for the corresponding speed in Fig 7.1(b). The values of efficiency and primary rms current (or values of any other computed variable) are found by interpolation of the computed results for the switching angles from the curve $\theta_{\text{con}}(\theta_c)$ at constant power and speed and are represented in the graphs of $\eta(\theta_c)$ and $I_1(\theta_c)$ in Fig 7.2(c) and (d) respectively.

The switch-on angle θ_c which corresponds to the maximum efficiency is found from the curve of $\eta(\theta_c)$ and the corresponding value of θ_{con} is obtained from the curve $\theta_{\text{con}}(\theta_c)$. The points corresponding to optimum switching angles at base and top speed are marked by M_B and M_T in graph θ_{con} vs θ_c (Fig 7.1(b)).

It is seen that the minimum primary rms current is obtained at the same switching angles which correspond to the maximum efficiency. This is because the iron losses are neglected in the non-linear mathematical model.

The method of searching for the optimum switching angles of the machine (presented above) can be applied at various speeds requiring constant power or constant torque (depending on the type of drive) and the control law for the speed of a given motor can be established.

7.3. Finding the Current Needed for Producing Base Torque at Standstill

The most important feature of the standstill condition is the current needed for producing base torque (i.e. the full torque at base speed). From the experimental results presented in Chapter 5 it is seen that this value of current* can be higher than the peak current in the running condition at full torque and base speed, and the switching devices and windings must stand this current during starting. Having an accurate mathematical model it is possible to find the current needed for producing base torque at standstill (I_s) without the difficulties associated with static torque measurements. The graphical method which is used to find the current I_s is demonstrated below on the model of the D90M2-4 motor.

From computed static torque curves $T(\theta, i) \Big|_{i=\text{const}}$ the values of ϵ -torque (T_ϵ - see definition in Section 5.5.2), where $\epsilon = 15^\circ$, are found and plotted against current (curve $T_\epsilon(i)$ in Fig 7.2). The value of current I_s , needed for producing base torque of 9.55 [Nm] at standstill, is found from the curve $T_\epsilon(i)$ and it is 14.4 [A].

The graphical methods for handling the computed results presented in this and the previous section are used in the following sections.

7.4 Effects of Changing the Number of Turns on the Performance of the Machine

In Chapter 2 the magnetic configuration of the machine was defined by the physical dimensions of the magnetic structure and the windings and the number of turns per phase. If the dimensions of the magnetic structure and the windings remain constant and only the number of turns per phase is changed, keeping the uniform distribution of turns within the winding cross-sectional area, then the shape of the field lines remains unchanged (the effective flux/mmF curves are unchanged)

* Having a transducer with a simple angular resolution in the starting mode of operation, starting torque is produced by only one phase switched on at a time.

and only the number of linkings changes for a given mmf. In terms of the $\psi(\theta, i) \Big|_{\theta=\text{const}}$ curves, which describe the machine, this means that only the scales of ψ and i are changed, whereas the shape of $\psi(\theta, i) \Big|_{\theta=\text{const}}$ curves remains the same and therefore the effect of changing the number of turns on the performance can be hypothetically examined by appropriate changes in the input table of data of the computer model of the machine as follows.

Consider a family of $\psi(\theta, i) \Big|_{\theta=\text{const}}$ curves corresponding to a given number of turns per phase of a given machine. If the number of turns is multiplied by a factor λ , then the values of the ordinates (ψ) of the curves change by λ (since the number of linkings changes by λ), and the values of the abscissas change by $\frac{1}{\lambda}$. Both the resistances (see Appendix 5A) and the inductances of phase windings change by λ^2 .

If the number of turns changes by λ , then the current I_s needed for producing the required torque at standstill, changes by $\frac{1}{\lambda}$ (since for the constant value of required torque $T(\theta, i) = \partial \Psi' / \partial \theta = \partial \int_0^i \psi di / \partial \theta$, the areas under $\psi(\theta, i) \Big|_{\theta=\text{const}}$ curves (co-energy) remain constant and hence the value of current to produce the required torque must change by $\frac{1}{\lambda}$). Therefore from this point of view it is desirable to have the largest possible number of turns. (The number of turns is limited by the required value of the output power - see below.)

The comparison of the performance when the number of turns changes is examined on the D90M2-4 motor supplied at 150 [V]. The computed performance of the motor for various numbers of turns (i.e. various values of factor λ) were represented using the procedure shown in Section 7.2 and the results corresponding to maximum efficiencies at base and top speed are summarised in Table 7.1. Inspection of this table shows that the maximum output power at top speed, which is obtained at $\theta_{\text{con}} = 30^\circ$ (fully-open conduction angle) and $\theta_c = -24^\circ$,

changes by $\frac{1}{\lambda^2}$ * when the number of turns changes by λ . Therefore the number of turns per phase can be increased until the maximum output power at top speed is greater or equal to the required output power (0.75 [kW]). For D90M2-4 machine the limiting number of turns per phase is 1.17×290 .

When $\lambda = 0.9$ (i.e number of turns is 0.9×290) the performance at base speed is worse than for $\lambda = 1$ (i.e for the original number of turns 290), but at top speed the efficiency is better when $\lambda = 0.9$ (the current at top speed is not critical since it is lower than the current at base speed).

When $\lambda = 1.1$ the performance at base speed is slightly better (with respect to the current) than those for $\lambda = 1$, but at top speed the efficiency is worse.

Taking an overall view of the performance and the value of current I_s , needed for producing the base torque of 9.55 [Nm] at standstill, the originally chosen number of turns ($N = 290$) is the best compromise for the D90M2-4 motor. The ratio of flux densities at base and top speed for $N = 290$ (from Table 7.1) is $1.74/1.04 = 1.67$. This result justifies the empirical formula $\psi_B/\psi_T \approx \sqrt{\omega_T/\omega_B}$ deduced in Section 5.2.8.

* The reason for this lies in the fact that the magnetic circuit of the machine is not saturated at top speed and therefore the current must change by $\frac{1}{\lambda^2}$ to maintain constant flux-linkage (since the voltage, speed and switching angles are constant) and hence the output power ($\frac{1}{2} i^2 \frac{dL}{d\theta} \omega$) changes by $\frac{1}{\lambda^2}$.

7.5 Computational Design Procedure

7.5.1 Design method

The essential constructional features of a switched reluctance motor are a stator with salient poles carrying spool type of windings and a rotor with salient poles. The essential electrical feature is that the phase windings are supplied by pulses of constant voltage which are switched in response to signals from a rotor-position sensor. Those features make the switched reluctance motor radically different from conventional electrical machines. In addition the saturation has been shown to be very significant factor.

The means for design which are available at this stage of machine development are:

- a) theoretical knowledge presented in previous chapters,
- b) the design philosophy applied in designing the experimental motors and the experimental results presented in Chapter 5,
- c) the analytical estimation of the minimum and maximum inductances presented in Chapter 3 and
- d) the non-linear mathematical model of motor described in Chapter 6.

The design method is based on using the non-linear computer model which requires specification of the electric and magnetic parameters of the machine (winding resistances and table $\psi(\theta, i)$). Since these parameters can be specified only if the dimensions of the machine are known, the initial values of the machine dimensions must be assumed according to the specifications of the machine. Using the cut-and-try technique, the appropriate dimensions, in the light of machine performance, can be found.

7.5.2 Production of the $\psi(\theta, i)$ table

For the purposes of computational design, based on using the non-linear computer model, it is necessary to establish a method for calculating the elements of the $\psi(\theta, i)$ table for given dimensions of the machine. The accurate calculation of the elements of the $\psi(\theta, i)$ table would require a 3-dimensional numerical field solution. However, even if the 3-dimensional numerical field solution were available, it would be very inconvenient for use in a basic design, since for each combination of the machine dimensions, 88* solutions (corresponding to the various rotor positions and values of current) would be required. This would be very expensive and time consuming. It will now be shown how a simple analytical method for the approximate estimation of the elements of the $\psi(\theta, i)$ table, can provide a very satisfactory prediction of the machine performance for basic design.

The method is based on estimating the values of the minimum and maximum inductances and constructing the intermediate parts of the $L(\theta, i)|_{i=\text{const}}$ curves by a piece-wise linear approximation. Fig 7.3 shows the curve $L(\theta, i)|_{i=\text{const}}$ of the D90M1 motor obtained by piece-wise linear approximation using the estimated values of L_0 and L_i . (These curves should be compared with those in Fig 5.10.) In Chapter 3 it has been shown that the minimum inductance can be estimated very accurately if the fringe flux at the ends of core is excluded. An allowance based on rough approximation for this fringe flux has been made, but such approximation gives an underestimate by 14% of the measured value of L_0 . (If this difference is expressed as percentage of the estimated value $L_0^{(e)}$, it is 16%.) The difference in percentages for the other types of constructed switched reluctance motor is very close to the one given above.** Therefore it can be empirically stated that $L_0 = 1.16 L_0^{(e)}$. The value of the minimum inductance shown in Fig 7.3 has been obtained by using this formula.

* 88 is proposed number of the elements in $\psi(\theta, i)$ table - see Section 6.4.7 and Appendix 6A.

** For $l/d = 1.0$.

The values of maximum inductance at 1, 2, 3, 4, 6, 9 and 14 [A] shown in Fig 7.3 have been obtained from the diagram in Fig 3.13.

If the angular increment between tabular points is $\Delta\theta$ and the angle θ_{\min} shown in Fig 7.3, which corresponds to the minimum inductance position, is the angle of first entry in the input data, then the angles θ_a and θ_b are generally given by

$$\theta_a = \text{last reading in minimum inductance region before overlap occurs } (\theta=0) = \theta_{\min} + [\text{INT} (|\theta_{\min}|/\Delta\theta)] \Delta\theta ,$$

$$\theta_b = \text{last reading in rising inductance region before full overlap} \\ = \theta_{\min} + [\text{INT} ((|\theta_{\min}| + s)/\Delta\theta) - 1] \Delta\theta .$$

The appropriate values of inductances at these angles have been found to be $1.2 L_o$ and $0.97 L_i$ respectively.

Thus, using the piece-wise linear approximation the $L(\theta, i)|_{i=\text{const}}$ curves are defined as follows:

$$\text{For } \theta = \theta_{\min} \quad , \quad L = L_o$$

$$\text{For } \theta_{\min} < \theta < \theta_a \quad , \quad L = L_o$$

$$\text{For } \theta = \theta_a \quad , \quad L = 1.2 L_o$$

$$\text{For } \theta_a < \theta < \theta_b \quad , \quad L = 1.2 L_o + \frac{0.97 L_i - 1.2 L_o}{\theta_b - \theta_a} (\theta - \theta_a)$$

$$\text{For } \theta = \theta_b \quad , \quad L = 0.97 L_i$$

$$\text{For } \theta_b < \theta < \theta_{\max} \quad , \quad L = L_i$$

$$\text{For } \theta = \theta_{\max} \quad , \quad L = L_i$$

The $\psi(\theta, i)$ table is obtained by multiplying the values of $L(\theta, i)$ with corresponding values of current.

The Figs 7.4(a) and (b) show the computed current waveforms of the D90M1 motor when the $\psi(\theta, i)$ table is obtained using the above method and when it is obtained by measurements. The computed performance for these two cases (output power, input power and efficiency) and their differences at two different operating conditions are shown in Table 7.2.

V	n	θ_c	θ_{con}		P_{out}	P_{in}	η
V	$\frac{rev}{min}$	o	o		W	W	%
150	750	-10.75	18.50	comp. $\psi(\theta, i)$	728	1330	54.7
				meas. $\psi(\theta, i)$	755	1313	57.5
				difference	-3.6%	+1.3%	-2.8
150	2195	-22.5	27.50	comp. $\psi(\theta, i)$	825	1142	72.2
				meas. $\psi(\theta, i)$	835	1147	72.8
				difference	-1.2%	-0.4%	-0.6

TABLE 7.2 Comparison between computed results when $\psi(\theta, i)$ table is obtained using piece-wise linear approximation and when it is obtained by measurements

The agreement is considered to be satisfactory and demonstrates the value of the analytical method for calculating the $\psi(\theta, i)$ table, given above, in a basic design procedure.

7.5.3 Basic design procedure

The design problem to be considered can be formulated as follows: For specified continuously rated output power, speed range, voltage and minimum efficiency, determine suitable dimensions of the magnetic structure and winding parameters of the switched reluctance motor.

As the first approach to the design, the following basic design parameters can be chosen independently according to the considerations made in Chapters 2 and 4 and experimental results presented in

Chapter 5:

- number of stator poles N_s ,
- number of rotor poles N_r ,
- normalised back iron width $C (= \frac{c}{d_o})$,
- normalised air-gap length of the rotor interpolar space $G_i (= \frac{g_i}{d_o})$,
- stator pole arc s and
- rotor pole arc r

Air-gap length g is chosen to be as small as possible in consistent with the manufacturing process, output power and top speed of the machine.

According to the specified requirements (output power and speed range) and using the equivalent induction motor as a guide, the initial values of stator outside diameter (d_o), rotor diameter (d) and core length (l) can be assumed.

Having assumed the dimensions of the magnetic circuit, the number of turns per phase can be estimated using the empirical formula deduced in Section 5.2.8.

$$\hat{\psi}_B / \hat{\psi}_T \approx \sqrt{\omega_T / \omega_B}$$

$$\therefore \psi_B \approx \frac{V \theta_{con} (T)}{\omega_T} \sqrt{\omega_T / \omega_B}$$

Hence the number of turns per phase

$$N \approx \frac{V \theta_{con} (T)}{\hat{B} A_{Fe} \omega_T} \sqrt{\omega_T / \omega_B}$$

$$\approx \frac{V \theta_{con} (T)}{\hat{B} l d (\sin \frac{s}{2}) \omega_T} \sqrt{\omega_T / \omega_B}$$

In this formula \hat{B} is peak flux density in stator pole root corresponding to the peak torque for which machine is rated and according to Chapter 5 and Table 7.1 the value of \hat{B} should not exceed 2.0 [T] ;

$\theta_{con} (T)$ is the conduction angle at top speed and its proposed

values* are: a) 1.5s for a traction drive (see Chapters 4 and 5) and b) 1.2s for a constant torque drive, i.e. when $\omega_T/\omega_B = 1$ (see Chapter 4).

Assuming that the winding geometry is defined as shown in Fig 5A.1 (see Appendix 5A), the cross-sectional area of the winding is given by expression 5A.1, i.e.

$$A_w = K_1 \left[\frac{d}{d_0} - K_2 \left(\frac{d}{d_0} \right)^2 \right] d_0^2$$

where

$$K_1 = \frac{1}{4} \frac{\sin \frac{\delta - s}{2}}{\cos \frac{\delta}{2} \cos \frac{\delta}{4}}$$

$$K_2 = \frac{\cos \frac{s}{2}}{\cos \frac{\delta}{2}} + \frac{3}{4} s$$

The total cross-sectional area available for one turn of both primary and secondary coils is

$$a_w = a_1 + a_2 = \frac{A_w}{N/2}$$

The optimum ratio of the primary and secondary cross-sectional areas per turn (a_1/a_2) when machine operates as motor is equal to I_1/I_2 (about 4). If the machine is designed to operate both as motor (when $I_1 > I_2$) and also to be capable of regeneration (when $I_1 < I_2$) (see Section 4.6), then the ratio a_1/a_2 should be closer to unity (depending on the duty cycle).

Having found a_1 and a_2 the suitable wire size can be chosen and the primary and secondary copper cross-sectional areas per turn, s_1 and s_2 , can be found and then the primary and secondary winding resistances per phase are (see Section 5.2.10)

$$R_1 = \rho \frac{2N(\ell + Kd)}{s_1}$$

* These values are related to a 4-phase 8/6 pole combination and 3-phase 6/4 pole combination machines both with ϕ/s about 3.0 and $k_d \leq 0.2$.

$$R_2 = \rho \frac{2N(\ell + Kd)}{s_2}$$

where ρ is specific resistivity and

$$K = \frac{\pi}{8} (s + \delta) \text{ (see Appendix 5A)}$$

Using the method presented in Section 7.5.1 the $\psi(\theta, i)$ table can be calculated for the assumed dimensions of the machine.

Having estimated the parameters R_1 , R_2 and $\psi(\theta, i)$ for assumed dimensions of the machine, its performance can be predicted using the non-linear mathematical model presented in Chapter 6. The performance for the required power, speed and voltage can be found using the methods presented in Sections 7.2 and 7.3.

The above procedure is repeated with a) various combinations of d and ℓ and b) various values of d_o , until the appropriate main dimensions of the machine d , ℓ and d_o , which provide satisfactory performance, are found. Then more detailed design consideration can be made if the means for 3-dimensional field solutions is available.

A flow chart for basic design procedure is shown in Fig 7.5.

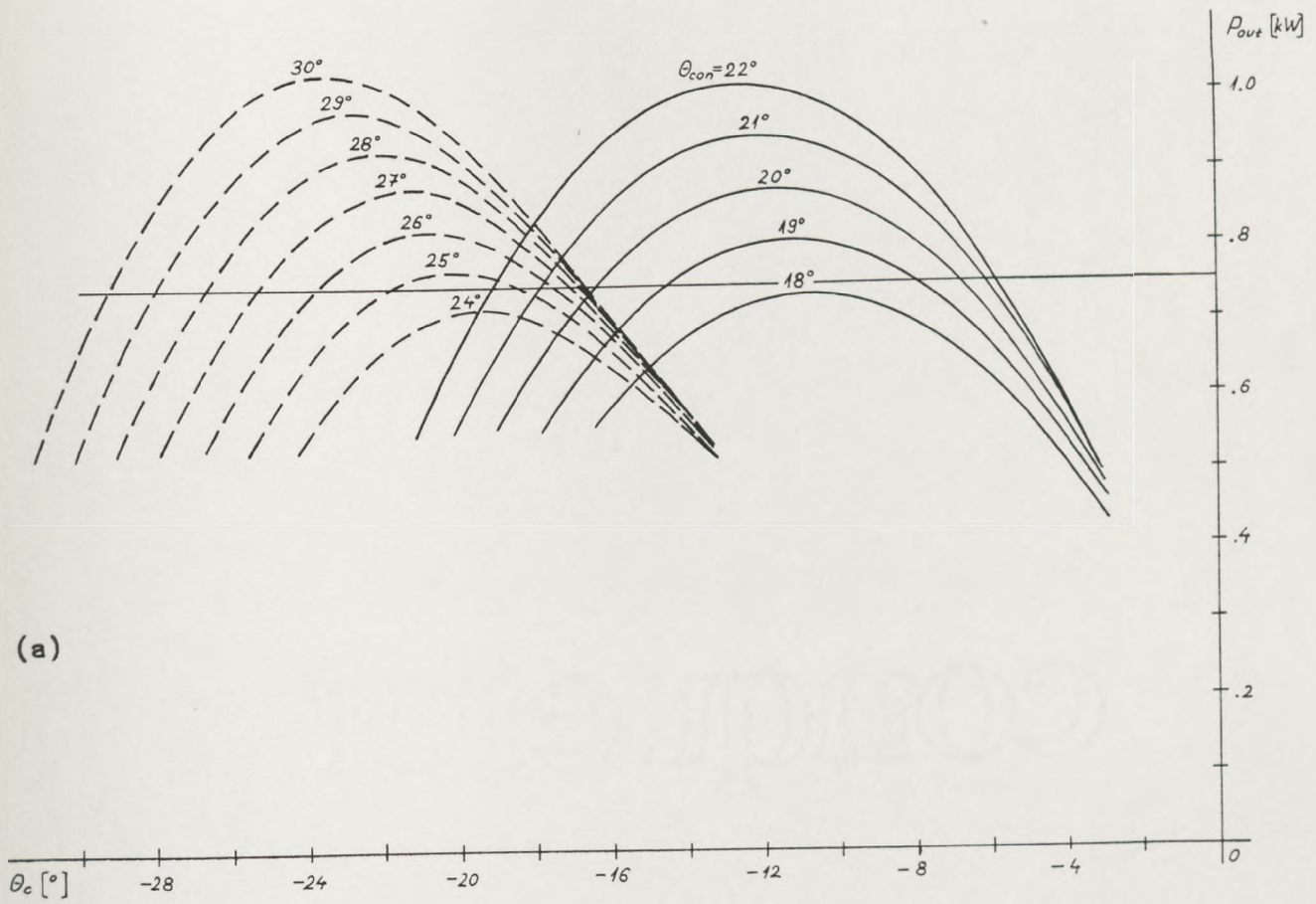
7.6 Conclusions

The great potential of the non-linear mathematical model of the switched reluctance motor for design purposes has been presented.

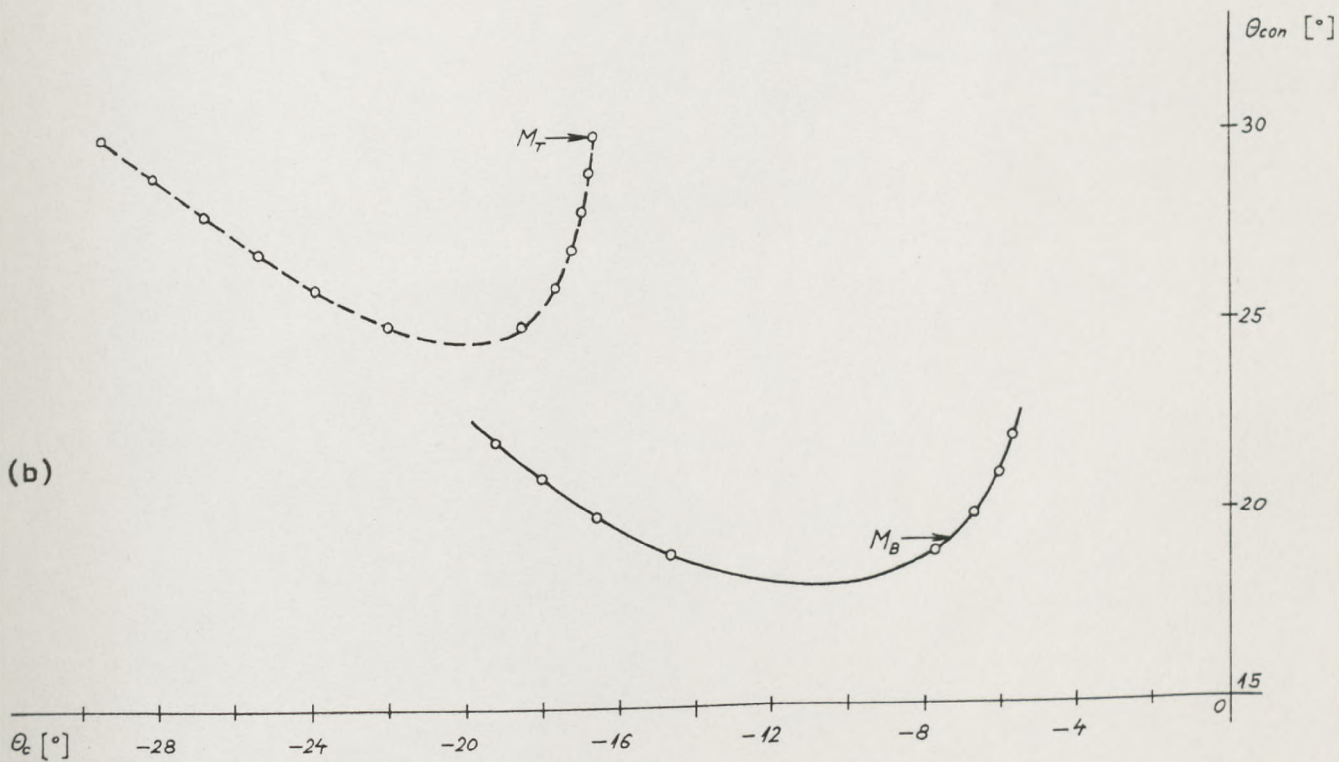
Using the non-linear mathematical model the effect of hypothetical changes to the number of turns has been examined on the D90M2-4 motor (0.75 [kW] 750 to 2250 $\left[\frac{\text{rev}}{\text{min}} \right]$) and it has been found, in the light of machine performance at standstill, base and top speed, that the original number of turns, i.e. the one which was estimated in the designing of the machine, is the best compromise. This indicates that the method of estimating the number of turns presented in

Chapter 5 is appropriate.

The design procedure presented in this chapter, represents the synthesis of the previous work and in particular it emphasises the essential roles of the minimum and maximum inductance estimations and non-linear mathematical model. Assuming that the fringe flux at the ends of core is well estimated by using the estimation given in Chapter 3 and the empirical factor given above, then it may be considered that the accuracy of the method, given above, for prediction of the performance of the machine from given dimensions is satisfactory. More detailed design will be possible when the 3-dimensional numerical field solution becomes available for the use in switched reluctance motors.



(a)



(b)

Continued

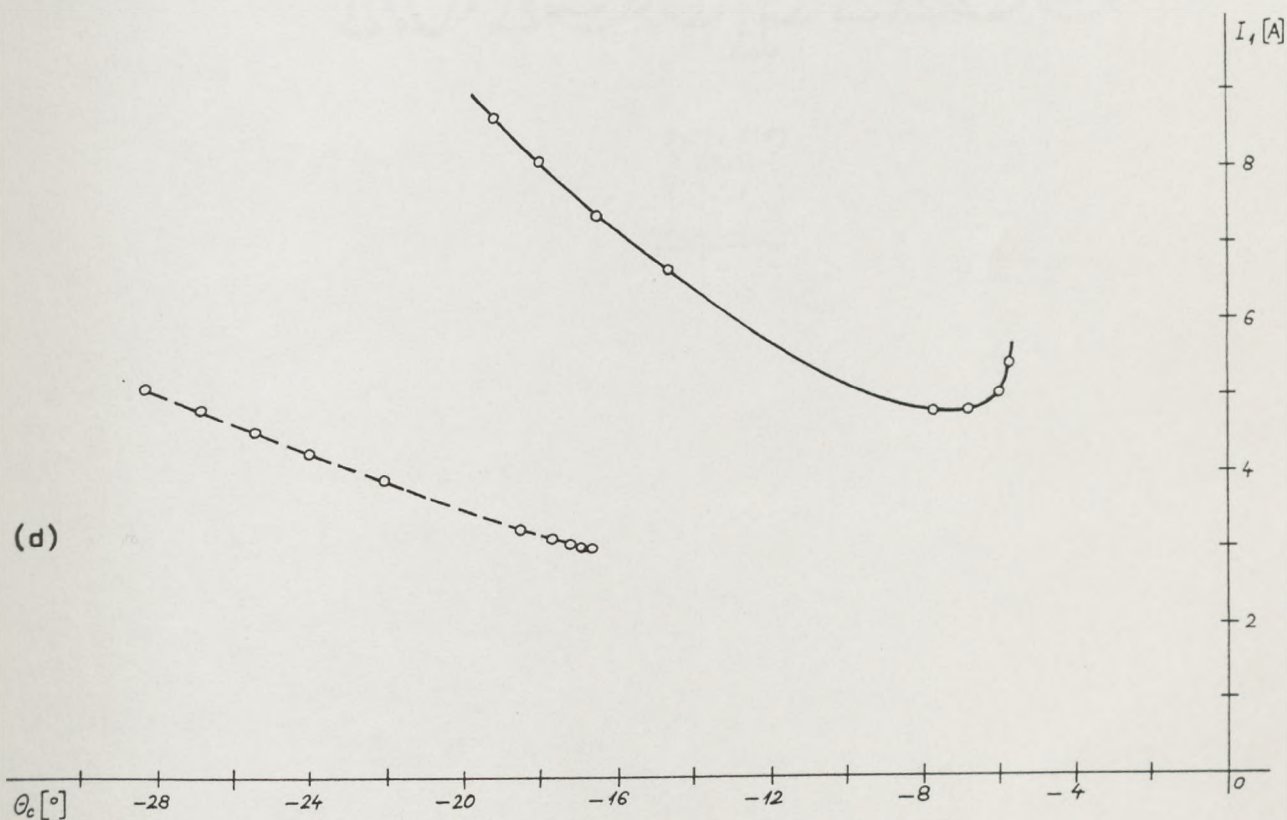
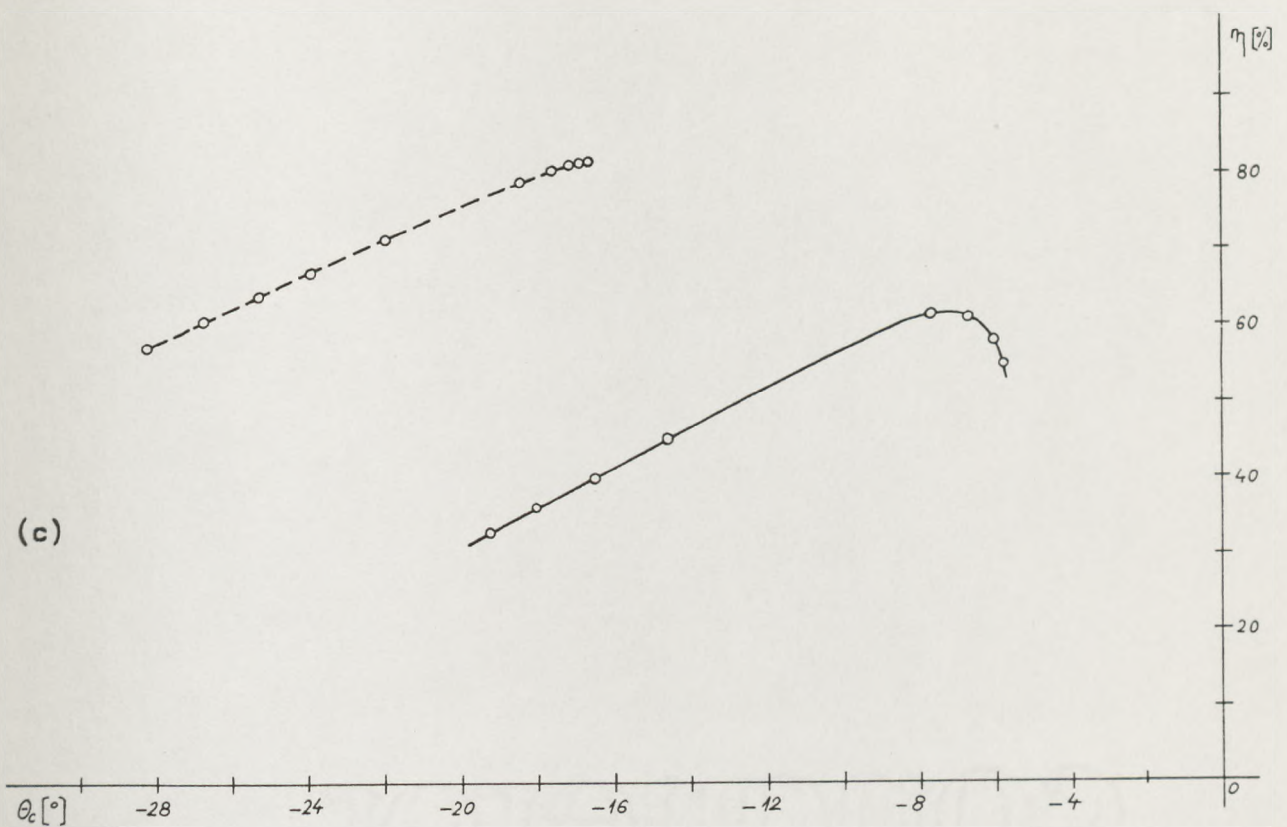


FIG 7.1 Computed performance of D90M2-4 motor at 150 [V]
 base speed ($n_B = 750 \left[\frac{\text{rev}}{\text{min}} \right]$)
 top speed ($n_T = 2250 \left[\frac{\text{rev}}{\text{min}} \right]$)

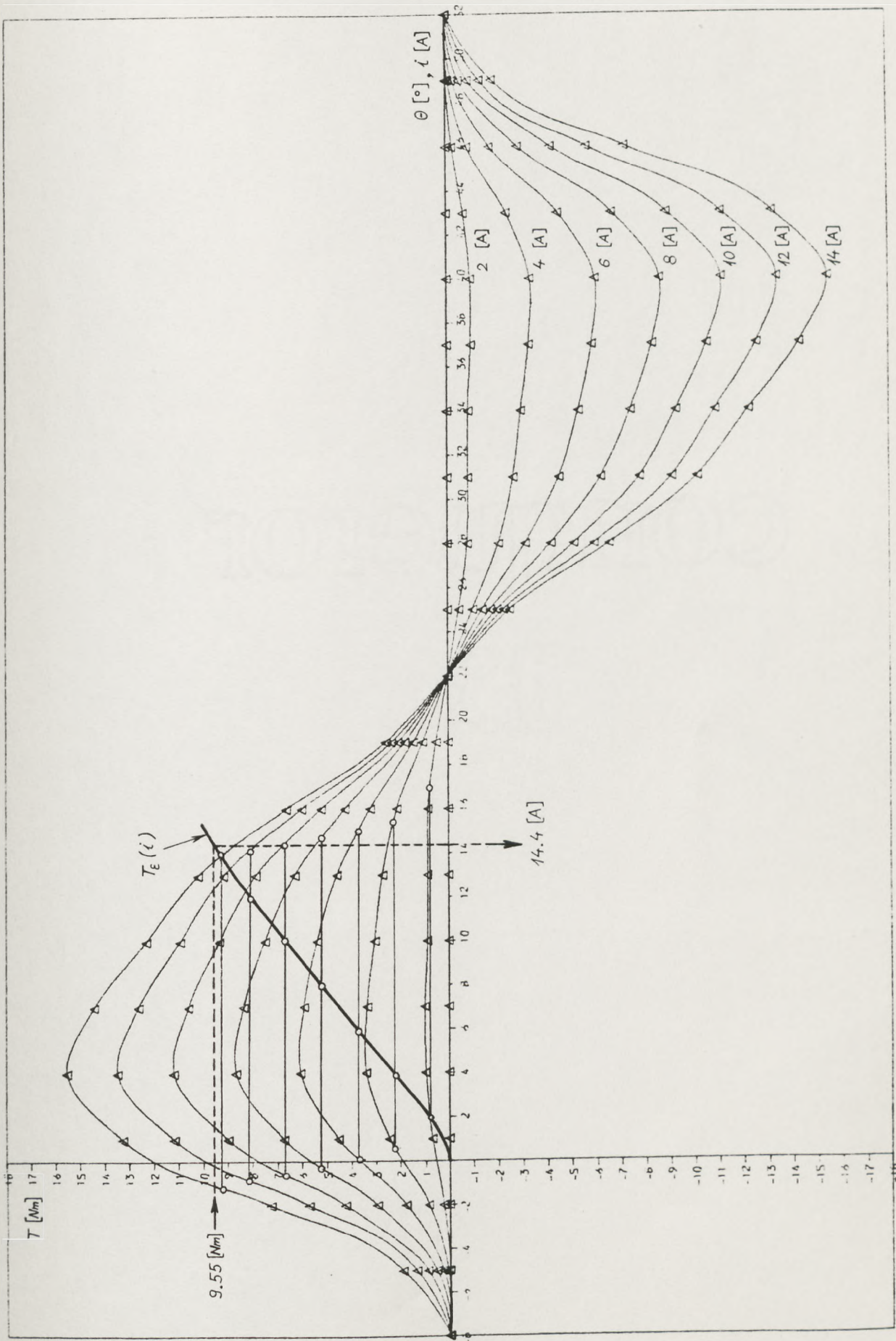


FIG 7.2 Computed static torque curves od D90M2-4 motor

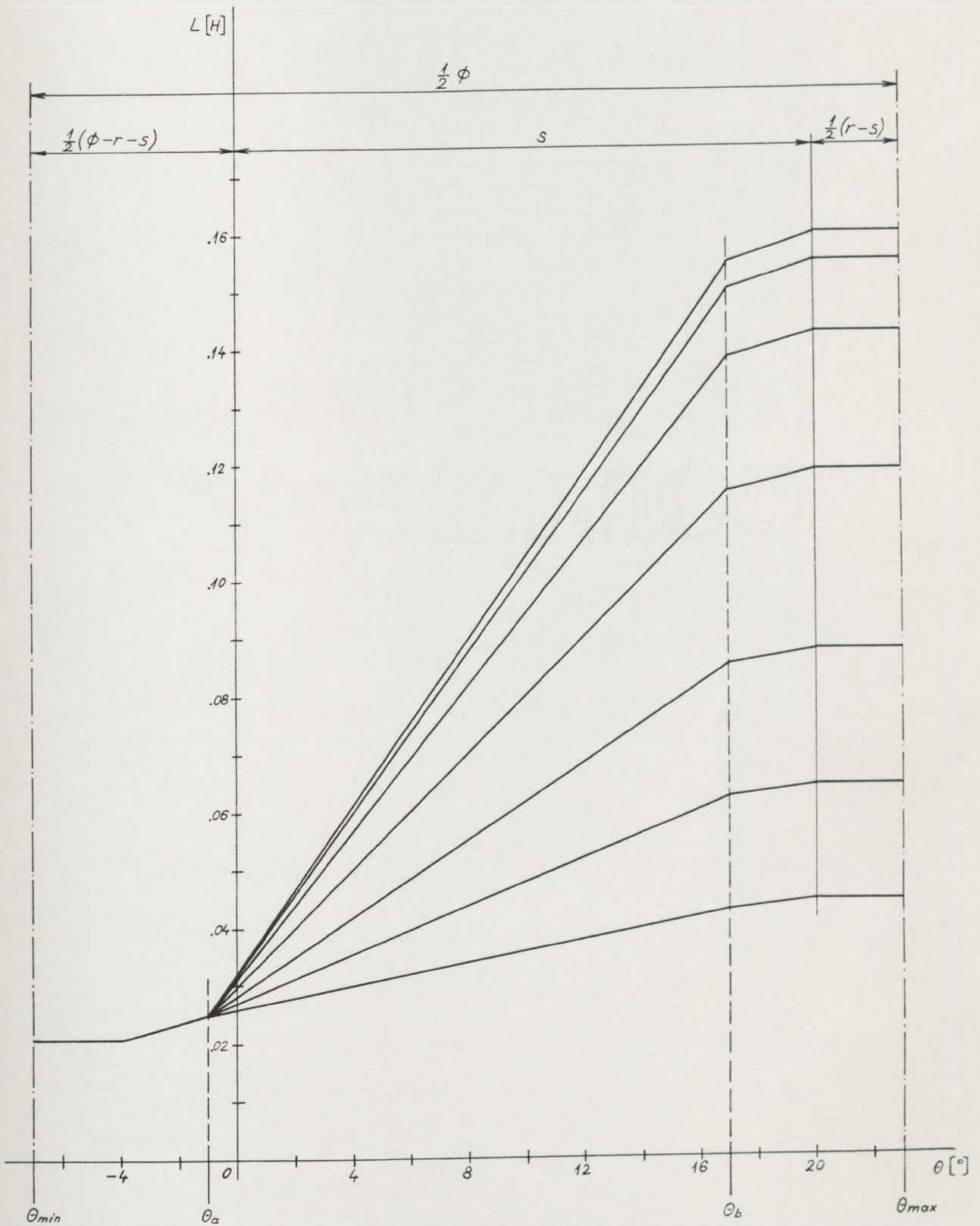


FIG 7.3 Piece-wise linear approximation of $L(\theta, i) \Big|_{i=\text{const}}$ curves of D90M1 motor using analytically estimated values L_0 and L_1

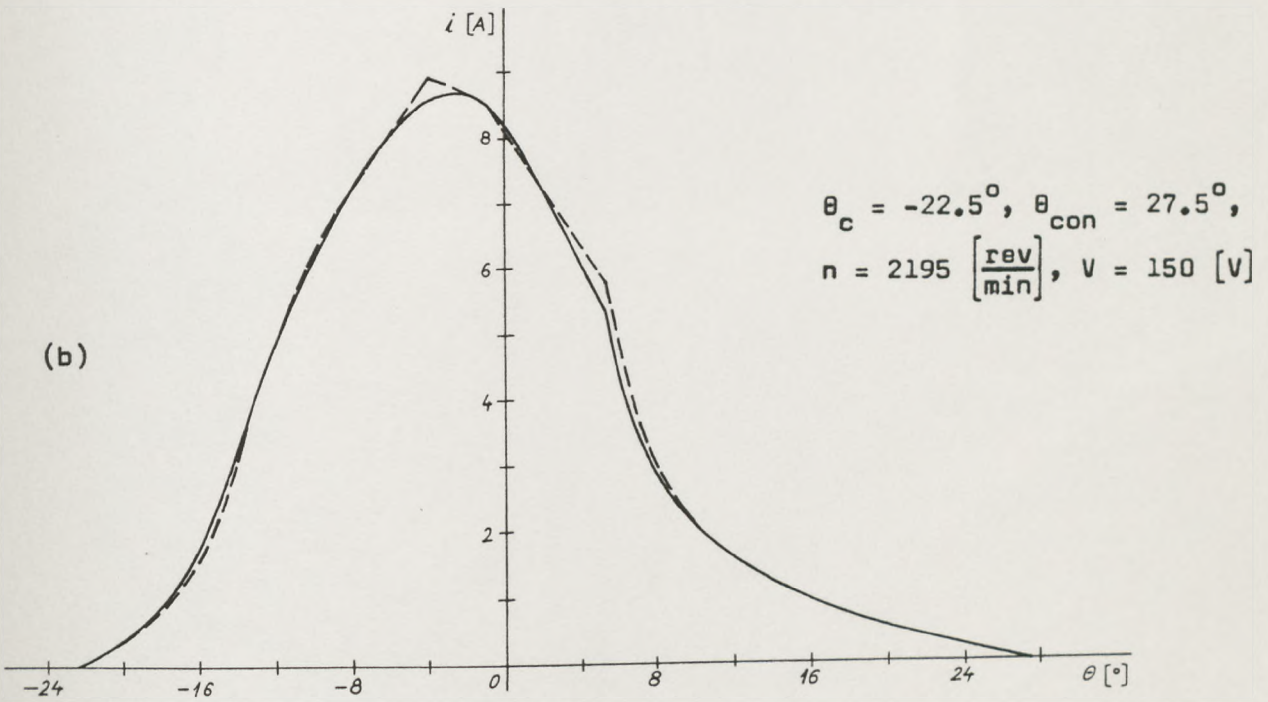
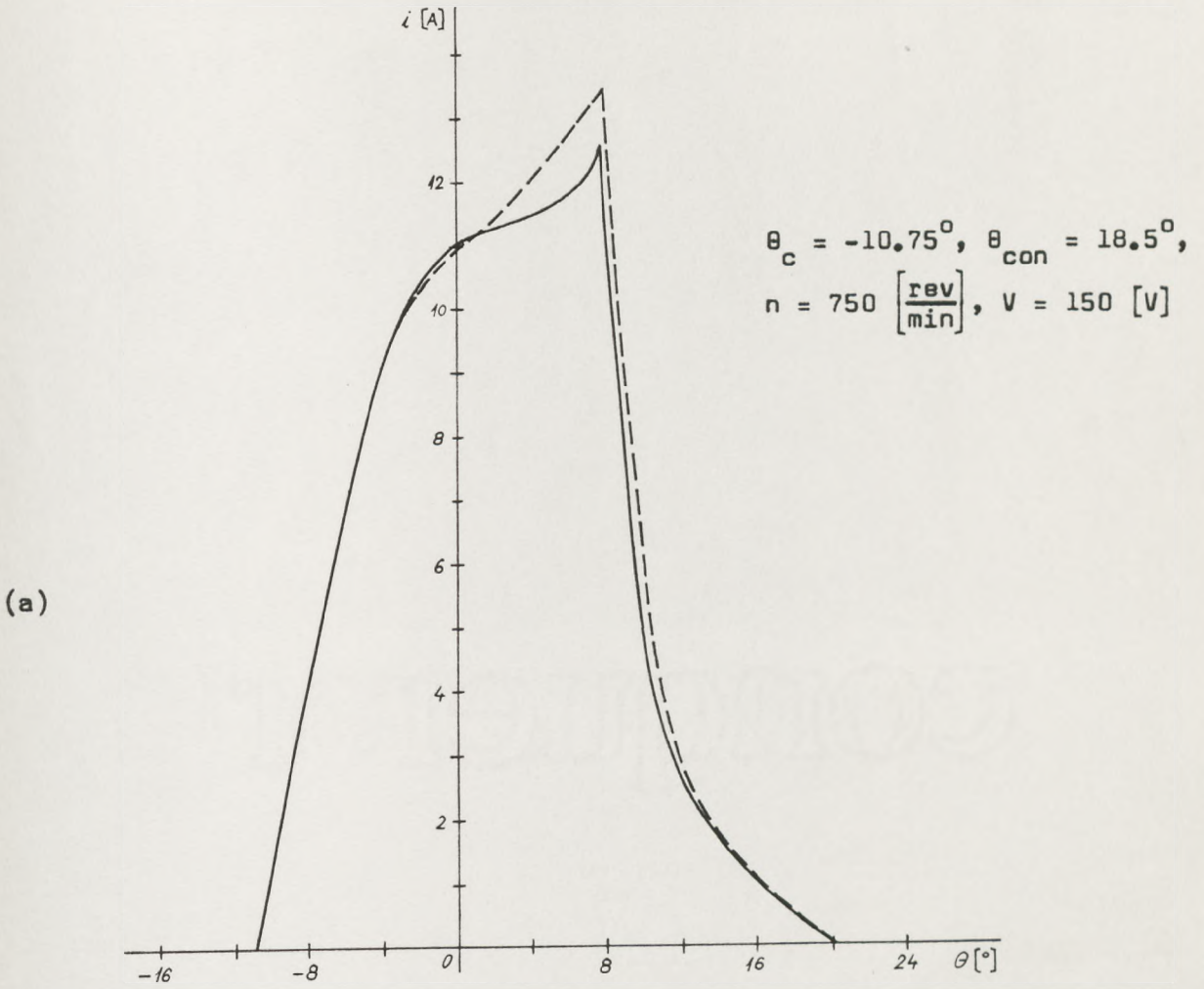


FIG 7.4 Computed current waveforms of D90M1 motor

————— when $\psi(\theta, i)$ table is obtained by measurement

----- when $\psi(\theta, i)$ table is obtained by piece-wise linear approximation

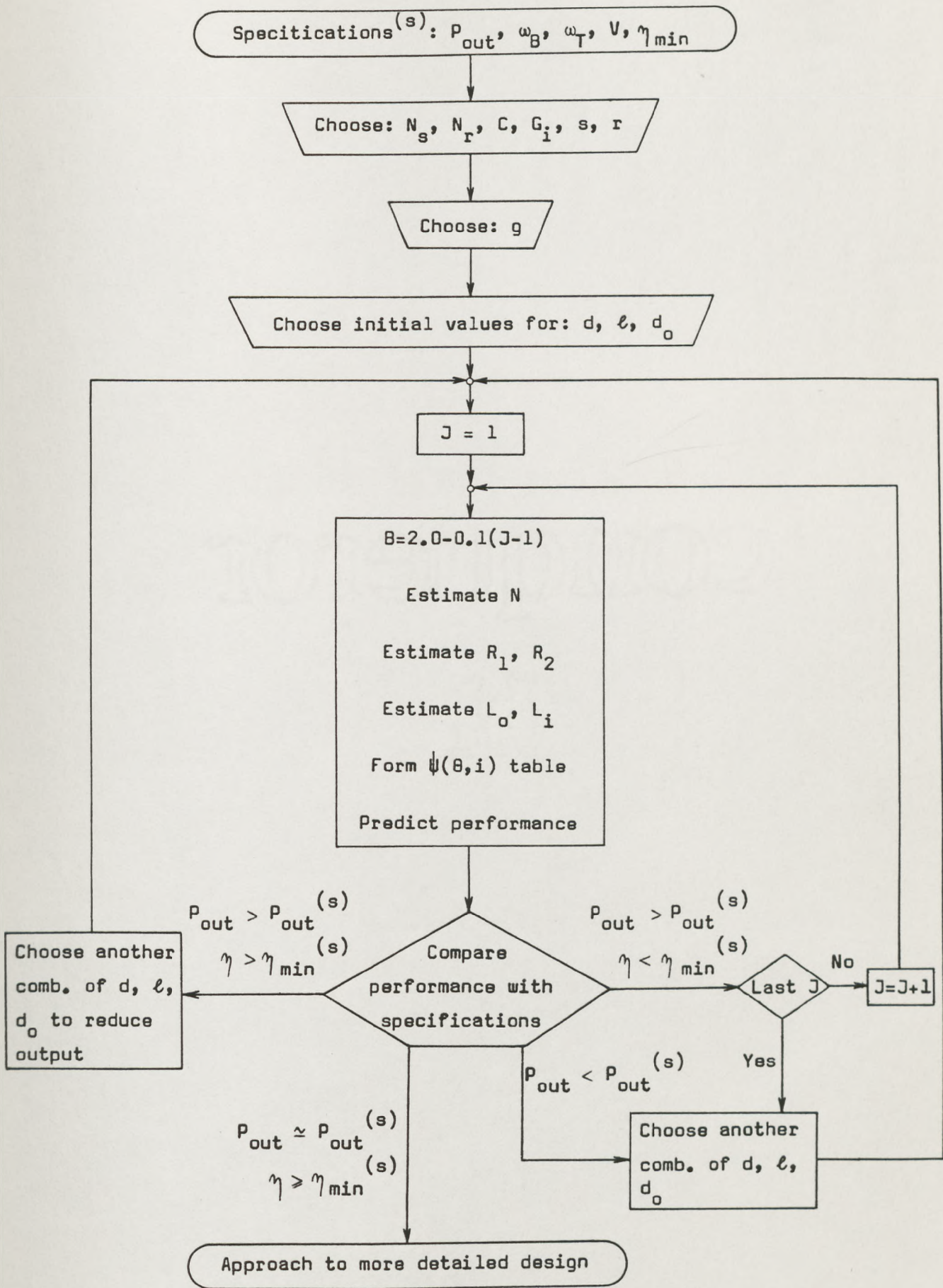


Fig 7.5 Flow chart for basic design procedure

CHAPTER 8

PROTOTYPE OF VOLTAGE CONTROLLED DRIVE

8.1 Introduction

A series of experimental switched reluctance motors was introduced in Chapter 5. These motors were designed to meet a traction type of torque-speed characteristic with an output power of 0.75 [kW] over the range 750 to 2250 $\left[\frac{\text{rev}}{\text{min}}\right]$ at 150 [V]. The performance of the motors was examined and it was found that the D90M2-4 motor had the best overall performance (see Figs 5.15 and 5.20). The running performance was examined in the constant power region where the machine was controlled by switching angles using the digital rotor-position sensor.

It has been deduced in Chapter 4 that control in the constant torque region should be achieved by controlling the voltage.

The object of the work presented in this chapter is to design a simple prototype of a rotor-position sensor and converter for a constant torque, voltage controlled, reversible drive using the existing D90M2-4 motor, and to examine its performance. For simplicity the system should preferably use only two optical heads and avoid such relatively complex processes as the generation and counting of high frequency pulses.

8.2 Rotor-Position Sensor

The design of the rotor-position sensor for a constant torque, voltage controlled, reversible drive is determined by several requirements which are imposed on the drive:

- i) capability for self-starting from any rotor position,
- ii) reversibility with identical performance in both directions,
- iii) design simplicity of the position sensor and associated logic circuitry.

The prototype of the rotor-position sensor designed to fulfill these requirements is shown in Fig 8.1. It consists of

- a) An interrupter disc with slots and teeth of 30° ,
- b) Two optical heads O_1 and O_2 ('Optron' OPB-813S slotted optical switch comprising an infra-red emitter and a photo-transistor has been found suitable),
- c) A mounting ring which supports the optical heads.

The interrupter disc is fixed on the shaft in such a position that the leading tooth edges, with respect to the forward direction of rotation, are aligned with the rotor pole leading edges.

The optical heads are fixed on the mounting ring and the angle between them is 75° . (The angle 75° is equivalent to the angle between two phases, ie $\epsilon (= 15^\circ)$, since the complete cycle of the changing the variables, ϕ , is 60° . The reason for the angle of 75° being used (instead of the 15°) is the convenience for manufacturing.)

The mounting ring is positioned with respect to the stator so that the angle between the axis of the phase 1 and the axis of the optical head O_1 is equal to $\frac{1}{2}(\delta-r)$, ie 10.5° (due to the requirement for symmetrical performance in both direction of rotation - see below). Fig 8.2 shows the positions of the optical heads with respect to the stator and the position of the interrupter with respect to the rotor. The operation of the rotor-position sensor is described below.

Let X and Y be the signals (logical variables) which are obtained from photo-transistors of optical heads (the logical value 1 corresponds to the 'off' state of the photo-transistor), and let the X-signal lead the Y-signal. Each of the X and Y signals has a value 1 for 30° and value 0 also for 30° , and they are shifted by 15° with respect to each other.

In the 'forward' (F) direction of rotation, according to Fig 8.2, the signal X is associated with the optical head O_2 and signal Y with O_1 . The set of signals defined by logical functions X·Y,

$\bar{X}\cdot Y$, $\bar{X}\cdot\bar{Y}$, $X\cdot\bar{Y}$ have the value 1 for 15° and are shifted by 15° (which is equal to the angular displacement ϵ between two adjacent phases), and the set of signals defined by logical functions X , Y , \bar{X} , \bar{Y} have value 1 for 30° and are also shifted by 15° (Fig 8.3).

In either of these sequences of Figs 8.2 or 8.3(a) the phases are switched in appropriate order for forward direction of rotation, ie 1-2-3-4.

The first set of signals is more appropriate for the switching in the 'starting' mode of operation ($\theta_c = -0.5^\circ$, $\theta_{con} = 15^\circ$), since a larger minimum torque on the starting torque curve (Fig 8.9) is obtained than in the case of switching by the second group of signals. (If the value of the minimum torque on the starting torque curve does not exceed the rated torque of the motor, the current rating of the drive must be increased.) However, in the 'running' mode of operation the second set of signals is more appropriate for the switching of the four phases, since then early turn on and fully-open conduction angles ($\theta_c = -15.5^\circ$, $\theta_{con} = 30^\circ$) are provided.

In the 'reverse' (R) direction of rotation, according to Fig 8.2, the signal X is associated with the optical head O_1 and signal Y with O_2^* . The phases should be switched in sequence 4-3-2-1, and this sequence of switching is achieved if the phase 1, 2, 3, 4 are switched by either of the following sets of signals $\bar{X}\cdot\bar{Y}$, $\bar{X}\cdot Y$, $X\cdot Y$, $X\cdot\bar{Y}$ or \bar{X} , Y , X , \bar{Y} in the indicated order (Fig 8.3(b)). Again, the first set of signals is appropriate for the switching in the starting mode, of operation and the second set is more appropriate for the switching in the running mode of operation.

If the machine is rotating in the forward direction, then switching over the logic into the mode for the reverse direction, (or vice

* The same optical heads, O_1 and O_2 , can be used for both the forward and reverse direction of rotation, since in the rotor position at which the edge of the interrupter tooth is aligned with the axis of the optical head O_1 , the rotor pole axis is aligned with the axis of the stator interpolar space (Fig 8.2).

versa), the machine will regenerate, performing the braking action. More effective braking is achieved by switching over the logic into the starting mode together with switching into the reverse direction.

Thus, with the simple rotor-position sensor and the D90M2-4 motor, the following switching angles are convenient for use

- a) $\theta_c = - 0.5^\circ$, $\theta_{con} = 15^\circ$ (starting mode)
- b) $\theta_c = - 15.5^\circ$, $\theta_{con} = 30^\circ$ (running mode)
- c) $\theta_c = 29.5^\circ$, $\theta_{con} = 15^\circ$ (regeneration-braking mode)

8.3 Converter

Fig 8.4 shows the block-diagram of the drive. (The power flow is represented by thick lines, and controlling signals by thin lines.) The converter consists of a switching unit and overcurrent detector, switching logic, frequency-voltage converter, mode selector and dc chopper. Circuit diagrams are given below.

The following symbols are used to represent the signals in circuit diagrams:

X	}	signals from optical heads,
Y		
S & R		signal for starting/running modes,
N & B		signal for normal/braking modes,
F & R		signal for forward/reverse modes,
1 & 3	}	signals from overcurrent detectors of the
2 & 4		
R_B		signal for switching the braking resistance

The control circuits are supplied from the 10 [V] dc power supply.

8.3.1 Switching unit and overcurrent detector

The switching circuit with bifilar windings of the motor is shown in Fig 8.5(a) and its operation has been considered in Section 2.5.

Phase switching power transistors are protected by snubbing circuits and by overcurrent protection. The function of the snubbing circuit (resistor/capacitor/diode network connected across the transistors) is double: to suppress the voltage spike due to leakage inductance between primary and secondary coils, and to reduce switching losses.

Overcurrent protection is achieved using resistive shunts which provide a voltage proportional to current for comparators operating the switching logic. Phases 1 and 3 are connected to one overcurrent detector and phases 2 and 4 to another. In this way the overcurrent detectors protect each phase separately (there is no conduction overlap between phases 1 and 3 or 2 and 4).

When the machine regenerates (braking action), the kinetic energy of the rotating inertia is fed back into the electrolytic capacitor across the dc supply and is dissipated in the resistor which is switched across the capacitor.

8.3.2 Switching logic

The signals from the two optical heads are passed into the logic circuit shown in Fig 8.5(b), which produces four switching signals (1, 2, 3, 4) in accordance with considerations presented in Section 8.2.

Two signals from current shunts are compared with reference levels which correspond to the limiting values of current in the phase switching power transistors.

8.3.3 Frequency-voltage converter

According to the value of frequency of the signal from the optical

head which is equal to the switching frequency of each phase

$f_{ph} = \frac{N n}{60} (= \frac{n}{10})$, the frequency-voltage converter (Fig 8.5(c)) produces the signal

$$S \text{ and } R = \begin{cases} 0, & f < f_T \\ 1, & f \geq f_T \end{cases}$$

where f_T is frequency which corresponds to the switching over of the logic from the starting to the running mode of operation (see Section 8.2). The converter is adjusted to switch over the logic at a speed of about 150 $\left[\frac{\text{rev}}{\text{min}} \right]$. The frequency-voltage converter also produces the voltage signal which is directly proportional to the frequency f_{ph} (motor speed). This signal may be used to complete a closed-loop speed control system.

8.3.4 Mode selector

The machine operating commands for the switching logic are achieved via the mode selector (Fig 8.5(d)). The machine can operate as motor in the forward or reverse direction of rotation ('FORWARD' and 'REVERSE' commands) and can perform braking action ('BRAKE' command).

In the braking mode of operation when the speed decays near to zero the main supply must be disconnected, otherwise the machine would begin to rotate in the opposite direction.

The main supply can also be disconnected without braking action ('STOP' command).

8.3.5 DC chopper

The motor speed is controlled by varying the dc supply voltage which is obtained from a dc chopper (Fig 8.5(e)) with mark-space control (pulse-width modulation). The dc chopper is supplied from a rectifier bridge.

The chopping frequency 10 [kHz] was convenient with relation to the available power transistor, switching losses, size of the smoothing

inductance and the ripple of current during the period of the chopping cycle (to provide approximately constant current during the period of chopping cycle). The chopper was designed for a maximum output voltage of 150 [V] and continuous current of 10 [A] (with relation to available power transistors).

The chopping transistor is protected by overcurrent protection (current time chopper), and switching losses are reduced by a snubber.

The auxiliary circuit of the dc chopper is supplied from an additional 10 [V] dc supply floating at the potential of the emitter of the chopping transistor. The optically coupled isolator is used to separate this 10 [V] dc supply from the voltage level of pulse generator and other control circuits.

8.4 Drive Assembly

Fig 8.4 shows the component parts of the machine and rotor-position sensor. Since this drive was built as a prototype for an industrial application the machine is ventilated by an external fan.

The prototype converter is shown in Fig 8.7. Fig 8.8 shows the complete drive (machine and converter).

8.5 Performance of the Motor

Fig 8.9 shows the starting torque curve at 10 [A]. It is seen that minimum torque is not much less (3.7%) than torque T_{ϵ} which could be obtained if the symmetrical reversibility of the drive were not required. (A small reduction of the rotor pole arc would allow T_{ϵ} to coincide with the minimum net torque, and hence avoid discontinuity in the net torque curve.)

The measured torque/speed and efficiency*/speed curves at various

* The efficiency takes into account device losses (snubbing circuits, switching transistors and diodes).

values of supply voltage are shown in Figs 8.10(a) and (b).

The torque/speed curves clearly show the 'series motor' type characteristic predicted in Chapter 2.

Figs 8.11(a) to (d) are derived from Figs 8.10(a) and (b) and show the supply voltage, efficiency, power loss and output power against speed at a constant torque up to the maximum value of supply voltage of 150 [V].

Fig 8.11(a) shows the control law for the speed of the prototype drive for constant torque. It can be seen that the speed is almost proportional to voltage at constant torque. The distortion at lower speeds, particularly at higher values of torque (current), is due to the iR drop which becomes an increasingly significant proportion of the supply voltage as the speed decreases.

The curve which shows the acceptable power loss for a D90 frame size induction motor* when the machine is continuously rated, is shown in Fig 8.11(c). From this figure it may be deduced that the switched reluctance motor may be continuously rated for the maximum torque of 4.75 [Nm] at 1500 $\left[\frac{\text{rev}}{\text{min}}\right]$ ($P_{\text{out}} = 0.75$ [kW]).

The hatched area in Fig 8.11(d) shows the acceptable continuous power ratings. The area is limited by the curve corresponding to the acceptable power loss and by that corresponding to maximum drive voltage (150 [V]). The motor may be continuously rated for the maximum output power of 0.8 [kW] at 1620 $\left[\frac{\text{rev}}{\text{min}}\right]$. The measured efficiency at this continuous rating is 70%.

However, the estimated ratings are pessimistic since the measured efficiency takes into account device losses (snubbing circuits, switching transistors and diodes). These losses depend on values of voltage and speed and, for example, at 150 [V] and 1600 $\left[\frac{\text{rev}}{\text{min}}\right]$ they are estimated to be about 50 [W]. Hence, the estimated efficiency of the motor at the output power 0.8 [kW] and speed 1600 $\left[\frac{\text{rev}}{\text{min}}\right]$ is about 73%.

* The continuous ratings of the D90 induction motors ('Brook Motors'), which frame size is the same as that of the D90M2-4 switched reluctance motor, are: 0.37 [kW] at 750 $\left[\frac{\text{rev}}{\text{min}}\right]$, 0.75 [kW] at 1000 $\left[\frac{\text{rev}}{\text{min}}\right]$, 1.1 [kW] at 1500 $\left[\frac{\text{rev}}{\text{min}}\right]$, 1.5 [kW] at 3000 $\left[\frac{\text{rev}}{\text{min}}\right]$.

8.6 Conclusions

A prototype of a simple rotor-position sensor and converter has been designed and constructed for a voltage controlled drive with the existing D90M2-4 motor. The drive provides self-starting capability, reversibility with identical performance in both directions and has a braking facility.

The experimental results have demonstrated that the machine can operate as a constant torque drive controlled by voltage. At a continuous rating 0.75 [kW], 1500 $\left[\frac{\text{rev}}{\text{min}}\right]$ the efficiency of the machine is about 73%. However, it has to be borne in mind that the switching angles at which the machine operates in the running mode are fixed at $\theta_c = -15.5^\circ$, $\theta_{\text{con}} = 30^\circ$. The optimum switching angles at the above rating are $\theta_c = -13.25^\circ$ and $\theta_{\text{con}} = 25^\circ$ (see Fig 5.20) when the efficiency of the drive is 76% and the estimated efficiency of the machine is 80%. It is clear that the simplicity of the drive results in a lower efficiency and hence a lower continuous rating.

The constant speed D90 induction motor develops 1.1 [kW] at 1500 $\left[\frac{\text{rev}}{\text{min}}\right]$, so that switched reluctance motor with a simple rotor-position sensor has a specific output of only 67% of the induction motor fed from a sinusoidal supply. However, the induction motor would be significantly derated if used as variable-speed drive with a square-wave inverter. Also the ratio primary/secondary cross-sectional area of the D90M2-4 switched reluctance motor is not optimum (see Section 5.6.2). The optimising of this ratio could improve the efficiency by about 3%, allowing a further increase in the rating.

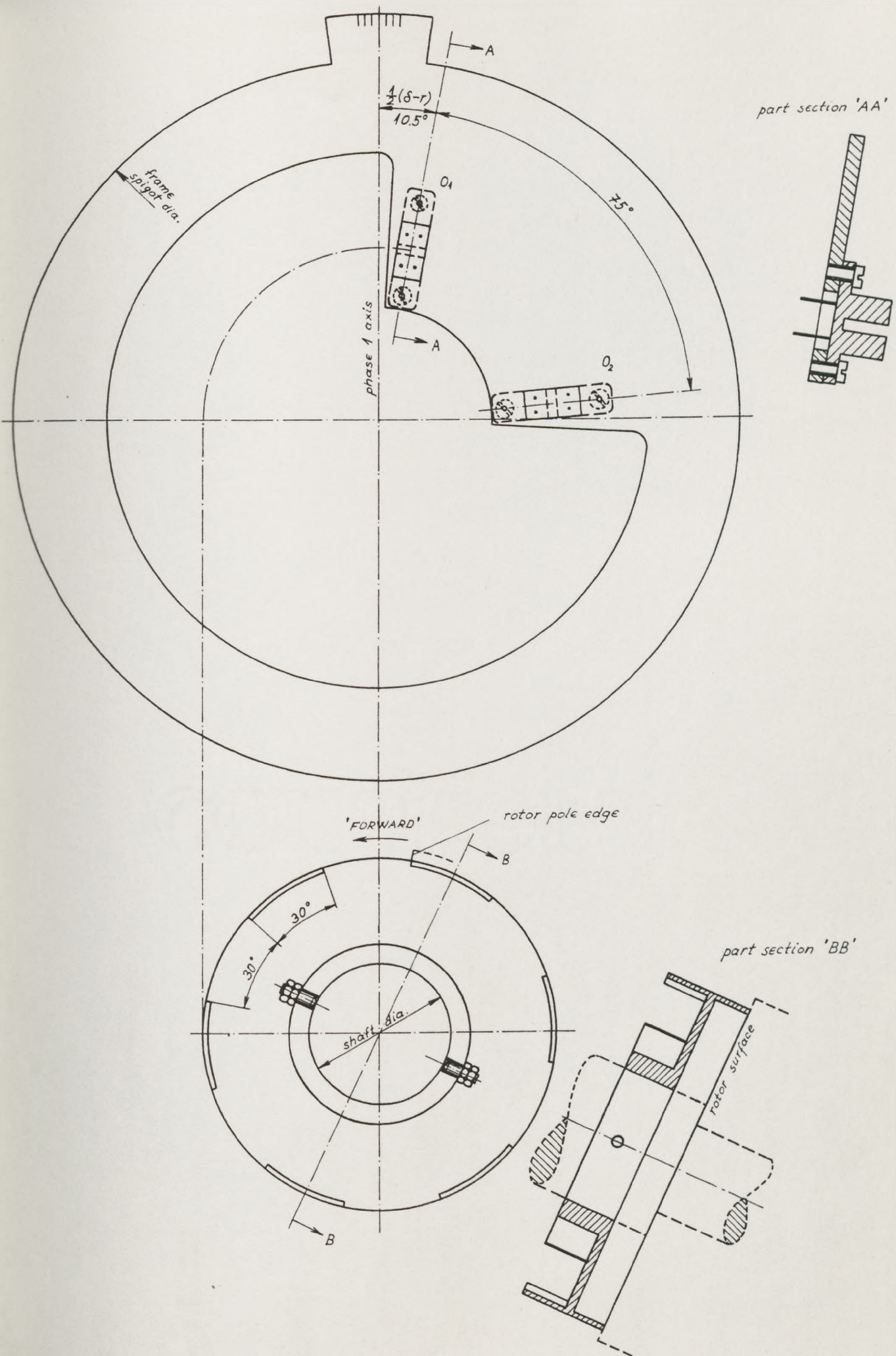


FIG 8.1 Rotor-position sensor

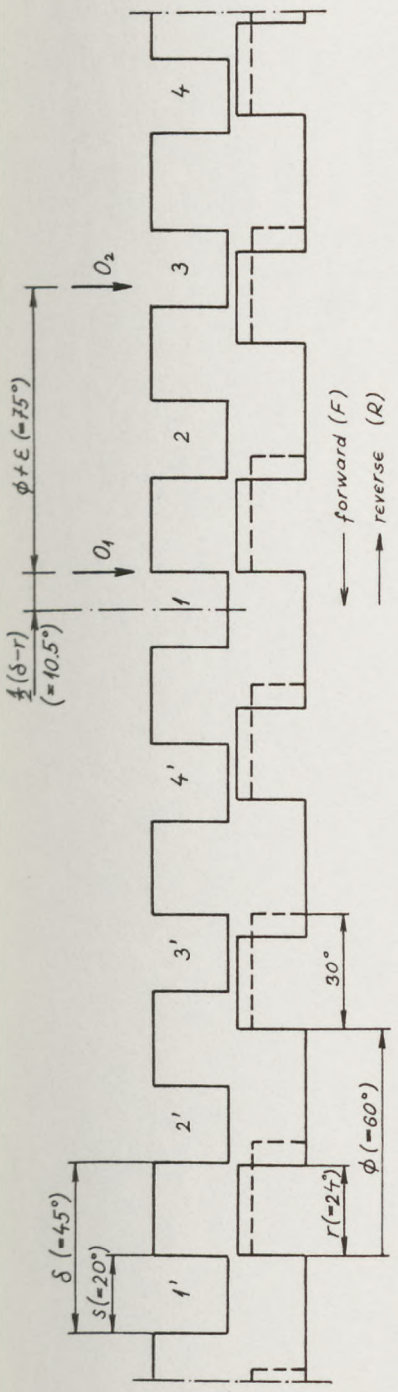


FIG 8.2 Position of the optical heads O_1 and O_2 with respect to the stator and position of the interruptor with respect to the rotor

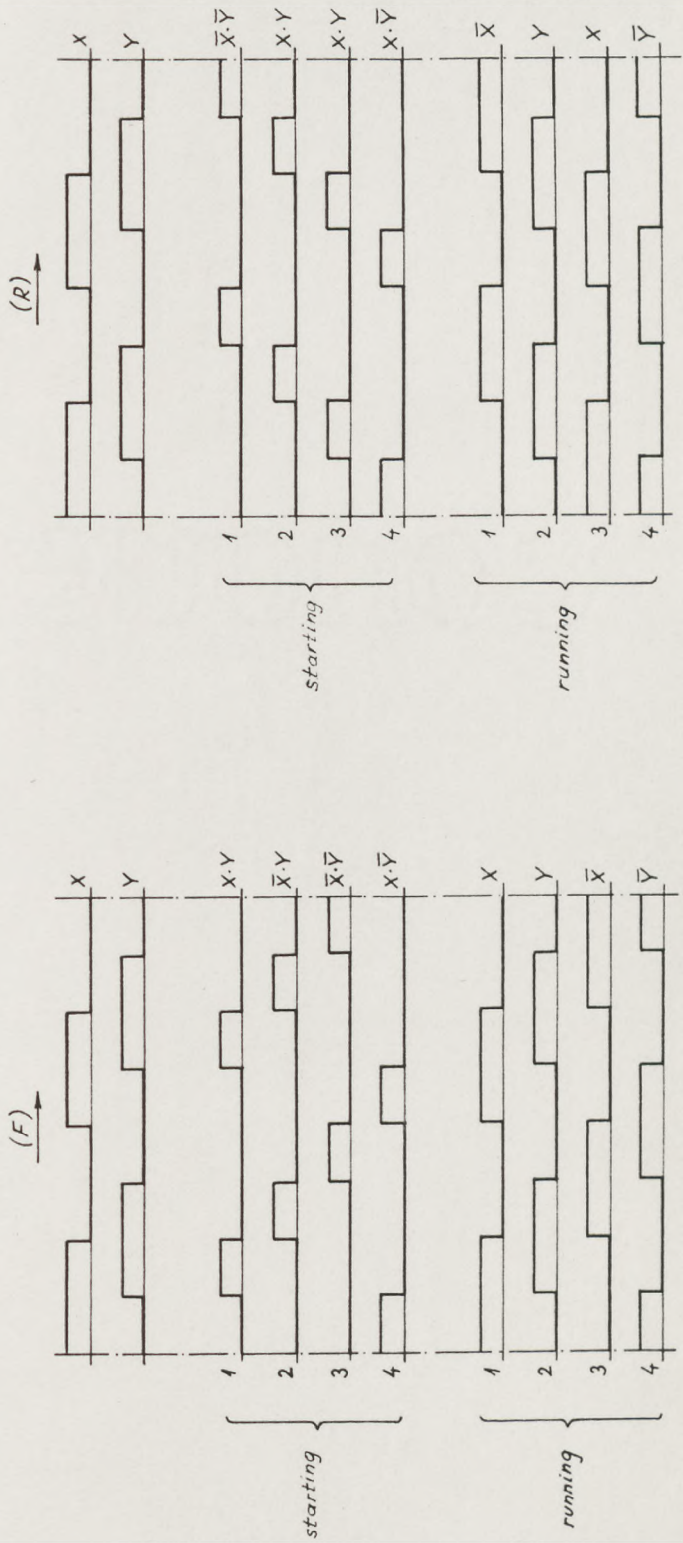


FIG 8.3 Logical variables X and Y and switching signals for (a) forward, and (b) reverse direction of rotation

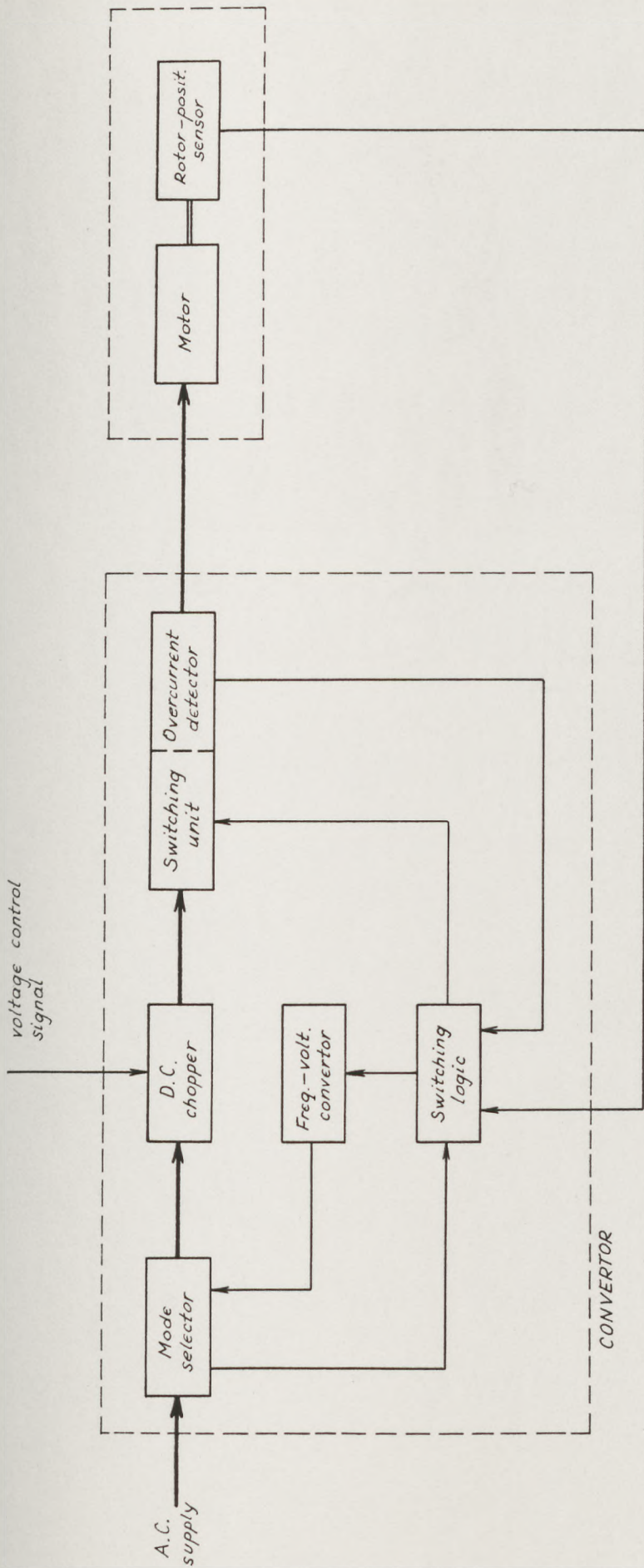


FIG 8.4 Block-diagram of voltage controlled drive

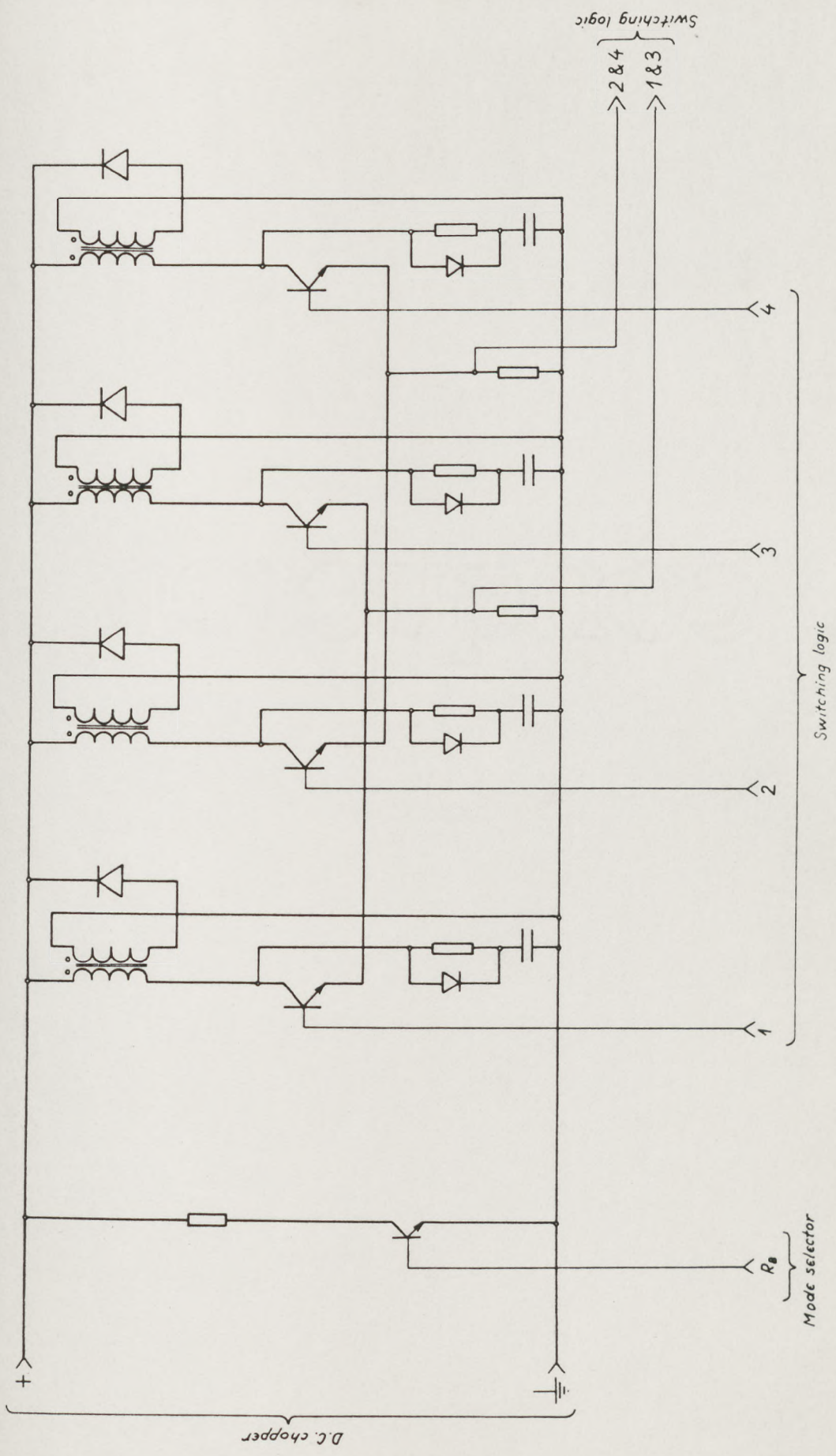


FIG 8.5(e) Switching unit and overcurrent detector

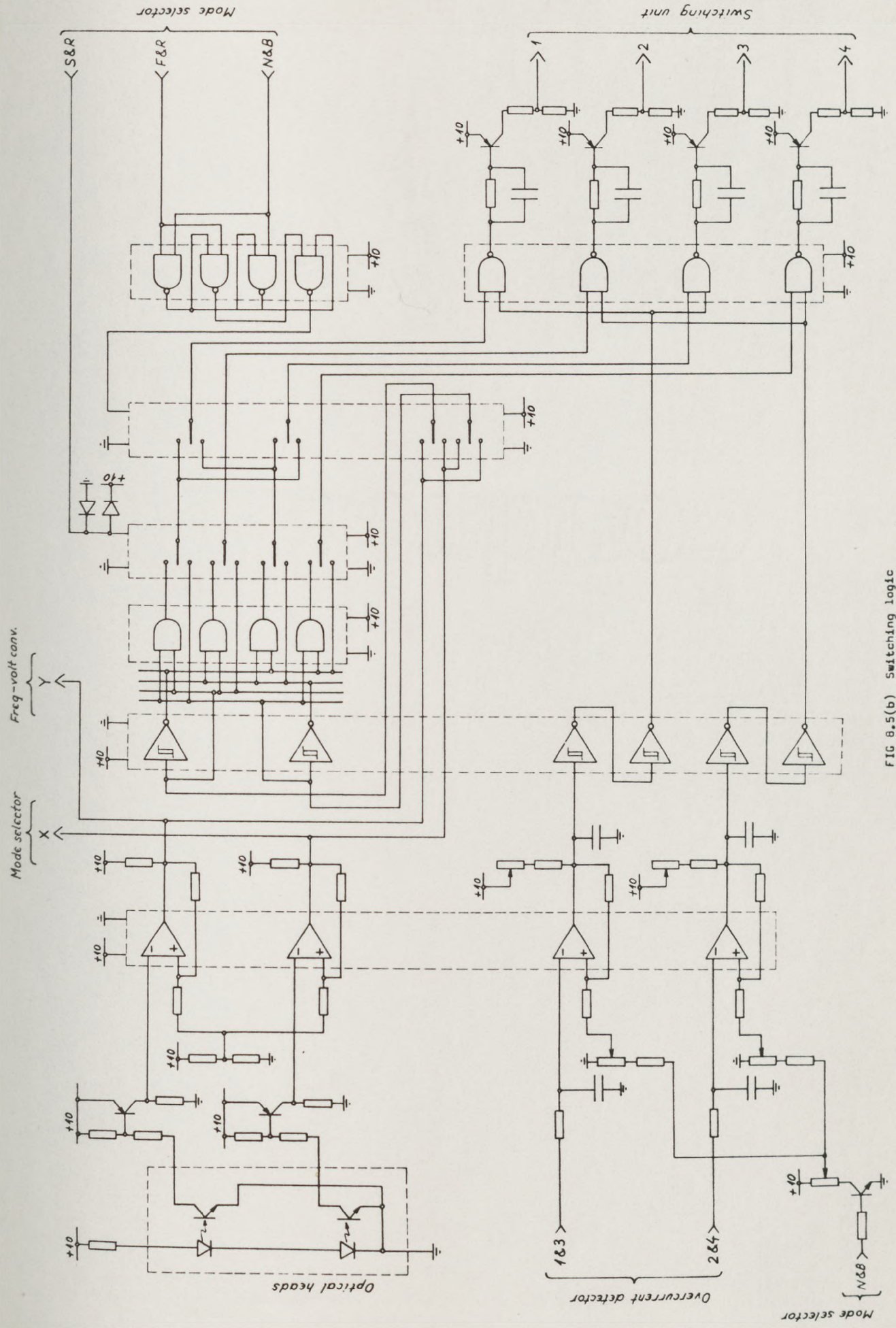


FIG 8.5(b) Switching logic

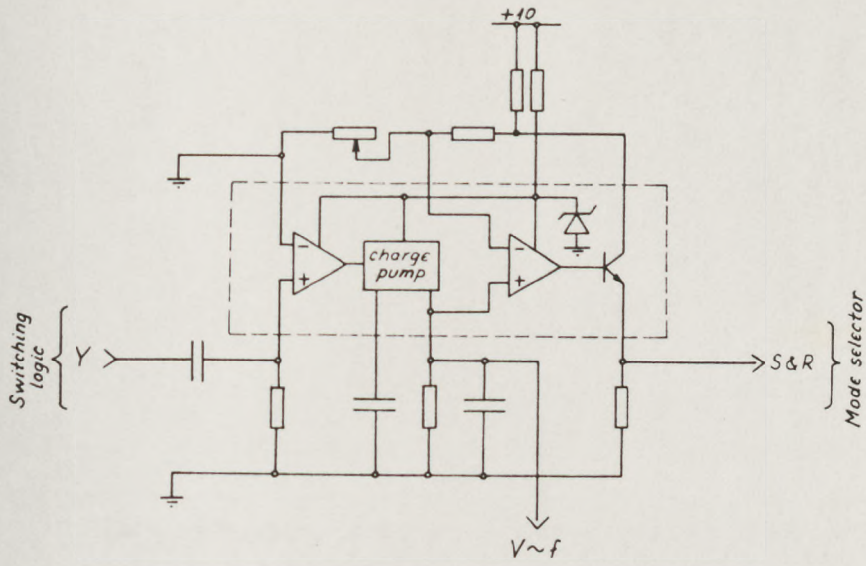


FIG 8.5(c) Frequency-voltage converter

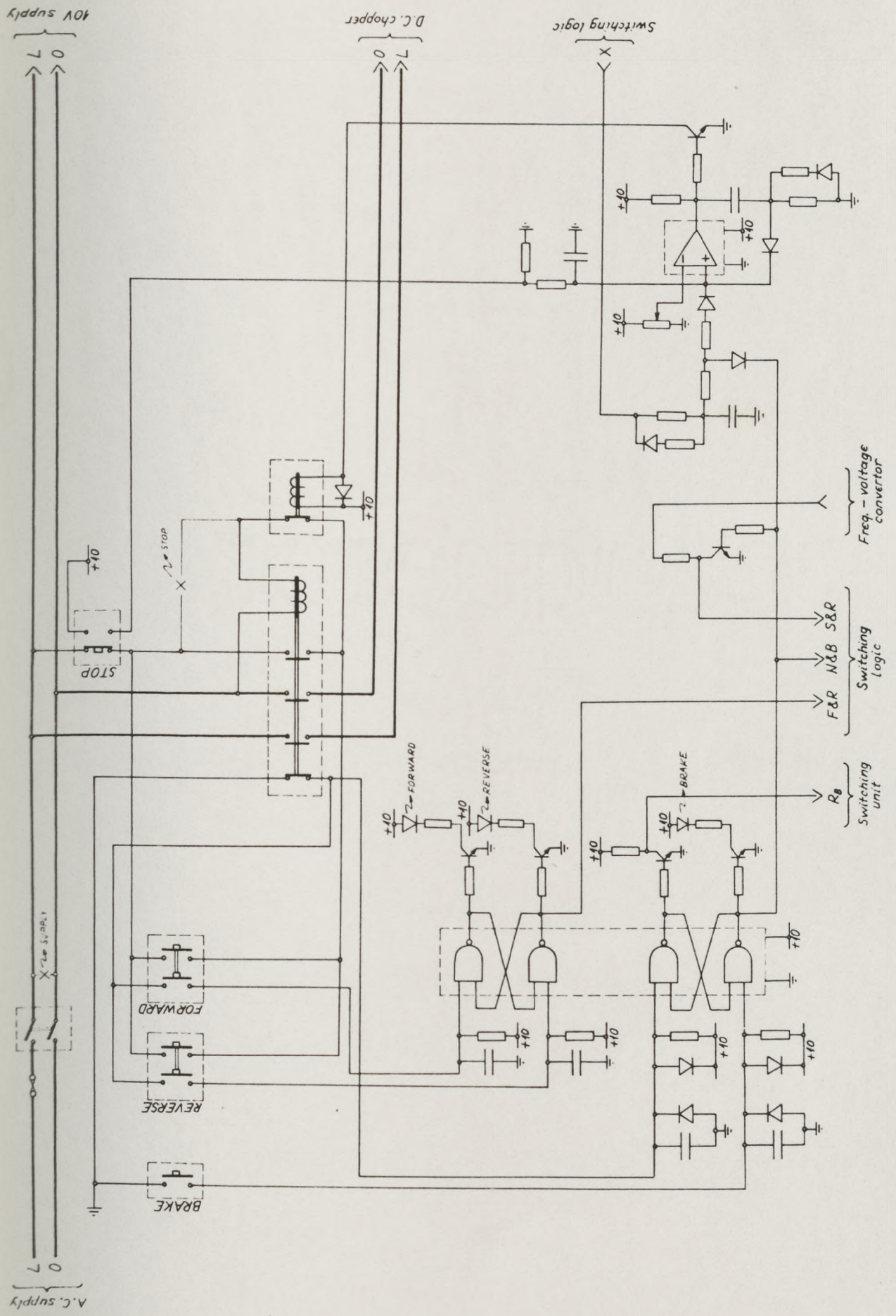


FIG 8.5(d) Mode selector

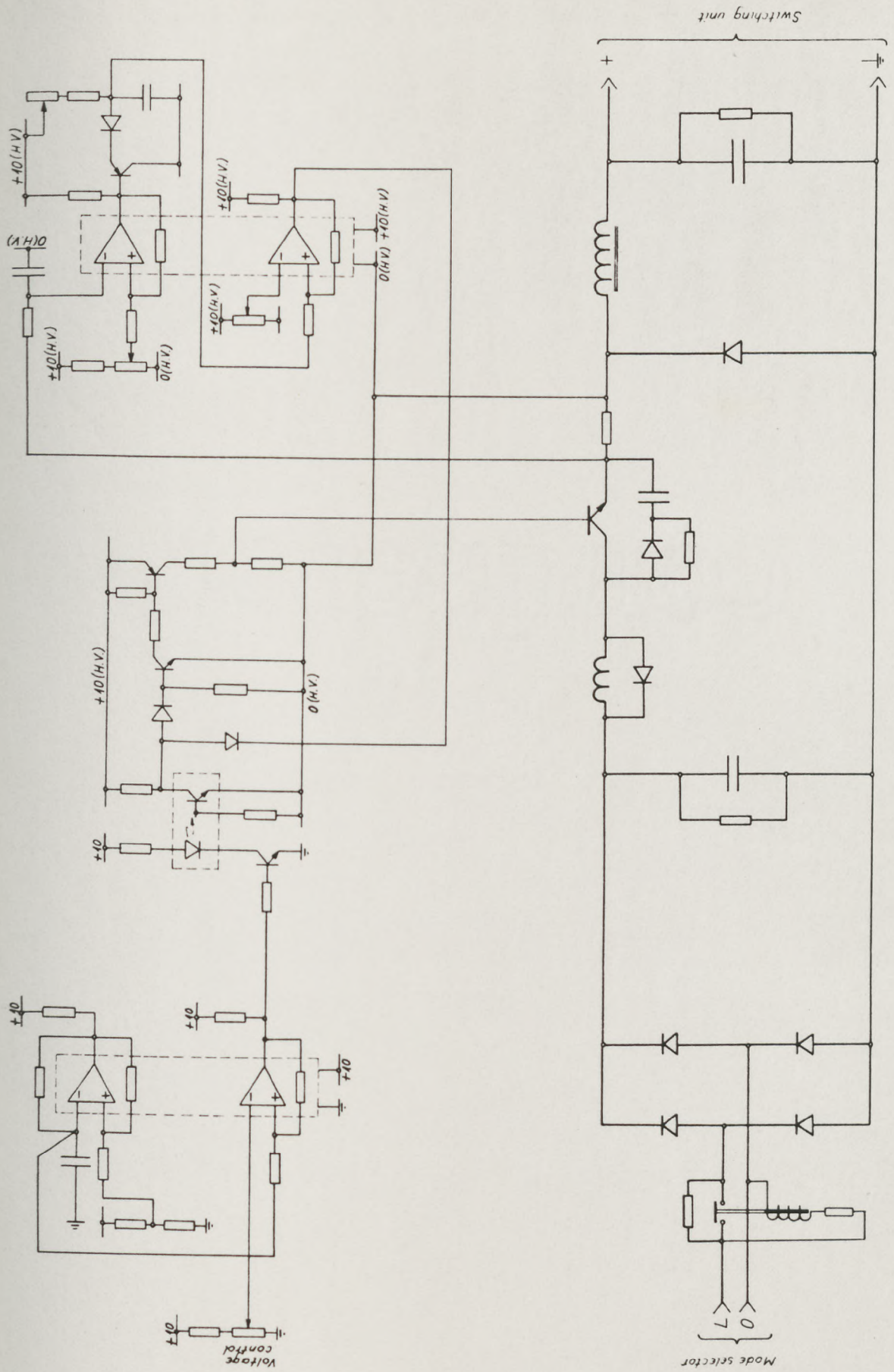


FIG 8.5(e) DC chopper

FIG 8.6 Component parts of the motor for voltage controlled drive



FIG 8.7 Converter for voltage controlled drive

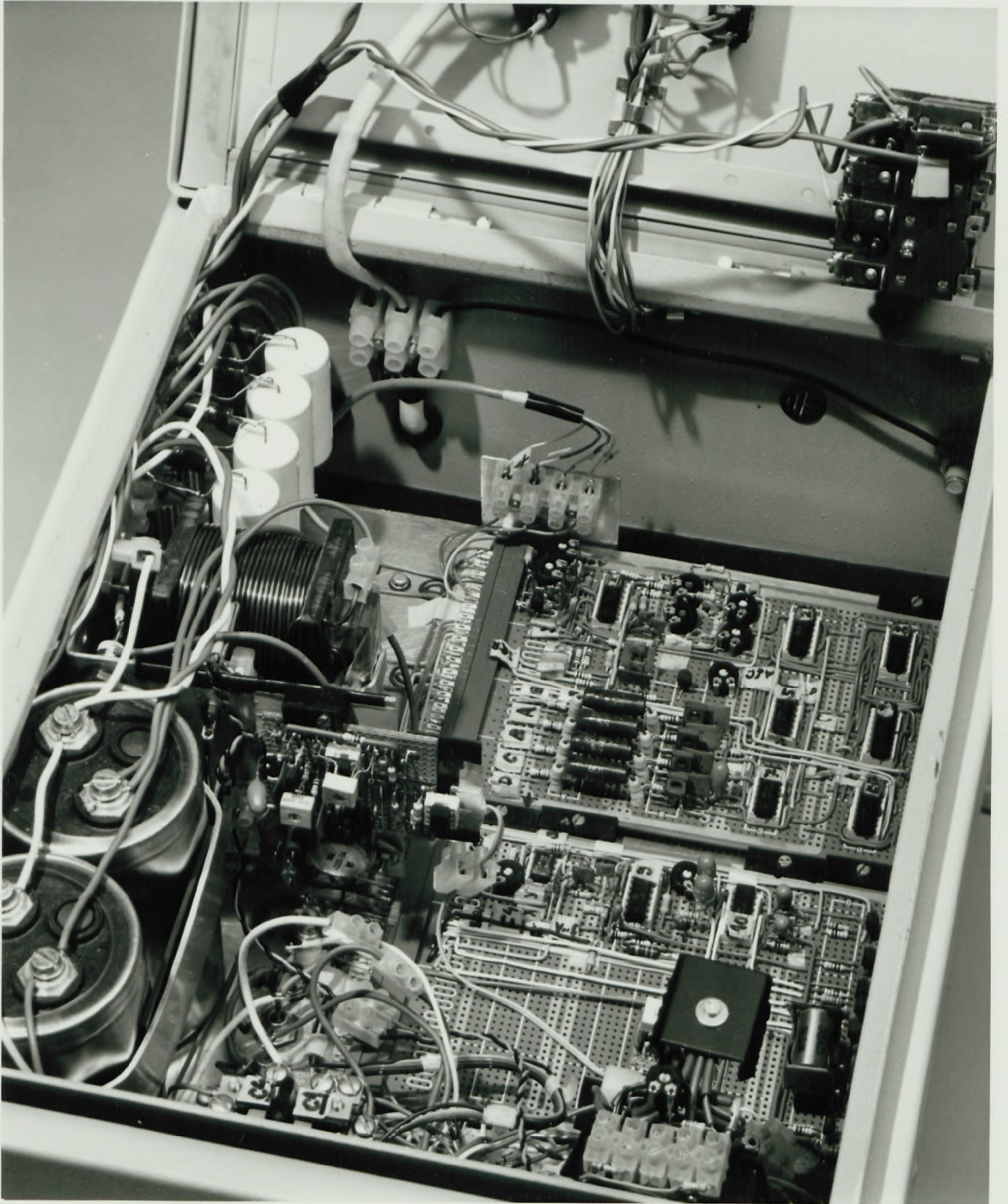


FIG 8.8 Prototype of voltage controlled drive



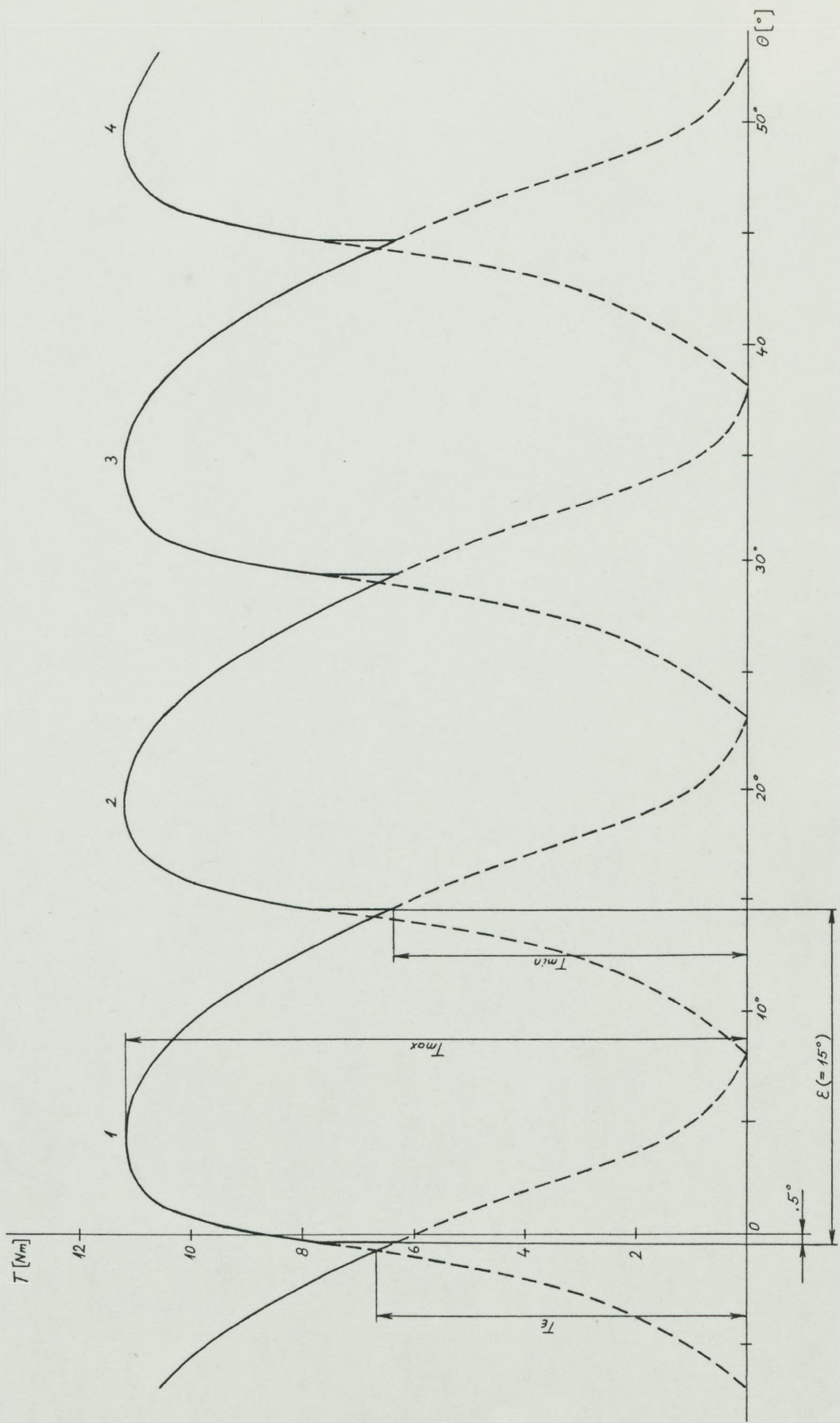


FIG 8.9 Starting torque curve of D90M2-4 motor at 10 [A]

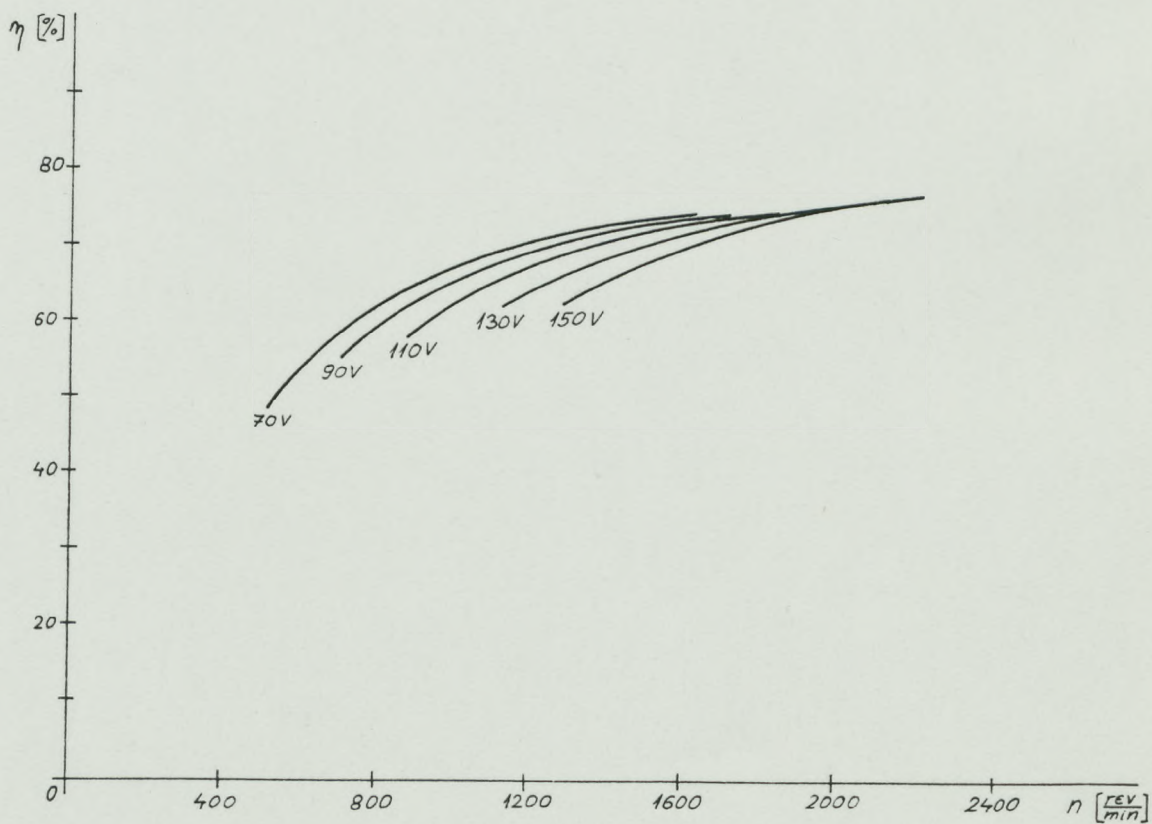
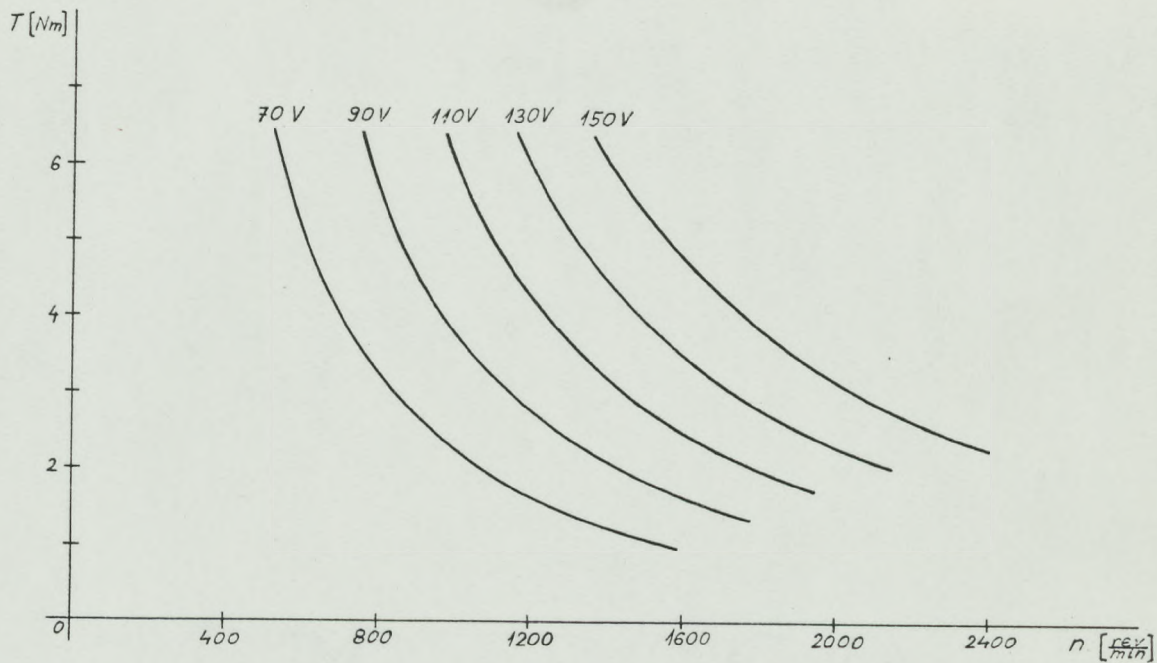
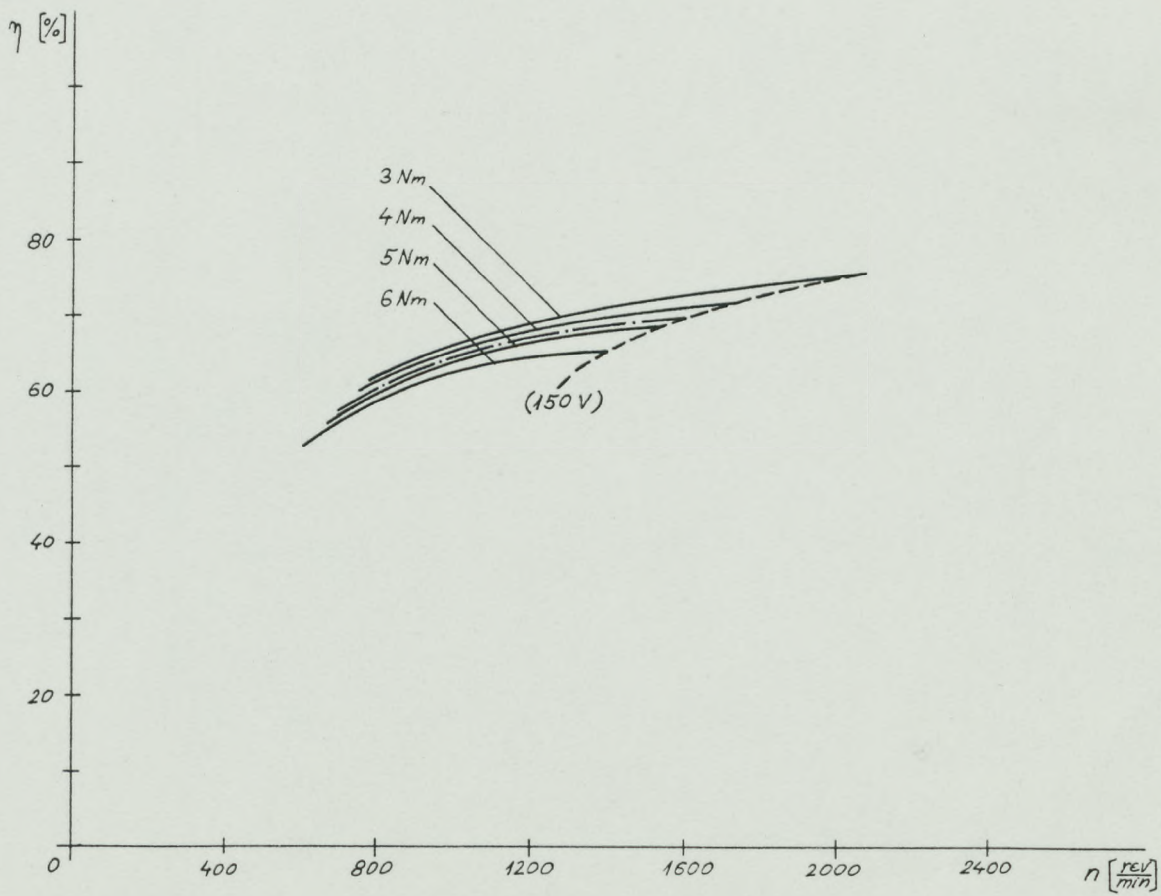
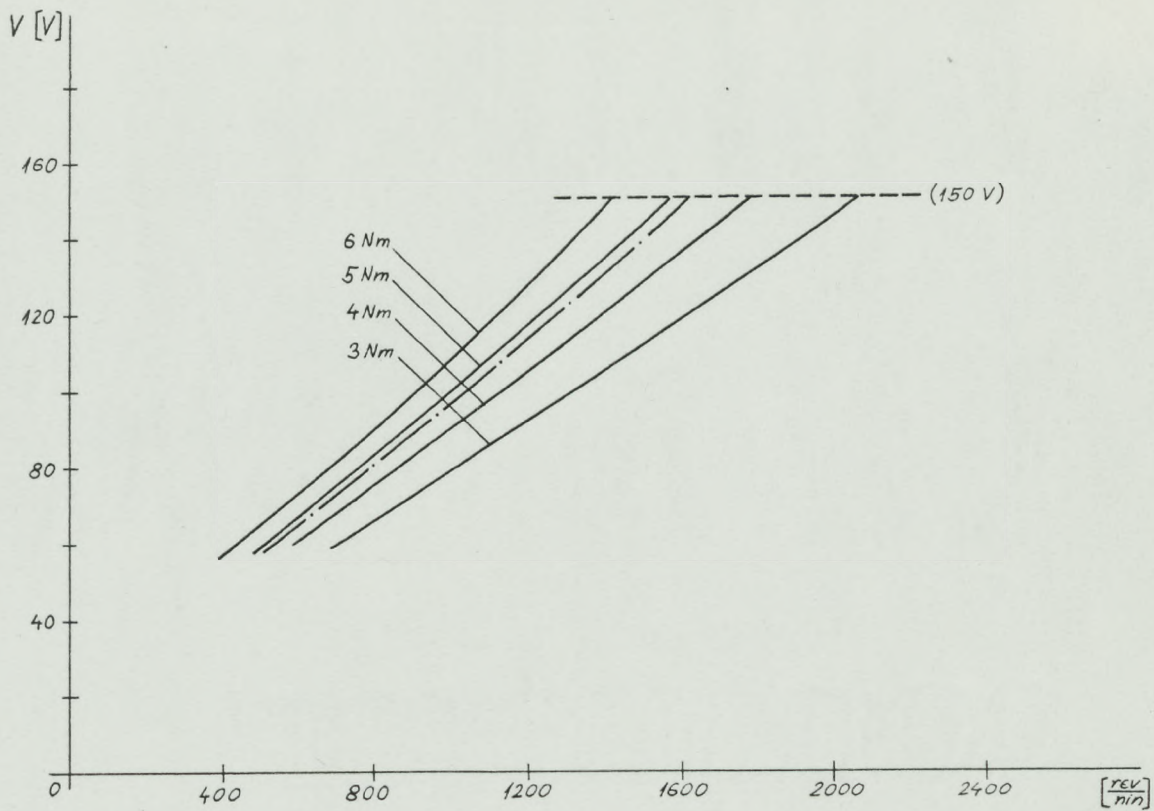


FIG 8.10 Torque and efficiency against speed curves at a constant supply voltage



Continued

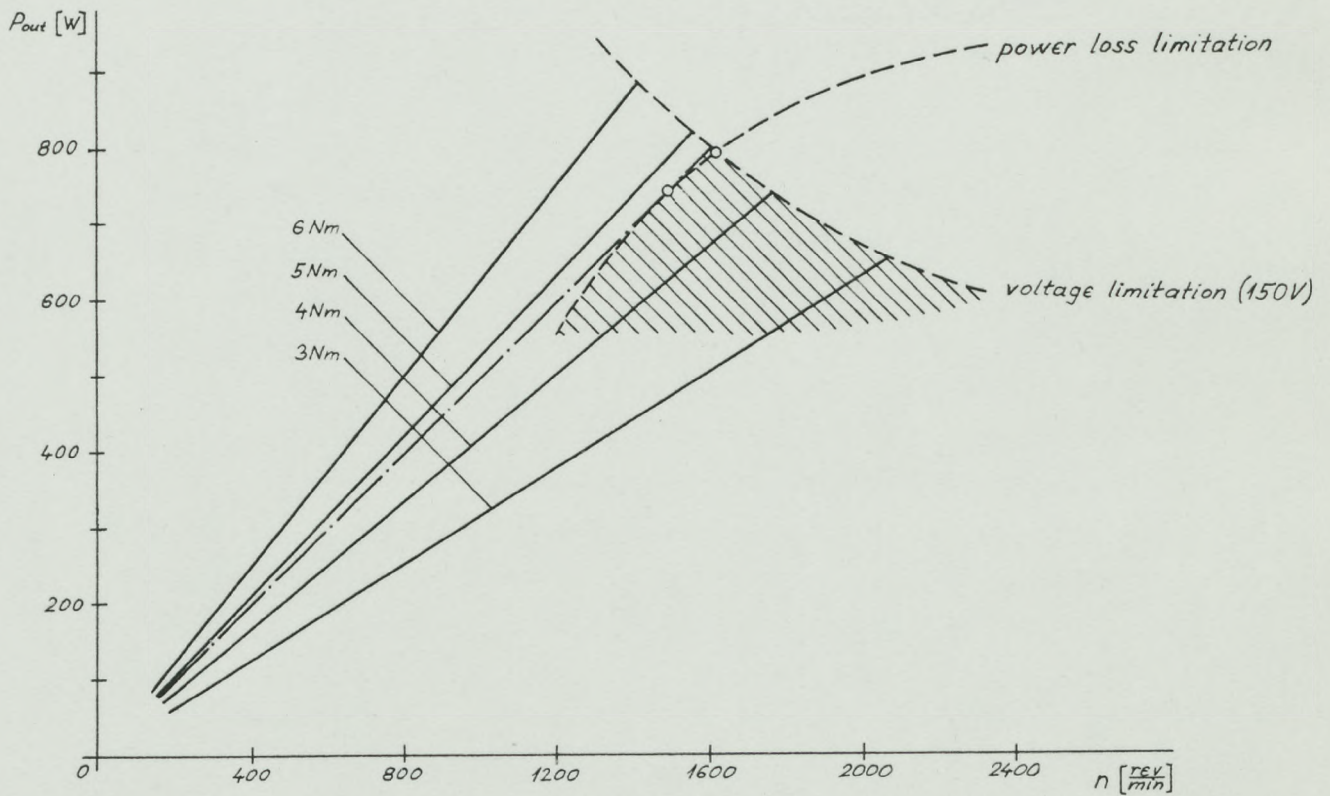
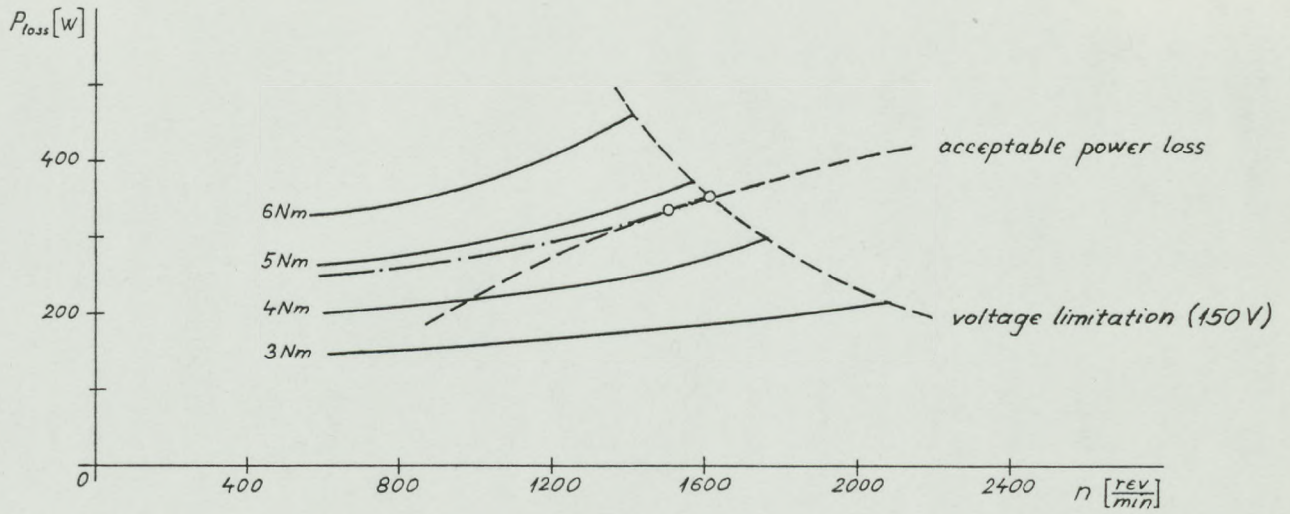


FIG 8.11 Supply voltage, efficiency, power loss and output power against speed at a constant torque up to the maximum value of supply voltage of 150 [V]

CHAPTER 9

CONCLUSION

The subject of the thesis has been the switched reluctance motor which is a machine based on reluctance principles in association with electronic switching. The motor has salient poles on both the stator and rotor, has no brushes, slip rings, coil slots or moving coils and uses only unidirectional currents in the simple coils which are on the stator poles. The pairs of opposite coils form phases which are switched onto a dc voltage supply by electronic switches which operate according to the position of the rotor poles relative to those of the stator. Using bifilar secondary coils as a means for returning the stored magnetic energy to the supply, the number of switching devices per phase is unity (half the number in variable-speed drives which use ac motors).

Although very simple, the drive system using a switched reluctance motor is capable of full motoring and regenerative operation over a wide speed range. Speed control in the constant torque region is achieved by controlling the voltage and the control in the constant power region is achieved by controlling the turn-on and off angles of the phase switches.

Although the complete and refined optimisation of the geometry of the switched reluctance motor has not been made, the experimental results have revealed that, having regard to the overall simplicity of the drive, its specific output and efficiency (particularly with increasing output power), the switched reluctance motor system compares favourably with the available dc systems which have so far dominated in variable-speed drives.

The switched reluctance motor system is attractive for many variable speed applications because of its simplicity, brushless construction, ruggedness, no maintenance, reliability, ease of manufacturing and cheapness. Having these features and a 'series' type of torque/speed characteristic with the possibility of operation over a wide speed range at constant power, the system is very attractive for traction

applications and in particular for battery powered electric vehicles since it requires a dc power source voltage.

Linear and nonlinear theoretical studies and experimental investigations on the prototype drives presented in this thesis have brought broad understanding of the machine operation and behaviour, and have shown the capabilities of the system. The mathematical model which has been developed and the proposed design procedure are useful means for further work. The attractiveness of the system is a stimulus for further work in the following fields of general interest:

- Optimisation of machine geometry with respect to the machine performance. The mathematical model can be used for this investigation but a three-dimensional numerical field solution for predicting the magnetic parameters from the given dimensions of magnetic structure is needed;
- Investigation of iron loss and implementation of its effect in the mathematical model. This is particularly important for machines of larger size;
- Work on the 3-phase system. Although this system has an apparently worse starting performance than the 4-phase system, it requires fewer switching devices and in addition it may have better running performance;
- Dynamic behaviour of the system.

A large number of specific fields for investigation will arise through various applications of the machine.

REFERENCES

1. P T Blenkinsop
A novel, self-commutating, singly-excited motor
PhD Thesis, October 1976
The University of Leeds, Department of Electrical and Electronic Engineering
2. P J Lawrenson, L A Agu
Theory and performance of polyphase reluctance machines
Proc IEE, Vol 111, No 8, Aug 1964, pp 1437-1445
3. V B Honsinger
Steady-state performance of reluctance machines
Trans IEEE, PAS 90, No 1, Jan/Feb 1971, pp 305-311
4. R Pohl
Theory of pulsating machines
Jour IEE, Pt II, 1946, pp 36-47
5. L E Unnewehr, W H Koch
An axial air-gap reluctance motor for variable speed applications
Trans IEEE, Jan/Feb 1974, pp 367-376
6. J V Byrne, J G Lacy
Characteristics of saturable stepper and reluctance motor
Proc of the IEE Conf on Small Electrical Machines
London, March 1976, pp 93-96
7. H Baush, B Rieke
Speed and torque control of thyristor-fed reluctance motors
Proc of Int Conf on Electrical Machines
Vienna, Sept 1976, pp I28.1-I28.10
8. A Hughes, P J Lawrenson, P P Acarnley
Effect of operating mode on torque-speed characteristics of VR motors
Proc of the Int Conf on Stepping Motors and Systems
University of Leeds, July 1976, pp 17-24

9. P P Acarnley
Analysis and improvement of the steady-state performance of
variable-reluctance stepping motors
PhD Thesis, October 1977
The University of Leeds, Dept of Electrical and Electronic Eng
10. J Čorda, N N Fulton, J M Stephenson
A study of the basic design parameters of switched reluctance
motors
Leeds University Publication, June 1977
11. M R Harris, A Hughes, P J Lawrenson
Static torque production in saturated doubly-salient machines
Proc IEE, Vol 122, No 10, Oct 1975, pp 1121-1127
12. H D Chai
Permeance model and reluctance force between toothed structures
Proc of the 2nd Symposium on Incremental Motion Control System
and Devices
University of Illinois, Chicago, May 1973, paper K
13. A L Jones
Permeance model and reluctance force between toothed structures
Proc of the 5th Symposium on Incremental Motion Control System
and Devices
University of Illinois, Chicago, May 1976, paper H
14. F W Carter
The magnetic field of the dynamo-electric machine
Jour IEE, 1926, pp 1115-1138
15. K C Mukherji, S Neville
Magnetic permeance of identical double slotting
Proc IEE, Vol 118, No 9, Sept 1971, pp 1257-1268
16. P A Ward, P J Lawrenson
Magnetic permeance of doubly-salient airgaps
Proc IEE, Vol 124, No 6, June 1977, pp 542-543

17. H C Roters
Electromagnetic Devices
Wiley, 1963
18. K J Binns, P J Lawrenson
Analysis and computation of electric and magnetic field problems
Pergamon Press, 1973
19. T Bosanac
Teoretska elektrotehnika
Tehnička knjiga - Zagreb, 1973
20. A E Clayton, N N Hancock
The performance and design of direct current machines
Pitman, 1971
21. M B Say
Alternating current machines
Pitman, 1976
22. C V Jones
The unified theory of electrical machines
Butterworths, 1967
23. L Fox, D F Mayers
Computing methods for scientist and engineers
Clarendon Press - Oxford, 1968
24. G Singh
Mathematical modelling of step-motor
Proc of the 1st Symposium on Incremental Motion Control System
and Devices
University of Illinois, Chicago, 1972, pp 59-148
25. I E D Pickup, D Tipping
Method for predicting the dynamic response of a variable
reluctance stepping motor
Proc IEE, Vol 120, No 7, July 1973, pp 757-765

26. I E D Pickup, D Tipping
Prediction of pull in rate and settling-time characteristics
of a variable-reluctance stepping motor and effect of stator-damping
coils on these characteristics
Proc IEE, Vol 123, No 3, March 1976, pp 213-219
27. J V Byrne, J B O'Dwyer
Saturable variable reluctance machine simulation using exponential
function
Proc of the Int Conf on Stepping Motors and Systems
University of Leeds, July 1976, pp 11-16
28. J Čorda, P J Lawrenson, J M Stephenson
Non-linear modelling of the doubly-salient switched reluctance
motor
Leeds University Publication, March 1977
29. A J C Bakhuizen, J G Niesten, M L G Thoone
Is saturation a blessing in disguise
Proc IEE, Vol 125, No 5, May 1978, pp 407-410
30. P J Lawrenson, D P Hodson, M R Harris
Electromagnetic forces in saturated magnetic circuits
Proc of the IEE Conf on Small Electrical Machines
London, March 1976, pp 89-92
31. J H Lang, R D Thornton
Power optimal excitation of variable reluctance motors
Int Quarterly: Electric Machines and Electromechanics,
No 2, 1978, pp 123-135
32. W H Koch
Thyristor controlled pulsating field reluctance motor system
Int Quarterly: Electric Machines and Electromechanics
No 1, 1977, pp 201-215
33. H Bausch, B Rieke
Performance of thyristor-fed electric car reluctance machines
Proc of Int Conf on Electrical Machines
Brussels, Sept 1978, E4/2-1

34. H Bausch, H J Kobler
Magnetic fields in traction machines for electric car
Proc of Int Conf on Electrical Machines
Brussels, Sept 1978, G1/1-1

35. J Simkin, C W Trowbridge
A comparison of the various scalar and vector potentials for
the numerical solution of the non-linear Poisson problem
Rutherford Laboratory Publication, Jan 1978

36. J M Peter, J C Baudier, J Redoutey, B Maurice, K Rischmueller
Power transistor in switching mode
Sescosem-Thomson-CSF, 1975

37. J M Stephenson, J Čorda
Computation of torque and current in doubly-salient reluctance
motors from nonlinear magnetisation data
Proc IEE, Vol 126, No 5, May 1979, pp 393-398